THERMODYNAMIC ANALYSIS OF TRIGENERATION SYSTEM

Thesis Submitted
In Partial Fulfillment of the Requirements
for the Degree of

DOCTOR OF PHILOSOPHY

By

AFTAB ANJUM
(Roll No. 2K16/PHDME/64)

Under the Supervision of

Dr. Samsher
Professor
Department of Mechanical Engineering
Delhi Technological University

Dr. R.S. Mishra
Professor
Department of Mechanical Engineering
Delhi Technological University

To the
Department of Mechanical Engineering

Delhi Technological University, Delhi
(Formerly Delhi College of Engineering)
Shahbad Daulatpur, Bawana Road, Delhi-110042, India. Delhi 110042, India

November 2024

ACKNOWLEDGEMENTS

Without the assistance of numerous people, the accomplishment of this research would not have been feasible. I want to start by expressing the gratitude to my supervisor, Prof. Radhey Shyam Mishra and Prof. Samsher (Presently: Vice Chancellor, HBTU Kanpur) for their unwavering support and inspiration. Their commitment towards research has always inspired me to put in a lot of effort and aim high. Their time, ideas, patience, and continuous input on all the research articles are greatly appreciated. I would also like to extend sincere gratitude to my research committee; Prof. Atul Kumar Agrawal **(**DRC Chairman) DTU Delhi; Prof. Imran Khan, Jamia Millia Islamia, New Delhi; Dr. A.K. Sharma, NIT Kurukshetra; Prof. Akhilesh Arora, DTU, Delhi; Dr. Naushad Ahmad Ansari, DTU, Delhi; Dr. Manjunath. K, DTU, Delhi. Additionally, I would want to express my gratitude to research scholars and colleagues who have always provided me with invaluable advice when needed. It gives me great pleasure to express my sincere gratitude to everyone who supported me during my doctoral studies. I am thankful to my parents and family members for their valuable guidance, persistent help and support during my PhD journey.

AFTAB ANJUM

DELHI TECHNOLOGICAL UNIVERSITY

(Formerly Delhi College of Engineering)
Shahbad Daulatpur, Main Bawana Road, Delhi-42

CANDIDATE'S DECLARATION

I, Aftab Anjum, hereby certify that the work which is being presented in the thesis titled "**Thermodynamic Analysis of Trigeneration System**" in partial fulfilment of the requirements for the award of the Degree of Doctor of Philosophy, submitted in the Department of Mechanical Engineering, Delhi Technological University is an authentic record of my own work carried out during the period from 01-08-2016 to 30-07-2024 under the supervision of Prof. R. S. Mishra and Prof. Samsher. The matter presented in the thesis has not been submitted by me for the award of any other degree of this or any other Institute.

Place: Delhi **AFTAB ANJUM**

Date: (2K16/PhD/ME/64)

DELHI TECHNOLOGICAL UNIVERSITY

(Formerly Delhi College of Engineering)
Shahbad Daulatpur, Main Bawana Road, Delhi-42

CERTIFICATE BY THE SUPERVISOR

Certified that **Aftab Anjum (**2K16/PHDME/64) has carried out their research work presented in this thesis entitled **"Thermodynamic Analysis of Trigeneration System"** for the award of **Doctor of Philosophy** from Department of Mechanical Engineering, Delhi Technological University, Delhi, under my supervision. The thesis embodies results of original work, and studies are carried out by the student himself and the contents of the thesis do not form the basis for the award of any other degree to the candidate or to anybody else from this or any other University/Institution.

Dr. Samsher
Professor, (Presently: Vice Chancellor, HBTU Kanpur)
Department of Mechanical Engineering
Delhi Technological University,
Delhi-110042

Dr. R.S. Mishra
Professor
Department of Mechanical Engineering
Delhi Technological University,
Delhi-110042

ABSTRACT

Energy is essential for sustaining human life and is a key indicator of a society's prosperity and development. However, rapid population growth and industrialization have significantly increased global energy demand for electricity, heating, and cooling, leading to energy crises. To meet this demand, excessive use of fossil fuels, which are already limited in availability, has become prevalent. Consequently, burning these fuels, particularly the emission of greenhouse gases like CO_2, has contributed to severe environmental issues such as global warming and climate change.

Addressing these challenges requires adopting advanced technologies to reduce global warming and enhance energy system efficiency. Various nations have proposed and implemented solutions to mitigate environmental impact. One promising approach is the use of trigeneration systems, which can meet rising energy needs in a cleaner, more sustainable and cost-effective manner. Trigeneration systems utilize waste heat recovery to produce electricity, heating, and cooling simultaneously from a single fuel source. Notably, helium turbine-based trigeneration systems, combined with efficient waste heat recovery through organic Rankine cycles, are widely employed in industrial applications, particularly in process industries. These systems offer high efficiency, low pollution, reduced capital costs, flexibility, and the capability to generate multiple forms of energy.

This thesis proposes novel helium turbine-based trigeneration systems (Combined Cooling, Heating, and Power systems) for the simultaneous generation of electricity, chilled water, and hot water. A solar power tower (SPT) system is a promising option to harness solar energy for solar thermal electricity generation via power cycles. These days, combined cycles, especially those based on the supercritical helium Brayton cycle, are very popular. The performance of different configurations of helium Brayton cycles (HBC) driven with SPT has been further investigated in this thesis work. Apart from this, organic Rankine cycle (ORC), ejector refrigeration system (ERC), cascaded vapour absorption refrigeration-vapour compression refrigeration (VAR-VCR) system, and cascaded ejector refrigeration-vapour compression refrigeration (ERS-VRS) system were used as bottoming waste heat recovery cycles. Also, a short analysis has been performed with a combined Rankine power and vapour absorption refrigeration (VAR) cycle, a CCHP system driven by a low-temperature heat source using various eco-friendly refrigerants for cooling, heating, and power

generation. Simultaneously, the effects of the working fluids on the system performance were investigated. First, the output of the SPT-based combined HBC and ORC with an ejector refrigeration integrated system for combined heating, cooling, power generation, and waste heat recovery was investigated.

The trigeneration system comprises a Brayton cycle using helium as the working fluid and an organic Rankine cycle (ORC) integrated with an ejector refrigeration system (ERS) to recover waste heat from the Brayton cycle. The Brayton cycle and ORC generate power, while the evaporator and condenser provide simultaneous cooling and heating, respectively. The heating and cooling effects were generated at 50°C and 10°C for building applications such as hospitals and hostels. Finally, when all the studied parameters are considered, the optimal system exhibits exergy and energy efficiency of 25.12% and 23.3%, respectively.

This study evaluates the performance of a combined helium Brayton cycle (HBC) and organic Rankine cycle (ORC) system, which incorporates a cascade vapour absorption-refrigeration (VAR) and vapour compression-refrigeration (VCR) system as the bottoming cycle. By using the ultra-low GWP working fluid R410a, the system aims to minimize global warming and ozone depletion. Designed for solar power tower (SPT) plants, this trigeneration system efficiently produces electricity, heat, and cooling at low temperatures using a high-temperature SPT heat source. It integrates cascaded VAR-VCR refrigeration technology with the helium Brayton cycle to deliver power, heating, and low-temperature cooling (-20°C) for applications like food preservation. The SPT plant achieves a power output of 14,865 kW, an exergy efficiency of 39.53%, and an energy efficiency of 28.82%. The coefficients of performance for cooling and heating are 0.5391 and 1.539, respectively. Exergy analysis indicates that the solar subsystem contributes to 78.18% of the total energy destruction in the plant. Key factors affecting performance include the temperatures of the evaporator, generator, helium turbine inlet, heliostat, and receiver efficiencies. This system outperforms configurations using supercritical CO_2 and Rankine cycles compared to prior studies.

Moreover, parametric analysis of the SPT-based combined HBC and ORC with cascade ERS-VRS integrated system was investigated. Effects of topping cycle parameters on combined cycle and ORC performance were also investigated. The organic Rankine (ORC) cycle, cascaded ejector refrigeration system (ERS), and vapour compression refrigeration (VCR) system have been implemented in the solar power tower (SPT)-based conventional helium Brayton cycle (HBC) to enhance the performance of the solar-based energy

generation system. It was concluded that the overall proposed solar plant (SPT-HBC-ORC-ERS-VCR) obtained energy efficiency, exergy efficiency, and network output of 60.66%, 35.55%, and 15585 kW, respectively.

The study's fourth phase involved a thermodynamic analysis of integrated systems combining rankine-absorption power and refrigeration cycles designed to simultaneously produce cooling and power. The system generates both outputs from a single heat source using a binary liquid mixture of water and ammonia as the working fluid. Key parameters influencing net power output, refrigeration output, and exergy efficiency include the heat source temperature, ambient temperature, refrigeration temperature, turbine intake pressure, turbine inlet temperature, and ammonia concentration in the solution. Results show that increasing the turbine inlet pressure improves the cycle's energy and exergy efficiencies. Energy dissipation primarily occurs in the heat exchanger exhaust, followed by losses in the heat exchanger, boiler, turbine, superheater, absorber, condenser, and rectifier. The system's energy and exergy efficiencies were evaluated and compared with energy loss distributions. This integrated cycle is well-suited for solar thermal power generation using cost-effective concentrating collectors, which can lower initial investment costs for solar thermal facilities.

Finally, a study of a combined power, heating, and cooling integrated system driven by a low-temperature heat source was examined using six ultra-low GWP eco-friendly refrigerants as working fluids. This study describes an integrated power, cooling, and heating cycle incorporating an ejector refrigeration system, an ORC, and condenser heating with a low-temperature heat source. Thermodynamics' first and second laws were used to analyze the performances of six distinct alternative refrigerants on the combined cycle. The influence of the most important parameters, including evaporator temperature, turbine entering temperature, heat source temperature, refrigeration output, exergy efficiency, entrainment ratio, thermal efficiency, total exergy destruction, and thermal efficiency of the stated system using different environmentally friendly working fluids (R-123, R-124, R-141b, R-290, R-134a, and R-152a), was studied. Out of all the working fluids employed in this study, R-152a and R-134a are the most appropriate from an energy efficiency and environmental perspective for the suggested combined cycle. Energy efficiency drops as evaporator temperature rises and increases as turbine inlet temperature rises, respectively. Conversely, if the heat fluid temperature of the heat source and turbine entering temperature rises, the

cycle's thermal efficiency also rises. Furthermore, studies have found that as evaporator temperature rises, the ejector's entrainment ratio drops and refrigeration output rises.

The findings of this study are expected to offer significant insights into helium turbine-based trigeneration systems, contributing to the advancement of energy solutions that are efficient, clean, sustainable, and economically viable. By addressing critical aspects of system performance and efficiency, the results can serve as a valuable resource for researchers, engineers, and policymakers aiming to develop and implement cutting-edge energy technologies. These advancements have the potential to support global efforts in reducing greenhouse gas emissions and promoting the widespread use of renewable energy sources, thereby fostering a transition to a more sustainable energy future.

Table of Contents

List of Tables

List of Figures

List of Symbols

SOX	Sulphur Oxides
CO_2	Carbon Dioxide
NOX	Nitrogen Oxide
RES	Renewable Energy Source
CSP	Concentrated Solar Power
FPC	Flat Plate Collector
PTSC	Parabolic trough Collector
LFR	Linear Fresnel Reflector
PDR	Parabolic Dish Reciever
SPT	Solar Power Tower
HTF	Heat Transfer Fluid
sCO_2	Supercritical Carbon Dioxide
SRC	Supercritical Rankine Cycle
ORC	Organic Rankine Cycle
ODP	Ozone Depletion Potential
GWP	Global Warming Potential
WHR	Waste Heat Recovery
HRSG	Heat Recovery Steam Generator
CCPP	Combined Cycle Power Plant
ERS	Ejector refrigeration System
gm	Gram
Mol. wt	Molecular Weight
KJ/Kg	Kilo Jule Per Kilogram
CCHP	Combined Coolnig, Heating and Power
EES	Engineering Equation Solver
HBC	Helium Brayton Cycle
COP	Coefficient of Performance
VAR	Vapor Absorption Refrigeration
VCR	Vapor Compression Refrigeration
KW	Kilo Watt
IHE	Internal Heat Exchanger
WHRU	Waste Heat Recovery UNIT
T	Temperature
HTF	Heat Transfer fluid
h	Specific Enthalpy(kJ/kg)
s	Specific Entropy(kJ/kg·K)
OT	Organic Turbine
ρ	Density
DNI	Direct Normal Irradiation
HT	Helium Turbine
SHE	Solution Heat exchanger
E	Evaporator
CC	Cascade Condenser
HRVG	Heat Recovery Vapor Generator
P	Pressure
0	Ambient Condition
PG	Propylene Glycol

EJE	Ejector
v	Velocity
pf	Primary Flow
sf	Secondary Flow
mf	Mixed Flow
d	Diffuser
vmf	Vapor Mass Fraction
imf	Initial Mass fraction
$\dot{m}$	Mass Flow rate(kg/s)
K	Kelvin
°C	Degree Celcius
C	Condenser
η	Efficiency
N	Number
A	Area (m^2)
ε	Effectiveness
$\dot{E}D$	Exergy Destruction Rate (kW)
$\dot{E}X$	Rate of exergy (kW)
$\dot{Q}$	Heat Rate (kW)
$\dot{W}$	Power (kW)
PR	pressure Ratio
TIT	Turbine Inlet Temperature
j	particular State
e	Exit
i	Inlet
μ	Entertainment Ratio
PPR	Pump Pressure Ratio
HTIT	Helium Temperature Inlet Temperature
HC	Helium Compressor
CIT	Compressor Inlet Temperature

Chapter 1

Introduction

1.1. General Introduction

Energy is crucial for sustaining human existence and serves as an indicator of prosperity and development in society. Despite significant advancements in renewable energy over the past few decades, approximately 80% of global energy consumption still relies on fossil fuels [1]. The dependency on fossil fuels leads to pollution, particularly the release of greenhouse gases like CO_2, contributing to environmental problems like climate change and global warming. Additionally, conventional power plants are relatively inefficient, converting only about 30%-35% of the fuel's available energy into power, with a significant portion of the remaining energy being released as low-grade heat that contributes to thermal pollution [2, 3].

The increasing emissions of greenhouse gases and their detrimental impact on the climate are significant global concerns. Greenhouse gas emissions are composed of several key constituents, including water vapour (H_2O), chlorofluorocarbons (CFCs), hydro-fluorocarbons (HFCs), carbon dioxide (CO_2), methane (CH_4), nitrous oxide (N_2O), and ozone (O_3). These gases trap heat in the atmosphere, leading to a warming effect known as the greenhouse effect. This phenomenon contributes to various environmental issues, such as rising global temperatures, melting polar ice, sea level rise, and more frequent and severe weather events. Addressing these emissions is critical for mitigating climate change and ensuring a sustainable future for the planet [4].

According to the International Energy Association (IEA), CO_2 is the leading contributor to global warming among all greenhouse gases, with its emission rates surging by 61% between 1990 and 2021 [5]. This significant increase is largely attributed to the rising global demand for power, heating, and cooling, as highlighted by various studies [2]. Fossil-fuel-based electricity, heating, and cooling are responsible for 65% of total CO_2 emissions, while the transportation sector accounts for the remaining 35%. This data underscores the critical need for transitioning to cleaner energy sources to mitigate the adverse environmental impacts of CO_2 emissions.

The growing energy demands driven by global population expansion and industrial activities have intensified the challenge of reducing CO_2 emissions. As development and urbanization increase, so does dependence on fossil fuels, underscoring the urgent need for efficient and sustainable energy solutions. Implementing renewable energy sources and improving energy efficiency across sectors is crucial to creating a more sustainable and environmentally friendly energy landscape [6].

The unprecedented consumption of fossil fuels is driven by the rapid increase in global energy demand, particularly in developing market economies experiencing significant population and industrial growth [7]. Additionally, fossil fuels are finite resources, meaning their availability is limited and cannot sustain indefinite use. As fossil fuel reserves diminish, the cost of energy production escalates due to rising fossil fuel prices. This situation highlights the pressing need for alternative energy sources to meet growing energy needs sustainably [8].

Despite significant advancements in renewable energy, it remains insufficiently reliable to fully replace fossil fuel-based power plants at this time. Natural gas is the cleanest among fossil fuels, as its combustion releases less CO_2 into the atmosphere. Consequently, natural gas-powered energy systems present a potentially viable option for meeting global energy demands. The energy sector often markets natural gas as the “bridge to renewable energy” and natural gas-powered systems as “bridge technology” [9]. It is crucial to employ cutting-edge design techniques to enhance the effectiveness and sustainability of natural gas-driven energy generation. This approach aims to optimize both economic and environmental aspects, ensuring that natural gas systems can effectively serve as a transitional solution while renewable energy technologies continue to develop.

1.2. Energy-related scenario

In recent years, the depletion of fossil fuels has accelerated at an alarming rate, creating an urgent need to transition to renewable energy resources. This transition is imperative to prevent the depletion of fossil fuels and to reduce the environmental damage triggered by greenhouse gas emissions and other contaminants. Commercial and non-commercial energy sources can be distinguished.

Hydroelectric power, wind energy, fossil fuels, and nuclear power are all commercial energy sources. These sources are highly anticipated and extensively used, particularly in developed countries such as the United States and those in Europe. In contrast, non-commercial energy sources consist of wood, agricultural residues, and animal waste. While these non-commercial sources are still important, they are less frequently used compared to their commercial counterparts.

The increased reliance on commercial energy sources in developed nations underscores the importance of investing in renewable energy technologies. This investment addresses the urgent need for sustainable energy, reduces dependency on depleting fossil fuel reserves, and minimizes environmental harm. [10].

These renewable energy sources are carbon-free and include hydropower, solar, nuclear power, and wind. Transitioning from coal to hydrocarbon-based energy and ultimately to alternative or renewable energy sources reduces carbon emissions and pollutants [11]. The data in Figure 1.1 depicts the production and consumption of various energy resources worldwide in 2014, emphasizing the transition to cleaner energy options.

1.2.1. Coal

Coal-fired power facilities are substantial emitters of carbon dioxide, as well as sulphur oxides (SOX), nitrogen oxides (NOX), and particulate matter, all of which have the potential to impair air quality significantly. Mishra [12] has highlighted various negative environmental impacts and health hazards linked to using low-quality coal and its transportation over long distances by diesel trains. In the Indian context, addressing these challenges is particularly difficult due to ecological, radio-ecological, and pollution-related concerns. The transportation of coal not only exacerbates air pollution but also poses risks to public health and the environment, making it a complex issue to manage.

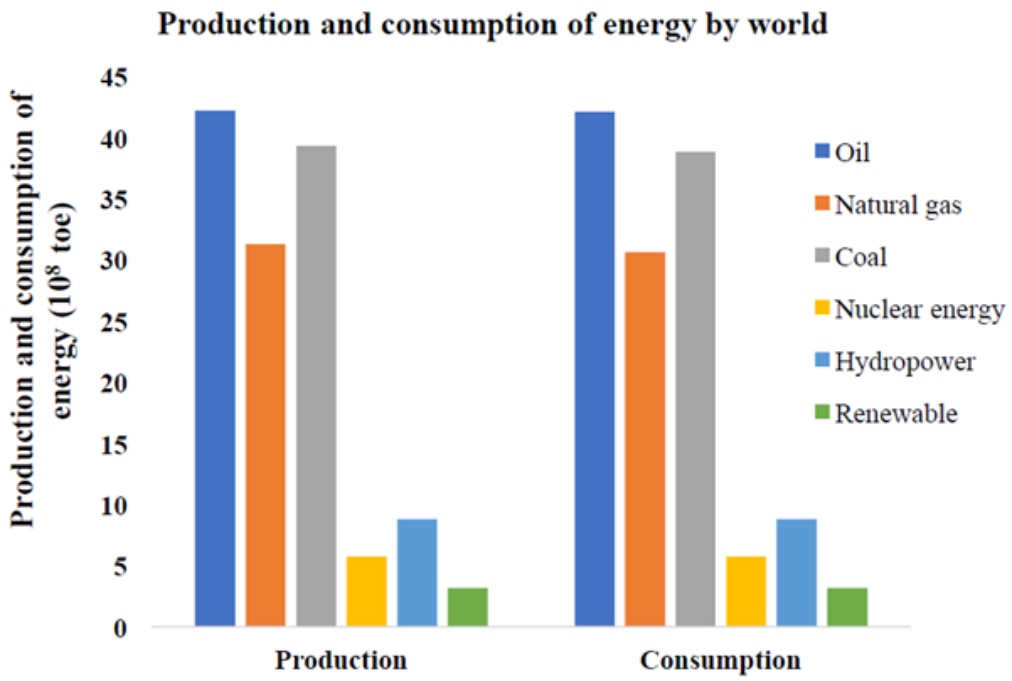

Figure 1.1 production and consumption of energy [11]

1.2.2. Natural gas and oil

India's energy requirements are both unsustainable and continually increasing, and its oil and natural gas reserves are inadequate to satisfy them. In 2009, crude oil production from India increased by as much as 81%, as illustrated in Figure 1.2.

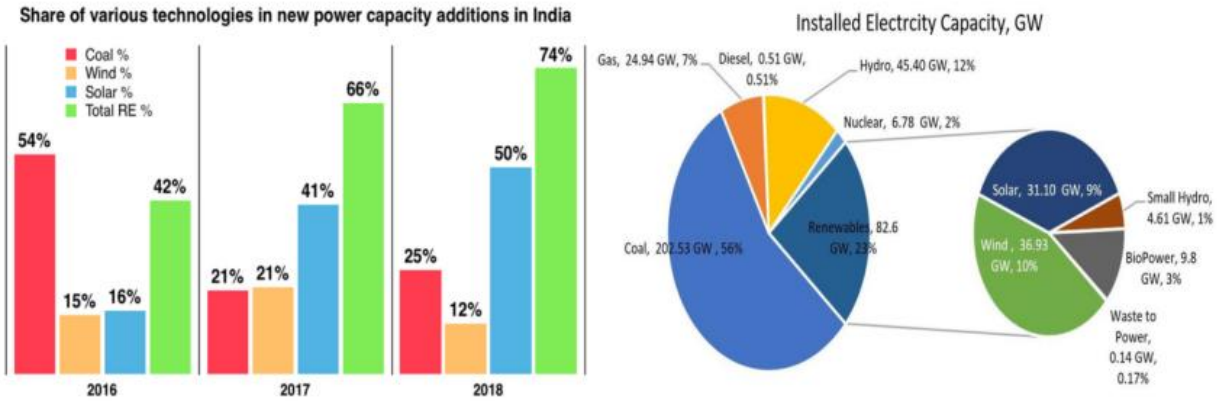

Figure.1.2 The fuel-wise growth in import dependence of the Indian energy sector [12]

Husain Ahmad reported oil prices' positive and negative impacts on the Indian economy [13]. On the positive side, the decrease in oil prices leads to immediate savings, enabling capital allocation to long-term assets that generate a high market return.

1.2.3. Hydro plant

India has utilized barely a quarter of its hydroelectric power capacity, unlike developed countries that have harnessed over 80% of their total potential [14]. In recent years, large hydroelectric projects in India have faced significant challenges due to local protests highlighting their adverse impacts on the climate, environment, and social fabric. Prominent examples of such resistance include the Narmada Bachao Andolan and the Anti-Tehri Dam movements, which have actively opposed the construction of major hydro projects on the Narmada and Ganges rivers, citing concerns over environmental degradation and displacement of local communities [15].

1.2.4. Nuclear power

India initiated its nuclear energy program in the 1960s by establishing the Tarapur nuclear power plant in 1969, which has a capacity of 320 MW. Throughout the years, the program has achieved incremental advancements, establishing twenty-two nuclear reactors distributed among seven nuclear power facilities. As of 2015, these reactors collectively generated a total of 6,780 MW of power. In addition, around five other reactors were being constructed at that time, with a total capacity of 3,300 MW [11]. In 2017, nuclear energy contributed to 3.22% of India's total power generation. For India to efficiently meet its increasing energy needs, improve energy security, and reduce environmental consequences, it is imperative to prioritize using renewable energy sources. This shift towards renewable energy is expected to significantly improve the overall energy landscape.

1.3. RES (Renewable energy sources)

Renewable energy sources (RES) are sustainable or "green" energy resources that aim to minimize environmental impacts and reduce secondary waste. The sun is the main provider of renewable energy, and efficiently harnessing RES can aid in reducing the adverse impacts of conventional energy sources on greenhouse gas emissions and global warming [16]. Three primary categories of energy resources are renewable energy, nuclear energy, and fossil fuels. Solar thermal, solar photovoltaic, small hydro, biomass, wind, and geothermal energy are the most promising alternative sources due to their continuous and sustainable energy generation

capabilities [17]. Furthermore, Figure 1.3 illustrates the various renewable energy resources and their applications in energy conversion.

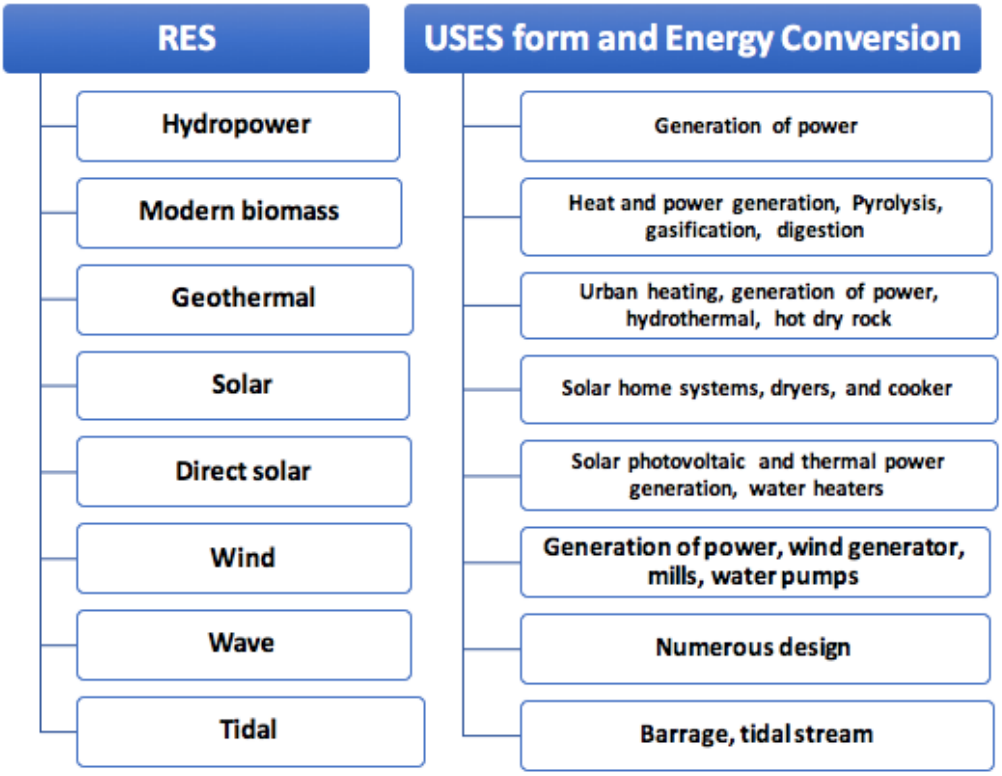

Figure 1.3 Renewable energy resources and their use in energy conversion [16, 17]

1.4. Solar energy

Solar energy is a renewable and environmentally friendly source of power. At a rate of approximately 3.8×10^{23} kW, the Earth absorbs approximately 1.8×10^{14} kW of the total energy emitted by the Sun [18]. On average, the Earth's surface receives about 1000 watts per square meter (W/m^2) of solar irradiation each day [19]. The solar constant, which measures the total solar energy reaching the Earth's surface per unit area when perpendicular to the incoming radiation, is approximately 1350 W/m^2 [20]. This value represents the intensity of solar energy received per unit area and time, providing a baseline for understanding solar energy availability.

1.4.1. Solar thermal power system

Solar concentrated energy is an increasingly valuable resource with great potential for providing electricity to the world's remote areas. These regions, although numerous, benefit from abundant solar irradiation, making solar energy a practical option for electricity generation there [21]. Solar thermal power systems [22] harness this solar energy through specialized devices to produce electricity directly. Sharma et al. [23] highlight that solar thermal electricity, or concentrated solar power (CSP), represents a burgeoning alternative energy technology with a notably low marginal cost of production. Ansari et al. [24] suggest that overcoming challenges to solar energy deployment in India involves exploring various strategies and optimizing the implementation of large-scale solar conversion techniques to manage resources efficiently and effectively.

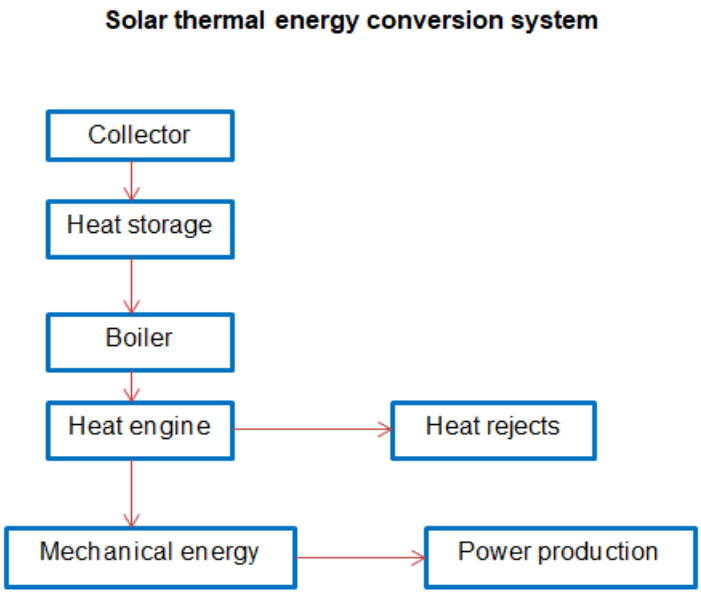

Figure 1.4 Solar thermal energy conversion systems

1.4.2. Solar collector

Solar collectors function as heat exchangers, converting solar radiation into thermal energy within a transport medium. They are a vital component of solar energy systems. A solar collector is a device that catches solar irradiation from the sun, turns it into thermal energy, and then transfers it to a fluid circulating through the collector. The fluid in question has the potential

to be either air, water, or oil. The thermal energy harnessed by the circulating fluid can be immediately employed for activities such as heating water and cooling indoor spaces. In addition, this energy can be stored in a thermal storage unit to be utilized during periods of reduced sunlight or at night [25]. Figure 1.5 illustrates the operation of a basic flat plate solar collector (FPC).

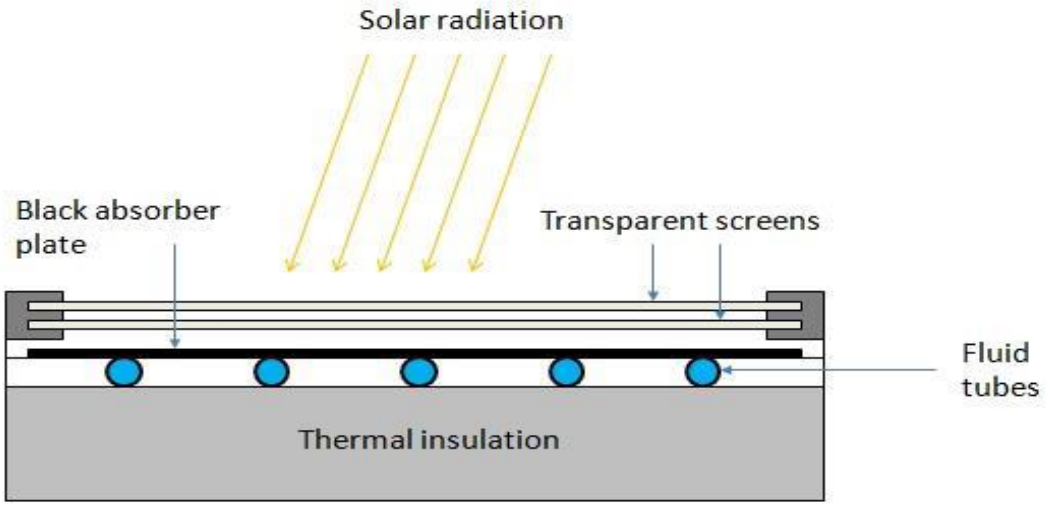

Figure 1.5 FPC in an exploded view (Credit: Mark Fedkin (modified after Duffie and Beckman, 2013)

Advantages of concentrating collectors compared to conventional flat plate collectors (FPC) [25]:

- A concentrating collector can achieve higher working fluid temperatures with the same energy-collecting surface area, leading to improved thermodynamic performance compared to an FPC.
- The thermal efficiency of a concentrating collector is enhanced due to its reduced heat loss area relative to the receiver's surface area.
- Concentrating collectors generally use less material and have a simpler design than FPCs, resulting in lower solar collecting surface area costs per unit.
- In concentrating collectors, the receiver has a smaller surface area relative to the amount of solar energy it produces. This allows for cost-effective measures, such as vacuum installation and selective surface treatment, to minimize heat losses and boost collector performance.

Disadvantages of concentrating collectors compared to traditional flat plate collectors (FPCs) [25]:

- Limited Diffuse Radiation Capture: Concentrating collectors primarily collect direct sunlight and are less effective at capturing diffuse radiation, which depends on the concentration ratio of the system.
- Requirement for Tracking Systems: These collectors need a tracking system to continuously align with the sun's position throughout the day, ensuring optimal performance.
- Maintenance Needs: Regular cleaning and maintenance are necessary for concentrating collectors due to their reflective surfaces, which can degrade over time and lose their reflectivity.

1.4.3. Technology of concentrated solar power (CSP)

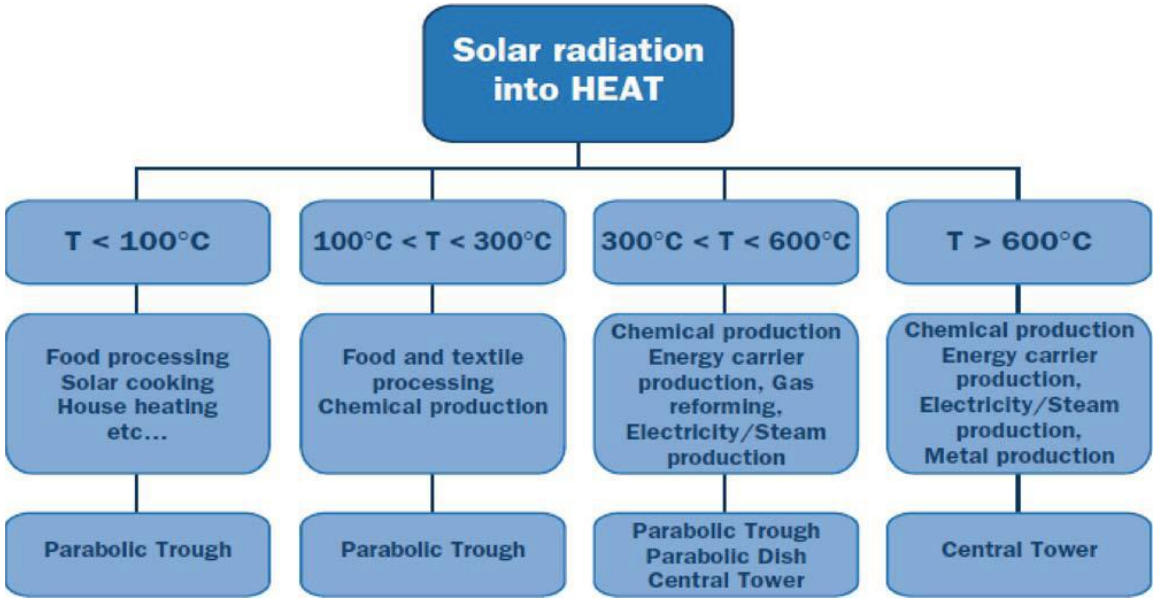

Figure 1.6 CSP system's application [26]

Concentrated Solar Power (CSP) systems utilize lenses or mirrors in conjunction with tracking devices to focus a broad area of sunlight into a concentrated beam. This concentrated thermal energy can then be harnessed to generate power in a conventional power plant setup. There are several advanced CSP technologies available, including Parabolic Trough Solar Collectors (PTSC), Linear Fresnel Reflectors (LFR), Parabolic Dish Receivers (PDR), and Solar Power

Towers (SPT). In these systems, intense sunlight heats a fluid, subsequently used to produce electricity and store energy for future use [26]. Figure 1.6 illustrates the diverse applications of CSP technology.

1.4.4. Central (heliostats) receiver system

The solar power tower (SPT) is the most recent technology among the different concentrated solar power (CSP) systems. The SPT system has various sophisticated sub-systems, including a receiver, a tower measuring 75-150 meters in height, an optional thermal storage system, a heliostat field with each heliostat covering an area of 50-150 square meters, and a power conversion system.

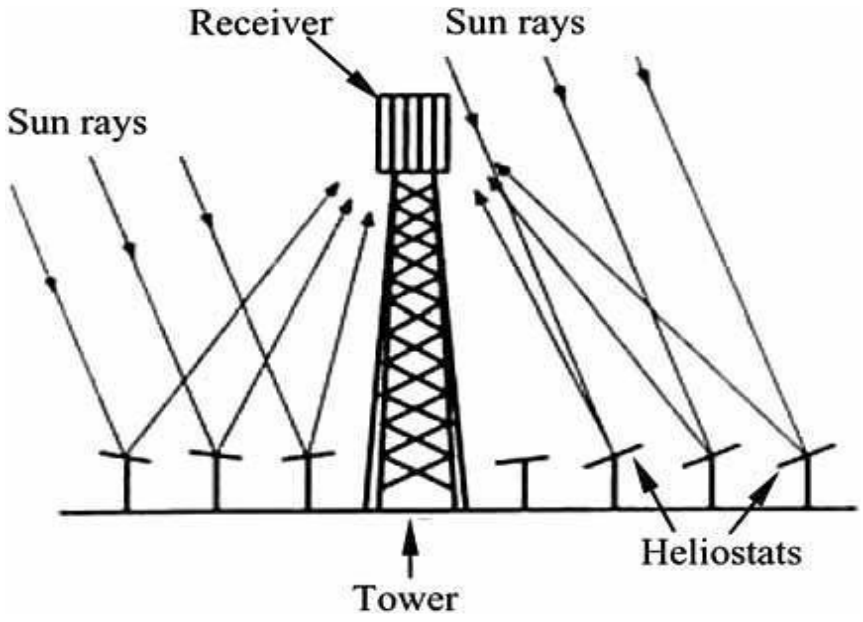

Figure 1.7 Diagram of central receiver tower [26]

Solar radiation is focused onto a central receiver by a field of heliostats, where it is harnessed to produce high-temperature heat for generating electricity or supplying industrial processes [27, 28]. The heat transfer fluid (HTF) receiver is at the top of a tower, surrounded by a vast array of heliostats that concentrate sunlight onto this central receiver, as depicted in Figure 1.7. Each heliostat has a unique monitoring system that guarantees that it remains focused on the receiver. The circulating HTF is heated by the concentrated sunlight, which is subsequently utilized to power a turbine. This approach enables the effective utilization of solar energy in various applications.

The solar power tower is the most cost-effective concentrated solar power (CSP) technology, known for its superior energy storage capabilities and performance. Examples include Barstow, California, and Sanlúcar la Mayor, Spain installations. Solar power towers offer advantages such as a high concentration range of 300 to 1500, improving energy capture and electricity conversion efficiency. Unlike parabolic trough collectors, solar power towers can reduce mid-term electricity costs by incorporating multiple intermediate stages within high-energy cycles. These stages utilize gas turbines to generate electricity at temperatures exceeding 1000°C, offering greater efficiency than the conventional Rankine cycle. [25].

1.5. Technology of supercritical carbon dioxide (sCO_2) cycle

When carbon dioxide (CO_2) is subjected to temperatures and pressures above its critical values (304.13 K and 7.38 MPa), it enters a state known as supercritical carbon dioxide (sCO_2). CO2 can be utilized as a working fluid in various energy conversion cycles in this supercritical state. The sCO_2 cycle is particularly versatile, allowing for the generation of heat from diverse sources, including waste heat from exhaust gases, natural gas, geothermal energy, solar thermal energy, and coal power [29]. This adaptability makes the sCO_2 cycle an efficient option for harnessing heat from multiple inputs. Figure 1.8 illustrates the fundamental principles of the sCO_2 cycle power conversion system.

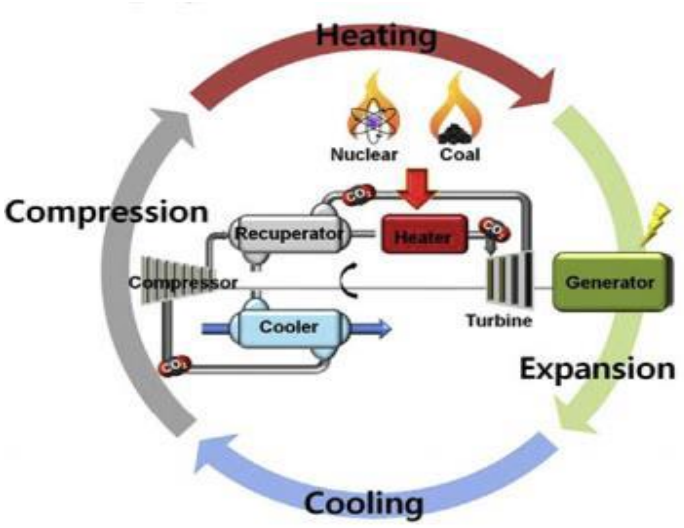

Figure 1.8 Principle of sCO_2cycle power conversion system [29]

Additional benefits of sCO_2 cycle technology include:

- The thermal efficiency of the sCO_2 cycle can be enhanced by up to 5% compared to the supercritical Rankine cycle (SRC) [29].
- The sCO_2 cycle allows for smaller turbo-machinery and can reduce the overall system size by up to four times compared to traditional SRC systems [29].
- The sCO_2 cycle's purification system requirements are less stringent than the SRC system's due to its operating pressure being above the CO_2 critical pressure (7.38 MPa). These results in simpler power conversion mechanisms than steam cycles [29].

CO_2 and helium, used in the sCO_2 cycle, are relatively more economical and pose less risk regarding ventilation systems designed to handle potential large-scale CO_2 releases in power conversion systems [29].

1.6. Technology of supercritical helium Brayton cycle (HBC)

The helium Brayton cycle has gained considerable interest in high-temperature power generation systems, having numerous helium Brayton cycle reactor systems already operational worldwide, including nine specific installations [30]. Helium can be used as a substitute for supercritical CO_2 (sCO_2) to enhance the heat transfer properties of the Brayton cycle, which improves the system's overall efficiency and reduces the number of compressor stages required. The helium Brayton cycle is currently being incorporated into the conceptual design of the third-circuit energy conversion system within advanced high-temperature reactor (AHTR) systems [31]. The solar-based helium Brayton system is also a promising option for high-temperature applications. The helium Brayton cycle can utilize high-temperature primary coolants and achieve efficiencies of up to 54% at 900°C with the use of triple-pressure recuperation and intercooling. Brayton cycles employing inert gas working fluids can exploit higher outlet temperature ranges, significantly boosting power conversion efficiency and potentially lowering capital costs for power conversion systems compared to traditional steam Rankine and sCO_2 cycles.

1.7. Organic Rankine cycle (ORC) technology

When it comes to generating electricity, gas or steam cycles often fall short both technically and economically for a diverse array of heat sources, particularly when the temperature and thermal power available from these sources are low. An organic Rankine cycle (ORC) system becomes a practical alternative in such scenarios. The ORC technology excels in generating electricity from small-scale heat sources and operates effectively at temperatures in the lower to medium range (below 400°C-500°C) [32]. This makes ORC a superior choice for converting low-temperature heat into electrical energy, whereas other methods may be impractical.

Organic Rankine cycle (ORC) technology functions similarly to a steam cycle, but instead of using refrigerants or hydrocarbons, it employs water as the working fluid. Water offers numerous benefits as a working fluid. It boasts high thermal and chemical stability, eliminating the need for decomposition. Its low viscosity translates to reduced pumping work, while its high latent and specific heat makes it an efficient energy carrier. Additionally, water is non-flammable and has a negligible ozone depletion potential (ODP) and global warming potential (GWP). Being abundant and cost-effective, water is readily available across the planet [33]. Compared with other selected organic fluids, the temperature-entropy (T-s) graph for water is illustrated in Figure 1.9.

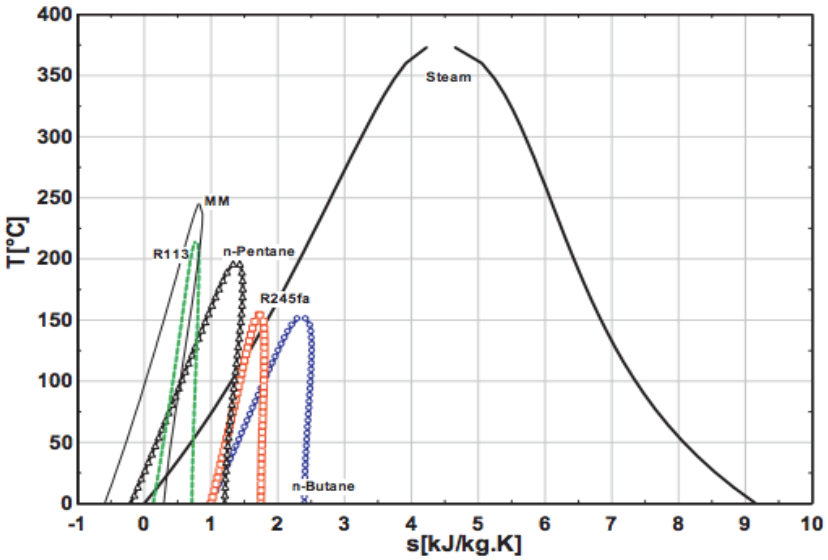

Figure 1.9 Temperature-entropy (T-s) graph for water and other selected organic fluids [33]

ORC-WHR (Organic Rankine Cycle - Waste Heat Recovery) is emerging as the fastest-growing company in the realm of ORC technologies, offering immense potential within the combined-cycle power plant sector. This rapid expansion is driven by increasing environmental concerns, such as rising oil prices and the pressing issue of climate change [34]. The ORC-WHR approach is recognized for its effectiveness, cleanliness, and safety in electricity generation. Figure 1.10 illustrates the configuration of components within an ORC system that harnesses thermal energy.

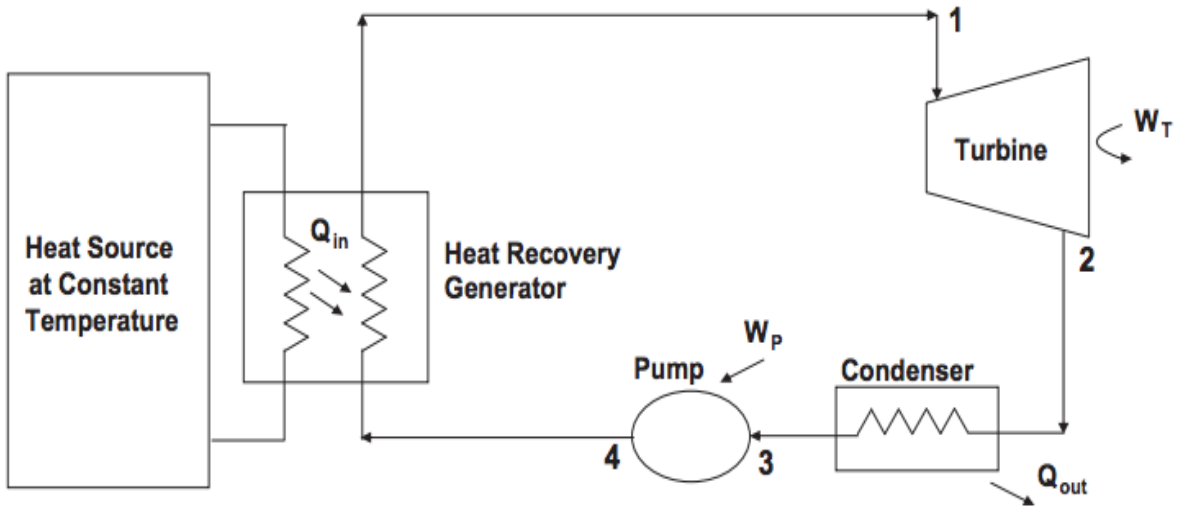

Figure 1.10 Basic components of ORC system [34]

- Moreover, the organic Rankine cycle (ORC) system offers several advantages over traditional steam-based power plants [34]:
- Lower Heat Requirements: The ORC system requires less heat for evaporation than steam-based systems.
- Efficient Evaporation: The ORC process operates at lower temperatures and pressures during evaporation.
- No Need for Superheating: Superheating is unnecessary since the expansion process occurs within the vapour phase. This eliminates the risk of blade erosion typically associated with steam turbines.

- Reduced Pressure Drop/Ratio: The ORC system experiences a smaller pressure drop and ratio due to the minimal temperature changes between evaporation and condensation. Consequently, it can utilize a simpler, single-stage turbine.

Table 1.1 Fluid property comparison of SRC and ORC system [34]

Parameters	**Steam cycle**	**ORC system**
Fluid used	Water	Organic compound
Boiling point	Higher	Lower
Critical temperature	Higher	Lower
Critical pressure	Higher	Lower
Condensing pressure	Lower	Acceptable
Viscosity	Lower	Relatively higher
Environmental impacts	No	High and depends on fluid
Toxicity	No	Yes
Specific heat	Higher	Lower
Availability	Available	Supply problem
Flammability	No	Yes and depends on fluid

1.7.1. Working fluid selection in ORC

Numerous scientific studies have been published on the selection of working fluids. These studies generally focus on comparing the thermodynamic efficiency of different fluids and are often based on a range of typical working fluids used in various applications [35]. Researchers typically analyze how different fluids perform regarding energy conversion efficiency, considering factors such as temperature range, pressure conditions, and fluid properties. This research helps in identifying the most effective fluids for specific thermodynamic cycles and applications. When selecting the most appropriate working fluid, several factors and guidelines should be taken into account [35]:

- **Thermal performance**: The working fluid should exhibit high power output and efficiency across the temperature range between the heat source and the sink. Key thermo-physical properties such as the critical point, specific heat, and density are interrelated factors that influence the output.
- **Saturation vapour curve:** A negative saturation vapour curve for wet fluids like water can lead to droplet formation during expansion stages. The vapour must be superheated before entering the turbine to prevent turbine damage. In the case of dry fluids, which have a positive saturation vapour curve, a recuperator can be employed.
- **High vapour density:** Fluids with low condensing pressures, such as silicon oils, require high vapour density. Low-density results in higher volume flow rates, necessitating larger heat exchangers to reduce pressure drops, significantly impacting device costs.
- **Low viscosity**: Fluids with low viscosity enhance heat transfer coefficients and reduce friction losses in heat exchangers for both vapour and liquid phases.
- **High heat transfer coefficient**: A high heat transfer coefficient is crucial for effective conductivity in heat exchangers.
- **Appropriate evaporating pressure**: High evaporating pressures can increase development costs and complexity, similar to the case with water.
- **Positive condensing gauge pressure**: The cycle's low pressure should exceed atmospheric pressure to prevent air infiltration.
- **High-temperature stability**: The chemical stability of the working fluid limits the maximum temperature of the heat source. Organic fluids, unlike water, may decompose or deteriorate at elevated temperatures.
- **Melting point**: The melting point of the working fluid should be lower than the lowest expected ambient temperature to prevent freezing.
- **High safety level**: Safety considerations include flammability and toxicity. Refrigerants are classified under ASHRAE Standard 34, which helps assess specific working fluids' safety.
- **Low ozone depletion potential (ODP)**: According to the Montreal Protocol, fluids with non-zero ODP are being phased out. New refrigerants should have an ODP of zero or very close to zero.

- **Low global warming potential (GWP)**: GWP is measured relative to CO_2. While some refrigerants have high GWP values, current regulations do not yet impose strict limits on high-GWP fluids.
- **Cost and availability**: Fluids commonly used in industries such as refrigeration and chemicals are generally more accessible and cost-effective.

1.8. Waste heat recovery (WHR) technologies

Waste heat refers to the thermal energy that is expelled into the environment by a process or equipment, which, if properly managed, could be harnessed for beneficial use. According to the second law of thermodynamics, releasing some thermal energy into the environment is an unavoidable consequence of converting heat into mechanical work [36]. This inherent energy loss implies that a significant portion of the fuel energy is wasted, contributing to potential thermal pollution. However, it is possible to capture and reuse some of this otherwise wasted energy by implementing waste heat recovery systems. This not only helps in reducing fuel consumption but also mitigates environmental damage [37].

The effectiveness of utilizing waste heat energy depends on several factors outlined below. Waste heat recovery (WHR) is influenced by various elements, including the principles of heat recovery operation, the specific needs of users, and the properties of the waste heat source. Each WHR method presents its own unique set of challenges, making the technology complex and multifaceted. Figure 1.11 illustrates a schematic representation of the various pathways for transferring waste heat energy.

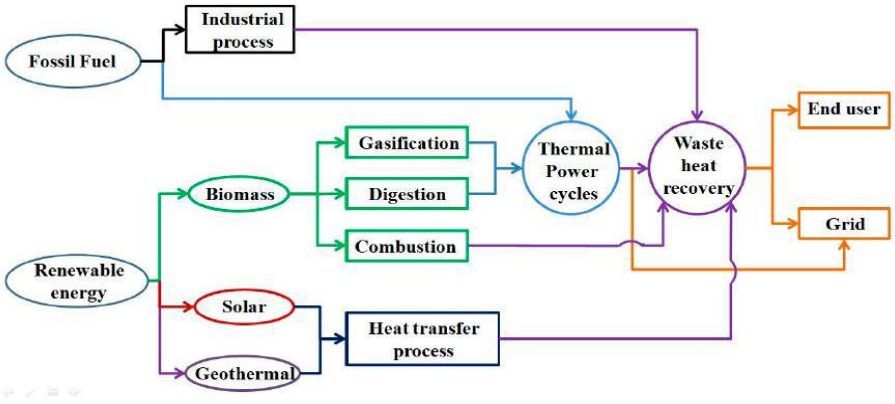

Figure 1.11 Waste heat recovery from various heat sources [38]

A crucial approach involves harnessing waste heat to fuel thermal cycles, thereby converting thermal energy into electricity. Among the methods studied extensively in recent years is the organic Rankine cycle (ORC), which utilizes organic fluids with lower boiling points. For the ORC to perform competitively, the waste heat temperature must range between 90°C and 250°C. On the other hand, the Kalina cycle, which employs a mixture of ammonia (NH_3) and water (H_2O) as its working fluid, operates effectively within a broader temperature range of 100°C to 450°C. This versatility allows the Kalina cycle to more closely align with the temperature profiles of various waste heat sources. Consequently, while the ORC excels in recovering waste heat at lower temperatures, both cycles offer promising solutions for improving energy efficiency and reducing thermal pollution.

Trigeneration systems represent a promising approach to meeting increasing energy demands in a cleaner and more cost-effective way [2, 6]. These systems operate on the principle of waste heat recovery, allowing them to simultaneously produce electricity, heating, and cooling from a single fuel source. Among these systems, gas turbine-based trigeneration systems are particularly advantageous for industrial applications, especially in process industries. They are favoured for their high efficiency, low pollution levels, relatively low capital costs, flexibility, and capability to provide multiple forms of energy [39-43]. Given that electricity, heating, and cooling are fundamental to energy consumption in residential, commercial, and public buildings globally, the development of efficient gas turbine-based trigeneration systems holds significant promise [2].

1.9. Integrated energy systems

In traditional power plants, more than 61% of the thermal energy is expelled via flue gas, leading to substantial losses in both energy and financial resources [44]. Figure 1.12 illustrates an energy flow diagram for such a power plant. This substantial loss of fuel energy to the environment underscores the need for enhanced waste heat recovery to improve fuel conversion efficiency in conventional power plants. One of the most effective methods for recovering this waste heat involves incorporating thermodynamic cycles into the primary energy conversion process [45]. Doing so makes it possible to capture and utilize the excess heat that would otherwise be wasted, thereby boosting the overall efficiency and reducing energy and cost losses.

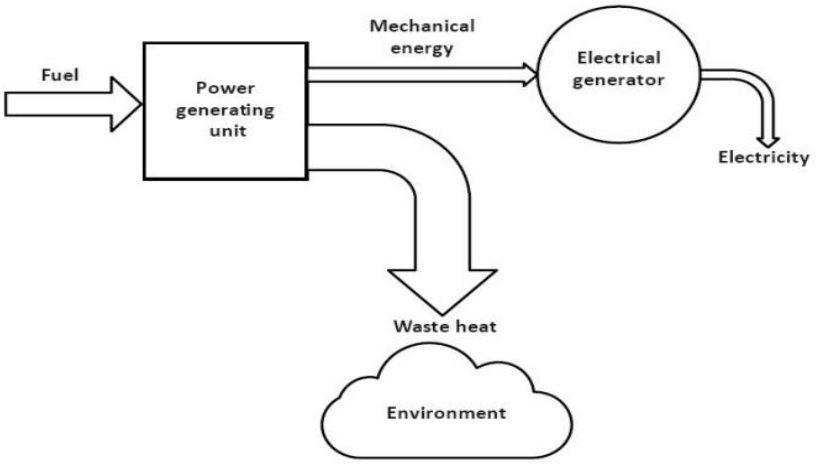

Figure 1.12 Energy flow diagram for a conventional power plant [2]

1.9.1 Cogeneration systems

The cogeneration system, often called a combined heat and power (CHP) system, represents one of the simplest forms of integrated energy systems. In such systems, the overall thermal efficiency usually ranges from 40% to 50%, reflecting the proportion of fuel converted into both electricity and heat [2]. In a typical CHP system, the exhaust gases from the prime mover are harnessed to generate either steam through a heat recovery steam generator (HRSG) or hot water via a heat exchanger. This process optimizes energy use by capturing waste heat that would otherwise be lost. An illustrative layout of a standard CHP system can be found in Fig. 1.13.

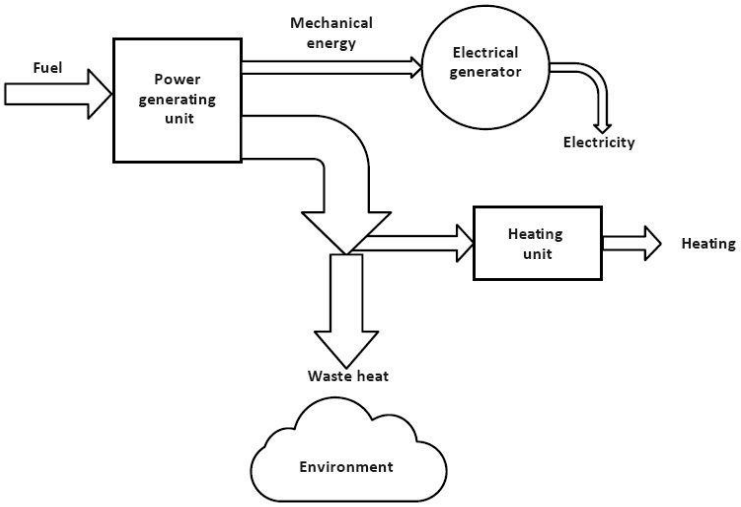

Figure 1.13 Energy flow diagram for a typical CHP system [2]

In this context, the Heat Recovery Steam Generator (HRSG) is essential for capturing waste heat from the gas turbine's exhaust and converting it into steam to drive the steam turbine cycle. Combined Gas Turbine-Steam Turbine (GT-ST) Combined Cycle Power Plants (CCPP) can achieve thermal efficiencies of up to 60% [43]. The steam produced by these integrated systems can also be utilized to power thermally driven cooling technologies, including absorption cooling systems (ACS), adsorption cooling systems (ADS), and ejector refrigeration systems (ERS). The chilled water from these cooling units can then be employed in heating, ventilation, and air conditioning (HVAC) systems. Since these integrated setups provide electricity and cooling, they are called Combined Power and Cooling (CPC) systems.

1.9.2. Trigeneration systems

Trigeneration systems are intended to generate electricity, cooling, and heating from a single fuel source. These systems are a more sophisticated version of combined heat and power (CHP) systems. In a trigeneration system, a portion of the steam produced is employed for cooling operations, while the remaining steam is employed for heating applications. These systems are also known as combined cooling, heating, and power (CCHP) systems [46]. An energy transmission diagram of a typical CCHP system is illustrated in Fig. 1.14 for visual representation.

A Combined Cooling, Heating, and Power (CCHP) system offers numerous benefits, including:

a) Enhanced Overall Efficiency: CCHP systems significantly increase the overall efficiency of energy use by simultaneously generating power, heat, and cooling from a single energy source, leading to more effective utilization of energy.
b) Decreased Fuel Costs and Greenhouse Gas Emissions: By optimizing energy conversion and reducing waste, CCHP systems lower fuel consumption, reducing fuel costs and decreasing greenhouse gas emissions.
c) Reduction in Greenhouse Gas Emissions: These systems contribute to a cleaner environment by minimizing the release of harmful greenhouse gases, further aiding in the fight against climate change.

d) Smaller Cooling System Requirements: The integration of cooling, heating, and power generation in a single system allows for a reduction in the size and capacity of separate cooling systems, leading to space and cost savings.

e) Lower Capital Costs: The efficiency and multifunctionality of CCHP systems can reduce the initial capital investment needed for separate heating, cooling, and power generation equipment.

f) Potential for Additional Revenue Streams: By generating electricity and thermal energy more efficiently, CCHP systems can create opportunities for additional revenue generation, such as selling excess power back to the grid or offering district heating and cooling services.

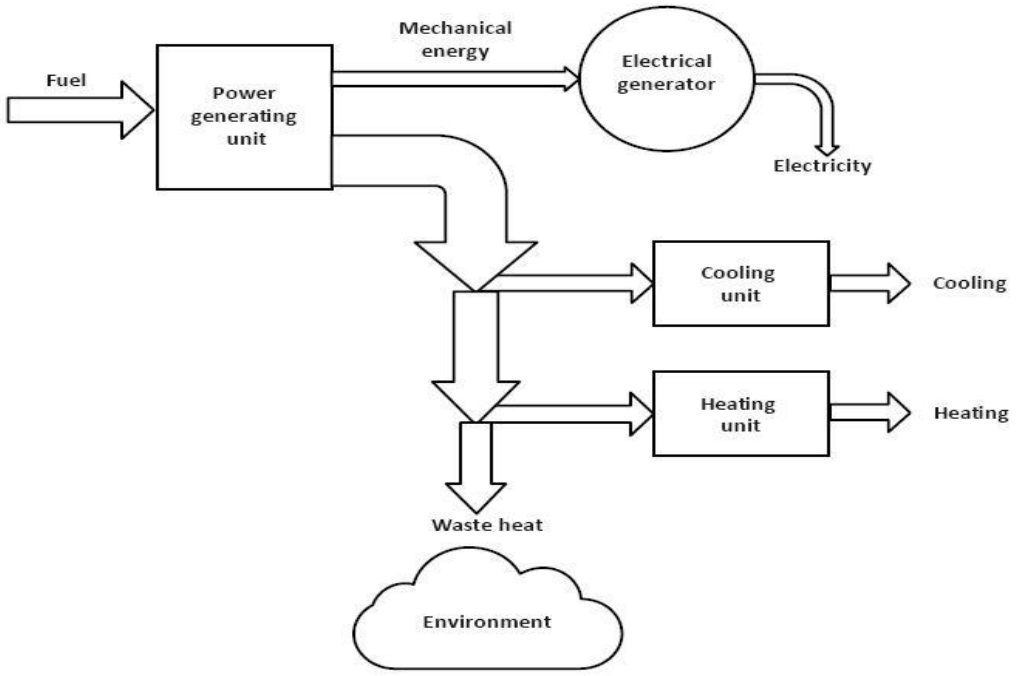

Figure 1.14 Energy flow diagram for a CCHP system [2]

A comprehensive strategy that integrates principles of energy analysis, exergy analysis, and environmental analysis [47] can be employed to design and develop thermal systems that are both highly efficient and environmentally friendly. The goals and contributions of analyzing a thermal system include the following [48, 49]:

a) Assess the heat and work interactions occurring within each component of the thermal system.

b) Identify the sources, magnitudes, and locations of exergy destruction and losses throughout the thermal system.
c) Evaluate the environmental impact associated with the pollution emitted by thermal systems.

Based on the above-mentioned literature gaps, the proposed research has been carried out with the key objective of "Energy and exergy analyses of four different combined power and cooling systems integrated with an external renewable heat source".

1.10. Conclusions from brief introduction

Based on the contents of this chapter, it is evident that addressing challenges related to energy conservation, atmospheric protection, and the increasing energy demands of the near future will significantly benefit from renewable energy sources (RES). It has been suggested that solar thermal power represents a promising alternative for electricity generation in India. Specifically, technologies like parabolic trough solar collectors (PTSC) and solar power towers (SPT) can generate heat at maximum temperatures of 400°C and 750°C, respectively, and are also capable of producing solar thermal electricity [50]. These innovations offer a viable path toward meeting future energy needs while mitigating environmental impacts.

Renewable Energy Systems (RES), especially concentrated solar power (CSP) systems, are anticipated to enhance the performance of supercritical CO_2 (sCO_2) and supercritical helium Brayton cycles in the near future. This study aims to evaluate the integration of the supercritical helium Brayton cycle (SPT) as an alternative to the sCO_2 cycle for power generation. Additionally, organic Rankine cycles (ORC) are employed to recover low-grade energy in bottoming low-temperature refrigeration cycles. The research explores combined power, cooling, and heating (CCHP) effects by assessing these cycles' exergy and energy efficiencies. Specifically, it examines the helium Brayton cycle as the topping cycle and evaluates the potential of ORC, Variable Refrigerant Air Conditioning (VAR), and Vapor Compression Refrigeration (VCR) systems as bottoming cycles to recover waste heat from the SPT-based helium Brayton cycle.

1.11. Outline of thesis chapter

The thesis is divided into six chapters; the outline of each chapter is structured as follows:

Chapter 1: Introduction

Starting with an overview of the present global energy landscape, this chapter emphasizes the urgent need for renewable energy sources (RES) to prevent energy crises and environmental issues in the near future, as well as the rapid depletion of fossil fuels. The following section then investigates the environmental consequences of the distribution of various fuels, including both conventional and unconventional sources, in the primary energy supply. Subsequently, the chapter investigates renewable energy scenarios and their integration into energy conversion technologies.

The discussion then transitions to comparing concentrating and flat-plate collectors (FPC) systems, assessing their respective advantages and disadvantages to support the selection of concentrating collectors (SPT) as the preferable heat source. Furthermore, the chapter examines the importance and advantages of the supercritical CO_2 (sCO_2) cycle, supercritical helium Brayton cycle, and Organic Rankine Cycle (ORC) mechanisms for various heat sources in various temperature environments.

The chapter also addresses the criteria for selecting working fluids for the ORC system to determine the most suitable option. It further develops into waste heat recovery technologies, including cogeneration and trigeneration energy systems. Finally, the chapter wraps up with an outline of the thesis, summarizing the key points discussed.

Chapter 2: Literature Review

This chapter comprehensively examines the current body of research on energy and exergy analysis for cogeneration and trigeneration systems. It specifically investigates integrating concentrated solar power (CSP) technologies with thermal cycles, such as the sCO_2 cycle and ORC systems, to investigate power generation, heating, cooling, and waste heat recovery (WHR). The literature review is divided into distinct sections: the first section explores the use of the sCO_2 cycle in trigeneration systems, while the second section focuses on ORC

systems, particularly their applications in power generation and WHR, with studies on combined cooling, heating, and power (CCHP), variable air volume (VAR) systems, vapour compression cycle (VCC), and ejector refrigeration systems. The chapter concludes with a summary of key findings from the literature, highlighting research gaps and setting the stage for future research goals.

Chapter 3: System Description

This chapter provides a comprehensive overview of various models across different sections. The first section summarises the SPT-based combined HBC and ORC integrated system with ejector refrigeration. The second section details the SPT-based combined HBC featuring a cascaded compression-absorption integrated system. In the third section, the focus shifts to the SPT-based combined HBC-ORC system, which includes a cascaded ejector-compression integrated system. The fourth section presents an integrated system combining Rankine and absorption power cycles with a heating process. Finally, the fifth section describes a system that integrates power, heating, and cooling cycles driven by a low-temperature heat source and utilizes various eco-friendly refrigerants. Additionally, this section compiles all parametric values for the selected combined cycles in a tabulated format.

Chapter 4: Methodology

This chapter concentrates on thermodynamic modeling, which involves simulating mathematical energy and exergy equations into computer code. This code aims to resolve these equations using computational numerical methods, specifically through the engineering equation solver (EES) software. The chapter is divided into five sections, each dedicated to discussing the mathematical modeling of different models, emphasizing their key assumptions.

Chapter 5: Results and Discussion

This chapter presents the findings of a study that examines the performance of solar-driven cycles using computational numerical techniques. The results are discussed in various sections, each addressing different aspects of the analysis. The first section focuses on evaluating a combined system of solar-powered turbines (SPT) with a helium Brayton cycle (HBC) and organic Rankine cycle (ORC) integrated with ejector refrigeration. It explores how different

system variables such as compressor pressure ratio, helium turbine inlet temperature, compressor inlet temperature, ORC turbine inlet temperature, pump pressure ratio, evaporator temperature, solar direct normal irradiation, and solar heliostat efficiency affect the system's performance. The analysis utilizes various working fluids to assess these effects. Additionally, this section compares and validates the HBC and ORC-Ejector Refrigeration System (ERS) performance with previous studies to confirm the accuracy and relevance of the current integrated system's results.

The second section provides a detailed parametric analysis of a combined HBC cascaded compression-absorption integrated system. Initially, the thermal efficiency of the standalone HBC cycle and the coefficient of Performance (COP) of vapour absorption refrigeration (VAR), vapour compression refrigeration (VCR), and the cascaded cycle were compared. Following this, a thorough parametric analysis of the integrated system was conducted, evaluating the thermal efficiency, exergy efficiency, and exergy destruction of each subsystem and the entire system. Key performance parameters considered include the compressor pressure ratio, compressor inlet temperature, helium turbine inlet temperature, generator temperature, evaporator temperature, cascade condenser temperature, absorber temperature, heliostat field efficiency, and receiver efficiency. The final subsection of the analysis presents a validation of the system’s performance by comparing it with previous research findings.

The third section focuses on the parametric analysis of the combined HBC and Organic Rankine Cycle (ORC) cascaded ejector-compression integrated system using the SPT. It further examines how varying the parameters of the topping cycle impacts the performance of both the bottoming ORC and the cascade cycle. Initially, the standalone HBC's thermal efficiency and the ORC-ERS system's parametric results were validated. The study further determined the energy efficiency, exergy efficiency, network output, heating effect, cooling effect, exergy destruction, and total output energy for each sub-system and the overall system. The investigation also analyzed how different system variables such as heliostat field efficiency, receiver efficiency, compressor pressure ratio, turbine inlet temperature, and compressor inlet temperature, pinch point temperature difference in the HRVG, entrainment ratio, cascade condenser temperature, and evaporator temperature affect system performance. The subsequent section presents the validation of the model.

In the fourth section, an analysis was conducted on the performance of a combined Rankine absorption power and refrigeration cycle integrated with a heating process. The computed results from this system were compared and validated against previously published data. The performance of the integrated system was evaluated under specified input parameters. The study explored how various system variables, such as the temperature of the heat source, turbine inlet pressure, and refrigeration temperature, affect the system's overall performance. Finally, the exergy distribution of the system's components in relation to the heat source energy was determined.

The fifth section explores a combined power, heating, and cooling cycle driven by a low-temperature heat source, utilizing various eco-friendly refrigerants. The system's computed results have been validated against previously published data. The output parameters of the proposed system, which were evaluated for six different eco-friendly refrigerants, include thermal efficiency, exergy destruction rate, exergy efficiency, ejector entrainment ratio, network output, and cooling effect. Performance was found to be influenced by factors such as evaporator temperature, turbine inlet temperature, and heat source temperature. Additionally, the distribution of input source energy across different system components was analyzed.

Chapter 6: Conclusions and future scopes

The current research focuses on developing a solar-based trigeneration system designed to improve the efficiency of solar power plants. The novel system proposed in this study incorporates a helium Brayton cycle (HBC) instead of traditional CO_2 or air Brayton cycles, using helium as the working fluid in the topping cycle to enhance overall performance. Four different trigeneration systems were analyzed for their ability to harness solar heat from a solar power tower (SPT) system, and their performance was compared against a conventional SPT-based helium Brayton cycle system. This approach optimizes solar plant efficiency by delivering power, heating, and cooling simultaneously. The key findings and conclusions are detailed in the final chapter of the thesis, which also outlines potential areas for future research in combined cooling, heating, and power (CCHP) systems.

Chapter 2

Literature review

2.1. Introduction

The current research on integrated energy systems, primarily cogeneration, cascaded, and trigeneration systems, is covered in this chapter. The use of thermal cycles, such as the sCO_2 cycle, HBC, and organic Rankine cycle system, for power production and waste heat recovery (WHR) to power integrated CCHP systems has been the subject of numerous studies in the literature. The literature review was done in a thorough manner and is divided into several sections:

The first section looks at the numerous research studies on utilising the sCO_2 cycle in terms of power generation and waste heat recovery. The second section then looks at the prior studies that have been done on the use of waste heat recovery and the HBC to produce power. The third section then goes over the performance studies that are now accessible in the realm of combined cycles, focusing on the ORC system, HBC, and sCO_2 cycle combined. The fourth portion also goes over the various refrigeration cycles depending on ORC. The fifth and final section covers the research on using renewable energy sources to run integrated combined cycles (CCHPs).

Furthermore, after completing the literature survey, the significant findings are discovered and described in the respective area. The research gaps are then recognized based on the breadth of previously published literature. Lastly, the thesis organization is provided in the final section of this chapter, which outlines the structural division of the thesis into its many divisions.

2.2. Supercritical CO_2 cycle applications

When used for WHR from a gas turbine, the sCO_2 Rankine cycle can reach high efficiency compared to the steam/water cycle because of its compact structure and simplicity, as stated by According to **Kim et al. [51]**, maximizing the cycle's thermal efficiency (η) as well as waste heat use could raise the net output power. Among the three methods, the split-cycle might offer the highest power under a range of operating circumstances, according to their comparison

of the energy and performance of the three distinct cycles. In addition, twelve distinct sCO_2 cycle topologies, including dual cascade, simple recuperated, single heated cascade, etc., were compared by **Kim et al. [52],** for gas turbine bottoming. Compared to the other configurations they looked at, their study showed that pre-compression and recompression cycles had better efficiency. They also recommended more investigation on the fusion of these two cycles.

A thermodynamic study on CO_2 centered power cycles was presented by **Cardemil and da Silva [53]**. They covered some topics, including cycle type (Brayton or Rankine), recuperator configurations, and operating conditions like heat source temperature and CO_2 upper and lower operating pressure. Furthermore, they evaluated the relative efficacy of energy conversion cycles using four working fluids: water, ethane, and toluene.

Mecheri et al. [54] examine the sCO_2 cycle's thermodynamic performance of coal-fired power plants. Research showed that a recompression cycle was required despite the low-temperature heat present in the flue gas from coal burning and that its efficiency differed from the typical Brayton cycle by more than 4.5%. Additionally, they discovered that a single reheat was a useful arrangement, increasing efficiency by 1.5% points as compared to a cycle without reheating. Furthermore, they concluded that the performance of the sCO_2 coal-fired power plant had improved by 6%, from roughly 46% to 48%, with the material already in place under the current operating conditions. Finally, while integrating the sCO_2 power cycle, several technological issues surfaced.

The thermodynamic performance of a power plant with a sCO_2 power cycle was examined by P**ark et al. [55].** Their findings demonstrated that, compared to the SRC system employed in the current coal-fired power plant, integrating the sCO_2 power cycle with the coal-fired power plant increased power production efficiency by 6%–7% and decreased the cost of energy by roughly 7%–13.6%.

Li et al. [56] examined how well R245fa-based ORCs and trans-critical CO_2 (tCO_2) power cycles performed for low-grade power generation in an experimental study. Furthermore, 80 kWe micro-turbine CHP unit's exhaust flue gases were used. They also looked into how performance is impacted by important operational limitations like mass flow rate and input heat

flux. The study found that with a tCO_2 system and an R245fa-based ORC, power generation and overall efficiency could greatly increase with a fixed input heat flux and larger mass flow rates.

The possibility of preheating the sCO_2 power system is examined by **Song et al. [57]**. Researchers noted that the original technique employed low-temperature jacket cooling water for preheating the sCO_2 fluid. Their thermodynamic analysis determined that the system could provide up to 63.7 kW of net power at the maximum preheating temperature. Subsequently, they added a regeneration branch to the enhanced preheating sCO_2 system, significantly increasing the regeneration heat load. The modified system's greatest net power production was recorded at 68.4 kW, 7.4% more than the original system's. Finally, they came to the conclusion that 6.9% more engine output power (996 kW) could be added to the upgraded WHR preheating system.

Neises and Turchi [58] examines the various sCO_2 cycle configurations' performance, cost, and design. They discovered that although the recompression cycle is the most expensive, it can achieve higher thermal efficiency and partial cooling cycles due to its requirement for larger turbo-machinery capacity. Finally, they disclose that the power tower's partial cooling cycle generates more net electricity and is also a less expensive choice.

Combined super-critical (sCO_2) and transcritical (tCO_2) cycles as a bottoming cycle was suggested by **Fan et al. [59]**. The sCO_2-tCO_2 cycle can run at 10% to 100% of the generator capacity, reaching efficiencies between 24.5% and 65.7%, according to their extended multi-objective optimization under partial load conditions. Additionally, they performed a sensitivity analysis on design parameters such as the pressure and flow split ratio to evaluate cycle's performance.

The sCO_2 recompression Brayton cycle, in conjunction with the transcritical carbon dioxide cycle as a bottoming cycle backed by a CSP system, was thoroughly analyzed by **Khatoon et al. [60].** They discovered that increasing waste heat and decreasing cooling water flow increased the combined cycle's efficiency. In the SPT system, molten salt was used to power the sCO_2 recompression cycle. They concluded that high temperatures might also be effectively utilized with the sCO_2 cycle.

Yu et al. [61] looked at the recovery of waste heat from IC engine exhaust using four various configurations of sCO_2 cycle. For every system, they computed exhaust heat recovery

ratios and η. According to the study, the pre-compression cycle's 5.8 MPa and the recuperated cycle's 7.65 MPa had the highest exhaust heat recovery ratios.

Ma et al. [62] examined how solar power towers (SPT) and the sCO_2 cycle could work together. Even though the sCO_2 Brayton cycle is becoming more popular in SPT plants as a cost-effective energy source, they used an exergoeconomic method to determine the best way to combine primary compression intercooling and the recompression sCO_2 Brayton cycle. They contrasted their findings with those obtained by thermodynamic optimization, which seeks to maximize the system's energetic efficiency.

In their analysis of the sCO_2 Brayton cycle's performance for CSP applications, **Garg et al. [63]** compared it with trans-critical and sub-critical cycles and discovered that the supercritical cycle's η peaks at about 85 bar before beginning to decline. Conversely, raising the low-side pressure increases the efficiency (η) of both trans-critical and sub-critical cycles. Additionally, they show that the sCO_2 cycle can provide power with a η_{th} of more than 30% even at low source temperatures of 820 K.

Chacartegui et al. [64] investigated various combined cycle configurations using a CO_2 gas turbine topping cycle to overcome issues with the solar power plant receiver's size and construction. At the supercritical compressor's intake pressure, this ratio varied between 0.7 and 0.85. Additionally, their research showed that adding CO_2 to the topping cycle increases total efficiency by three percentage points as compared to the air cycle.

The cascaded solar and biomass energy-driven sCO2 system was proposed by **Wang et al. [65]**, who also executed an energy and exergy analysis to assess the system's viability. According to their findings, thermal efficiency can reach 40% and energy efficiency varies over time. According to their statement, the efficiency value will be at its lowest point, whereas the direct normal irradiance (DNI) will be at its highest point. This might be the result of poor use of the excess energy that the solar receiver collected. They also discovered the solar field's maximal energy destruction.

Compared to supercritical and superheated steam cycles, the sCO_2 Brayton cycle offers the possibility of greater cycle efficiency at temperatures suitable for CSP applications, according to **Neises and Turchi [66].** Additionally, they look into how well basic,

recompression and partial cooling cycles work. They concluded that the partial cooling cycle was preferable to the recompression cycle. This was advantageous since it made it possible to employ more affordable thermal energy storage systems that sparked the creation of more thermally efficient receivers.

Chacartegui et al. [67] studied implementing CO_2 Brayton cycles in CSP plants with central receivers. They discovered that because of its more intricate design, improved heat recovery, and capacity to operate in supercritical conditions at the compressor's input, the recompression cycle (arrangement 2) delivered higher cycle efficiency. Additionally, sCO_2-ORC used in solar power plants can increase power output by 7% for central receivers operating at maximum temperatures.

2.3. Helium Brayton cycle (HBC) applications

Helium Brayton cycles were investigated by **Sánchez et al. [68]** as power cycles to achieve great thermal efficiency. The maximum temperature of the energy source is quite low due to its working conditions, which restricts the cycle's thermal performance. Their research aims to assess the potential of the helium Brayton cycles as power cycles. In particular, the effects of reheating and intercooling have been investigated. A helium Brayton cycle's maximum thermal efficiency of over 36% has been achieved by adding multiple intercooling stages, and adding a reheating mechanism may help the cycle's efficiency rise to 37%.

Energy conversion cycles were examined by **Kusterer et al. [69]**, who took into account mixed or Brayton cycles in addition to their primary focus on water/steam cycles (Rankine cycles). Their study includes a thermodynamic analysis of many closed helium Brayton cycles (HBC). They demonstrated that a Helium Brayton Cycle can attain ηth of at least 46%. The turbine inlet temperature, which must be at least 900 °C, is a crucial component of this efficiency, meaning the pressurized receiver must endure even greater temperatures.

A unique combined power cycle for solar power tower (SPT) systems was reported by **Khan et al. [70]**, which combined an HBC and aCO_2 cycle. The potential of this device to generate carbon-free energy through waste heat recovery is examined. Using exergoeconomic and thermodynamic analyses, the study contrasts the working of the SPT-HBC-tCO_2 cycle with that of the basic SPT-HBC cycle. According to the findings, SPT-HBC-tCO_2 costs 1.613 US

cents per kWh for electricity while achieving 34.68% energy efficiency and 32.39% thermal efficiency. Improvements of 13.21% in thermal efficiency and 13.18% in exergy efficiency are shown in this combined cycle.

A unique linked cycle intended for power generation in solar power towers was proposed by **Zare et al. [71].** The system recovers waste heat from a closed Brayton cycle on helium by incorporating two organic Rankine cycles. Both 1stand 2nd laws of thermodynamics were used to analyse the system. According to the results, the power plant achieves an energy efficiency of more than 30%. Furthermore, the study discovers that the suggested power cycle performs better in these solar power plants than alternative Rankine and supercritical CO_2 systems under comparable circumstances.

A novel working fluid composition, a mixture of N_2O–He, was investigated by **Miao et al. [72]**. Key factors, including the split ratio, pressure ratio, etc., were the subject of extensive investigation and adjustment. The proposed revolutionary working fluid cycle performs better than cycles employing N_2O (with a 5.1% variance) and CO_2 (with a 6.5% deviation).

Bi et al. [73] investigated the design of an integrated hydrogen liquefaction system by combining the steam methane reforming (SMR) method with the use of LNG cold energy. According to their comparison analysis, the suggested procedure lowers the specific energy consumption (SEC) from 10.780 kWh/kg to 7.95 kWh/kg and increases it from 0.1205 to 0.1634.

Zhou et al. [74] examined a combined cycle based on the supercritical Brayton cycle that uses helium as the working fluid. For improving waste heat recovery (WHR), the suggested system combines the conventional Brayton cycle, an absorption chiller, and the organic Rankine cycle. The objectives of multi-objective optimization and thermodynamic and economic analysis are to lower power costs and increase energy efficiency. As compared to the basic system, the combined cycle reduced power costs and energy efficiency by 11.9% and 14.5%, respectively, under ideal circumstances. Moreover, this new system works better than supercritical CO_2 systems and Rankine cycle-based systems, according to comparisons with previous studies.

A binary gas mixture of helium and xenon was investigated by **Malik et al. [75]** for use as the working fluid in the axial compressor of nuclear power facilities located on land. They thoroughly examined the thermo physical characteristics of this helium-xenon mixture and found

that it provides a 7% greater heat transfer coefficient at the necessary conditions. They could lower the high-temperature gas-cooled reactor's (HTGR) compressor from 16 to 3 stages in the closed Brayton cycle (CBC).

2.4. RES integrated ORC system

The working fluid utilized in an ORC plant determines its efficiency and profitability [76]. This supports the literature on choosing fluids for various heat recovery applications, which summarizes the qualities of suitable fluids [77–82]: Low viscosity, High latent heat of vaporization, High density, and Noncorrosive. High specific heat, High thermal conductivity, Nontoxic and nonflammable, High energetic/energetic efficiency, Low ODP, low GWP, Low cost and good availability, Stable at high temperature, More critical parameters (temperature, pressure), etc.

An exergy analysis of an Organic Rankine Cycle (ORC) was carried out by **Mago [83],** who assessed several organic fluids, including R245fa, R123, R142b, isobutene etc., with critical temperatures ranging from 407.7 to 524.9 K, According to the study, the ORC could produce in the range of 13.8 and 30 kW at a temperature of 503 K for exhaust. The study also demonstrated how important it is to consider the fluid's critical temperature while selecting a working fluid. Energy performance is improved when a fluid's critical temperature is closer to the exhaust temperature because this reduces the pinch point temperature discrepancy.

Ahmadi et al. [84] created a thermodynamic model that combines a gas turbine cycle, an ORC system, a single-effect absorption chiller, and a domestic water heater to supply electricity, heating, and cooling. Moreover, analyzing energy and exergy, they evaluated the effects on the environment. According to their findings, this tri-generation system uses less energy than gas turbine cycles or traditional combined heat and power systems. Furthermore, they discovered that the combustion chamber undergoes the greatest exergy destruction because of the substantial temperature differential linking the working fluid and the flame and the irreversibility of chemical reactions.

Al-Sulaiman et al. [85] evaluated the operation of a new approach for combined power, heating, and cooling that is based on PTSC and ORC. They also considered three different configuration options: solar, solar with storage, and storage mode. In addition to three scenarios,

heating-cogeneration, cooling-cogeneration, and electrical power, ultimately, their findings show that the maximum electrical efficiency was discovered to be 15%, 7%, and 6.5%, respectively. On the other hand, the maximum power, heating, and cooling efficiency was around 47%, 42%, and 94%, respectively.

The working of a toluene ORC and NH_3/CO_2-based cascade refrigeration system was examined by **Lizarte et al. [86]** for applications involving low-evaporation temperatures, or 55°C to 30°C. They discovered that the highest overall system COP and energetic efficiency were 0.8 and 31.5%, respectively, as compared to the ORC evaporation temperatures.

In 2020, **Song et al. [87]** conducted an analysis of the SORC to recover waste heat from low-grade waste heat at low temperatures. They found that the R152a fluid was the most effective fluid in terms of producing the highest net power and thermal efficiency and that SORC is a suitable method for recovering waste heat from industrial sources.

Zhou [88] claims that because the organic fluid's supercritical condition achieves an improved thermal match, reducing irreversibility, the Supercritical Organic Rankine Cycle (SORC) has greater conversion efficiency than the traditional ORC. According to their technical analysis, a hybrid plant based on the SORC performs better thermodynamically than one based on the subcritical ORC. Furthermore, their energy study reveals that a supercritical hybrid plant attains an exergetic efficiency of between 27–34%, whereas a subcritical hybrid plant's exergetic efficiency ranges from roughly 23–32%.

Chen et al. [89] looked into how well supercritical Rankine cycles and ORC systems converted waste heat into electricity. Additionally, they demonstrated that isentropic and dry fluids work better in ORC systems since wet fluids require superheating. However, because of the consequences of superheating, employing dry fluids may harm cycle efficiency. They also investigated the application of low critical pressures and temperatures for fluids in the supercritical Rankine cycle.

The effectiveness of a direct vapour generation SORC system powered by linear Fresnel Reflector (LFR) concentrators was assessed by **Xu et al. [90].** They talked about how the receiver evaporator's intricate two-phase problems are avoided by the supercritical process. Comparing cyclohexane to other working fluids, they found that it obtained a greater overall

efficiency of 19.7%. They observed that the efficiency of the ORC improved faster than the efficiency of the LFR system with growing turbine input temperatures, resulting in a greater overall efficiency, when they compared this system to a conventional subcritical ORC system.

Wang et al. [91] investigated how the SORC system's performance was affected by the inlet temperature of the cooling water. They discovered that when the cooling water inlet temperature rises from 20°C to 30°C, thermal efficiency reduces by 19%, 11%, and 11%, while the net power output of the ORC decreases by 30%, 21%, and 16%, respectively, with the specified flue gas temperatures.

The ORC, WHR potential was examined by **Braimakis et al. [92]**, who discovered that the critical temperature of the working fluid affects the system's energy efficiency. According to their research, propane has the potential to increase efficiency by up to 18%. They also pointed out that cycle performance might be improved in subcritical and supercritical circumstances by employing zeotropic binary mixes rather than pure fluids. Furthermore, their investigation revealed that these blends provide better second-law efficiency than their individual components, maybe as high as 60% with supercritical cyclopentane-propane, contingent upon heat source temperature.

Moloney et al. [93] state that the subcritical ORC is more effective for geothermal energy than the conventional ORC. As part of their research, they evaluated a range of safe and non-toxic fluids and performed analysis at the turbine's inlet.

Shaaban [94] used the steam Rankine cycle and ORC as bottoming cycles to recover waste heat from solar-integrated combination cycles examination. After testing fifteen different ORC working fluids, the author found that R1234ze (Z) offered the optimum balance of thermoeconomic, environmental, and safety features.

According to **Guo et al. [95],** the heat source and sink profile must be considered while choosing the optimal working fluid. Additionally, they noted that pure fluids may perform better than combinations in situations with a low-temperature gradient and a high heat source input temperature. Additionally, their research shows that the mixtures function better when the heat source's intake temperature drops, which raises the temperature gradient of the heat sink and the heat source.

A 250 kW ORC system using a turbine expander and working fluids like R245fa was researched by **Fu et al. [96].** The power output of 242 kW and η_{th} of 8.3% was found in their results, with the evaporation and condensation temperatures being 104.4°C and 32.3°C, successively. They also observed a ±1.7 kW variation in the net power output. Their results showed enhanced system stability and great WHR applications.

The working of the parallel double evaporator ORC (PDORC) and the traditional ORC was compared by **Dai et al. [97].** They investigated how zeotropic mixes and multi-evaporator systems can improve ORC performance efficiently. Four parameters were used to assess the systems' performance: heat exchanger area, cycle efficiency, net power production, and heat exchanger area per net power output. They employed both pure organic fluids and zeotropic mixes to create sub-models for condensers and evaporators. For performance optimization, a GA was used to match the two statistically.

The ORC system has been highlighted by **Wang et al. [98]** as a potentially useful technology for reclaiming energy from the waste heat generated through engines. They suggested a dual-loop ORC system to improve energy recovery from coolant and engine exhaust fumes. This system would consist of two cascading ORCs. This strategy might raise the effectiveness of energy recovery overall. Their study concentrated on a regenerative dual-loop ORC system for compressed natural gas engine WHR employing R1233zd and R1234yf.

Furthermore, **Singh and Mishra [99]** carried out an exergy and energy study of a supercritical ORC integrated with a parabolic trough solar collector (PTSC)**.** The suggested working fluids for the supercritical ORC include cyclohexane, toluene, R152a, and isobutene. The performance measures investigated in this study were the fuel depletion ratio, expansion ratio, rate of energy degradation, improvement potential, irreversibility, and expansion rates. According to the data, exergy efficiency rises steadily with increasing solar irradiation intensity and turbine inlet pressure; R600a exhibits the highest exergy efficiency of all the fluids tested.

Hoang [100] examined using the ORC as a bottoming cycle to recover heat from diesel engine exhaust waste. They revealed that although a system combined with a diesel engine could reach up to 90% thermal efficiency, an ORC could only achieve up to 25%. Diesel engines produce the most pollutants and CO_2 emissions but are also essential for transportation,

agriculture, and small to medium-sized stationary generators. In actuality, though, over 60% of the energy generated during the combustion of an air-fuel mixture is wasted as waste heat and is instead released into the atmosphere.

A comparison and optimization study of single and dual-pressure evaporation ORCs was carried out by **Li et al. [101]**. In comparison to the single-pressure evaporation ORC, they discovered that the dual-pressure evaporation ORC produced more work. Additionally, the maximum work output rose for nine distinct working fluids as the heat source temperature dropped, with maximum increments ranging from 21.4% to 26.7%.

The energy, exergetic, and financial performance of a solar-powered trigeneration system were examined by **Bellos et al. [102].** They said an ORC that discards heat can be fed by PTSC and a storage tank to the heat pump. They also optimize the system's performance. They discovered an internal return rate of 20.02% and a payback period of 5.33 years, indicating a workable system.

A study on the hybrid ORC powered by solar energy (PTSC) and waste heat (temperature variations between 150°C and 300°C) was conducted by **Bellos and Tzivanidis [103].** They chose four distinct fluids: n-pentane, MDM, cyclohexane, and toluene. According to their findings, toluene may produce the most amount of electricity, ranging from 479 kW to 845 kW.

Power systems utilizing the steam Rankine cycle (SRC), ORC, and steam ORC (S-ORC) were created by **Zhang et al. [104]**. Using numerical models, they calculated and compared these three systems' power output, operating pressure, and efficiencies. The outcomes demonstrated that as the temperature was 150 and 210 °C, the ORC attained the best exergy efficiency and power production. On the other hand, the S-ORC outperformed the SRC and ORC systems in terms of thermal and energy efficiency.

Moloney, Almatrafi, and Goswami [105] performed a parametric study of the SORC system and concluded that the SORC is more efficient than the ORC for low-temperature heat sources. Additionally, after conducting a thermal analysis of the SORC, **Sadon and Islam [106]** found that it outperformed the basic ORC with a preheater in terms of both power output and thermal efficiency.

2.5. Application of ORC system for VCR, VAR, ejector and cascade cycle

Li et al. [107] studied selecting the optimal working fluid for a combined ORC-VCC system. Butane was found to be the best working fluid for this system, considering temperature differences at the boiler outlet ranging from 30 to 55 °C, with evaporation and condensation temperatures varying between 60 to 90 °C and -15 to 15 °C, respectively. At a boiler outlet temperature of 90 °C, the system's overall COP was found to be 0.47 when using butane.

Hu et al. [108] examined how well an ORC-VCC system running on solar energy performed. They came to the conclusion that the temperature of generation and condensation affects the amount of ice produced as well as cooling power. R245fa was chosen as the suitable fluid for this application. Ice production per unit meter square collecting area and cooling power with R245fa were 7.61 kg/m^2/day and 126.44 W/m^2, respectively.

A model for a low-temperature heat-activated combination ORC-VCC system was projected by **Moles et al. [109]**. The system's electrical and thermal coefficients of performance (COPs) were found to range from 15 to 110 and 0.30 to 1.10, respectively. Furthermore, HFO-1234ze (E) was found to be an appropriate working fluid to improve efficiency.

According to **Wu et al. [110],** little exergy loss in the VAR cycle's component parts and maximal exergy loss in the reactor. Finally, their exergo-economic optimization results show that, as compared to the sCO_2 cycle, the combined structure has greater first and second law efficiency by 26.12% and 2.73%, respectively.

Saleh [111] examined ORC's energy and exergy analysis integrated with a VCC system. After considering system performance and environmental considerations, he concluded that R602 was a suitable working fluid. In particular, the system achieved a maximum COP of 0.99, an exergy efficiency of 53.8%, a turbine pressure ratio of 12.2, and a working fluid total mass flow rate of 0.005 kg/s-kW utilizing R602 at a condenser temperature of 25°C.

Li et al. [112] focused on optimization strategies while comparing the combination sCO_2/lithium bromide-water system with the sCO_2/ammonia-water system. An energy and exergy study of a combined ORC system with single and double evaporator VCC designs was done by **Pektezel and Acar [113].** They discovered that R600a was the system's ideal working

fluid. They also found that the combined cycle with a single evaporator had a better COP and exergy efficiency than the arrangement with two evaporators.

The study of the regenerative ORC-VCC system was carried out by **Javanshir et al. [114].** They stated that the boiler and turbine had the highest amounts of energy destruction and that the product's total unit cost was $60.7/GJ.

Patel et al. [115] proposed an innovative trigeneration system that integrates the ORC with a vapour compression–absorption cascade refrigeration cycle. Using n-pentane as the working fluid for the ORC, the proposed system's calculated energy and exergy efficiencies are 79.02% and 46.7%, respectively.

Patel et al [116] presented the thermo-economic optimization of a cascaded vapour compression-absorption refrigeration system powered by an ORC and waste heat. In this setup, using a dry working fluid, the ORC generates power to drive the VCRS. Additionally, the high-temperature organic working fluid from the expander outlet meets the thermal needs of the vapour absorption refrigeration system. While this method effectively provides cooling at low temperatures, its practical limitations include complexity and high initial capital costs. The system's energetic efficiency is calculated at 22.3% for cooling-only mode and 79% for cogeneration mode (cooling and heating).

Patel et al. [117] proposed a novel solar-biomass ORC system combined with a cascaded system for low-temperature cooling applications. They conducted a thermo-economic study to assess the system's performance and commercial feasibility. In contrast, for the linear Fresnel reflector (LFR) based system, the solar fraction was 0.179 due to lower annual efficiency, but the BEP was lower at 7.43 years due to a smaller LFR field and reduced biomass energy generation costs.

Faruque et al. [118] presented a unique cascade design for a compression absorption refrigeration system. They used parametric tests, genetic algorithm optimization, and energy and exergy analysis to assess the suggested system using two distinct refrigerant combinations. Their results demonstrated that by employing the R41 and LiBr/H_2O combination, the suggested system could attain a 15.39% improvement in COP and exergy efficiency over the conventional cascade absorption cycle at an evaporator temperature of -35 °C.

Askari et al. [119] presented an integrated refrigeration system that uses linear Fresnel solar collectors to power the ejector-cascade compression (R1234yf)–absorption (LiBr–H2O) cycle, organic Rankine cycle (ORC, using toluene), and thermoelectric generator (TEG). To assess the effect of parameters on performance, such as heat transfer areas, solar field size, ideal dimensions for the thermal energy storage (TES) system, and the levelized cost of cooling energy (COC), they performed a thermo-economic analysis. Compared to the system without an ejector, the results demonstrated that adding the ejector increased the system's efficiency and the cascade cycle's coefficient of performance by 27.02% and 51.19%, respectively.

Using R1234yf as the refrigerant, **Li et al. [120]** studied the working attributes of an ejector-expansion refrigeration cycle (EERC). Additionally, they used R1234yf and R134a to compare the performance of EERC systems. According to the study, at 40°C for condensing and 5°C for evaporation, R1234yf attained a peak volumetric cooling capacity (VCC) of 2590.76 kJ/m^3 and a coefficient of performance (COP) of 5.91. All things considered, the R1234yf EERC works better than the traditional refrigeration cycle, particularly at greater condensing and lower evaporation temperatures. In addition, the R1234yf cycle exhibits better VCC and COP than the R134a cycle.

Wang et al. [121] proposed a novel combined power and refrigeration cycle for cogeneration that integrates the Rankine cycle with the ejector refrigeration cycle by placing an extraction turbine between the heat recovery vapour generator (HRVG) and the ejector. This combined cycle, powered by flue gas from a gas turbine or engine, solar energy, geothermal energy, and industrial waste heat, can simultaneously produce both power and refrigeration.

As an alternative to absorption cooling systems, **Lianga et al. [122]** investigated a heat-driven cooling system that combined a transcritical CO_2 (T-CO_2) refrigeration cycle with a supercritical CO_2 (S-CO_2) power cycle. They suggested that this integrated system could cool refrigerated cars so that food may be preserved by using engine waste heat recovery. According to their research, a combined S-CO_2/T-CO_2 cycle that uses a single cooler functions similarly and is technically possible thermodynamically. With the S-CO_2/T-CO_2 system, there is enough heat in the exhaust gas to chill the vehicle compartment that is refrigerated efficiently.

Khan et al. [123] presented an innovative combined cycle that uses a supercritical Brayton cycle with helium as the working fluid to produce power. This novel cycle provides additional heating and low-temperature cooling for food storage by combining a cascaded vapour absorption-compression refrigeration technology with the conventional Brayton cycle for waste heat recovery. The predicted plant's energy, exergy efficiency, and power output were determined to be 28.82%, 39.53%, and 14,865 kW, respectively. The cooling coefficient (COP) was measured at 0.5391, and the heating coefficient at 1.54 at 850 W/m² of direct normal irradiation.

Mosaffa [124] presented a novel geothermal-driven combined power and dual ejector refrigeration (CPDER) system using a zeotropic mixture. According to the study, the evaporator's outlet temperature and capacity have the greatest influence on refrigeration capacity, whereas the turbine's outlet pressure and mixture composition have the most effects on overall exergy destruction and net power output. A tri-objective optimisation approach was also used to find the ideal operating conditions, emphasising energy efficiency, energy efficiency, and total unit cost. The energy and energy efficiency of the suggested CPDER system improved by 6.0% and 11.9%, respectively, according to the optimization results.

Modi et al. [125] conducted energy and exergy assessments of a single-effect li-Br absorption system. Their findings showed that as the generator temperature increases from 750°C to 1100°C, both the coefficient of performance (COP) and exergy efficiency improve. The generator and absorber were identified as having the highest levels of exergy destruction.

A thermodynamic analysis of a unique combined cooling and power system powered by low-grade heat sources and an ammonia-water mixture was carried out by **Wang et al. [126].** They looked into energy destruction to understand how energy is dispersed across the many components. The findings showed that the main locations of energy destruction are heat exchangers.

Rashidi et al. [127] created a computer program to analyze a combined power and ejector cooling cycle using R123 as the working fluid. Their study assessed how different operational parameters affect the cycle's performance. They found that the boiler and ejectors experience the greatest energy losses. They also observed that the evaporator temperature

increases with the first and second law efficiencies. Moreover, as the turbine inlet pressure increases, the 1st law efficiency improves while the 2nd law efficiency decreases.

Habibzadeh et al. [128] assessed the thermodynamic performance of an ejector refrigeration cycle with combined power in their 2013 study. They determined the ideal turbine and pump input pressures for the selected working fluid to reduce the cycle's overall thermal conductance. Furthermore, energy and exergy evaluations of comparable systems were carried out by Dai et al. [129], Agrawal et al. [130], Khaliq [131], and Khaliq et al. [132].

Refrigeration plays several crucial roles in human life, including air conditioning, cooling, preserving fruits and vegetables, maintaining pharmaceutical products, and controlling environmental conditions. Many researchers have investigated using solar power as a heat source for absorption and ejector refrigeration systems. In the ejector refrigeration system, the ejector is a key component that increases pressure without directly using mechanical energy. As a result, an ejector that boosts pressure is simpler and safer than a compressor or pump.

Keenan et al. [133] established the foundational concept of the ejector cycle built on gas dynamics, which was later developed further by **Huang et al. [134]** and **Ouzzaneet et al. [135].** Their simulations of a solar absorption system using LiBr-H_2O revealed a relationship between the hot water input temperature, coefficient of performance (COP), and the absorption surface area. **Khaliq et al. [136]** found that the overall exergy destruction in NH_3-H_2O systems is greater than in LiBr-H_2O systems. They identified the generator and absorber as the primary sources of energy destruction and suggested that increasing the absorber temperature could enhance exergetic efficiency.

2.6. RES integrated combined cycles (CCHP)

An exergoeconomic analysis of the sCO_2/tCO_2 and sCO_2/ORC configurations was carried out by **Wang and Dai [137].** Furthermore, their analysis showed that the sCO_2/ORC cycle's total product unit cost is somewhat less than the sCO_2/tCO_2 cycle's.

Khaliq et al. [138] proposed an innovative cogeneration system combining the Rankine power cycle with the absorption refrigeration cycle to recover industrial waste heat and generate electricity and refrigeration. Their findings indicate that as the gas inlet temperature increases,

the first law efficiency decreases while the power-to-cooling ratio increases. Conversely, as the pinch point temperature rises, the first law efficiency improves, but both energy efficiency and the power-to-cooling ratio decrease.

Njoku et al. [139] examined the working of a combined plant integrated with an ORC and a VAR cycle. Their study evaluated the energy, exergy, and environmental sustainability indices. The results revealed that the ORC, using R113 and powered by waste heat from the combined cycle power plant, generated an additional 7.5 MW of electricity. Furthermore, the VAR cycle, which cooled the inlet air stream to 15°C in the gas turbine plants, contributed an extra 51.1 MW of electricity.

An energy and exergy analysis of a system comprising a solar parabolic trough collector, an ORC acting as the bottoming cycle, and a basic recuperated sCO_2 cycle was carried out by **Singh and Mishra [140]**. At a solar irradiation of 0.85 kW/m², they discovered that the fuel depletion ratio was 0.2583. According to their investigation, the system's energy and exergetic efficiencies both increased as sun irradiation increased.

In 2014, **Akbari and Mahmoudi [141]** performed an exergoeconomic study of a combined R-SCO_2 Brayton cycle and ORC system. They evaluated eight different ORC working fluids. Using EES software, they optimized both the thermodynamic and economic operation of the combined cycle. Their results indicated that the combined cycle achieved up to 11.7% higher energy efficiency compared to the R-SCO_2 Brayton cycle and had a total product unit cost 5.7% lower than the basic recompression cycle.

The efficiency of a combination ORC-VCRS using low-grade thermal energy was examined by **Saleh [142]**. A variety of working fluids were taken into consideration, such as hydrocarbons, hydrofluorocarbons (HFCs), and hydrofluoroolefins (HFOs). The performance of the system was examined in relation to changes in the isentropic efficiencies of the compressor and expander, as well as variations in the temperatures of the evaporator, condenser, and boiler. It was discovered that although while the total mass flow rate per kW of cooling capacity decreased, the overall COP of the system improved once the temperature of the boiler and evaporator rose along with the isentropic efficiency of the compressor and expander. The fluids with the maximum COP values for the system were found to be R600 and R245fa.

According to **Polyzakis et al. [143]**, gas turbine power plants have somewhat lower capital costs than steam power plants. Additionally, they compared the various gas turbine cycle configurations, including simple, intercooled, reheated, and intercooled, and optimized based on combined cycles. Their research revealed that a reheated gas turbine was ideal configuration because of the turbine's high exhaust gas temperature, which can lead to a high bottoming steam cycle thermal efficiency. Lastly, they said that a gas turbine cycle that is optimized could result in a combined cycle power plant that is more efficient and saves a significant amount of money.

Ersayin and Ozgener [144] used the 1^{st} and 2^{nd} laws of thermodynamics to study a combined cycle power plant. It was discovered that the plant had an energy efficiency of 56% and an energy efficiency of 50.04%. The combustion chamber, among other components, had the maximum rate of exergy destruction, as per their investigation. Additionally, they pointed out that lowering extra air in the combustion chamber and adjusting the A/F ratio might lower energy and exergy losses, enhancing the combined cycle power plant's first and second law efficiencies.

Using a zeotropic mixture, **Hou et al. [145]** conducted a thermodynamic investigation of a novel combined $RSCO_2$ cycle and regenerative ORC. Using a GA for multi-objective optimization, they discovered that the most efficient zeotropic mixture was R236fa/R227ea.

Song et al. [146] evaluated how different recuperative ratios of the sCO_2 cycle, the initial temperature of the heat source, and the overall heat load affected the performance of the ORC as a bottoming cycle. They designed cycles with: one with a pre-cooler and one without. They suggested that incorporating a bottoming cycle could improve residual heat recovery and enhance the system's thermal efficiency.

According to **Javanshir et al. [147]**, the best thermal efficiency is achieved when R141b and an ORC are combined when the cycle's maximum temperature is less than 300°C. Additionally, their investigation revealed that the best cycles for maximum temperatures between 300°C and 650°C were CO_2 regeneration Brayton cycles with recompression and Rankine/ORC cycles. They also found that the regenerative Brayton cycle with recompression and the combined Brayton/ORC cycle obtained the highest η_{th} for maximum pressures and cycle temperatures exceeding 650°C.

An exergy analysis using SPTC was carried out on a thermal power system by **Al-Sulaiman [148]**. To generate power, the study investigated a mixed cycle technique that used an SRC as the topping cycle and an ORC as the bottoming cycle. The ORC employed a variety of refrigerants, including R134a, R152a, etc, in addition to ammonia. The investigation showed that exergy efficiency rises with solar radiation; the maximum exergy efficiency of the combined cycle utilizing R134a was 26%, and the exergy efficiency of the R152a-based cycle was an additional 25%. Furthermore, the study discovered that the solar collector which accounted for about 70% of all energy losses was mostly to blame for energy destruction.

With an emphasis on low-temperature thermal energy storage, **Gao et al. [149]** examined a parameter and optimized high-temperature solar sCO_2 and ORC combined power system with a storage device. Their research showed that while the system's overall thermal efficiency drops, greater compressor input temperatures cause an increase in the ORC's intake turbine temperature as well as the system's power output ratio.

Al-Zahrani and Dincer [150] analyzed the energy and exergy performance of a solar-powered sCO_2 Brayton cycle integrated with an ORC. Their study found that the CO_2 Brayton cycle achieved an energy conversion efficiency of about 40% and an energy efficiency of roughly 69%. The total power output was approximately 102.7 MWe, using a mirror area of 450,000 m^2.

Using statistical analysis and exergy, **García et al. [151]** studied the ammonia-water power and cooling cycle. Their findings show that variables like ammonia content, pressure ratio, turbine efficiency, and the heat exchanger's pinch point temperature have a big effect on the cycle's performance. They discovered that the combined cycle performed best with an ideal pressure ratio of around 14 and an ammonia composition of roughly 0.47 at the absorber outlet. They also noticed that the thermal performance of the linear Fresnel reflector (LFR) collector field was comparable to that of the solar parabolic trough collector (SPTC) field, despite the LFR having 40% larger mirror area.

2.7 Important literature review on recent studies

To meet the energy needs of tiny structures in remote places, **Saini et al. [152]** developed a revolutionary solar-driven compact and sustainable integrated system. Energy, economic, and

environmental studies are conducted. By taking into account the temperature of the generator, evaporator, and condenser, pinch point temperature differential. Raising the temperature of the generator or evaporator lowers the cost of cooling and power while increasing energy efficiency, CO_2 emissions, and heating expenses. Raising the condenser temperature raises CO_2 emissions and increases heating costs while lowering energy efficiency, cooling expenses, and power prices.

To find an environmentally viable solution for upcoming energy needs and human luxury, **Saini et al. [153]** investigated three distinct topologies of solar-driven combined cooling, heating, and power (CCHP) systems. They compared the thermodynamic performance of these configurations assessing many factors such as performance index, irreversibility etc.—using solar energy. The analysis revealed that Configuration-1 achieved the highest power output and total energy efficiency, whereas Configuration-3 delivered the greatest heating output and performance index.

Dabwan et al. [154] presented the outcome of a study on the thermodynamic, economic, and environmental aspects of power plants using parabolic trough collectors. The study includes an analysis of the facilities' hourly and annual performance with varying sizes of gas turbines and solar fields. Additionally, a theoretical approach for optimizing solar integration has been developed and demonstrated.

An inventive solar-powered trigeneration system with a thermal energy storage unit (TESU) was presented by **Sheykhlou et al. [155]**. Double-effect absorption chillers, a modified Rankine cycle, and parabolic dish collectors are all part of this system. During solar operation, the study evaluated the sensitivity of a number of variables, such as energy and exergy efficiency, power-to-heating and cooling ratios, heating capacity, input energy, and net output power. The findings demonstrated that the various operating modes attained respective energy and exergy efficiency of 15.53%, 14.47%, and 8.58%, and overall energy efficiencies of 97.23%, 81.98%, and 40.23%.

An experimental assessment of the energy efficiency of a trigeneration system using a solar PVT-assisted heat pump in an industrial setting was carried out by **Coca-Ortego et al. [156]**. Their results show that this solar-powered system can provide power, heat, and cooling

efficiently. Even though it contributes less to heat production, the PVT system's solar thermal component is important for providing hot water for household usage. On the other hand, the heat pump compressor gains a lot from the solar electricity produced. A variety of performance metrics were used to examine the system's performance.

A tri-generation system to simultaneously produce different final energy forms for an office building was studied by **Chen et al. [157].** The carbon price is incorporated to monetize the emissions, and extensive optimization is carried out to optimize the energy, environmental, and economic benefits. With the maximum solar energy utilization rate, the suggested system outperforms the conventional system in terms of energy performance and environmental advantages by 41.7% and 41.4%, respectively. In the best scenario, the economic performance increases by just 14.4%, although at the lowest solar energy usage rate.

Tsimpoukis et al. [158] proposed the implementation of a supercritical CO_2 trigeneration system to serve a refrigerated warehouse in Athens. They analyzed the system's energy performance and assessed its financial benefits compared to a system that solely relies on ejector refrigeration. Under the selected nominal conditions, the power production efficiency was found to be 11.77%, the combined power and refrigeration production efficiency was 66.09%, and the overall trigeneration efficiency reached 163.70%.

Alharthi et al. [159] investigated combined energy system that integrates a power generation unit (TCP), a single-double-effect absorption chillers, and a solar collector utilizing CO_2 as the heat transfer medium. They analyzed how temperature variations at the pump inlet and evaporator of the absorption chillers affect power generation, refrigeration performance, cooling exergy, and the overall CCHP efficiency.

An optimization of a solar-powered combined cooling, heating, and power (CCHP) system was reported by **Wang et al. [160]**. A solar collector with a flat plate was used to capture solar radiation. To generate energy and cooling capacity, the CCHP system integrated an ORC with an ejector refrigeration cycle. For optimization purposes, a mathematical model of the solar-powered CCHP system was created. It was discovered that the optimal values for the total heat transfer area and average useable output were 46.16 m^2 and 6.40 kW, respectively. The ideal

values for the combined cooling and power (CCP) mode were 5.84 kW for the average usable output and 58.74 m² for the total heat transfer area.

A novel micro solar combined CCHP cycle that uses the ORC for both summer and winter operations was proposed by **Boyaghchi et al. [161].** A storage tank was created to balance the supply and demand of solar energy for the CCHP system in order to guarantee steady and continuous functioning. According to the study, under ideal circumstances, the η_{th}, energy efficiency, and total product cost rate increased dramatically to 28%, 27%, and 17% in the summer from 4%, 13%, and 4%, respectively, during the winter.

A novel cogeneration system for electricity, cooling, and heating was presented by **Mahdavi et al. [162].** To improve efficiency, zeotropic mixtures are used as the working fluids in the dual-pressure ORC and ejector refrigeration cycles. The main source of power for the system is solar collectors with parabolic troughs. Under certain circumstances, such as using pentane and isobutane as the zeotropic working fluids and keeping the sun radiation rate (DNI) constant at 1000 W/m², optimal performance was attained. The system had an overall exergy loss of 22.19 MW, with peak energy and exergy efficiencies of 15.81% and 20.26%, respectively.

You et al. [163] proposed a trigeneration system utilizing solid oxide fuel cells (SOFCs) to simultaneously produce power, cooling, heating. The system features key components including a heat exchanger, a steam ejector refrigerator (SER), a gas turbine, an ORC, and an SOFC. Their analysis revealed that while increasing the fuel cell current density lowers both the system's average cost and its environmental impact per unit of energy, higher SOFC inlet temperatures, working pressures, pinch point temperature differentials, and generator evaporation pressures lead to increased costs and environmental effects. Optimization of the system aimed to realize the best exergy-based working; however, even with optimization, the system's energy efficiency was reduced by 7.64%.

Bellos and Tzivanidis [164] investigated a solar-driven trigeneration system optimized under various criteria. The system utilizes parabolic trough collectors to supply heat to the generator and includes an ejector, an evaporator for cooling, and a condenser for heating. For applications such as hotels, the system provides cooling at 10°C and heating at 50°C, which are

typical for building temperatures. The optimal configuration achieved an energy efficiency of 11.26%, with a cash flow for energy savings of 7.694 €/h, and an overall efficiency of 87.39%.

Three varieties of helium-regenerated Brayton cycles were examined by **Li et al. [165]:** the single-reheat cycle with intercooling, the cycle with intercooling, and the double-reheat cycle with intercooling. These cycles aim to improve the efficiency of solar power towers operating at temperatures above 1300°C. With the largest temperature differential of 1028.5 °C and the highest energetic efficiency of 65.32% were all attained by the optimized cycle. The best cycles had energetic efficiencies of 55.91%, 61.57%, and 65.28%, in that order.

A new multigeneration plant featuring two thermoelectric generators, a PEM unit, a home water heater, a steam Rankine cycle, a supercritical CO_2 Brayton cycle, a methane-powered Brayton cycle, and a multi-effect desalination process was introduced by **Kelem et al. [166].** Their research focuses on CO_2 emissions, energy and energy efficiency, and environmental and thermodynamic studies. The system's freshwater generating capacity, net power output, and hydrogen production rate were determined to be 1336 kW, 0.002004 kg/s, and 0.954 kg/s, respectively. Furthermore, measurements showed that the plant's energy and efficiency were 55.76% and 52.17%, respectively.

Two unique sCO_2 cycles were proposed by **Sun et al. [167]** for gas turbine waste heat recovery. The two systems' energy, exergy, and exergoeconomic analyses are examined. This research can aid in investigating the possibilities of cutting-edge waste heat recovery systems. As a result, the suggested systems offer fresh approaches to using gas turbine waste heat more affordably and serve as models for designing comparable cycles.

Khan et al. [168] studied the thermodynamic performance of two different configurations: the sCO_2 cycle/ORC (configuration-1) and sCO_2 cycle/parallel double evaporator ORC (PDORC) (configuration-2). Both configurations were evaluated with a solar power tower (SPT) as the heat source. The study found that, with a direct normal irradiation (DNI) of 950 W/m^2, adding a basic ORC or PDORC to the standalone inter-cooled cascade sCO_2 cycle improved thermal efficiency by 2.3% and 6.7%, respectively. The waste heat recovery ratios for PDORC and basic ORC were 0.1775 and 0.1197, respectively. Configuration-2 demonstrated an

optimal thermal efficiency of 52.34%, surpassing configuration-1 in waste heat recovery performance.

Qin et al. [169] created a novel combined cycle system with a transcritical CO_2 refrigeration cycle and a supercritical CO_2 recompression Brayton cycle to recover waste heat from a marine turbine for power generation and refrigeration. Through a parametric sensitivity analysis, they investigated how different system characteristics affect the system's performance and economy. After that, multi-objective optimization was used to adjust the system's settings. Furthermore, the low-temperature heat exchanger is essential to the system's total exergy destruction.

The integration of power cycles, thermal energy storage, and heliostat fields was the main topic of **Khatoon et al. [170]**. Supercritical carbon dioxide Brayton cycles are becoming increasingly common because they function better at extremely high temperatures than standard Rankine cycles. According to their findings, the integrated system's efficiency increases when recompression cycles are used; this improvement ranges from 39% to 45%. With regeneration cycles, the average net power production was calculated to be 37.17 MW, and with recompression cycles, it was 39.04 MW.

Anjum et al. [171] developed a trigeneration system for SPT plants that efficiently produce power, heating and cooling at low temperatures from a high-temperature SPT heat source. This trigeneration unit integrates a cascaded vapour compression-absorption refrigeration system and a helium Brayton cycle for power generation to create heating and low-temperature cooling benefits for food preservation. The numerical technique of exergy energy analysis was performed using engineering equation solver software to evaluate the performance of the proposed SPT plant. The power output, exergy and energy efficiency of the SPT plant were found as 14,865kW, 39.53% and 28.82%, respectively. The coefficient of performance values for cooling and heating were observed as 0.5391 and 1.539, respectively. Exergy evaluation revealed that approximately 78.18% of the total energy destruction of the entire plant is attributed to the solar subsystem only. Furthermore, a parametric investigation shows that the temperature of the evaporator, generator and helium turbine inlet, and the efficiency of the heliostat and receiver all have a significant impact on the plant performance. Furthermore, a comparative analysis with

relevant previous studies has shown that the proposed system outperforms systems based on supercritical CO_2 cycles and the Rankine cycles.

Anjum et al. [172] proposed a novel trigeneration system that was presented to utilize the SPT for combined power generation, heating, and cooling. The trigeneration system consists of a helium Brayton cycle and organic Rankine cycle (ORC) with an ejector refrigeration system for recovering the waste heat. The power was produced by the helium Brayton cycle and ORC turbine, whereas cooling and heating were produced simultaneously by the condenser and evaporator. The heating and cooling effects were generated at 50°C and 10°C for building applications such as hospitals and hostels. Finally, the optimal system exhibits exergy and energy efficiency of 25.12%and 23.3%, respectively, when all the studied parameters are considered. Apart from this power output, heating and cooling productions were observed as 14,998, 60.52 and 8.25kW, respectively, at the 2.3 of compressor pressure ratio, 197.2°C of inlet temperature of ORC turbine.

2.8. Outcomes of the literature review

1. RES can be used as an energy source for the high-temperature supercritical cycle, like high-temperature fuel cells, CSP systems, and geothermal power plants [173].
2. Of the several CSP technologies, SPT has a wide temperature range of 150–1500°C. SP produces high-temperature heat for power generation through a high energy cycle or industrial process supplies [174,180].
3. the PTSC system is the most developed type of CSP system and demonstrates its ability to function in a commercial setting; nevertheless, it may eventually face competition from the LFR system since its temperature range (60°C to 500°C) is smaller than that of the SPT system [22, 76, 174].
4. Even in the 400°C temperature range, compactness and simplicity can make it more economical than SRC in the sCO_2 cycle and HBC [184].
5. The specific volume will undoubtedly drop if the helium fluid is compressed at its critical point in the HBC cycle, which lowers the compression work. As a result, the cycle's overall size decreased, and its efficiency increased [30].
6. It is realistically possible to recover waste heat from gas turbine cycles based on helium cycles, instead of SRC [51]. As a result, the HBC cycle might take the role of the SRC to increase thermal efficiency [31].
7. Due to the working fluid's compression when in a liquid state or, in this instance, the fact that liquid water is incompressible, SRC can achieve high efficiency at low turbine input temperatures. Since air is a compressible fluid requiring a high inlet turbine temperature, the gas turbine cycle necessitated a significant amount of compression effort, which raised material concerns.
8. The sCO_2 cycle's thermal efficiency is not appreciably higher than the SRC because of the above-mentioned factors. Aside from this, the gas turbine cycle and SRC are advantages of the HBC cycle. Hence, unlike SRC, a large turbine inlet temperature might be given with fewer material problems because HBC will be compressed in an incompressible area [70].
9. The helium Brayton cycle (HBC) fluid stays dense throughout because the system operates above the critical point, and the minimum pressure is higher than in the gas Brayton cycle and SRC. The HBC cycle requires ten times less turbo-machinery than the

SRC cycle because of the higher fluid density, which causes the volumetric flow rate to decrease [70].

10. The cold side flow in the recuperator of the HBC cycle has a specific heat that is two to three times higher than the hot side flow. As a result, the helium flow in the recompression configuration is split to maximize heat recovery and offset the variation in specific heat in the LTR unit. Decreasing waste heat may improve the recompression cycle's thermal efficiency [68].
11. Because of its low working temperature, ORC can recover heat from various sources, including solar energy, geothermal heat, biomass, and industrial waste heat [33].
12. The solar-powered ORC's efficiency increases as the inlet turbine temperature rises, and when the temperature rises above the critical point, thermal efficiency increases even more as the inlet turbine pressure rises [149].
13. Using the superheat left over from the expansion process, the ORC's recuperator may be used to warm the working fluid following the pump. The cycle's efficiency is increased by this technique [77].
14. The SORC can be used when the working fluid's critical temperature is much lower than the heat source temperature. Nonetheless, when the fluid's critical temperature is marginally lower than the heat source temperature, both the SORC and subcritical ORC are feasible [82].
15. The helium Brayton cycle is an attractive substitute for power plants due to its simplicity, compactness, superior economy, sustainability, low capital cost due to the small size of the equipment and plant footprint, enhanced safety, and high cycle efficiency, among other reasons [71, 72].
16. Considering his low cost, abundance in nature, non-flammability, non-hazardous nature, and ability to withstand higher temperatures, he is a notable and promising option for a working fluid [73].
17. In both SORC and subcritical ORC, the internal heat exchanger is used to preheat the liquid before evaporation if the organic fluid vapours at the turbine outlet are hot enough; however, vapours are cooling down before entering in the condenser. As a result of this process, the cycle's overall efficiency can be increased [191].

18. The ORC can be used to recover heat from a source with a temperature range of 90°C to 350°C [191].
19. An ORC system can use an internal heat exchanger known as a recuperator or regenerator, particularly when working with dry or isentropic fluids. By using this component, the evaporator's pinch limitation can be further relaxed by lowering the amount of thermal energy collected from the heat source. High thermal efficiency and power production are thus possible for the same heat input conditions by using working fluids with greater flow rates in the ORC until the pinch conditions are restored [192].
20. Compared to SRC, a substantially smaller cycle pressure ratio and a comparatively higher turbine exit temperature have been observed in the case of HBC cycles; as a result, thermal efficiency increases due to the significant quantity of heat recovered [74].
21. SRC is primarily suitable for a heat source with a maximum temperature of more than 500°C and can use high-pressure steam or water as the circulating working fluid. In summary, SRC is inappropriate for low temperature and pressure conditions since it demands high operational temperature and pressure [104].
22. When the heat source temperature is between 150 and 210 degrees Celsius, the ORC's power-generating capacity is higher than that of the steam-ORC and SRC. When the heat source temperature rises to 200 degrees Celsius, the ORC's power-generating capacity is clearly lower than that of SRC. When the heat source temperature reaches 350 degrees Celsius, the ORC and SRC's power generating capacity are extremely close [104].
23. When connected to any power cycle, the VCR system and the VAR system can also use solar energy. Because of the compressor, VCRs demand more power than any other cooling system. Its COP is higher than that of the VAR system, though. Consequently, the VCR system must be powered by solar energy.
24. SPT-based trigeneration system performance and energy and exergy efficiency are enhanced when combined with ORC and cascaded refrigeration cycle [118, 124].
25. Buildings such as hospitals and hostels, among others, could benefit from simultaneous heating and cooling when a cascade refrigeration cycle linked with an ORC and power cycle based on an SPT plant is used [119, 127, and 128].

26. For food storage and industrial applications, a cascaded VAR-VCR integrated ORC-based trigeneration system powered by a solar plant may produce cooling and heating effects at -40°C and 80°C, respectively [115, 123].
27. Using the waste heat from the ORC to generate additional power and power the ejector refrigeration system can further enhance the performance of the SPT-based HBC [127, 132].

2.9. Research gap in literature

A large body of research has been done in the areas of cascaded refrigeration cycles, ORC-integrated WHR systems, and CSP-based CCHP cycles. The following section discusses several significant topics that have been raised in this context by previous research, along with the gaps in knowledge that resulted from those findings.

- While many researchers focused on examining the combined power and absorption refrigeration cycle, relatively few studied the combined organic Rankine cycle and ejector refrigeration cycle's performance.
- Research on the performance assessment of solar power tower (SPT) powered combination cycles, which use waste heat to power organic Rankine cycles as bottoming cycles and helium Brayton cycles as topping configurations, is extremely sparse.
- The results of a thorough literature review indicate that the parametric analysis of the SPT-integrated combined solar-operated helium Brayton cycle with cascaded vapour absorption refrigeration-vapour compression refrigeration (VAR-VCR) system has not yet been completed.
- The literature assessment revealed that very little research has been done on the Brayton cycle with helium serving as the working fluid for power plants' low-temperature cooling while utilizing the high-temperature heat from the SPT system.
- Not much research has been done on the effectiveness of different helium Brayton cycle configurations that use the waste heat, SPT driven in conjunction with bottoming organic Rankine cycle-ejector refrigeration cycle (ORC-ERC) system.

- The helium Brayton cycle powered by solar energy and employing waste heat to power an ORC-integrated cascaded ejector-compression refrigeration system has been parameterized and studied.

2.10. Research objectives

1. Thermodynamic analysis of combined power, cooling and heating system.
2. Thermodynamic analysis of combined power and absorption-compression cascaded refrigeration system.
3. Thermodynamic analysis of combined power cycle using ejector-compression cascaded refrigeration system.
4. Thermodynamic analysis of combined power cycle using vapour absorption refrigeration system and heating process.
5. Thermodynamic analysis of combined power, heating and cooling cycle using low-temperature heat source with various eco-friendly refrigerants.

Chapter 3

System Description

This chapter overviews the relevant important figures and input parameters for the considered thermodynamic cycles. The description of the SPT-based helium Brayton cycle (HBC) with different configurations of combined power, cooling and heating (CCHP) system integrated with ORC, ERC, VAR, and VCR to recover waste heat from the topping cycle by acting as a bottoming cycle has been explored.

3.1. Description of SPT-based combined HBC and ORC with ejector refrigeration integrated system

In this system, SPT has been identified as the heat source. SPT is the newest technology that powers cycles at high temperatures and is highly developed for commercial use. It can withstand temperatures between 300°C and 2000°C [28]. To enhance the Brayton cycle's potential for power generation, sCO_2 can replace helium (He), thereby increasing the system efficiency and decreasing the number of stages of the compressor [30]. However, the idea behind the solar-powered helium Brayton system is an appealing option in high-temperature applications. When it comes to power conversion systems, Brayton cycles with inert gas working fluids can be more cost-effective than steam Rankine and sCO_2 cycles by utilizing the larger outlet temperature range of the systems to achieve significant increases in power conversion efficiency. [31]. Helium is regarded as the working fluid in each of the models that have been considered, the reason for choosing He as a working fluid in these models has been covered in the previous chapter. The performance of the SPT-based HBC can be further improved by utilizing the waste heat by incorporating ORC that developed extra power.

The current model of an integrated combined cycle was developed to enhance the performance of the HBC based on SPT by utilizing the waste heat for extra power and additional heating and cooling effects. This model aims to make an efficient integrated trigeneration system for CCHP application for the SPT plant. The proposed system's exergy and energy analysis was carried out to examine its utility. Also, parametric analysis was performed to investigate the impact of the different parameters of the SPT system and combined cycle on the performance of the SPT-based plant. Figure 3.1 shows the schematic diagram of the integrated system powered

by the SPT. This suggested system is composed of three subsystems. The first one is the SPT subsystem, in which the receiver and heliostats work as the main components. Air is considered as the heat transfer fluid (HTF) flowing through the central receiver due to its stability at the high-temperature application [74].

The second system is the supercritical Brayton cycle, which receives the heat from HTF through an internal heat exchanger (IHE). Here, as the working fluid, helium is used rather than supercritical carbon dioxide. The bottoming combined ORC-ERS is considered the third subsystem powered by the waste heat recovery unit (WHRU) using the heat from the topping HBC. The path of helium in the HBC can be described as helium at the lowest temperature and pressure (state 1) compressed through the helium compressor (HC) to state 2. The compressed helium stream passes through the recuperator (states 2–3) and enters the IHE, where it receives the heat from the HTF (states 3–4). This high-temperature helium stream in supercritical vapour form enters into the helium turbine (HT), where it expands and turbine work is obtained (state 4–5). This stream still has a small amount of heat and enters into the recuperator, where it relieves heat to a cold stream of helium (state 5–6). Still, some amount of heat remains. This amount of heat is received by bottoming combined ORC-ERS via WHRU (process 6–7). Then, the helium stream passes via a precooler (process 7–1), where it gains the temperature that is required at the inlet of the helium compressor by rejecting heat to cooling water.

The bottoming cycle includes the combined ORC-ERS operated by waste heat through the WHRU. The working fluid of the bottoming cycle is heated in WHRU and becomes superheated vapour (state 9). This superheated vapour goes to the ORC turbine (OT), expands there, and obtains power. After the OT (state 10), the fluid is a lower-pressure superheated vapour. The primary flow that enters the ejector is this stream, which is ‘‘mixes with another (secondary flow). The secondary flow is a saturated, low-pressure vapour originating from the evaporator (state 14). State 9’s mass flow rate is (m_g), State 14’s mass flow rate is (m_e), and State 11’s mass flow rate at the ejector’s outlet is (m_c). The condenser, where the heating is created, receives the stream from the ejector output. In all of the examples of this study that were looked at, the condenser’s temperature level was set to 50℃. This temperature is typical of the demand for heating in the construction industry. The stream is converted to liquid after the condenser

(state 12), and it is then split into two different currents. The one substream having mass flow travels through the evaporator to generate the cooling effect.

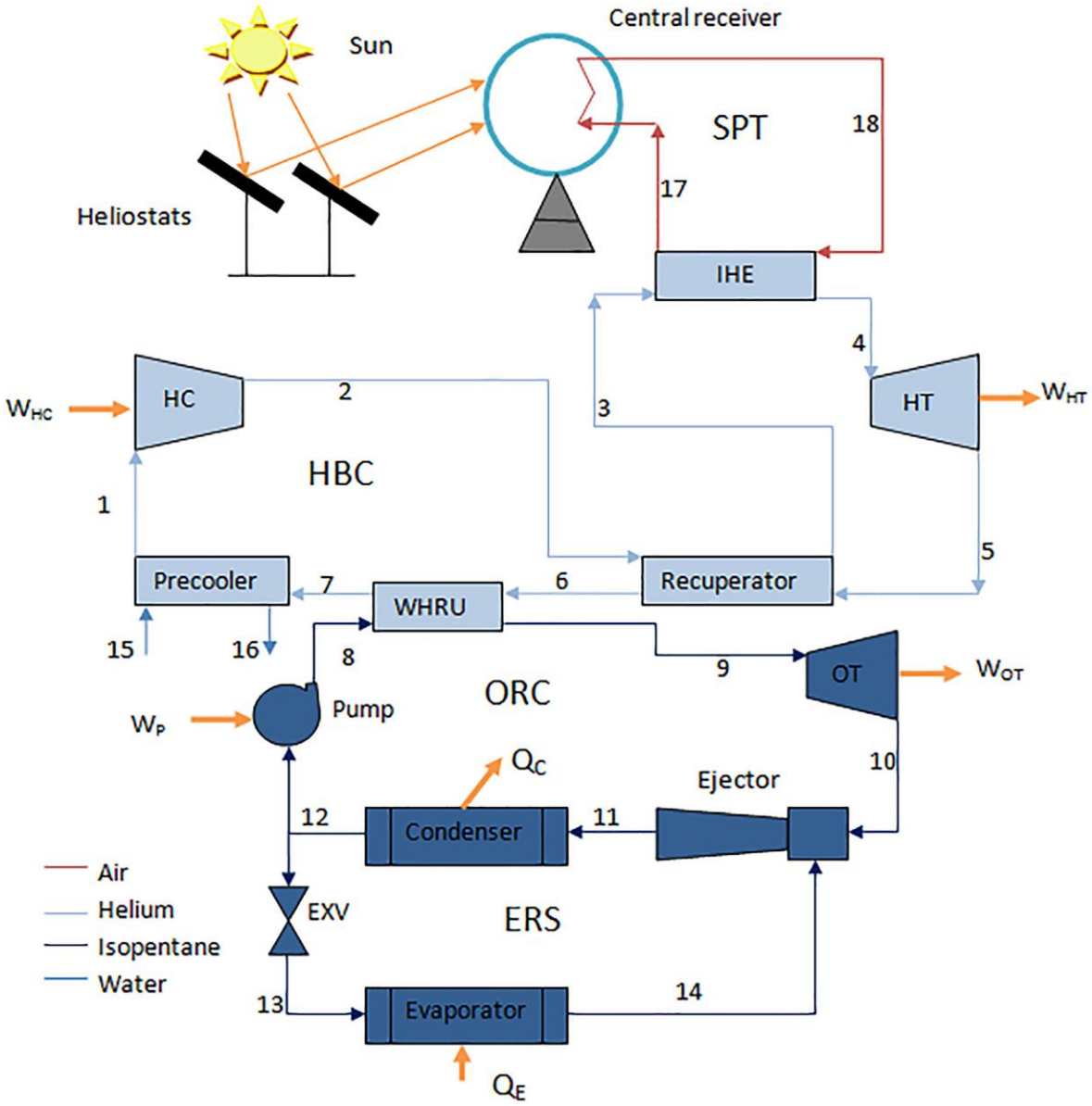

Figure 3.1 Schematic diagram of the SPT based integrated HBC and ORC-ERS system.

The pressure is decreased with enthalpy conservation before the evaporator at a throttling valve (state 13). The 10℃ as the evaporator temperature has been set. At this temperature, the cooling demands for building applications can be satisfied. The pressure of the other sub-stream increases as it approaches the liquid pump, creating a high-pressure sub-cooled liquid (state 8). This stream, which enters the generator with a mass flow rate of m_g, absorbs heat via helium.

For the investigation, the operating conditions of the integrated HBC-ORC-ERS system are mentioned in Table 3.1.

Table 3.1 Simulation data of the considered system for the analysis

Operating condition	Value
Designed efficiency of Heliostat field (η_{field})	0.6428 [71]
Heliostat's number (N_{hel})	624 [71]
Solar irradiation (DNI)	850 W/m^2 [163, 194, 195]
Each heliostat reflective area (A_{hel})	9.45×12.84 m^2 [71,163]
Aperture area of the receiver (A_{rec})	68.1 m^2 [71]
Designed efficiency of the Receiver (η_{rec})	0.75 [74]
Maximum inlet temperature at HBC	800 ℃ [71]
Isentropic efficiency of helium compressor (η_{HC})	0.88 [74]
Effectiveness of heat exchanger (ε)	0.9 [71, 74]
HC inlet pressure (P_1)	2500 kPa [71]
helium turbine isentropic efficiency (η_{HT})	0.9 [74]
OT isentropic efficiency (η_{OT})	0.8 [71]
OT inlet temperature (T_8)	197.2 ℃
Pinch point difference in condenser	5 ℃ [71]
WHRU- Pinch point	10 ℃ [71, 163]
Sun's apparent temperature (T_{Sun})	4500 K [196]
Ambient temperature (T_0)	25 ℃
Ambient pressure (P_0)	101.3 kPa
IHE pressure loss	2% [71]
Pressure loss in WHRU/recuperator	1% [71]
Ejector diffuser designed for efficiency	0.95 [164]
Ejector mixing designed for efficiency	0.85 [164]
Ejector nozzle designed for efficiency	0.9 [164]

Isopentane is the working media in the ORC-ERS system that is being studied. It is a dependable answer because isopentane has been investigated in other research investigations in related configurations [123, 197]. However, isopentane has not been investigated in ORC-ERS as a waste heat recovery system; therefore, our study is particularly interested in its selection. Dry fluid isopentane has a critical pressure and temperature of 3380 kPa and 187.2℃ respectively. This fluid has a low GWP of 20, an approximate zero ozone depletion potential, and is A3 ASHRAE safe [163, 197].

3.2. Description of SPT based combined HBC and ORC with cascade VAR-VCR integrated system

The description of the SPT-based HBC system was covered in the preceding section. Additionally, The ORC was utilized as the bottoming cycle [123,197] incorporated with a cascaded VAR-VCR cycle that uses the solar heat from the high-temperature SPT system to recover waste heat from the topping cycle for heating applications and cooling effect at low temperatures for food preservation, etc. Therefore, the proposed trigeneration system is able to produce CCHP utilizing the high-temperature SPT heat source. There are the following objectives of the present work;

- To make a tri-generation (HBC-VAR-VCR) system for CCHP application for the SPT plant.
- To determine the suggested CCHP system's exergetic and energetic performance.
- To perform the parametric analysis on the proposed system to examine the impact of various parameters.
- To perform performance comparison analysis of the proposed energy generation system using earlier research conducted under similar SPT working conditions.

As seen in Figure 3.2, this suggested system comprises four subsystems. The first is the SPT subsystem, in which the receiver and heliostats are the main components. Air is considered as the heat transfer fluid (HTF) flowing through the central receiver due to its stability at the high-temperature application [74]. The second system is HBC, which receives the heat from HTF through an internal heat exchanger (IHE). Here, helium is used as the working fluid instead of supercritical carbon dioxide. The bottoming cascading VAR-VCR is the third and fourth

subsystem powered by the generator using the heat from the topping cycle. The path of helium in the HBC can be described as helium at the lowest temperature and pressure (state 1) compressed through the helium compressor (HC) to state 2. The compressed helium stream passes through the recuperator (states 2 to 3) and enters the IHE, where it receives the heat from the HTF (states 3 to 4). This high-temperature helium stream in supercritical vapour form enters into the helium turbine (HT), where it expands and turbine work is obtained (states 4 to 5). This stream still has a small amount of heat and enters into the recuperator, where it relieves heat to a cold stream of helium (states 5 to 6). Still, some amount of heat remains. This amount of heat is received by the bottoming cascaded VAR-VCR cycle via the generator (processes 6 to 7). Then, the helium stream passes via a precooler (process 7 to 1), where it gains the temperature that is required at the inlet of the helium compressor by rejecting heat to cooling water.

The arrangement creates the cascade VAR-VCR system (states 8 to 21) by thermally combining the VCR system (states 8 to 11) and the VAR system (states 12 to 21) through the common condenser called cascade condenser (CC). VAR cascading lowers the VCR unit condenser's temperature (CC) while reducing energy consumption in the compressor. A cascaded refrigeration system requires both electricity and low-temperature heat as energy inputs. The refrigerant in a VCR system is throttled by the expansion valve-2 (EV2) from cascaded condenser pressure (state 8) to evaporator (Evap) pressure (state 9). Then vapor-liquid mixture (PG-Water)/chilled water moves through the evaporator to provide the cooling load. It evaporates the liquid-vapour mixture to the saturated vapour of the refrigerant (state 10). This saturated vapour is compressed isentropically in the compressor (Comp) (state 10 to 11) to reach the pressure of the CC. After the compressor, the refrigerant is in the superheated vapour form, transfers the heat load to the VAR cycle through the CC and converts into the saturated liquid (states 11 to 8).

VAR system considered the mixture of LiBr-H_2O as the absorbent and refrigerant fluid. The VAR system is used for food preservation; therefore, NH_3-H_2O is not used here. In the VAR system, the heating load supplied by the VCR system is absorbed by the refrigerant (H_2O), as previously mentioned. The H_2O evaporates completely and reaches the state 12. In the absorber, the saturated solution absorbs the LiBr water by rejecting the heat at the temperature of 25°C to 35°C. This process heat (at low grade) is used for applications like drying, heating water and

bleaching etc. The rich absorbent-refrigerant (H_2O-LiBr) mixture (state 13) is pumped to the generator (state 15), passing through the solution heat exchanger (SHE). In the generator, water vapour escapes from the mixture by taking the heat from the HBC system. The hot, weak solution in the refrigerant transfers the heat to the rich solution of referent through the SHE (states 16 to 17). Then, a weak solution in refrigerant reduces the pressure through the pressure-reducing valve (PRV) (states 17 to 18). The generator's (state 19) water vapour condenses through the condenser (Cond), producing low-grade heat (25 °C – 35 °C) that can be used for a variety of external purposes, including pasteurizing, cleaning, drying, bleaching, and heating household water. Condensation is the process that turns the water vapour into a saturated liquid (state 20). Moreover, the liquid refrigerant flows via the expansion valve (EV1), enters the absorber, and then recalculates in the cycle.

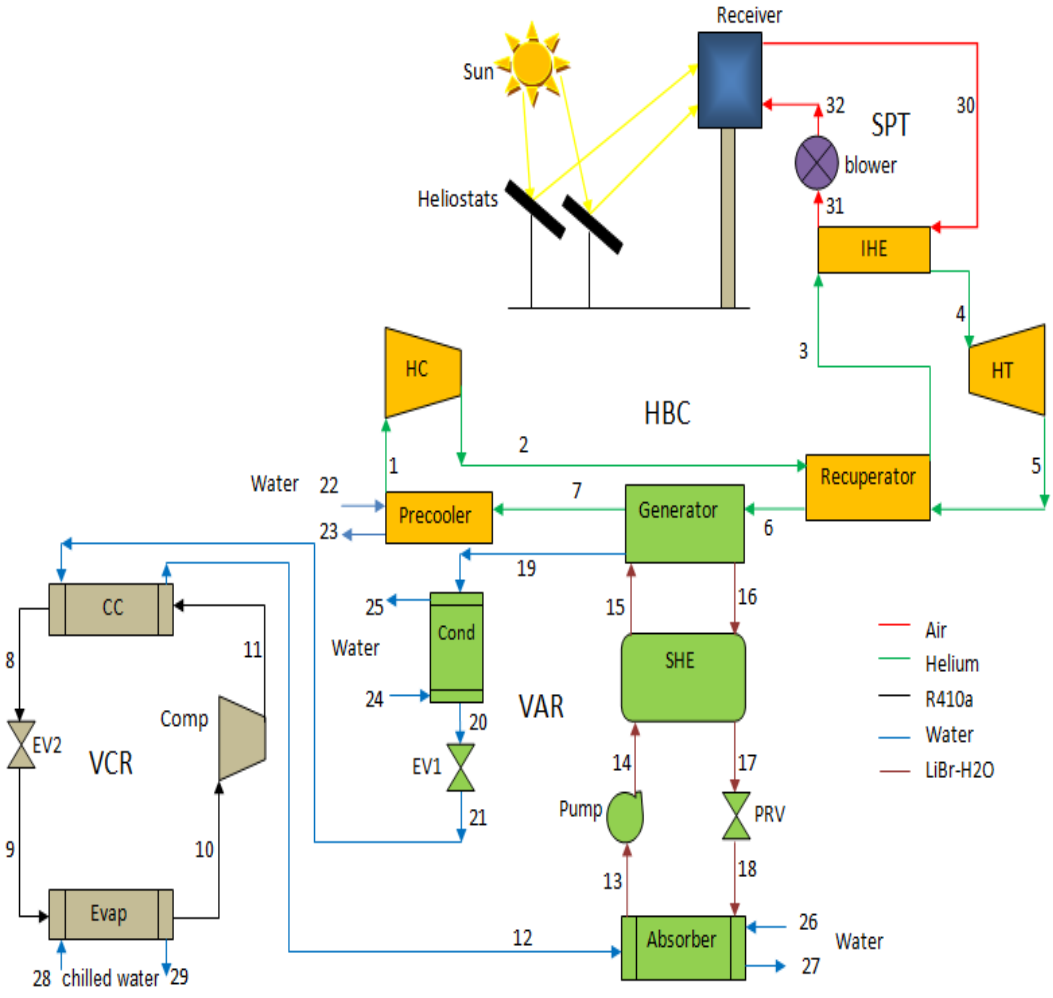

Figure 3.2 Schematic diagram of combined solar-based CCHP system

The suggested system could be used somewhere with moderate to high potential for solar energy. It is more appropriate because of its higher thermodynamic efficiency, more compact design, and less running expenses. Although PTSCs are the most common and economically appropriate technique for solar collectors, SPT systems have recently gained popularity [187] and are developing more quickly. The first-ever commercial SPT is held at the PS10 facility in Seville, Spain. Its technological aspects are illustrated in numerous publications. Each heliostat area in this system, which directs DNI towards a receiver located 115 meters above the ground, is around 121 m³. This project's yearly production of power is planned to be 23 GWhe [180]. Nevertheless, the Ivanpah power plant in California, USA, is the largest SPT in the world. It comprises three 140 m towers with a rated capacity of 390 MW and more than 170,000 heliostats. In September 2013, the system's first unit was connected to the electrical grid [199].

Table 3.2 lists the input data and other assumed values and designed parameters. The PS10 SPT plant was the basis for selecting the heliostat size in the current study. Located in Seville, Spain, this is the world's first commercial bike powered by SPT [187]. The system's actual operating conditions and limitations are also considered while selecting the thermodynamic parameters. For example, the maximum temperature value for T_4 is constrained by the heat source temperature of nearly about 1000°C [70] of the SPT system. It is ensured that helium attains supercritical fluid conditions in the HBC by choosing the appropriate compressor pressure ratio and pressure range.

For the investigation, the specifications of the proposed solar-based CCHP system are given in Table 3.2.

Table 3.2 Operating parameters considered for the developed plant

Parameter	Value
Sun's apparent temperature (T_{Sun})	4500 K [71,196]
HT isentropic efficiency (η_{HT})	0.9 [74]
Receiver aperture area (A_{rec})	68.1 m^2 [180]
Heliostat's area (A_{hel})	9.45×12.84 m^2 [180]
Efficiency of receiver (η_{rec})	0.9 [196]
Heliostat's count (N_{hel})	500 [180,167]

Field efficiency of heliostat (η_{field})	0.75 [196]
Pressure ratio of HC (CPR)	2.5 [167]
Inlet Pressure of HC (P_1)	2500 kPa [71]
Effectiveness of recuperator (ε)	0.9 [71, 74]
HC- isentropic efficiency (η_{HC})	0.88 [74]
Highest temperature of HBC (T_4)	850°C [70,180]
Solar irradiation (DNI)	850 W/m^2 [71,180]
CC- minimum temperature difference ($\Delta T_{min,cc}$)	8 °C [115-117]
Cascade condenser water temperature at outlet (T_{12})	6 °C [115-117]
Isentropic efficiency of VCR compressor (η_{Comp})	0.85 [115-117]
Absorber temperature (T_{13})	37 °C [116]
Condenser inlet temperature (T_{24})	27 °C [115-117]
Generator temperature (T_{19})	80 °C [116]
Absorber outlet temperature (T_{27})	32 °C [115-117]
Isentropic efficiency of VAR pump (η_{Pump})	0.9 [115-117]
Effectiveness of SHE (ε_{SHE})	0.7 [115-117]
Refrigeration effect ($\dot{Q}_e$)	30.7 kW [115-117]
Ambient pressure (P_0)	101.3 kPa [70,167]
Evaporator outlet (PG-chilled water) temperature (T_{29})	-15 °C [115-117]
Absorber inlet water temperature (T_{26})	27 °C [115-117]
Condenser outlet water temperature (T_{25})	32 °C [115-117]
Atmospheric temperature (T_0)	25 °C [115-117]

3.3. Description of SPT based combined HBC and ORC with cascade ERS-VRS integrated system

The recuperation methods employed by the cascade cycle before the cooler help to reduce excess heat, and the extra heat that is recovered and used for an expansion phase in a different turbine could enhance the heat supply. The temperature of the final exhaust output is extremely low even though there is just one heat exchanger [51,236].

This study used a bottoming system that combined an ejector system with an ORC to produce more electricity and offer simultaneous heating and cooling benefits for facilities like hospitals and hostels. This study was the first to use ORC-ERS as the bottoming cycle for the HBC system operated by the SPT plant [168,197]. This statement defines the current research novelty. The present study's objectives are;

- To develop a tri-generation system for the SPT plant incorporating a cascaded ejector and vapour compression that can produce heating and cooling effects at -40°C and 80°C, respectively, for industrial applications and food storage.
- To examine the suggested trigeneration system's performance using energy and exergy analysis.
- To investigate how the various SPT system key components and combined cycle influence plant performance using parametric analysis

Figure 3.2 shows the suggested system schematic diagram. The proposed integrated system is powered by the SPT sub-system as its heat source, air has been employed as the heat transfer fluid (HTF) because it is easily accessible and economical. HBC absorbs heat from the SPT subsystem through its internal heat exchanger (IHE). In the topping cycle, helium operates as the working fluid rather than sCO_2; the remaining heat is sent to the bottoming combination ORC-ERS via a heat recovery vapour generator (HRVG). The working fluid flow direction can be explained by taking into account that heated, high-temperature helium enters the turbine-1 (T1) (states 4-5) through the intermediate heat exchanger, or IHE. The helium expands once turbine-1 (T1) gets heat from the solar power tower (SPT) system. Subsequently, the expanded stream then moves to a colder stream, which absorbs the heat from the expanded stream, after entering the recuperator (states 5–6). Furthermore, the ORC-ERS system at the bottom absorbs the remaining

leftover heat through the HRVG (states 6-7). It was further compressed using compressor-1 (C1) (states 1-2). The cold stream of helium passes through the HTR (states 2-3) and then arrives at the IHE. The HRVG heats the bottoming coupled ORC-ERS in contrast to the topping cycle. Condenser heating was obtained through the bottoming cycle for industrial applications. Isopentane is employed as the working fluid in the ORC-ERS system analysis.

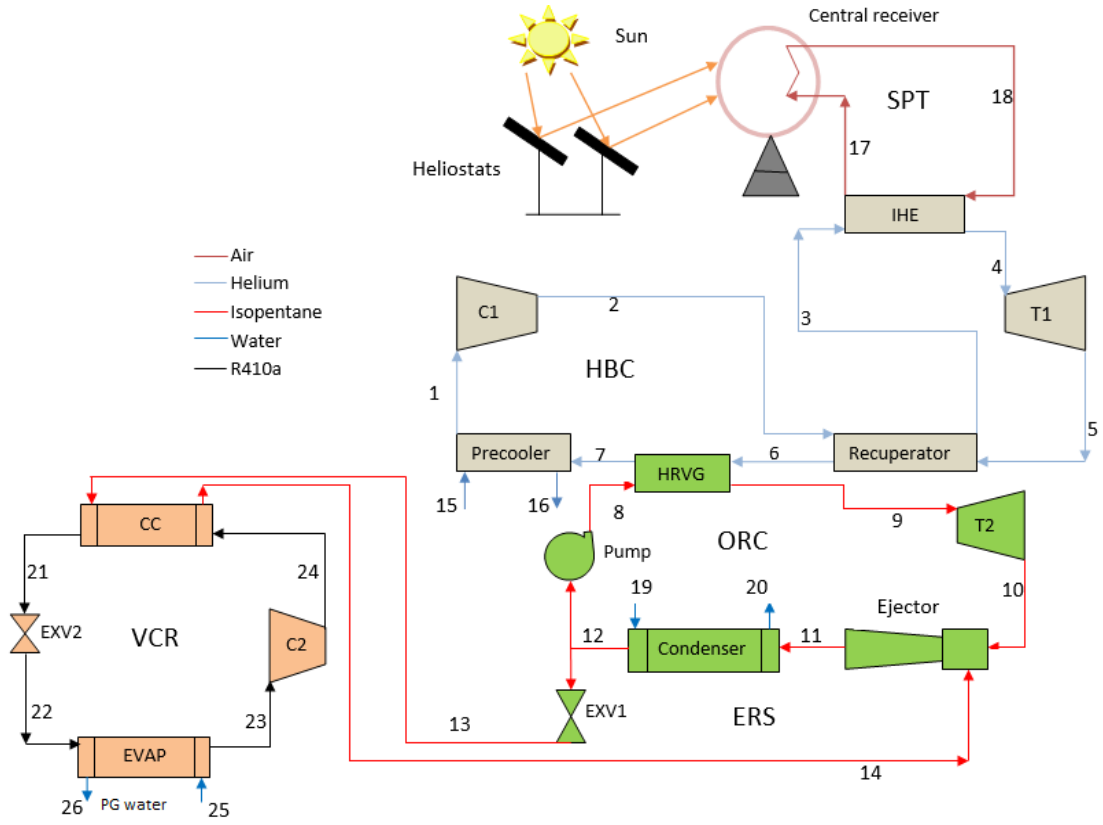

Figure 3.3 Schematic diagram of the suggested solar-based integrated system

This response might be deemed trustworthy since isopentane has been examined in similar conditions in previous studies [197, 200]. This study is particularly noteworthy for its choice of isopentane, which has not previously been examined in the context of ORC-ERS. Through the cascaded condenser (CC), the VCR system works, and -40 °C cooling was obtained from the evaporator (EVAP) for food storage application using Propylene-Glycol (PG) water as a cooling medium. The VCR system uses R410a as its operating fluid. The anhydrous fluid isopentane has a critical temperature of 187.2 °C and a critical pressure of 3380 kPa with a low GWP of 20 and nearly no ability to deplete the ozone layer, this fluid is rated as A3 ASHRAE safe [197, 200].

Table 3.3 lists the input data, other assumed values and designed parameters for investigating the proposed solar based trigeneration system.

Table 3.3 Simulation data considered for the proposed trigeneration system

Operating condition	Value
The efficiency of receiver (η_{rec})	0.75 [74]
Aperture area of the receiver (A_{rec})	68.1 m^2 [71]
Field efficiency of heliostat (η_{field})	0.6428 [71]
Heliostat's area (A_{hel})	9.45×12.84 m^2 [71,123]
Heliostat's number (N_{hel})	624 [71]
Solar irradiation (DNI)	850 W/m^2 [123]
T1 inlet temperature (T_4)	850 °C [74]
Isentropic efficiency of compressor-1 (η_{C1})	0.89 [71]
C1- input pressure (P_1)	2500 kPa [71]
T1- isentropic efficiency (η_{T1})	0.93 [129,115]
T2- isentropic efficiency (η_{T2})	0.8 [71]
ORC inlet temperature (T_9)	197.4 °C
IHE-Effectiveness (ε)	0.95 [115]
Condenser pinch	5 °C [71]
HRVG pinch	10 °C [71, 123]
Cascade condenser temperature (T_{CC})	-10 °C
Evaporator temperature (T_{EVAP})	-40 °C
Sun's temperature (T_{Sun})	4500 K [71, 196]
Environment temperature (T_0)	25 °C
Environment pressure (P_0)	101.3 kPa
Ejector's mixing efficiency	0.85 [164]
Ejector's nozzle efficiency	0.9 [164]
Ejector's diffuser efficiency	0.95 [164]

3.4. Description of combined Rankine-absorption power and cooling cycle with heating process integrated system

This study considers combining the Rankine power cycle with the vapour absorption refrigeration cycle to generate electricity and refrigeration from a single low-temperature heat source, such as solar or geothermal energy. Owing to the internal working components, the structure under consideration, and the cycle's presumed ideal conditions, it can produce a larger refrigeration output related to other cycles involving power and refrigeration [202]. This combined cycle can potentially lower the capital cost of a solar thermal power plant and is best suited for solar thermal electricity employing economical concentrating collectors.

The considered cycle in this study, as shown in Figure 3.4, is used where a saturated base mixture leaves the absorber towards the pump (path 4) and its pressure is increased by the pump (path 5). After that, it travels via path 6 to the heat exchanger to get heated before being sent to the rectifier. The rectifier is divided into two streams: the enriched ammonia vapour (path 10) and the weak ammonia solution (path 13). A heater is located under the rectifier where the weak solution of ammonia-water is heated and turns into saturated vapour (path 7). The weak saturated solution is heated by the superheater and is sent to the turbine (path 8). After going via a pressure relief valve, the enriched ammonia vapour is transformed into liquid inside the condenser, decreasing its pressure (path 1 to 2). In this always unalloyed path, ammonia is entirely converted into vapour by the evaporator (path 3). The absorber subsequently takes up this stream, which uses the expanded weak dilution from path 9 inside the turbine. The ammonia water basic dilution is created once here, and the cycle is completed. The heat source fluid is first passed through the superheater (path 14), and then, via path 15, enters the steam boiler. It then travels along path 16 and exits to the surroundings after using path 17 to pass via the heat exchanger.

For the analysis, the base case conditions of the considered integrated system are summarized in Table 3.4.

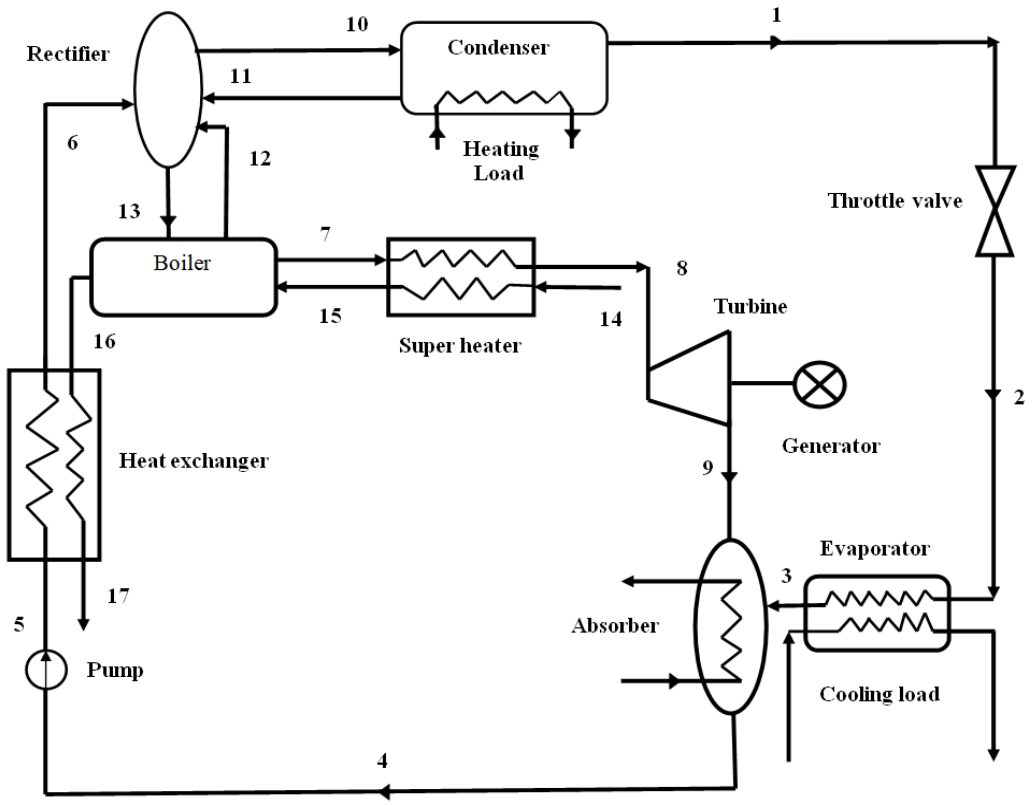

Figure 3.4 Schematic diagram of the integrated power and refrigeration system

Table 3.4 Main assumptive operating conditions for the analysis [201]

Ambient temperature (°C)	20
Ambient pressure (MPa)	0.10135
Inlet pressure of turbine (MPa)	2.5
Inlet temperature of turbine (°C)	285.0
Turbine's isentropic efficiency (%)	85
Refrigeration temperature (°C)	−25
Operating fluid temperature (°C)	300
Operating fluid mass rate (kg/s)	20
Pinch point temperature difference (°C)	15
Pump's isentropic efficiency (%)	70
Mass fraction of ammonia	0.34

3.5. Description of combined power, heating and cooling integrated system driven by Low-temperature heat source using various eco-friendly refrigerants

The heat sources at low temperatures, like waste heat, solar energy, fossil fuel combustion, etc., are abundant. Since it converts low-temperature energy into more useful forms of energy with higher system efficiency and lower pollutant emissions, the ORC and power generation systems that use a binary mixture as the working fluid are a promising solution to the energy turmoil and pollution-related problems of recent decades. Analysing the integrated combined heating, cooling and power (CCHP) and waste heat recovery has enhanced the system's overall efficiency by efficiently utilising low-temperature heat sources [128, 204].

The current study illustrates the parametric study of ORC and ERS integrated with the fluid at low temperatures using the eco-friendly operating fluids (R-123, R-124, R-141b, R-290, R-134a and R-152a) as the operating fluid.

The proposed cycle's schematic diagram is shown in Figure 3.5, which includes the ORC and ejector refrigeration. The components mainly include a heat generator (HRVG), a turbine (T), an ejector (EJE), a condenser (C), a pump (P), a regenerator (RE), a valve (EV) and an evaporator (E). The suggested system can be operated by low-grade heat, such as exhaust gas from an engine, industrial waste heat, solar heat, etc.

The heat source fluid temperature may be used to increase the temperature of high-pressure refrigerants through the HRVG. Refrigerants in a superheated state get expanded across the turbine to get power production. Entering the ejector at state-5, the partially extracted vapour is a primary flow. On the other hand, vapour fluids enter the ejector at state 13 as a secondary flow. Consequently, the above two fluids are allowed to mix across the mixing section, followed by an abrupt shock, after which there will be an increase in pressure. The mixed flow leaves from the ejector at state-7 and gets combined with the flow at state-6, leaving the turbine. The combined vapour at state-8 is allowed to cool at the low-pressure regenerator, and finally, at state-9, It enters the condenser. The stream outflows from the condenser at state-10 are separated into two parts. The first stream flows inside the pump while the second one flows inside the evaporator, followed by a decrease in pressure through the valve. The vapour gets vaporized

across the evaporator by transferring heat with the environment to get the desired refrigeration output, and finally, the stream enters the ejector as a secondary flow.

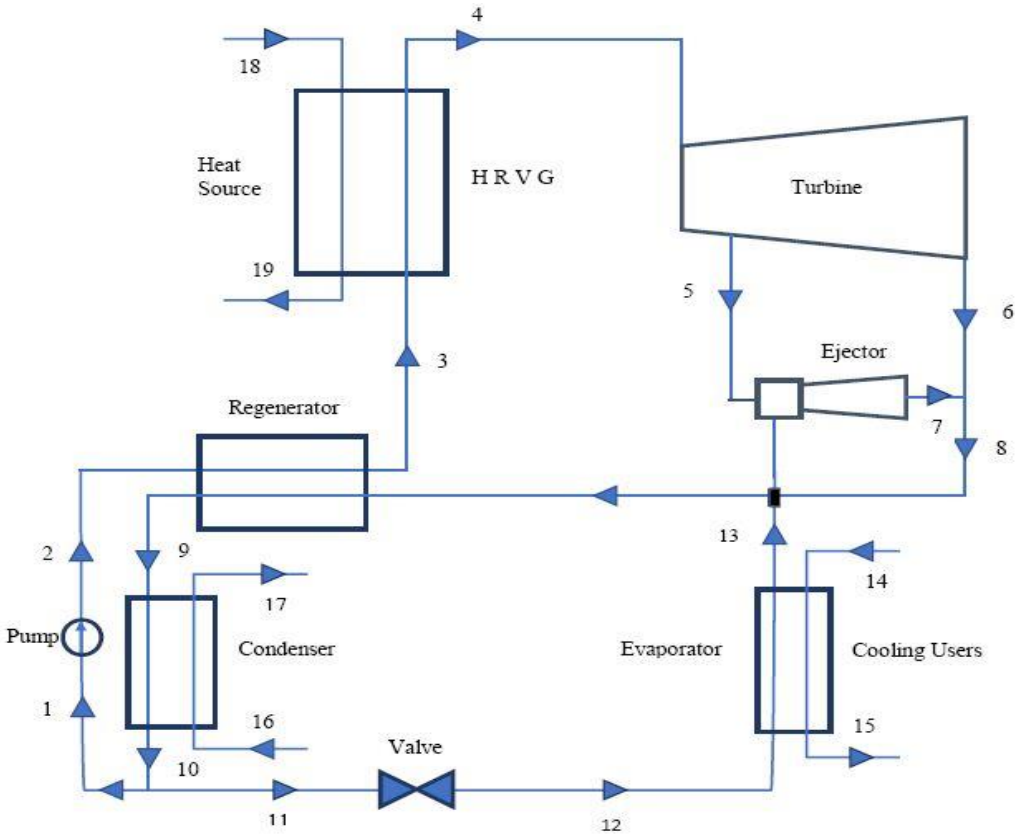

Figure 3.5Schematic diagram of the integrated power and refrigeration system

On the other hand, pump-provided pressurized liquid enters the regenerator, and finally, the vapour gets a superheated state as it enters the HRVG. The baseline conditions for analysis of the proposed ORC and ejector cooling system are illustrated in Table 3.5.

Table 3.5Main assumptive parameters considered for combined cycle [204]

Ambient Temperature (K)	298.15
Ambient Pressure (MPa)	0.10135
Turbine's input temperature (K)	373.15
Turbine's input pressure (MPa)	0.6
Turbine's back pressure (MPa)	0.2
Evaporator temperature (K)	263.15
Turbine’s Isentropic efficiency (%)	85

Pump’s isentropic efficiency (%)	80
Extraction ratio	0.35
Operating fluid mass rate (kg/s)	75
Power/cooling	2.5
Mass rate of cooling water (kg/s)	20
Efficiency of the HRVG (%)	100
Variation in temperature at pinch point (°C)	10.0
Ejector’s nozzle efficiency (%)	90
Ejector’s mixing chamber efficiency (%)	85
Ejector’s diffuser efficiency (%)	85

3.5.1. Refrigerants under consideration

High GWP refrigerants, particularly those that leak into the environment during operation or maintenance, greatly increase greenhouse gas emissions, one of the main contributors to global warming [123]. In an effort to slow global warming, the Kyoto Protocol put further limitations on using conventional refrigerants in 1997 because of their high greenhouse gas content (GWP). So, the primary characteristics of the most recent government regulations are the complete prohibitions and gradual phase-down of several common refrigerants in the market and limitations on the maintenance of equipment that uses HFCs. The major objective of these laws is to lessen the harmful emissions and replace these refrigerants with ecologically suitable alternatives [185]. Choosing the appropriate working fluids is usually the first stage in a cycle analysis [131]. A variety of factors must be fulfilled regarding the ideal working fluid. When selecting a working fluid, three important factors need to be considered: the possibility for ozone depletion, global warming and the desired different physical and chemical properties because they impact the environment. Since the stated cycle consists of ORC and an ejector-cooling system, the appropriate thermodynamic parameters must be present in the working fluid to get the generation of electricity and refrigeration effect simultaneously. Numerous studies have been done on various working fluids for ORC systems [157], but operating fluids utilized in the ORC are also applicable to the ejector refrigeration system.

In order to achieve optimal thermo-physical properties at optimal temperature and pressure, the ORC faces challenges in selecting its working fluid because, above its maximum temperature, it loses its chemical stability [200]. The ORC system uses three different types of working fluids: moist, isentropic, and dry. Because the expander output produces high-quality vapour, dry and isentropic operating is more appropriate than using other types of fluids [111]. Consequently, eight working fluids, isopentane, R-123, R-124, R-141b, R-290, R-134a, R-152a, and R410a, were taken into consideration for the ORC analysis in this study due to the above-mentioned reasons as well as low-temperature applications. The safety group categorization for each refrigerant consists of two or three alphanumeric characters (e.g., B1 or A2L). The numeral (with or without a suffix letter) signifies flammability, whereas the first character represents toxicity. There are two classifications of toxicity: class A (low toxicity) and class B (severe toxicity). The four flammability classes are 1, 2L, 2, or 3 [205]. The environmental information, thermal characteristics, security, and different operating fluids selected for every model in the thesis are listed in Table 3.6.

Table 3.6 Characteristics of organic working fluids [200,205].

Operating fluid	P_c (MPa)	T_c (℃)	T_b (℃)	Weight (kg/mole)	Type	ODP	GWP	Life span (years)	Safety group
Isopentane	3.38	187.2	27.8	72.1	D	0	20	0.009	A3
R-123	3.668	183.7	27.8	152.93	D	0.020	77	1.3	B1
R-124	3.624	122.3	-11.9	136.5	NA	0.022	609	NA	A1
R-152A	5.37	126.95	-24.7	66.05	D	0	124	1.2	A3
R-290	4.247	96.68	-42.1	44.10	W	0	~20	0.041	A3
R-134a	4.059	101	-26.1	102.03	I	0	1430	14	A1
R410a	4.90	72.8	-48.5	72.6	D	0	2088	4.9	A1
R141b	4.21	204.35	32	116.94	NA	0	1.2	4.6	A1

Chapter 4

Mathematical Modeling

The study of thermodynamic modelling of the models under consideration has been conducted in this chapter using mathematical equations. At first, the mathematical modelling of SPT was examined; subsequently, the modelling of a combined HBC and ORC with ejector refrigeration integrated system based on SPT was examined, SPT-based combined HBC and ORC with cascade VAR-VCR integrated system, SPT-based combined HBC and ORC with cascade ERS-VRS integrated system, combined Rankine-absorption power and refrigeration cycle with heating process integrated system and combined power, heating and cooling integrated system driven by Low-temperature heat source using various eco-friendly refrigerants. Additionally, an engineering equation solver is used to solve the mathematical equations after they have been programmed into computer code.

4.1. Modeling of SPT system

On the basis of energy and exergy conservation equations, thermal modelling equations for the proposed system were derived, taking the following assumptions into account.

a) The steady state conditions were ultimately attained by all system components.
b) Each component disregards friction loss and pressure.
c) Although all thermodynamic processes are adiabatic, they are not isentropic.
d) Neglecting the energy resulting from the height and velocity of each component.
e) The simulation is supported by the presumed input data and keeping the heliostat and receiver parameters constant, as indicated in Table 3.1.
f) Heat transfer fluid (HTF), i.e. Air temperature inlet to the IHE, has been taken 1000℃ [28].
g) The inlet temperature of the working fluid is 50℃ lower than the HTF temperature at the inlet to the IHE as a result of thermal losses.
h) The SPT modelling equations have been derived from previous studies [60, 206], and each component has been considered as a control volume.

The direct solar heat incident upon the heliostat field is defined as [60, 206]:

$$\dot{Q}_{Solar} = G_b \cdot A_h \cdot N_h \quad (4.1.1)$$

Where, $G_b$the solar irradiation per unit area is also known as direct normal irradiation (DNI), A_h is the single heliostat area (m^2), and N_h is the number of heliostats. Even so, a portion of that heat is dissipated into the environment as a result of the heliostat's efficiency. Therefore, the precise quantity of heat that is acquired via the heliostat field is denoted as [60, 206];

$$\dot{Q}_h = \dot{Q}_{solar} \cdot \eta_h \quad (4.1.2)$$

Where η_h represents the efficiency of the heliostat. Heat transfer fluid flows through the solar receiver, where this quantity of heat is directed. However, a portion of the heat is lost in the atmosphere. The solar center receiver's heat availability is subsequently evaluated as [60, 206];

$$\dot{Q}_r = \dot{Q}_h \cdot \eta_r = \dot{Q}_h - \dot{Q}_{loss,r} \quad (4.1.3)$$

Where, $\eta_r$is the receiver thermal efficiency, is defined as [60];

$$\eta_r = \alpha - [\zeta \cdot f_{view} \cdot \sigma \cdot T_R^4 + h_{conv} \cdot f_{conv} \cdot (T_R - T_{air})]/G_b \cdot \eta_h \cdot C_R \quad (4.1.4)$$

Here, TR represents the surface temperature of the solar receiver, and C_R, the concentrated ratio. The solar emittance is denoted by ζ. It is possible to approximate the calculation of heat loss as [60];

$$T_R = T_1 + \delta T_R \quad (4.1.5)$$

Where T_1 represents the turbine's inlet temperature and δT_R denotes the solar receiver's approach temperature. The table contains the geometric and operating values of the heliostat field and solar receiver. 3.1.

4.2. Modeling of SPT based combined HBC and ORC with ejector refrigeration integrated system

The current framework has been analyzed with the following assumption:

(1) Each component works on thermodynamic steady-state conditions.

(2) Assumed pressure loss for each component of the HBC has been listed in Table 3.1.

(3) Changes in kinetic and potential energy were considered negligible.

(4) Designed efficiencies and effectiveness of heat exchangers, turbines, compressors, pumps, etc., are assumed.

The present proposed plant is divided into three subsystems for thermodynamic modelling. First is the solar subsystem, which includes heliostats and a receiver as the main component. The second is HBC, and the third one is the combined ORC-ERS system. Each component in the proposed model has been considered as the thermodynamic system for thermodynamic modelling. The computational software Engineering Equation Solver (EES) is employed to simulate the thermodynamic model of each component in the system. Therefore, the control volume approach following steady-state equations has been used for energy and exergy evaluation.

4.2.1. Energy and exergy balance equation for the component of the proposed cycle

Taking the control volume approach the equation for the energy and exergy balance equation following steady-state conditions can be written as;

$$\dot{Q}_{CV} - \dot{W}_{CV} + \sum(\dot{m}_i h_i) - \sum(\dot{m}_e h_e) = 0 \quad (4.2.1)$$

$$\dot{ED} = \dot{EX}_{in} - \dot{EX}_{out} \quad (4.2.2)$$

where $\dot{EX}_{in}$ and $\dot{EX}_{out}$ denote the rate of exergy entering and exiting the control volume, respectively, and $(\dot{ED})$ denotes the rate at which exergy is destroyed within the component. The heat and work interaction from the control volume are denoted by $\dot{Q}_{CV}$ and$\dot{W}_{CV}$ respectively. The concept of exergy is used to evaluate second-law performance. The kinetic/potential exergy is disregarded for the considered system, and the chemical exergy for the considered system would be eliminated due to the absence of the combustion process. In the absence of chemical exergy

and energy due to velocity and height (due to the absence of chemical concentration in the specified system), the physical flow exergy can be expressed as;

$$\dot{E}X_j = \dot{m}\cdot[(h_j - h_0) - T_0(s_j - s_0)] \quad (4.2.3)$$

Where j denotes the particular state and $\dot{E}X_j$ is the physical exergy at the j^{th} state.

Modelling the solar sub-section is vital because the sun serves as the system's primary propulsion system. The solar component is simulated using models derived from previous publications [71, 74]. The solar portion consists of two main components: the receiver and the heliostat field. Where,A_{hel} refers to the reflective area of the heliostat. Heliostats focus the energy from the sun's radiation on the receiver that is situated at the top of the power tower. The sun irradiation per unit area (DNI) and total area of the heliostat field (A_{hel}) determine thetotal solar heat obtained by the heliostats. The expression to determine total solar heat is:

$$\dot{Q}_{Sun} = DNI \cdot A_{hel} \cdot N_{hel} \quad (4.2.4)$$

Where, N_{hel} refers to the number of heliostats used.

Amount of the solar heat received by the receiver from the heliostats is determined by the heliostat field efficiency (η_{field}). This energy's rate can be stated as follows:

$$\dot{Q}_{rec,in} = \eta_{field}\cdot\dot{Q}_{Sun} = \eta_{field}\cdot DNI \cdot A_{hel} \cdot N_{hel} \quad (4.2.5)$$

Where, η_{field} is the heliostat field efficiency (optical), and expressed as [71, 74];

$$\eta_{field} = \eta_{cos}\cdot\eta_{spb} \cdot \eta_{int} \cdot \eta_{att}\cdot\eta_{ref} \quad (4.2.6)$$

The variables $\eta_{cos}, \eta_{spb}, \eta_{int}, \eta_{att}, \eta_{ref}$ represents the efficiencies of the cosine effect, shading and blocking, interception efficiency, atmospheric attenuation and heliostats reflectivity respectively. It is vital to note that this current research relies on actual values from an existing SPT plant, and the determination of these values falls outside the scope of this study.

The receiver absorbs a heat amount denoted by $\dot{Q}_{rec,in}$, while $\dot{Q}_{rec,loss}$ is the amount of heat loss to the environment due to different modes of heat transfer. The remaining heat $\dot{Q}_{rec,net}$is then transferred to the HTF. The efficiency of heat transfer of the receiver is described as [71];

$$\eta_{rec} = \frac{\dot{Q}_{rec,net}}{\dot{Q}_{rec,in}} \quad (4.2.7)$$

$$\dot{Q}_{rec,in} = \dot{Q}_{rec,in} + \dot{Q}_{rec,loss} = \dot{m}_{air}(h_{16} - h_{17}) + \dot{Q}_{rec,loss} \quad (4.2.8)$$

The mathematical equations used for thermodynamic modelling of the trigeneration system based on the position numbers shown in Figure 3.1 have been illustrated below. Equations for energy and exergy analysis of each component based on input data provided in Table 3.1 are given below:

The energy equation for the heliostat field is expressed as;

$$\dot{Q}_{rec,in} = \eta_{field} \cdot DNI \cdot A_{hel} \cdot N_{hel} \quad (4.2.9)$$

The energy equation for the Receiver can be expressed as;

$$\dot{Q}_{rec,in} = \dot{m}_{air}(h_{18} - h_{17}) + \dot{Q}_{rec,loss} \quad (4.2.10)$$

The energy equation for an internal heat exchanger (IHE) can be expressed as;

$$\dot{Q}_{IHE} = \dot{m}_{air} \cdot (h_{16} - h_{17}) + \dot{m}_{He} \cdot (h_4 - h_3) \quad (4.2.11)$$

Work obtained by helium turbine (HT) and its efficiency can be expressed as;

$$\dot{W}_{HT} = \dot{m}_{He} \cdot (h_4 - h_5) \quad (4.2.12)$$

$$\eta_{HT} = \frac{(h_4 - h_5)}{(h_4 - h_{5s})} \quad (4.2.13)$$

Work input given to the helium compressor (HC) and its efficiency can be expressed as;

$$\dot{W}_{HC} = \dot{m}_{He} \cdot (h_2 - h_1) \quad (4.2.14)$$

$$\eta_{HC} = \frac{(h_{2s} - h_1)}{(h_2 - h_1)} \quad (4.2.15)$$

The energy balance equation for waste heat recovery unit (WHRU) can be expressed as;

$$\dot{m}_{He} \cdot (h_6 - h_7) = \dot{m}_g \cdot (h_9 - h_8) \quad (4.2.16)$$

The energy balance equation for the precooler can be expressed as;

$$\dot{m}_{He} \cdot (h_7 - h_1) = \dot{m}_{water} \cdot (h_{16} - h_{15}) \quad (4.2.17)$$

The energy balance equation for the recuperator and its effectiveness can be expressed as;

$$(h_3 - h_2) = (h_5 - h_6) \quad (4.2.18)$$

$$\varepsilon_{Recuperator} = \frac{(T_3 - T_2)}{(T_5 - T_2)} \quad (4.2.19)$$

The heat transfer equation of the condenser can be expressed as;

$$\dot{Q}_C = \dot{m}_c (h_{11} - h_{12}) \quad (4.2.20)$$

Work obtained by ORC turbine (OT) and its efficiency can be expressed as;

$$\dot{W}_{OT} = \dot{m}_g (h_9 - h_{10}) \quad (4.2.21)$$

$$\eta_{OT} = \frac{(h_9 - h_{10})}{(h_9 - h_{10s})} \quad (4.2.22)$$

Work input is given to pump (P) and its efficiency can be expressed as;

$$\dot{W}_P = \dot{m}_g (h_8 - h_{12}) \quad (4.2.23)$$

$$\eta_P = \frac{(h_{8s} - h_{12})}{(h_8 - h_{12})} \quad (4.2.24)$$

The equation for expansion valve (EXV) can be given as;

$$h_{12} = h_{13} \quad (4.2.25)$$

The equation for evaporator (E) can be given as;

$$\dot{Q}_E = \dot{m}_c (h_{14} - h_{13}) \quad (4.2.26)$$

The equation for ejector can be given as;

$$\dot{m}_c \cdot h_{11} = \dot{m}_g \cdot h_{10} + \dot{m}_e \cdot h_{14} \quad (4.2.27)$$

Additionally, this section will address the exergy analysis of the combined system. After presuming that there is no heat loss in the component, the exergy balance equation is applied to calculate the exergy destruction and exergy of each component. [207].

The exergy equation for the heliostat field is expressed as;

$$\dot{Q}_{Sun} \cdot \left(1 - \frac{T_0}{T_{ref,Sun}}\right) = \dot{Q}_{rec,in} \cdot \left(1 - \frac{T_0}{T_{ref,hel}}\right) + \dot{E}D_{hel} \quad (4.2.28)$$

The exergy equation for the receiver can be expressed as;

$$\dot{E}X_{17} + \dot{Q}_{rec,in} \cdot \left(1 - \frac{T_0}{T_{ref,hel}}\right) = \dot{E}X_{18} + \dot{Q}_{rec,loss} \cdot \left(1 - \frac{T_0}{T_{rec}}\right) + \dot{E}D_{rec} \quad (4.2.29)$$

The exergy equation for an internal heat exchanger (IHE) can be expressed as;

$$\dot{E}X_{16} - \dot{E}X_{17} = \dot{E}X_4 - \dot{E}X_3 + \dot{E}D_{IHE} \quad (4.2.30)$$

The exergy equation for a helium turbine (HT) can be expressed as;

$$\dot{E}X_4 = \dot{E}X_5 + \dot{W}_{HT} + \dot{E}D_{HT} \quad (4.2.31)$$

The exergy equation for a helium compressor (HC) can be expressed as;

$$\dot{E}X_1 = \dot{E}X_2 - \dot{W}_{HC} + \dot{E}D_{HT} \quad (4.2.32)$$

The exergy equation for the helium recuperator can be expressed as;

$$\dot{E}X_5 - \dot{E}X_6 = \dot{E}X_3 - \dot{E}X_2 + \dot{E}D_{Recuperator} \quad (4.2.33)$$

The exergy balance equation for Precooler can be expressed as;

$$\dot{E}X_7 - \dot{E}X_1 = \dot{E}X_{16} - \dot{E}X_{15} + \dot{E}D_{Preooler} \quad (4.2.34)$$

The exergy balance equation for waste heat recovery unit (WHRU) can be expressed as;

$$\dot{E}X_6 - \dot{E}X_7 = \dot{E}X_9 - \dot{E}X_8 + \dot{E}D_{WHRU} \quad (4.2.35)$$

The exergy equation for the condenser (C) can be given as;

$$\dot{E}X_{11} - \dot{E}X_{12} = \dot{Q}_C \cdot \left(1 - \frac{T_0}{T_C}\right) + \dot{E}D_C \quad (4.2.36)$$

The exergy equation for the ORC turbine (OT) can be given as;

$$\dot{E}X_9 = \dot{E}X_{10} + \dot{W}_{OT} + \dot{E}D_{OT} \quad (4.2.37)$$

The exergy equation for pump (P) can be given as;

$$\dot{E}X_{12} = \dot{E}X_8 - \dot{W}_P + \dot{E}D_P \quad (4.2.38)$$

The exergy equation for evaporator (E) can be given as;

$$\dot{E}X_{13} - \dot{E}X_{14} = \dot{Q}_E \cdot \left(1 - \frac{T_0}{T_C}\right) + \dot{E}D_E \quad (4.2.39)$$

The exergy equation for ejector can be given as;

$$\dot{E}X_{10} + \dot{E}X_{14} = \dot{E}X_{11} + \dot{E}D_{ejector} \quad (4.2.40)$$

The exergy equation for the expansion valve (EXV) can be given as;

$$\dot{E}X_{12} - \dot{E}X_{13} = \dot{E}D_{EXV} \quad (4.2.41)$$

The simulation code incorporates each of these relationships, and it was generated using EES software. To determine all unknown parameters, the program retrieves thermodynamic characteristics from its collection of property functions, including state point thermodynamic properties, heat and work interactions, and exergy rates for each stream.

4.2.2. Energy and exergy efficiency of the proposed system

The ratio of net output power to the energy or exergy input available with the sun irradiation on the heliostat field is the overall energy and exergy efficiency for the researched solar power plant. [196, 164]:

$$\eta_{en} = \frac{\dot{W}_{net} + \dot{Q}_E + \dot{Q}_C}{\dot{Q}_{Sun}} \quad (4.2.42)$$

$$\eta_{ex,} = \frac{\dot{W}_{net} + \dot{Q}_E \cdot \left(1 - \frac{T_0}{T_E}\right) + \dot{Q}_C \cdot \left(1 - \frac{T_0}{T_C}\right)}{\dot{Q}_{Sun} \cdot \left(1 - \frac{T_0}{T_{ref,Sun}}\right)} \quad (4.2.43)$$

Where, $T_{ref,Sun}$ is thesun's apparent temperature that was used as the equivalent temperature of the source of heat for exegetic evaluation [196].$\dot{W}_{net}$ is the net power output of the plant evaluated as:

$$\dot{W}_{net} = \dot{W}_{HT} - \dot{W}_{HC} + \dot{W}_{OT} - \dot{W}_{pump} \quad (4.2.44)$$

4.2.3. Ejector modeling

The main sections of the analyzed ejector are shown in Figure 4.1. The device has one outlet and two inlets. The OT (state 10) generates the primary flow, whilst the evaporator (state 14) generates the secondary flow. These flows combine at the mixing portion, then go to the throat region and finally to the diffuser region after that. The state point 11 is the ejector's outlet. More particular, the pressure of the flow pressure decreases (state pf2) when it enters the ejector's motive nozzle (point pf1). The pressure of the stream secondary flow (state sf_1) declines as it enters the ejector's suction nozzle (state point sf2).The two streams' decreased pressure readings are equal (P_{low}). Due to the ejector's design, the pressure differential ($P_{sf1}-P_{low}$) is rather minimal. Furthermore, it is crucial to reiterate that in order for the state points pf_2 and $sf_2$to be mixed (mf) in the mixing section, their respective pressure levels must be the same. The pressure level is assumed to be constant in the throat section and to rise at the end of the diffuser (Pd) in this modelling. The condenser device's pressure level and its level of pressure at the ejector exit are the same.

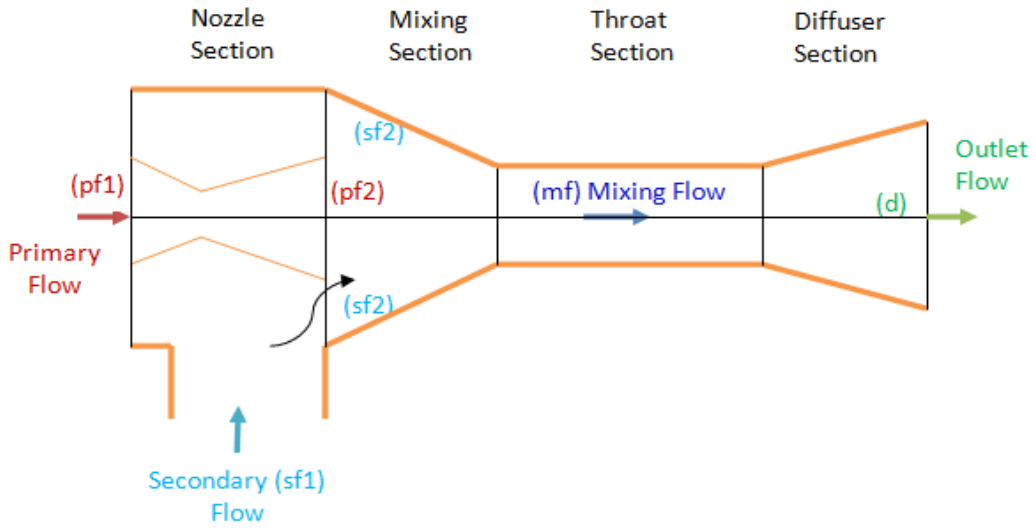

Figure 4.1 Model of ejector device for the mathematical modelling

The following lists the major presumptions of ejector modeling [164, 120]:

a) Throughout the mixing procedure, the pressure levels are constant.
b) There is no mixing of the secondary and primary streams prior to the entry of the throat portion, where both streams obtained equal pressure.

c) Throughout the mixing process, momentum, as well as energy, is preserved.
d) The flow is expected to be a single-dimensional homogenous equilibrium flow with steady-state conditions.
e) At the entry points and the outflow, it presumes that there is no velocity.
f) The non-ideal process in the ejector portions is modelled using efficiency modelling.
g) The ejector has thermal insulation, so it doesn't lose heat to the surroundings.

(a) Motive nozzle

It is crucial to note that at the state point (pf1), the inflow velocity is insignificant. The motive nozzle's energy conservation can be expressed as follows:

$$h_{pf1} = h_{pf2} + \frac{{V_{pf2}}^2}{2} \quad (4.2.45)$$

Also, its nozzle efficiency (η_n) is expressed as:

$$\eta_n = \frac{(h_{pf1} - h_{pf2})}{(h_{pf1} - h_{pf2,s})} \quad (4.2.46)$$

The state point (pf2,s) is an optimum position when taking into account the amount of entropy at the state point (pf1) and a pressure level (P_{low}) that is lower than the secondary flow pressure (P_{sf}). The pressure drop is typically a few kPa and relies on the working fluid and ejector design [120]:

(b) Suction nozzle

The suction nozzle's energy efficiency and energy balance can be expressed as follows. It is crucial to note that at the state point (sf1), the inflow velocity is insignificant.

$$h_{sf1} = h_{sf2} + \frac{{V_{sf2}}^2}{2} \quad (4.2.47)$$

$$\eta_n = \frac{(h_{sf1} - h_{sf2})}{(h_{sf1} - h_{sf2,s})} \quad (4.2.48)$$

The state (sf2,s) is the optimum point because it has the lowest secondary flow pressure (P_{sf}) and the lowest state point (sf1) entropy.

(c) Mixing section

The entertainment ratio (μ) is a crucial variable for ejector modelling. The entertainment ratio (μ) is the ratio of the mass flow rate of secondary flow to the primary flow can be expressed as:

$$\mu = \frac{m_{sf}}{m_{sf}} \tag{4.2.49}$$

As was seen in the previous hypotheses, the pressure in the mixing section is equal to P_{low}. The primary equations that describe the mixing process are shown here. The ideal conservation of momentum may be expressed as follows:

$$V_{pf} + \mu \cdot V_{pf} = (1 + \mu) \cdot V_{mf,s} \tag{4.2.50}$$

The mixing efficiency (η_m) [121] is used to account for friction losses along with other non-ideal elements and is described as:

$$\eta_m = \frac{{V_{mf}}^2}{{V_{mf,s}}^2} \tag{4.2.51}$$

The final mixed flow velocity is derived through the combination of Eq. (16) and (17).

$$V_{mf} = \sqrt{\eta_m} \cdot \left(\frac{1}{1+\mu} \cdot V_{pf} + \frac{\mu}{1+\mu} V_{sf}\right) \tag{4.2.52}$$

The conversion energy can be written as:

$$(1 + \mu) \cdot \left(h_{mf} + \frac{{V_{mf}}^2}{2}\right) = \left(h_{pf} + \frac{{V_{pf}}^2}{2}\right) \cdot \mu \cdot \left(h_{sf} + \frac{{V_{sf}}^2}{2}\right) \tag{4.2.53}$$

d) Diffuser section

After neglecting the flow velocity at the exit of the diffuser i.e at point (d), the energy balance equations and the diffuser efficiency were expressed as;

$$h_d = h_{mf} + \frac{{V_{mf}}^2}{2} \tag{4.2.54}$$

$$\eta_d = \frac{(h_{d.s} - h_{mf})}{(h_d - h_{mf})} \tag{4.2.55}$$

The state point (d,s), isentropic point at the condition point (mf) and pressure (P_d) which is equal to the condenser pressure.

4.3. Modeling of SPT based combined HBC and ORC with Cascade VAR-VCR integrated system

The following assumptions were made while analyzing the present work as follows:

a) Each component works on thermodynamic steady-state conditions.
b) Assumed pressure loss for each component of the HBC has been listed in Table 3.2 [70].
c) Change in kinetic and potential energy was considered as negligible.
d) Isentropic efficiencies and effectiveness of heat exchangers, turbines, compressors, pumps, etc., are assumed.
e) During the examination of the VAR-VCR system, heat and pressure loss in the heat exchangers and pipes were neglected [115].
f) At the specific pressure and temperature LiBr-H2O is assumed in equilibrium in the generator and absorber [115].
g) Water cooling is provided in the condenser and absorber.
h) Cooling water temperature and pressure have been assumed and given in Table 3.2[115].
i) States 8, 10, 12, and 20 are taken as the saturated states [115].

During the thermodynamic modelling of the proposed system, the complete plant is divided into two subsystems. The first subsystem is the solar system, which includes the receiver and heliostats as the prime components while neglecting the effect of the blower. The second subsystem is the trigeneration unit (HBC-VAR-VCR) for thermodynamic study.

4.3.1. Energy and exergy balance equation for the components of the proposed system

Each component was considered as the thermodynamic system while applying the energy/exergy balance equations. Therefore, following the control volume/steady state equations were considered for calculating the energy and exergy interactions from the components;

$$\dot{Q}_{CV} - \dot{W}_{CV} + \sum(\dot{m}_i h_i) - \sum(\dot{m}_e h_e) = 0 \quad (4.3.1)$$

$$\dot{ED} = \dot{X}_{in} - \dot{X}_{out} \quad (4.3.2)$$

Where,$\dot{X}_{in}$ and $\dot{X}_{out}$refers total exergy interaction at the inlet and outlet of the control volume, respectively. $\dot{E}D$ is the exergy destruction within the component. The concept of exergy is used to evaluate second-law performance. The four components of total exergy for a fluid stream are as follows [67]:

$$\dot{X}_j = \dot{X}_{ph} + \dot{X}_{ch} + \dot{X}_{ke} + \dot{X}_{pe} \quad (4.3.3)$$

The systems under discussion do not take into account the kinetic/potential exergy. Additionally, the balancing equations would negate the chemical exergy for the HBC and trigeneration system. Thus, the total exergy for these systems can now be mathematically represented as:

$$\dot{X}_j = \dot{X}_{ph} \dot{=} \dot{m}\cdot[(h_j - h_0) - T_0(s_j - s_0)] \quad (4.3.4)$$

Modelling the solar sub-section is essential due to the sun's role as the primary propulsion system. This section is simulated using models that have been developed from previous literature [70, 74]. The solar sub-section consists of two main components: the receiver and the heliostat field. The term "A_{hel}" represents the area of each heliostat. Heliostats concentrate the solar radiation onto the receiver located at the apex of the power tower. The total solar heat obtained by the heliostats is determined by the direct normal irradiance (DNI) of the sun and the total area of the heliostat field (A_{hel}). The formula representing this parameter is:

$$\dot{Q}_{solar} = DNI \cdot A_{hel} \cdot N_{hel} \quad (4.3.5)$$

The amount of solar heat received by the receiver from the heliostats is determined by the heliostat field efficiency (η_{field}). This energy's rate can be stated as follows:

$$\dot{Q}_{rec} = \eta_{field}\cdot\dot{Q}_{solar} \quad (4.3.6)$$

Where, η_{field} is determined as [70, 74];

$$\eta_{field} = \eta_{cos}\cdot\eta_{s\&b} \cdot \eta_{int} \cdot \eta_{att} \cdot \eta_{ref} \quad (4.3.7)$$

The variables $\eta_{int}, \eta_{att,}\eta_{cos}, \eta_{ref}, \eta_{s\&b}$ represent the efficiencies associated with the interception efficiency, atmospheric attenuation, cosine effect, heliostat reflectivity, shading and blocking respectively. It is vital to note that this current research relies on actual values from an existing SPT plant, and the determination of these values falls outside the scope of this study.

The receiver absorbs a heat amount is denoted by$\dot{Q}_{rec,in}$, while $\dot{Q}_{rec,loss}$ is the amount heat loss to the environment due to different modes of heat transfer. The remaining heat $\dot{Q}_{rec,net}$ is then transferred to the HTF. The efficiency of heat transfer of the receiver is described as [70];

$$\eta_{rec} = \frac{\dot{Q}_{rec,net}}{\dot{Q}_{rec,in}} \tag{4.3.8}$$

The net heat transfer through the receiver can be defined as;

$$\dot{Q}_{rec,net} = \dot{m}_{air}\cdot(h_{30} - h_{31}) \tag{4.3.9}$$

$$\dot{Q}_{rec,net} = \dot{Q}_{rec,in} + \dot{Q}_{rec,loss} \tag{4.3.10}$$

The thermodynamic modelling equations of the trigeneration system (HBC-VAR-VCR) are listed below. EES code has been developed for solving these equations using the given data in Table 3.2 together. Using the EES library of the property functions, the state point thermodynamic properties, heat and work interactions, and exergy rate at every state have been calculated.

The mathematical equations used for thermodynamic modelling of the trigeneration system based on the position numbers shown in Figure 3.2 has been illustrated below. Equations for energy and exergy analysis of each component based on input data provided in table 3.2 are given below:

The energy equation for the heliostat field is expressed as;

$$\dot{Q}_{rec,in} = \eta_{field}\cdot DNI \cdot A_{hel} \cdot N_{hel} \tag{4.3.11}$$

The energy equation for the receiver can be expressed as;

$$\dot{Q}_{rec,in} = \dot{m}_{air}(h_{30} - h_{31}) + \dot{Q}_{rec,loss} \tag{4.3.12}$$

The energy equation for an internal heat exchanger (IHE) can be expressed as;

$$\dot{Q}_{IHE} = \dot{m}_{air}\cdot(h_{30} - h_{31}) + \dot{m}_{He}\cdot(h_4 - h_3) \tag{4.3.13}$$

Work obtained by helium turbine (HT) and its efficiency can be expressed as;

$$\dot{W}_{HT} = \dot{m}_{He}\cdot(h_4 - h_5) \tag{4.3.14}$$

$$\eta_{HT} = \frac{(h_4 - h_5)}{(h_4 - h_{5s})} \quad (4.3.15)$$

Work input given to the helium compressor (HC) and its efficiency can be expressed as;

$$\dot{W}_{HC} = \dot{m}_{He} \cdot (h_2 - h_1) \quad (4.3.16)$$

$$\eta_{HC} = \frac{(h_{2s} - h_1)}{(h_2 - h_1)} \quad (4.3.17)$$

The energy and mass balance equation for generator (g) can be expressed as;

$$\dot{Q}_g = \dot{m}_{19} \cdot h_{19} + \dot{m}_{16} \cdot h_{16} - \dot{m}_{15} \cdot h_{15} \quad (4.3.18)$$

$$\dot{m}_{15} = \dot{m}_{16} + \dot{m}_{19} \quad (4.3.19)$$

The energy balance equation for the precooler can be expressed as;

$$\dot{m}_{He} \cdot (h_7 - h_1) = \dot{m}_{water} \cdot (h_{23} - h_{22}) \quad (4.3.20)$$

The energy balance equation for the recuperator and its effectiveness can be expressed as;

$$(h_3 - h_2) = (h_5 - h_6) \quad (4.3.21)$$

$$\varepsilon_{Recuperator} = \frac{(T_3 - T_2)}{(T_5 - T_2)} \quad (4.3.22)$$

The heat transfer equation of the VAR condenser can be expressed as;

$$\dot{Q}_c = \dot{m}_{19}(h_{19} - h_{20}) = \dot{m}_{water} \cdot (h_{25} - h_{24}) \quad (4.3.23)$$

The equation for expansion valve-1 can be expressed as;

$$h_{20} = h_{21} \quad (4.3.24)$$

The equation for absorber (a) can be expressed as;

$$\dot{Q}_a = \dot{m}_{12} \cdot h_{12} + \dot{m}_{18} \cdot h_{18} - \dot{m}_{13} \cdot h_{13} \quad (4.3.25)$$

$$\dot{m}_{13} = \dot{m}_{12} + \dot{m}_{18} \quad (4.3.26)$$

$$x_{16} \cdot \dot{m}_{18} = x_{13} \cdot \dot{m}_{13} \quad (4.3.27)$$

Work input given to pump (P) and its efficiency can be expressed as;

$$\dot{W}_P = \dot{m}_{13}(h_{14} - h_{13}) \quad (4.3.28)$$

$$\eta_P = \frac{(h_{14s} - h_{13})}{(h_{14} - h_{13})} \quad (4.3.29)$$

The energy balance equation for solution heat exchanger (SHE) and its effectiveness can be expressed as;

$$\dot{m}_{16} \cdot h_{16} - \dot{m}_{17} \cdot h_{17} = \dot{m}_{15} \cdot h_{15} - \dot{m}_{14} \cdot h_{14} \quad (4.3.30)$$

$$\varepsilon_{SHE} = \frac{(T_{16} - T_{17})}{(T_{16} - T_{14})} \quad (4.3.31)$$

The equation for pressure reducing valve can be expressed as;

$$h_{17} = h_{18} \quad (4.3.32)$$

The equation for cascade condenser (cc) can be given as;

$$\dot{Q}_{cc} = \dot{m}_{12}(h_{12} - h_{21}) = \dot{m}_8(h_{11} - h_8) \quad (4.3.33)$$

$$\Delta T_{min,cc} = T_8 - T_{21} \quad (4.3.34)$$

The equation for expansion valve-2 can be given as;

$$h_8 = h_9 \quad (4.3.35)$$

The equation for evaporator (e) can be given as;

$$\dot{Q}_e = \dot{m}_9(h_9 - h_{10}) = \dot{m}_{PG-water} \cdot (h_{28} - h_{29}) \quad (4.3.36)$$

The equation for VCR compressor can be given as;

$$\dot{W}_{Comp} = \dot{m}_{10}(h_{11} - h_{10}) \quad (4.3.37)$$

$$\eta_{Comp} = \frac{(h_{11s} - h_{10})}{(h_{11} - h_{10})} \quad (4.3.38)$$

Additionally, this section will address the exergy analysis of the combined system. After presuming that there is no heat loss in the component, the exergy balance equation is applied to calculate the exergy destruction and exergy of each component. [207].

The exergy equation for the heliostat field is expressed as;

$$\dot{Q}_{Sun} \cdot \left(1 - \frac{T_0}{T_{ref,Sun}}\right) = \dot{Q}_{rec,in} \cdot \left(1 - \frac{T_0}{T_{ref,hel}}\right) + \dot{E}D_{hel} \quad (4.3.39)$$

The exergy equation for the receiver can be expressed as;

$$\dot{X}_{31} + \dot{Q}_{rec,in} \cdot \left(1 - \frac{T_0}{T_{ref,hel}}\right) = \dot{X}_{30} + \dot{Q}_{rec,loss} \cdot \left(1 - \frac{T_0}{T_{rec}}\right) + \dot{E}D_{rec} \quad (4.3.40)$$

The exergy equation for an internal heat exchanger (IHE) can be expressed as;

$$\dot{X}_{30} - \dot{X}_{31} = \dot{X}_4 - \dot{X}_3 + \dot{E}D_{IHE} \quad (4.3.41)$$

The exergy equation for a helium turbine (HT) can be expressed as;

$$\dot{X}_4 = \dot{X}_5 + \dot{W}_{HT} + \dot{E}D_{HT} \quad (4.3.41)$$

The exergy equation for a helium compressor (HC) can be expressed as;

$$\dot{X}_1 = \dot{X}_2 - \dot{W}_{HC} + \dot{E}D_{HC} \quad (4.3.42)$$

The exergy equation for the helium recuperator can be expressed as;

$$\dot{X}_5 - \dot{X}_6 = \dot{X}_3 - \dot{X}_2 + \dot{E}D_{Recuperator} \quad (4.3.43)$$

The exergy balance equation for precooler can be expressed as;

$$\dot{X}_7 - \dot{X}_1 = \dot{X}_{22} - \dot{X}_{23} + \dot{E}D_{Preooler} \quad (4.3.44)$$

The exergy balance equation for the generator can be expressed as;

$$\dot{X}_{15} + \dot{Q}_g \cdot \left(1 - \frac{T_0}{T_g}\right) = \dot{X}_{19} + \dot{X}_{16} + \dot{E}D_g \quad (4.3.45)$$

The exergy equation for VAR condenser (c) can be given as;

$$\dot{X}_{19} - \dot{X}_{20} = \dot{Q}_c \cdot \left(1 - \frac{T_0}{T_c}\right) + \dot{E}D_c \quad (4.3.47)$$

The exergy equation for expansion valve-1 can be given as;

$$\dot{X}_{20} - \dot{X}_{21} = \dot{E}D_{EV1} \quad (4.3.48)$$

The exergy equation for the absorber can be given as;

$$\dot{X}_{13} + \dot{Q}_a \cdot \left(1 - \frac{T_0}{T_a}\right) + \dot{ED}_g = \dot{X}_{12} + \dot{X}_{18} \quad (4.3.49)$$

The exergy equation for the pump can be given as;

$$\dot{X}_{13} = \dot{X}_{14} - \dot{W}_P + \dot{ED}_{Pump} \quad (4.3.50)$$

The exergy equation for solution heat exchanger (SHE) can be given as;

$$\dot{X}_{16} + \dot{X}_{14} = \dot{X}_{15} + \dot{X}_{17} + \dot{ED}_{SHE} \quad (4.3.51)$$

The exergy equation for pressure reducing valve can be given as;

$$\dot{X}_{17} - \dot{X}_{18} = \dot{ED}_{PRV} \quad (4.3.52)$$

The exergy equation for cascade condenser (cc) can be given as;

$$\dot{X}_{11} + \dot{X}_{21} = \dot{X}_{12} + \dot{X}_8 + \dot{ED}_{cc} \quad (4.3.53)$$

The exergy equation for expansion valve-2 can be given as;

$$\dot{X}_8 - \dot{X}_9 = \dot{ED}_{EV2} \quad (4.3.54)$$

The exergy equation for evaporator (e) can be given as;

$$\dot{X}_9 - \dot{X}_{10} = \dot{Q}_e \cdot \left(1 - \frac{T_0}{T_e}\right) + \dot{ED}_e \quad (4.3.55)$$

The equation for the VCR compressor can be given as;

$$\dot{X}_{10} + \dot{W}_{Comp} = \dot{X}_{11} + \dot{ED}_{Comp} \quad (4.3.56)$$

The simulation code, which was developed with EES software, incorporates each of these relationships. In an effort to ascertain all parameters that are unknown, the application extracts thermodynamic characteristics from its database of property functions. This includes state point thermodynamic properties, work and heat interactions, and exergy rates for each stream.

4.3.2. Energy and exergy efficiency of the proposed system

The overall plant exergy and energy efficiency is defined as the ratio of required output in terms of exergy/energy to the total exergy/energy supplied that is available at heliostats with solar radiation. Mathematically, the energy and exergy efficiency of the overall plant is expressed as [70, 73]:

$$\eta_{en,plant} = \frac{\dot{W}_{net}+\dot{Q}_e+\dot{Q}_a+\dot{Q}_c}{\dot{Q}_{solar}} \quad (4.3.57)$$

$$\eta_{ex,plant} = \frac{\dot{W}_{net}+\dot{X}_e+\dot{X}_a+\dot{X}_c}{\dot{Q}_{solar}\cdot\left(1-\frac{T_0}{T_{Sun}}\right)} \quad (4.3.58)$$

Where, T_{Sun} refers to the sun's temperature (apparent). For the calculation of sun exergy, its value has been taken as 4500 K [196]. The net output power ($\dot{W}_{net}$) of the plant has been calculated as;

$$\dot{W}_{net} = \dot{W}_{HT} - \dot{W}_{HC} - \dot{W}_{Comp} - \dot{W}_{pump} \quad (4.3.59)$$

The trigeneration system/combined cycle energy and exergy efficiency are defined as the ratio of required output in terms of exergy/energy to the total energy/exergy supplied by the IHE to the trigeneration system/combined cycle. Mathematically, its energy and exergy efficiency are expressed as [73, 74,115 and 117]:

$$\eta_{en,comb} = \frac{\dot{W}_{net}+\dot{Q}_e+\dot{Q}_a+\dot{Q}_c}{\dot{Q}_{IHE}} \quad (4.3.60)$$

$$\eta_{ex,comb} = \frac{\dot{W}_{net}+\dot{X}_e+\dot{X}_a+\dot{X}_c}{(\dot{X}_{30}-\dot{X}_{31})} \quad (4.3.61)$$

Where, $(\dot{X}_{30} - \dot{X}_{31})$ refers to the exergy supplied by the IHE to the trigeneration system (HBC-VAR-VCR) [74].

4.3.3. Coefficient of performance (COP) for heating and cooling effect

It mentioned that heat rejected through the VAR condenser and absorber was used as the heating effect for drying, bleaching domestic water heating etc. Therefore, its heating performance was calculated using the COP of heating. COP of heating can be expressed as [118,219];

$$\mathrm{COP_h} = \frac{\dot{Q}_a + \dot{Q}_c}{\dot{Q}_g + \dot{W}_{Comp} + \dot{W}_P} \tag{4.3.62}$$

However, the cooling effect is taken by the evaporator only. Therefore, COP for cooling can be evaluated as [118,220];

$$\mathrm{COP_c} = \frac{\dot{Q}_e}{\dot{Q}_g + \dot{W}_{Comp} + \dot{W}_P} \tag{4.3.63}$$

The individual COPs of the VAR and VCR can also be defined as the useful output to the input energy to that cycle. COP of the VAR system is calculated as:

$$\mathrm{COP_{VAR}} = \frac{\dot{Q}_{cc}}{(\dot{Q}_g + \dot{W}_p)} \tag{4.3.64}$$

However, the COP of the VCR system is calculated as;

$$\mathrm{COP_{VCR}} = \frac{\dot{Q}_e}{\dot{W}_{Comp}} \tag{4.3.65}$$

4.4. Modeling of SPT based combined HBC and ORC with cascade ERS-VRS integrated system

When analyzing the current system, the following presumption was made:

a) There will be one-dimensional flow and steady-state operation for every component.
b) It is assumed that the components' pressure loss is as shown in Table 3.3.
c) Kinetic and potential energy were disregarded.
d) Table 3.3 reports the isentropic efficiencies of the turbine, pump, and compressor based on assumptions.

4.4.1. Energy and exergy balance equation for the components of the proposed system

In order to conduct a thermodynamic study, the complete system is partitioned into three subsystems: the solar power tower (SPT), the helium Brayton cycle (HBC), and the organic Rankine cycle-ejector refrigeration cycle-vapor compression refrigeration cycle (ORC-ERS-VCR). Each element of the system is assigned a thermodynamic model, which is subsequently simulated using the computer application Engineering Equation Solver (EES). The energy and exergy balance equation in steady-state conditions can be expressed using the control volume approach as follows:

$$\dot{Q}_{CV} - \dot{W}_{CV} + \sum(\dot{m}_i h_i) - \sum(\dot{m}_e h_e) = 0 \quad (4.4.1)$$

$$\dot{ED} = \dot{EX}_{in} - \dot{EX}_{out} \quad (4.4.2)$$

The terms $\dot{EX}_{in}$ and $\dot{EX}_{out}$ denote the rates at which energy is added to and subtracted from the control volume, respectively. The work and heat transfer within the control volume are represented by $\dot{W}_{CV}$ and $\dot{Q}_{CV}$ correspondingly. By excluding potential and kinetic energy as well as chemical exergy, the physical flow exergy can be mathematically represented as:

$$\dot{EX}_j = \dot{m}[(h_j - h_0) - T_0(s_j - s_0)] \quad (4.4.3)$$

Where, $\dot{EX}_j$ represents the physical exergy at j^{th} state. The quantity of solar thermal energy that is transmitted through direct normal irradiance (DNI) from the sun to the receiver is contingent upon the efficiency of the heliostat field. On Earth, the past alterations are influenced by both

spatial and temporal factors. The latter, however, depends on the configuration of the pitch. The receiver can harness the residual solar energy into usable heat. Hence, the total amount of heat entering the receiver can be determined by calculating the net inlet heat [71, 123];

$$\dot{Q}_{rec,in} = \eta_{field} \cdot \dot{Q}_{Sun} = \eta_{field} \cdot DNI \cdot A_{hel} \cdot N_{hel} \quad (4.4.4)$$

Where, is heliostat field efficiency η_{field} is expressed as [71];

$$\eta_{field} = \eta_{cos} \cdot \eta_{s\&b} \cdot \eta_{int} \cdot \eta_{att} \cdot \eta_{ref} \quad (4.4.5)$$

Where,η_{ref}, η_{int}, $\eta_{s\&b}$, η_{att} and η_{cos} and, are represents heliostats reflectivity, interception efficiency, shading and blocking, atmospheric attenuation and cosine effect efficiency, respectively. The calculations of these efficacies are not the scope of this study, and its true values have been taken from existing solar power plants.

However, the receiver efficiency and heat transfer are expressed as [196];

$$\eta_{rec} = \frac{\dot{Q}_{rec,net}}{\dot{Q}_{rec,in}} \quad (4.4.6)$$

$$\dot{Q}_{rec,in} = \dot{Q}_{rec,net} + \dot{Q}_{rec,loss} = \dot{m}_{air} \cdot (h_{16} - h_{17}) + \dot{Q}_{rec,loss} \quad (4.4.7)$$

The thermodynamic modelling equations of the trigeneration system (HBC-ORC-ERS-VCR) are listed below. EES code has been developed for solving these equations using the given data in Table 3.3 together. Using the EES library of the property functions, the state point thermodynamic properties, heat and work interactions, and exergy rate at every state have been calculated.

The mathematical equations used for thermodynamic modelling of the trigeneration system based on the position numbers shown in Figure 3.3 has been illustrated below. Equations for energy and exergy analysis of each component based on input data provided in Table 3.3 are given below:

The energy equation for heliostat field is expressed as;

$$\dot{Q}_{rec,in} = \eta_{field} \cdot DNI \cdot A_{hel} \cdot N_{hel} \quad (4.4.8)$$

Energy equation for Receiver can be expressed as;

$$\dot{Q}_{rec,in} = \dot{m}_{air}(h_{18} - h_{17}) + \dot{Q}_{rec,loss} \quad (4.4.9)$$

The energy equation for an intermediate heat exchanger (IHE) can be expressed as;

$$\dot{Q}_{IHE} = \dot{m}_{air}\cdot(h_{16} - h_{17}) + \dot{m}_{He}\cdot(h_4 - h_3) \quad (4.4.10)$$

Work obtained by turbine-1 (T1) and its efficiency can be expressed as;

$$\dot{W}_{T1} = \dot{m}_{He}\cdot(h_4 - h_5) \quad (4.4.11)$$

$$\eta_{T1} = \frac{(h_4 - h_5)}{(h_4 - h_{5s})} \quad (4.4.12)$$

Work input given to compressor-1 (C1) and its efficiency can be expressed as;

$$\dot{W}_{HC} = \dot{m}_{He}\cdot(h_2 - h_1) \quad (4.4.13)$$

$$\eta_{C1} = \frac{(h_{2s} - h_1)}{(h_2 - h_1)} \quad (4.4.14)$$

The energy balance equation for the recuperator and its effectiveness can be expressed as;

$$(h_3 - h_2) = (h_5 - h_6) \quad (4.4.15)$$

$$\varepsilon_{Recuperator} = \frac{(T_3 - T_2)}{(T_5 - T_2)} \quad (4.4.16)$$

The energy and mass balance equation for a heat recovery generator (HRVG) can be expressed as;

$$\dot{m}_{He}\cdot(h_6 - h_7) = \dot{m}_g\cdot(h_9 - h_8) \quad (4.4.17)$$

The energy balance equation for the precooler can be expressed as;

$$\dot{m}_{He}\cdot(h_7 - h_1) = \dot{m}_{water}\cdot(h_{16} - h_{15}) \quad (4.4.18)$$

The heat transfer equation of condenser (COND) can be expressed as;

$$\dot{Q}_{COND} = \dot{m}_c(h_{11} - h_{12}) \quad (4.4.19)$$

Work obtained by turbine-2 (T2) and its efficiency can be expressed as;

$$\dot{W}_{T2} = \dot{m}_g\cdot(h_9 - h_{10}) \quad (4.4.20)$$

$$\eta_{T2} = \frac{(h_9 - h_{10})}{(h_9 - h_{10s})} \quad (4.4.21)$$

Work input given to pump (Pump) and its efficiency can be expressed as;

$$\dot{W}_{Pump} = \dot{m}_g(h_8 - h_{12}) \quad (4.4.22)$$

$$\eta_{Pump} = \frac{(h_{8s} - h_{12})}{(h_8 - h_{12})} \quad (4.4.23)$$

The equation for expansion valve-1 can be expressed as;

$$h_{12} = h_{13} \quad (4.4.24)$$

The equation for cascade condenser (CC) can be given as;

$$\dot{Q}_{CC} = \dot{m}_{13}(h_{14} - h_{13}) = \dot{m}_{21}(h_{11} - h_8) \quad (4.4.25)$$

$$\Delta T_{min,cc} = T_{21} - T_{13} \quad (4.4.26)$$

The equation for the evaporator (EVAP) can be given as;

$$\dot{Q}_{EVAP} = \dot{m}_{23}(h_{23} - h_{22}) \quad (4.4.27)$$

The equation for ejector can be given as;

$$\dot{m}_c \cdot h_{11} = \dot{m}_g \cdot h_{10} + \dot{m}_e \cdot h_{14} \quad (4.4.28)$$

Equation for compressor-2 (C2) can be given as;

$$\dot{W}_{C2} = \dot{m}_{He}(h_{24} - h_{23}) \quad (4.4.28)$$

$$\eta_{C2} = \frac{(h_{24s} - h_{23})}{(h_{24} - h_{23})} \quad (4.4.29)$$

The equation for expansion valve-2 can be expressed as;

$$h_{21} = h_{22} \quad (4.4.30)$$

Furthermore, in this section, exergy analysis of the combined system is also to be discussed. Exergy destruction and exergy in each component are calculated by applying the exergy balance equation for each component after assuming no heat loss in the component [207].

The exergy equation for the heliostat field is expressed as;

$$\dot{Q}_{Sun} \cdot \left(1 - \frac{T_0}{T_{ref,Sun}}\right) = \dot{Q}_{rec,in} \cdot \left(1 - \frac{T_0}{T_{ref,hel}}\right) + \dot{E}D_{hel} \quad (4.4.31)$$

The exergy equation for the receiver can be expressed as;

$$\dot{E}X_{17} + \dot{Q}_{rec,in} \cdot \left(1 - \frac{T_0}{T_{ref,hel}}\right) = \dot{E}X_{18} + \dot{Q}_{rec,loss} \cdot \left(1 - \frac{T_0}{T_{rec}}\right) + \dot{E}D_{rec} \quad (4.4.32)$$

The exergy equation for an intermediate heat exchanger (IHE) can be expressed as;

$$\dot{E}X_{16} - \dot{E}X_{17} = \dot{E}X_4 - \dot{E}X_3 + \dot{E}D_{IHE} \quad (4.4.33)$$

The exergy equation for turbine-1 (T1) can be expressed as;

$$\dot{E}X_4 = \dot{E}X_5 + \dot{W}_{T1} + \dot{E}D_{T1} \quad (4.4.34)$$

The exergy equation for compressor-1 (C1) can be expressed as;

$$\dot{E}X_1 = \dot{E}X_2 - \dot{W}_{C1} + \dot{E}D_{C1} \quad (4.4.35)$$

The exergy equation for the recuperator can be expressed as;

$$\dot{E}X_5 - \dot{E}X_6 = \dot{E}X_3 - \dot{E}X_2 + \dot{E}D_{Recuperator} \quad (4.4.36)$$

The exergy balance equation for HRVGcan be expressed as;

$$\dot{E}X_6 - \dot{E}X_7 = \dot{E}X_9 - \dot{E}X_8 + \dot{E}D_{HRVG} \quad (4.4.37)$$

The exergy balance equation for precooler can be expressed as;

$$\dot{E}X_7 - \dot{E}X_1 = \dot{E}X_{16} - \dot{E}X_{15} + \dot{E}D_{Preooler} \quad (4.4.38)$$

The exergy equation for the condenser (COND) can be given as;

$$\dot{E}X_{11} - \dot{E}X_{12} = \dot{Q}_{COND} \cdot \left(1 - \frac{T_0}{T_{COND}}\right) + \dot{E}D_{COND} \quad (4.4.39)$$

The exergy equation for turbine-2 (T2) can be given as;

$$\dot{E}X_9 = \dot{E}X_{10} + \dot{W}_{T2} + \dot{E}D_{T2} \quad (4.4.40)$$

The exergy equation for the pump can be given as;

$$\dot{E}X_{12} = \dot{E}X_8 - \dot{W}_P + \dot{E}D_{Pump} \quad (4.4.41)$$

The exergy equation for expansion valve-1 can be given as;

$$\dot{E}X_{12} - \dot{E}X_{13} = \dot{E}D_{EXV1} \quad (4.4.42)$$

The exergy equation for cascade condenser (CC) can be given as;

$$\dot{E}X_{13} + \dot{E}X_{24} = \dot{E}X_{21} + \dot{E}X_{14} + \dot{E}D_{CC} \quad (4.4.43)$$

The exergy equation for the evaporator (EVAP) can be given as;

$$\dot{E}X_{23} - \dot{E}X_{22} = \dot{Q}_{EVAP} \cdot \left(1 - \frac{T_0}{T_{EVAP}}\right) + \dot{E}D_{EVAP} \quad (4.4.44)$$

The exergy equation for ejector can be given as;

$$\dot{E}X_{10} + \dot{E}X_{14} = \dot{E}X_{11} + \dot{E}D_{ejector} \quad (4.4.45)$$

The exergy equation for compressor-2 (C2) can be given as;

$$\dot{E}X_{23} = \dot{E}X_{24} - \dot{W}_{C2} + \dot{E}D_{C2} \quad (4.4.46)$$

Equation for expansion valve-2 (EXV2) can be given as;

$$\dot{E}X_{21} - \dot{E}X_{22} = \dot{E}D_{EXV2} \quad (4.4.47)$$

These relationships are all incorporated into the simulation code, which was created using EES software. The application extracts thermodynamic characteristics from its collection of property functions to attempt to determine all of the parameters that are not known, including state point thermodynamic properties, heat and work interactions, and also exergy rates for each stream.

4.4.2. Energy and exergy efficiency of the proposed system

Energy efficiency refers to the ratio of net output power to the energy made available by the sun's irradiation on the heliostat field. Exergy efficiency, on the other hand, refers to the ratio of net output power to the exergy made available by the sun's irradiation on the heliostat field. The mathematical energy and exergy efficiency of the solar plant are formally defined as [196,164]:

$$\eta_{en,Plant} = \frac{\dot{W}_{net} + \dot{Q}_{EVAP} + \dot{Q}_{COND}}{\dot{Q}_{Sun}} \quad (4.4.48)$$

$$\eta_{ex,Plant} = \frac{\dot{W}_{net,Plant} + \dot{Q}_{EVAP} \cdot \left(1 - \frac{T_0}{T_E}\right) + \dot{Q}_{COND} \cdot \left(1 - \frac{T_0}{T_{COND}}\right)}{\dot{Q}_{Sun} \cdot \left(1 - \frac{T_0}{T_{Sun}}\right)} \quad (4.4.49)$$

Where, T_{Sun} is the apparent temperature of the sun used as the exergy assessment [196].However, $\dot{W}_{Plant}$ of the plant is expressed as:

$$\dot{W}_{Plant} = \dot{W}_{T1} + \dot{W}_{T2} - \dot{W}_{C1} - \dot{W}_{C2} - \dot{W}_{pump} \quad (4.4.50)$$

The trigeneration system/combined cycle energy and exergy efficiency are defined as the ratio of required output in terms of exergy/energy to the total energy/exergy supplied by the IHE to the trigeneration system/combined cycle. Mathematically, its energy and exergy efficiency are expressed as [73, 74,115 and 117]:

$$\eta_{en,comb} = \frac{\dot{W}_{net}+\dot{Q}_e+\dot{Q}_a+\dot{Q}_c}{\dot{Q}_{IHE}} \quad (4.4.51)$$

$$\eta_{ex,comb} = \frac{\dot{W}_{net}+\dot{X}_e+\dot{X}_a+\dot{X}_c}{(\dot{X}_{30}-\dot{X}_{31})} \quad (4.4.52)$$

Where, $(\dot{X}_{30} - \dot{X}_{31})$ refers to exergy supplied by the IHE to trigeneration system (HBC-ORC-ERS-VCR) [196].

4.5. Modeling of combined Rankine-absorption power and refrigeration cycle with heating process integrated system

Different operating conditions for the various working fluids taken into consideration in the analysis are studied and compared for the thermodynamic modelling of the low-temperature heat source-based integrated system. By studying the mass, energy, and exergy balances for each component, this analysis is carried out utilizing the cascade utilization of energy and exergy approach. The process model was created using the engineering equation solver (EES) program.

4.5.1. Energy and exergy balance equation for the components of the proposed system

In order to determine the efficiency of the combined refrigeration and power cycle, it is necessary to consider the fluid conditions at various points. This section evaluates several relationships for each fluid state within the cycle components. The analyzed cycle includes essential components such as the heat exchanger, turbine, pump, boiler, and pressure relief valve, which are paired with more intricate equipment such as the rectifier, condenser, and absorber. Each component of the cycle functions as a volume control device, utilizing a working fluid to facilitate heat transmission. The cycle's energy and mass balances are shown as [84]:

$$\Delta\left[\sum_{out}^{in} m_i\right]=0 \quad (4.5.1)$$

$$\Delta\left(\sum_{out}^{in} m_i . h_i\right)+\Delta\left[\sum_{out}^{in} Q_j\right]+ \Delta\left[\sum_{out}^{in} W_k\right]=0 \quad (4.5.2)$$

Additionally, refrigerant mass expression is valid in the absorber and rectifier

$$\Delta\left[\sum_{out}^{in} x_{i.} m_i\right]=0 \quad (4.5.3)$$

This section should describe the study of various modes of the working fluid at different stages, as seen in Figure 3.4.

Path 4 (pump's inlet)

The absorber operates under the assumption that the mixture remains in a fully saturated state. The density level of the base dilution is governed by the minimum pressure and temperature of the absorber. The ambient temperature is presumed to be 5 °C below the discharge temperature of the absorber. Currently, the assumed flow rate is the reference flow rate, and all other flows in the system are calculated as a fraction of this reference flow rate. Moreover, it is recommended that the density should be the same as the density of the base dilution.

$$T_4=T_0+5 \quad (4.5.4)$$

$$P_4 =p_{min} \quad (4.5.5)$$

x_4= The Density of the base dilution (4.5.6)

m_4= Reference flow rate (4.5.7)

Path 5 (Pump outlet)

The pump is employed to elevate the pressure of the base dilution. Subsequently, the pressure that is being assessed may reach its utmost level. Pressure and enthalpy can be readily determined by obtaining the pump's isentropic factor.

$$P_4=P_{max} \quad (4.5.8)$$

$$s_{isentropic} = s_4 \quad (4.5.9)$$

$$x_5 = x_4 \quad (4.5.10)$$

$$m_5 = m_4 \quad (4.5.11)$$

$$m_P = m_4 \times (h_5 - h_4) \quad (4.5.12)$$

Under isentropic conditions, $h_{isentropic}$ the enthalpy of the pump discharge stream for compression is calculated.

$$\eta_P = \frac{h_5 - h_4}{h_{isetropic} - h_4} \quad (4.5.13)$$

Path 6 (the inlet of the rectifier and the outflow stream of the heat exchanger)

The base dilution's temperature is elevated following its heating by the heat exchanger. The mass flow rate and density of ammonia dilution in this state are equivalent to those in state 4, and the temperature is 15 degrees lower than the boiler discharge temperature. The conditions of state 6 are as follows:

$$T_6 = T_{16} - 15 \quad (4.5.14)$$

$$p_6 = p_5 \quad (4.5.15)$$

$$x_6 = x_4 \quad (4.5.16)$$

$$m_6 = m_4 \quad (4.5.17)$$

Path 10, 11, 12 and 13 (input and output of rectifier)

After passing through the heat exchanger, the base dilution reaches the rectifier. Inside the rectifier, the subsequent relationships are in effect:

$$\Delta\left[\sum_{out}^{in} m_i\right]=0 \quad (4.5.18)$$

$$\Delta\left[\sum_{out}^{in} x_i . m_i\right]=0 \quad (4.5.19)$$

The density of 0.9999 for the dilution is taken into account for path 10. The vapour mass fraction ("IMF") and the initial mass fraction ("IMF") are necessary for the calculation of the mass transfer within the rectifier. The calculation can be performed as follows: [157]:

$$vmf_R = \frac{x_4 - x_{13}}{x_{10} - x_{13}} \quad (4.5.20)$$

$$imf_{R=} \frac{x_{10} - x_4}{x_{10} - x_{13}} \quad (4.5.21)$$

The quantity of mass transfer inside the rectifier is then calculated using "vmf" and "imf" in another relationship. The temperature and pressure are equivalent to those of path 13.

$$T_{10} = T_{13} = T_R \quad (4.5.22)$$

$$p_{10} = p_{13} = p_{max} \quad (4.5.23)$$

$$m_{10} = vmf_R \times m_4 \quad (4.5.24)$$

$$m_{13} = imf_R \times m_4 \quad (4.5.25)$$

Path 7 (stream exiting the steam boiler and entering the superheater)

The rectifier isolates the reduced dilution, which is heated to the temperature at which it turns into a vapour after going through the boiler. The temperature in the boiler is equivalent to the dilution temperature, while the pressure is at its maximum level. The specifications of state 7 are defined below:

$$T_7 = T_B \quad (4.5.26)$$

$$p_7 = p_{max} \quad (4.5.27)$$

$$x_7 = x_{13} \quad (4.5.28)$$

$$m_7 = m_{13} \quad (4.5.29)$$

Path 8 (Turbine's inlet)

The diluted ammonia solution will reach a very high temperature and can be considered superheated once it passes through the boiler and the superheater. The pressure is at its maximum and the temperature is equal to that of the heat exchanger. Moreover, the mass flow rate and density of dilution are identical to those of state 7. The superheater functions within the specified conditions:

$$T_8 = T_{HE} \quad (4.5.30)$$

$$p_8 = p_{max} \quad (4.5.31)$$

$$x_8 = x_7 \quad (4.5.32)$$

$$m_8 = m_7 \quad (4.5.33)$$

Path 9 (turbine's output Stream)

Table 3.4 can be used to determine the turbine's isentropic factor. The combined cycle's minimum pressure is the turbine's outlet pressure. Additionally, the density of the dilution at this stage is predetermined. Consequently, the subsequent relationships can be employed to assess the conditions of the turbine's discharge stream:

$$p_9 = p_{min} \quad (4.5.34)$$

$$S_{iseniropic} = S_8 \quad (4.5.35)$$

$$x_9 = x_8 \quad (4.5.36)$$

$$W_T = m_8 \times (h_8 - h_9) \quad (4.5.37)$$

The isentropic enthalpy of expansion within the turbine can be determined under these conditions. The real enthalpy at the turbine's outlet point is determined using the following equation:

$$\eta_T = \frac{h_8 - h_9}{h_8 - h_{isetropic}} \quad (4.5.38)$$

Path 1 (Condenser's outlet stream)

After passing through the condenser, the enriched ammonia dilution is transformed into a liquid. The density of 0.9999 is proposed, and the temperature is assumed to be 5°C higher than the ambient temperature. The conditions of state 1 are outlined below:

$$p_1 = p_{max} \quad (4.5.39)$$

$$T_1 = T_0 + 5 \quad (4.5.40)$$

$x_1 = 0.9999$ (4.5.41)

$m_1 = m_{10}$ (4.5.42)

Path 2 (evaporator's inlet stream)

The pressure relief valve considerably reduces enriched dilution, resulting in low pressure. The following conditions are present within the valve, and it seems obvious that the other conditions will remain constant.

$h_2 = h_1$ (4.5.43)

$p_2 = p_{min}$ (4.5.44)

$x_{2 =} x_1$ (4.5.45)

$m_2 = m_1$ (4.5.46)

Path 3 (evaporators output Stream)

The concentrated solution is transformed into a liquid and its pressure is decreased to the lowest extent. After going through the evaporator and being cooled by refrigeration, its temperature is 5 °C below the surrounding temperature. Thus far, the prerequisites are delineated as follows:

$T_3 = T_0 - 5$ (4.5.47)

$p_3 = p_{min}$ (4.5.48)

$x_3 = x_2$ (4.5.49)

As follows, the absorber will combine streams 3 and 9. The base dilution is reformed after passing through this apparatus. The absorber is subject to the following conditions:

$\Delta\left[\sum_{out}^{in} m_i\right]=0$ (4.5.50)

$\Delta\left(\sum_{out}^{in} m_i \,.\, h_i\right)+\Delta\left[\sum_{out}^{in} Q_j\right]+ \Delta\left[\sum_{out}^{in} W_k\right]=0$ (4.5.51)

$\Delta\left[\sum_{out}^{in} x_i \,.\, m_i\right]=0$ (4.5.52)

4.5.2. Energy and exergy efficiency of the proposed system

The thermal and energy efficiencies of the system can be used to assess its performance. The usable energy output divided by the total energy intake is known as the first law of thermodynamics and is expressed as follows [115-117]:

$$\eta_1 = \frac{W_{net} + Q_E}{Q_{in}} \tag{4.5.53}$$

where W_{net} is the output power of the turbine, which is reduced by the input power to the pump. The total heat input added to the cycle is denoted as Q_{in}. The refrigeration output through the evaporator is denoted as Q_E.

The exergy output divided by the exergy input to the cycle is known as exergy efficiency. Exergy input is interpreted as the heat source's available energy change. The exergy output is the total of the exergy from the refrigeration system. The exergy efficiency of the stated combined cycle is as follows:

$$\eta_2 = \frac{W_{net} + Q_E}{E_{in}} \tag{4.5.54}$$

Where, E_{in} is the heat source fluid exergy and E_{eva} is the exergy associated with refrigeration output which is defined as follows:

$$E_{in} = m_g\,[(h_g - h_o) - T_o(s_g - s_o)] \tag{4.5.55}$$

$$E_E = m_{evap}\,[(h_{evap,i} - h_{evap,o}) - T_o(s_{evap,i} - s_{evap,o})] \tag{4.5.56}$$

4.5.3. Exergy destruction rate for each component of the proposed system

Assume that P_o and $T_o$represent the reference atmospheric pressure and temperature as the defined dead state, with the understanding that minimal heat is being rejected into the environment by each component. For the combined cycle, the exergy destruction rate of each component can be approximated as follows [95, 202]:

For pump (P):-

$$\dot{E}D_P = \dot{E}_4 - \dot{E}_5 - \dot{W}_P \quad (4.5.57)$$

For heat exchanger (HE):-

$$\dot{E}D_{HE} = \dot{E}_5 + \dot{E}_{16} - \dot{E}_6 - \dot{E}_{17} \quad (4.5.58)$$

For rectifier (R):-

$$\dot{E}D_R = \dot{E}_6 + \dot{E}_{11} + \dot{E}_{12} - \dot{E}_{10} - \dot{E}_{13} \quad (4.5.59)$$

For boiler (B):-

$$\dot{E}D_B = \dot{E}_{13} + \dot{E}_{15} - \dot{E}_{12} - \dot{E}_7 - \dot{E}_{16} \quad (4.5.60)$$

For superheater (SH):-

$$\dot{E}D_{SH} = \dot{E}_7 + \dot{E}_{14} - \dot{E}_{15} - \dot{E}_8 \quad (4.5.61)$$

For turbine (T):-

$$\dot{E}D_T = \dot{E}_8 - \dot{E}_9 - \dot{W}_T \quad (4.5.62)$$

For condenser (C):-

$$\dot{E}D_C = \dot{E}_{10} - \dot{E}_{11} - \dot{E}_1 \quad (4.5.63)$$

For evaporator (E):-

$$\dot{E}D_E = \dot{E}_2 - \dot{E}_3 + \dot{E}_E \quad (4.5.64)$$

For throttle valve (TV):-

$$\dot{E}D_{TV} = \dot{E}_1 - \dot{E}_2 \quad (4.5.65)$$

For absorber (A):-

$$\dot{E}D_A = \dot{E}_9 - \dot{E}_4 + \dot{E}_3 \quad (4.5.66)$$

The total exergy destruction is given as

$$\dot{E}D_{Total} = \dot{E}D_P + \dot{E}D_{HE} + \dot{E}D_R + \dot{E}D_B + \dot{E}D_{SH} + \dot{E}D_T + \dot{E}D_C + \dot{E}D_E + \dot{E}D_{TV} + \dot{E}D_A \quad (4.5.67)$$

4.6. Modeling of combined power, heating and cooling integrated system driven by Low-temperature heat source using various eco-friendly refrigerants

Different operating conditions using various operating fluids taken into consideration during analysis are studied and compared for the thermodynamic modelling of the low-temperature heat source-based integrated system. The following assumptions are considered for this analysis [148]:

a) The system is at steady state condition.
b) Flow resistance losses in various components are discarded.
c) The pressure drops and heat dissipation in the cycle components are neglected.
d) The throttling process in expansion valves is isentropic.

By studying the energy and exergy equations for every element present in the system, this analysis is carried out utilizing the cascade utilization of the energy and exergy approach. The process model was created using the EES software, and the important parameters for key state transitions in the suggested cycle for an environmentally friendly refrigerant were derived from the Standard Reference Database (NIST), 23 REFPROP 6.01 (1998). The main element of the suggested system is an ejector; a one-dimensional continuous constant pressure flow model is used to evaluate their performances [61].The basic idea of the current model was first proposed by [133], and it was improved by [124] and then [135]. Entrainment ratio (μ) a vital component of the ejector, establishes the relation between secondary fluid mass rates with respect to that of primary rate exiting the turbine and by using the mass, momentum, and energy equation, the following formulation for the entrainment ratio, which may be written as [185]:

$$\mu = \sqrt{\frac{\eta_n\ \eta_m \eta_d\ (h_{pf,n1} - h_{pf,n2s})}{(h_{mf,ds} - h_{mf,m})}} - 1 \quad (4.6.1)$$

The primary flow in the ejector is composed mostly of three sections, and conservation of energy equations for this flow are provided as mentioned below:

$$\dot{m}_{pf}\, h_{pf,n2} + \dot{m}_{pf} \frac{u_{pf,n2}^2}{2} = \dot{m}_{pf}\, h_{pf,n1} + \dot{m}_{pf} \frac{u_{pf,n1}^2}{2} \quad (4.6.2)$$

The nozzle's efficiency can be calculated as:

$$\eta_n = \frac{h_{pf,n1} - h_{pf,n2}}{h_{pf,n1} - h_{pf,n2s}} \quad (4.6.3)$$

The momentum equation for the mixing section is stated as:

$$\dot{m}_{pf} u_{pf,n2} + \dot{m}_{sf} u_{sf,n2} = (\dot{m}_{pf} + \dot{m}_{sf}) u_{mf,ms} \quad (4.6.4)$$

The energy equation for the diffuser section is stated as:

$$\frac{1}{2}\left(u_{mf,m}^2 - u_{mf,ds}^2\right) = h_{mf,ds} - h_{mf,m} \quad (4.6.5)$$

The efficiency of the diffuser section is stated as:

$$\eta_d = \frac{h_{mf,ds} - h_{mf,m}}{h_{mf,d} - h_{mf,m}} \quad (4.6.6)$$

The extraction ratio is calculated by dividing the turbine's extracted mass rate to the turbine's inlet mass rate is given as:

$$E_r = \frac{\dot{m}_{extr}}{\dot{m}_T} = \frac{\dot{m}_5}{\dot{m}_4} \quad (4.6.7)$$

The entrainment ratio of the ejector can be calculated as:

$$\mu = \frac{\dot{m}_{sf}}{\dot{m}_{pf}} = \frac{\dot{m}_{13}}{\dot{m}_5} \quad (4.6.8)$$

The driving pressure ratio is stated as follows:

$$\alpha = \frac{P_{extr}}{P_C} = \frac{\text{Turbine pressure}}{\text{Condenser pressure}} \quad (4.6.9)$$

4.6.1. Energy and exergy balance equation for the components of the proposed system

Using the energy conservation and exergy balance equations that is applicable in circumstances with minimal variations in the kinetic and potential energy under steady state and control volume approach, is as follows:

$$\dot{Q} - \dot{W} = \sum \dot{m}_e h_e - \sum \dot{m}_i h_i \quad (4.6.10)$$

$$\dot{E} - \dot{W} = \sum \dot{m}_e e_e - \sum \dot{m}_i e_i + \dot{I} \quad (4.6.11)$$

Where $\dot{Q}$ totals heat input and $\dot{W}$ represents work output respectively, $\dot{m}$ represents the mass rate and h represents the enthalpy of the flowing stream, $\dot{I}$ is the irreversibility rate produced due to the production of entropy in the different components of the system, $\dot{E}$ represents the exergy production rate in repercussion of heat transfer with the environment at temperature T, which can be expressed as:

$$\dot{E} = \sum(1 - \frac{T_o}{T})\dot{Q} \quad (4.6.12)$$

The total exergy production rate and the specific flow exergy may be obtained as follows:

$$e = (h - h_o) - T_o(s - s_o) \quad (4.6.13)$$

$$\dot{E} = \dot{m}e \quad (4.6.14)$$

Then, each system component is subjected to energy conservation with the previously mentioned assumptions, and is expressed as follows:

For HRVG:

$$\dot{m}_h(h_{19} - h_{18}) = \dot{m}_4(h_4 - h_3) \quad (4.6.15)$$

For Turbine (T):

$$\dot{W}_T = \dot{m}_4(h_4 - h_5) + (\dot{m}_4 - \dot{m}_5)(h_5 - h_6) \quad (4.6.16)$$

For ejector (EJE):

$$\dot{m}_{pf}h_5 + \dot{m}_{sf}h_{13} = h_7(\dot{m}_{pf} + \dot{m}_{sf}) \quad (4.6.17)$$

For regenerator (Reg):

$$\dot{m}_4(h_3 - h_2) = \dot{m}_9(h_9 - h_8) \quad (4.6.18)$$

For Condenser (C):

$$\dot{Q}_C = \dot{m}_9(h_9 - h_{10}) \quad (4.6.19)$$

For Pump (P):

$$\dot{W}_P = \dot{m}_1(h_2 - h_1) \quad (4.6.20)$$

For expansion valve (E.V):

$$h_{11} = h_{12} \quad (4.6.21)$$

For evaporator (E):

$$\dot{Q}_E = \dot{m}_{sf}(h_{13} - h_{12}) = \dot{m}_{12}(h_{13} - h_{12}) \quad (4.6.22)$$

The thermodynamic efficiencies of the proposed cycle might be used to assess its performance. The ratio of usable net output energy to the total energy intake is known as thermal efficiency as per the thermodynamics first law and it can be presented as follows [185]:

$$\eta_{thermal} = \frac{\dot{W}_{net} + \dot{Q}_E}{\dot{Q}_{in}} \quad (4.6.23)$$

Where $\dot{W}_{net}$ represents the turbine's net power production from the turbine is, $\dot{Q}_E$ is the output from refrigeration and $\dot{Q}_{in}$ represents the total heat input HRVG provides to the cycle. The ratio of output exergy to the input exergy is known as exergy efficiency [128,131]. Input exergy is interpreted as the amount of available energy that is accessible from the heat source fluid. The output exergy is the total of the exergy from the refrigeration system and the net power output.

$$\eta_{exergy} = \frac{\dot{W}_{net} + \dot{E}_E}{\dot{E}_{in}} \quad (4.6.24)$$

Where $\dot{E}_{in}$ the exergy of the heat is the source fluid and $\dot{E}_E$ represents the refrigeration exergy produced in the evaporator, which is given as:

$$\dot{E}_{in} = \dot{Q}_{in}\left(1 - \frac{T_o}{T_{hi}}\right) \quad (4.6.25)$$

$$\dot{E}_E = \dot{m}_{sf}[(h_{12} - h_{13}) - T_o(S_{12} - S_{13})] \quad (4.6.26)$$

Assume that P_o and T_o represent the reference atmospheric pressure and temperature considering the defined environment condition with the understanding that minimal heat is being rejected into the surroundings by every element [129]. The rate of exergy destruction for every element in the stated cycle may be approximated using the following equations:

For HRVG:

$$\dot{E}D_{HRVG} = \dot{E}_3 + \dot{E}_{18} - \dot{E}_4 - \dot{E}_{19} \quad (4.6.27)$$

For Turbine:

$$\dot{E}D_T = \dot{E}_4 - \dot{E}_5 - \dot{E}_6 - \dot{W}_T \quad (4.6.28)$$

For Ejector:

$$\dot{E}D_{EJE} = \dot{E}_5 + \dot{E}_{13} - \dot{E}_7 \quad (4.6.29)$$

For regenerator:

$$\dot{E}D_{Reg} = \dot{E}_2 + \dot{E}_8 - \dot{E}_3 - \dot{E}_9 \quad (4.6.30)$$

For condenser:

$$\dot{E}D_C = \dot{E}_9 + \dot{E}_{16} - \dot{E}_{10} - \dot{E}_{17} \quad (4.6.31)$$

For pump:

$$\dot{E}D_P = \dot{E}_1 - \dot{E}_2 - \dot{W}_P \quad (4.6.32)$$

For expansion valve:

$$\dot{E}D_{EV} = \dot{E}_{11} - \dot{E}_{12} \quad (4.6.33)$$

For evaporator:

$$\dot{E}D_E = \dot{E}_{12} - \dot{E}_{13} + \dot{E}_E \quad (4.6.34)$$

The total exergy destruction is given as

$$\dot{E}D_{Total} = \dot{E}D_{HRVG} + \dot{E}D_T + \dot{E}D_{EJE} + \dot{E}D_{Reg} + \dot{E}D_C + \dot{E}D_P + \dot{E}\dot{D}_{EV} + ED_E \quad (4.6.35)$$

Chapter 5

Results and discussion

In this chapter, the discussion has been made on the basis of results outcomes after the exclusively thermodynamic analysis has been carried out of the considered cycles, such as SPT-based combined HBC and ORC with ejector refrigeration integrated system, SPT-based combined HBC and ORC with cascade VAR-VCR integrated system, SPT-based combined HBC and ORC with cascade ERS-VRS integrated system, combined Rankine-absorption power and refrigeration cycle with heating process integrated system, and combined power, heating, and cooling integrated system driven by low-temperature heat source using various eco-friendly refrigerants. The EES software was used to construct the computer programs that modelled the chosen systems. The computed results of these programs are thoroughly covered in this chapter under the various sections.

5.1. SPT based combined HBC and ORC with ejector refrigeration integrated system

Parametric evaluation of the SPT-based combined HBC and ORC with ejector refrigeration integrated system has been carried out in this objective. Further, the results have been found using an EES, and the results of the current study have been compared and validated with the same previous research work and discussed in different sections.

5.1.1. Validation of the proposed system

The modelling technique is validated by comparing and validating the obtained findings of the derived models (HBC and ORC-ERS) with the data available in the previous literature. Figure 5.1 presents a comparison between the efficiency values of the single HBC used in this work and those reported by [71]. The data differs by only 0.24%, which is within an acceptable range. Research data from reference [67] is used to assess the accuracy of the bottoming model (ORC-ERS). The experiment used R123 as the working fluid, with the evaporator and condenser temperatures set at -10°C and 25°C, respectively. An appropriate adjustment is made to the model in order to facilitate a suitable comparison. The findings from reference [67] and the present model are compared across many parameters, as depicted in Table 5.1.The comparison results indicate that the maximum deviation was measured to be 1.5%, a minute value that

signifies a high level of precision. Consequently, the model that was created has undergone validation and may be considered reliable.

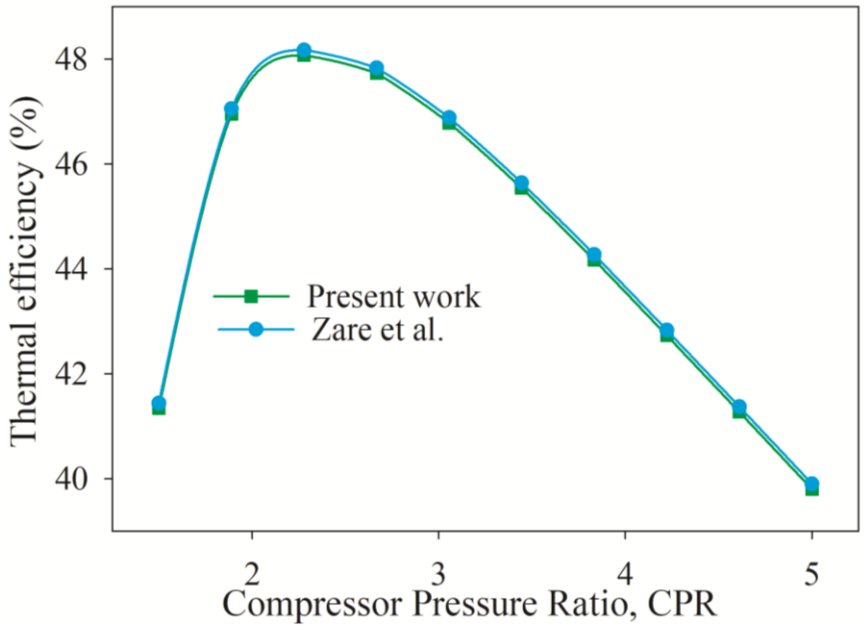

Figure 5.1 Verification of the helium Brayton cycle

Table 5.1 Verification of ORC-ERS

Parameters	Present study	Ref. [67]	Deviation (%)
h_9	477.7	474.2	0.73
h_{10}	451.4	451	0.08
h_{11}	447.12	445.4	0.38
h_{12}	221.2	220.1	0.49
h_{13}	220.9	220.1	0.36
h_{14}	376.54	375.5	0.27
h_8	220.97	220.8	0.07
Q_E	60.7	60.4	0.49
$\dot{m}_c$	5.39	5.310	1.5
$\dot{m}_e$	0.391	0.389	0.51
$\dot{W}_{net}$	111.2	110.7	0.004

5.1.2. Comparison of thermodynamic performance among different components of a system

Table 3.1 provides a comprehensive summary of the essential assumptions and input data required for simulating the system. Table 5.2 displays the value of the results obtained from the same study, specifically for all subsystems running at their optimal condition. The purpose of this table is to present fundamental information regarding the exergy and energy evaluation of the system being studied. Based on the information provided in Table 5.2, which is used in energy analysis, the complete power plant produced 14,998 kW of power with an overall energy efficiency of 23.3% out of the 64,358 kW of solar radiation energy. In SPT systems, the heliostat field loses the most energy (22989 kW, or 35.72% of the total solar heat), suggesting that the heliostat field's design is crucial. An approximation of 13365 kW of net power was obtained by the standalone HBC, whereas about 31027 kW of heat was absorbed through the IHE. The energy efficiency achieved was 43.07% under the specified operating circumstances, as indicated in Table 5.2. In addition, the energy conversion efficiency of the standalone ORC-ERS system was 12.26%. The waste heat recovery unit (WHRU) absorbed a total of 13261 kW of heat from the topmost heat balance control (HBC) system. A portion of the energy is converted into useful output, specifically power through an organic turbine (1567.23 kW), heating effect through a condenser (60.52 kW), and cooling effect for building purposes (8.25 kW). Nevertheless, the combined cycle (HBC-ORC-ERS) has a relatively high energy efficiency of 51.68%, as indicated in Table 5.2.

The exergy analysis indicates that the heliostat field has the highest rate of exercise destruction. This is due to the fact that it receives a greater quality of energy with a heating source of approximately 4500 K [195]. Additionally, the receiver, which functions at a temperature of about 1000 °C, experiences a large irreversibility upon receiving this radiation. [71, 74]. The heliostat's energy efficiency was determined to be 64.27%. In the IHE, the helium and HTF do not significantly differ in temperature since the IHE does not experience the combustion process, which is the main source of irreversibility in conventional power systems. Consequently, the HBC-ORC-ERS combined cycle has a high exergy efficiency of almost 64.4%. However, the power plant's overall exergy efficiency is quite low due to the significant exergy destructions in the receiver and heliostat field. The expansion valve had the lowest energy

destruction (102.5 kW) while the heliostats had the largest energy destruction (21465 kW, or 47.52% of the total energy destruction). Among the different components, the highest energy efficiency was found by the helium turbine (97.25%). The standalone HBC gave the energy efficiency around 59.36%. While the cogeneration system ORC-ERS obtained the energy efficiency around 46.55%. It was concluded that this was lowering the exercise efficiency due to the addition of more components through the ORC-ERS. The plant exergy destruction of the trigeneration system operated by the SPT plant was found to be 45593 kW. However, this plant obtained an energy efficiency of about 25.12%.

Table 5.2 Energy and exergy evaluation of integrated system at the specified operating parameters

Subsystem	Energy evaluation				Exergy evaluation			
	Input (kW)	Output (kW)	Loss (kW)	Energy efficiency	Input (kW)	Output (kW)	Loss (kW)	Exergy efficiency
Heliostat field	64358	41369	22989	64.26%	60094	38628	21465	64.27%
Solar receiver	41369	31027	10342	75%	38628	22515	16113	58.28%
HBC	31027	13365	17662	43.07%	22515	13365	9150	59.36%
ORC-ERS	13261	1633	11634	12.26%	3729	1736	1993	46.55%
HBC-ORC-ERS	31027	14998	16035	48.33%	22515	15101	8014	64.40%
Overall plant	64358	14998	49366	23.30%	60094	15101	45593	25.12%

A parametric evaluation is also done to check the effects of deferent variables on the power plant performance. The variation has been taken keeping constant other parameters listed in table 3.1. The effects of the parameters were discussed one by one in the rest of this section.

5.1.3. Effects on performance of compressor pressure ratio

The crucial variable that has to be looked into is the compressor pressure ratio (CPR). It had an impact on the compressor's material, or more specifically, its price. The trigeneration plant’s performance was examined with the CPR. As the CPR increased, figure 5.2 shows that the energy and energy efficiency climbed first, reaching a maximum at CPR of 2.3, and then

steadily dropped beyond it. Following the initial value of 2.3, it experiences a reduction. This trend can be described as follows: Prior to a CPR of 2.3, increasing the CPR will increase both expansion and compression work. However, in this specific range, the rate of improvement in expansion work surpasses the rate of growth in compression work. As a result, there is an increase in network output. This leads to improving the efficiency of the plant. After the CPR of 2.3, results were shown vice versa. The maximum values of energy and exergy efficiency were 48.33% and 64.4% for the combined ORC-ERS system, while for the overall plant; they were around 23.3% and 25.12%, respectively. The reason that perhaps a significant energy loss occurred in the cycle is that a very small amount of energy is lost because the energy loss is of extremely low quality, which accounts for the disparity between the cycle's energy and exergy efficiency and its high efficiency. Alone 83.20% of the total destruction of energy was destroyed in the solar field (heliostats and receiver). That means overall plant exergy destruction was found at 45593 kW, while 37578 kW were destroyed by solar fields only. The plants and the standalone HBC cycle's maximum net power production were found to be 14998 kW and 13365 kW, respectively, at a compression pressure ratio (CPR) of 2.3, which is the optimal value for CPR. Consequently, the ORC-ERS led to a significant increase of 1633 kW in net power output. Apart from the power output cooling and heating effect also first increased and then decrease with the CPR. The highest cooling and heating effects were found 8.82 kW and 60.56kW respectively at 2.3 of CPR. Explanation is same as the power output and energy and exergy conversion efficiencies.

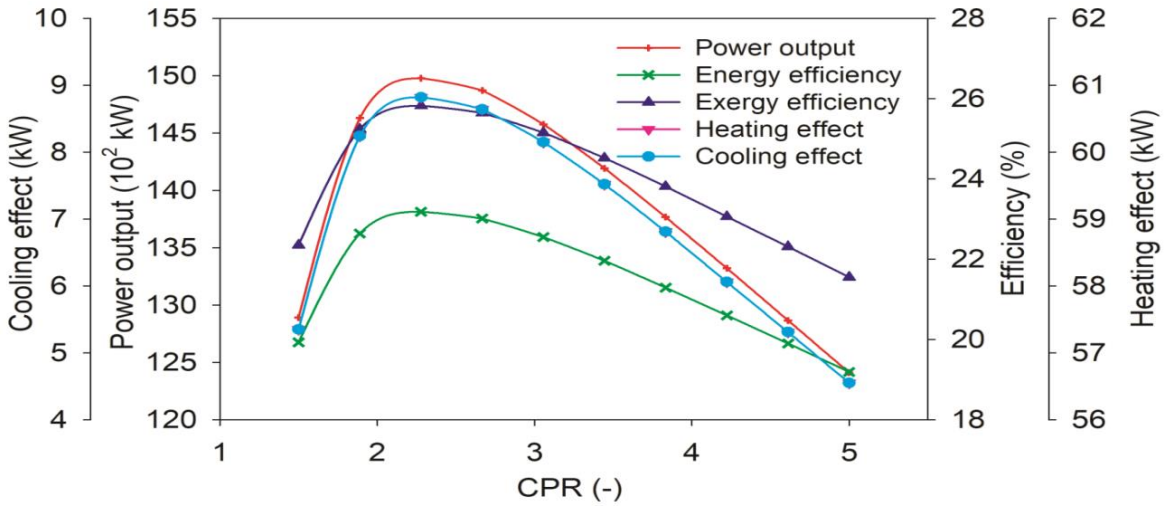

Figure 5.2 Performance outputs variation with the CPR

5.1.4. Performance effect of helium turbine inlet temperature

The system performance is influenced by the HTIT (helium turbine inlet temperature). According to Figure 5.3, when the HTIT climbed from 700 °C to 900 °C, the plant's total energy, exergy efficiency, and net power output improved from 21.36% to 24.65%, 23.87% to 27.4%, and 13808 kW to 15928 kW, respectively. The cause of it can be explained by the fact that the enthalpy differential over the turbine increased in tandem with an increase in the input temperature. It indicates that while net expansion work increased, net output power improved and the system's thermal performance increased as a result. This variance was measured at the optimal CPR of 2.3, 850 W/m^2 of DNI, and 197.5 °C of the OT inlet temperature. Apart from the efficiencies and net power output, HTIT also affects the cooling and heating effects. Cooling and the heating effect also increased with the HTIT. As the HTIT increased from 700°C to 900°C, the cooling and heating load increased from 6.87 kW to 10.40 kW and 55.87 kW to 59.4 kW respectively. It makes sense that as the HTIT climbed, the ORC turbine's input temperature rose as well. It indicates that there is more heat energy entering the ORC-ERS system, increasing the impacts of heating and cooling.

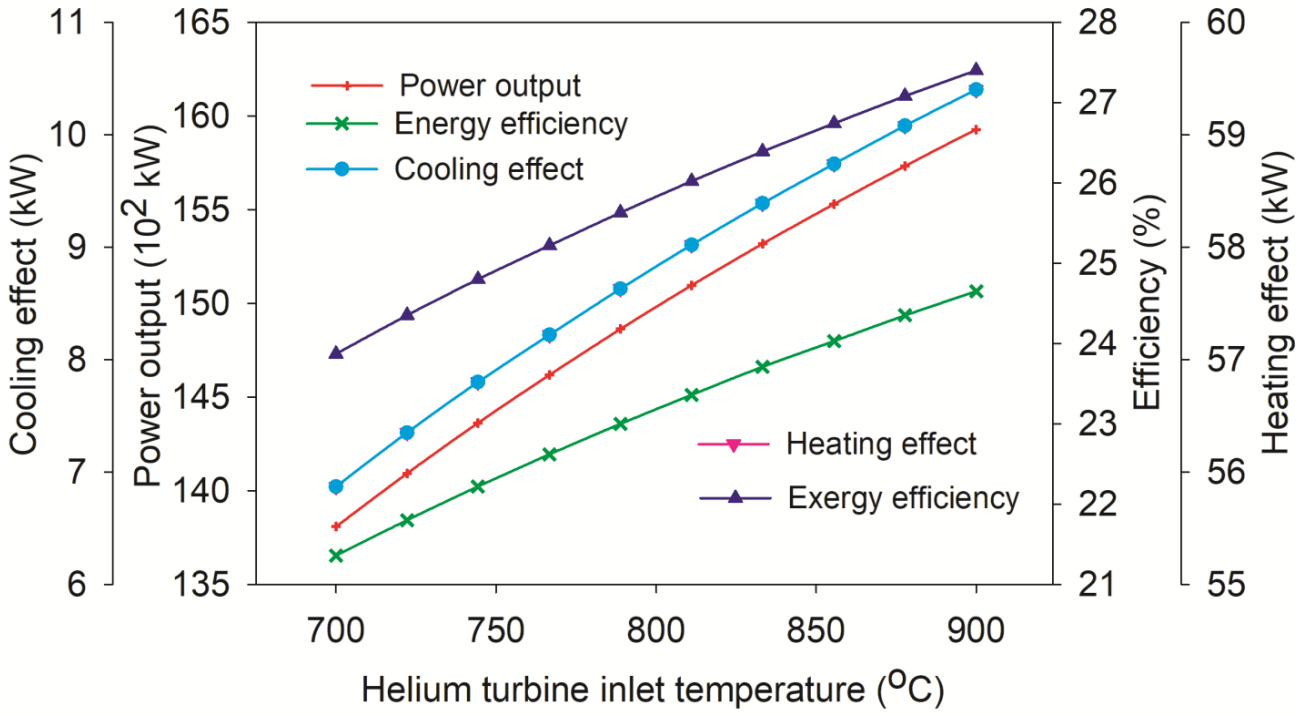

Figure 5.3 Performance variations with helium turbine inlet temperature (HTIT)

5.1.5. Compressor inlet temperature effect on system performance

The system's performance is known to be impacted by the compressor inlet temperature (CIT). As the compressor inlet temperature increased, the plant's overall efficiency and net output power declined. It can be explained that as the CIT increased, the enthalpy difference across the compressor increased, which led to the enhancement in compressor work. Consequently, figure 5.4 illustrates how the overall system performance was affected by CIT. It shows that power output dropped from 15034 kW to 14802 kW, respectively, as the temperature increased from 25°C to 35°C. Overall plant energy and exergy efficiency also decreased from 23.36% to 23% and 26.02% to 25.63%, respectively. CIT did not affect the cooling or heating loads. As CIT increased, the net work output from the OT also decreased, which means output heat that affects negligible change in evaporator and condenser loads.

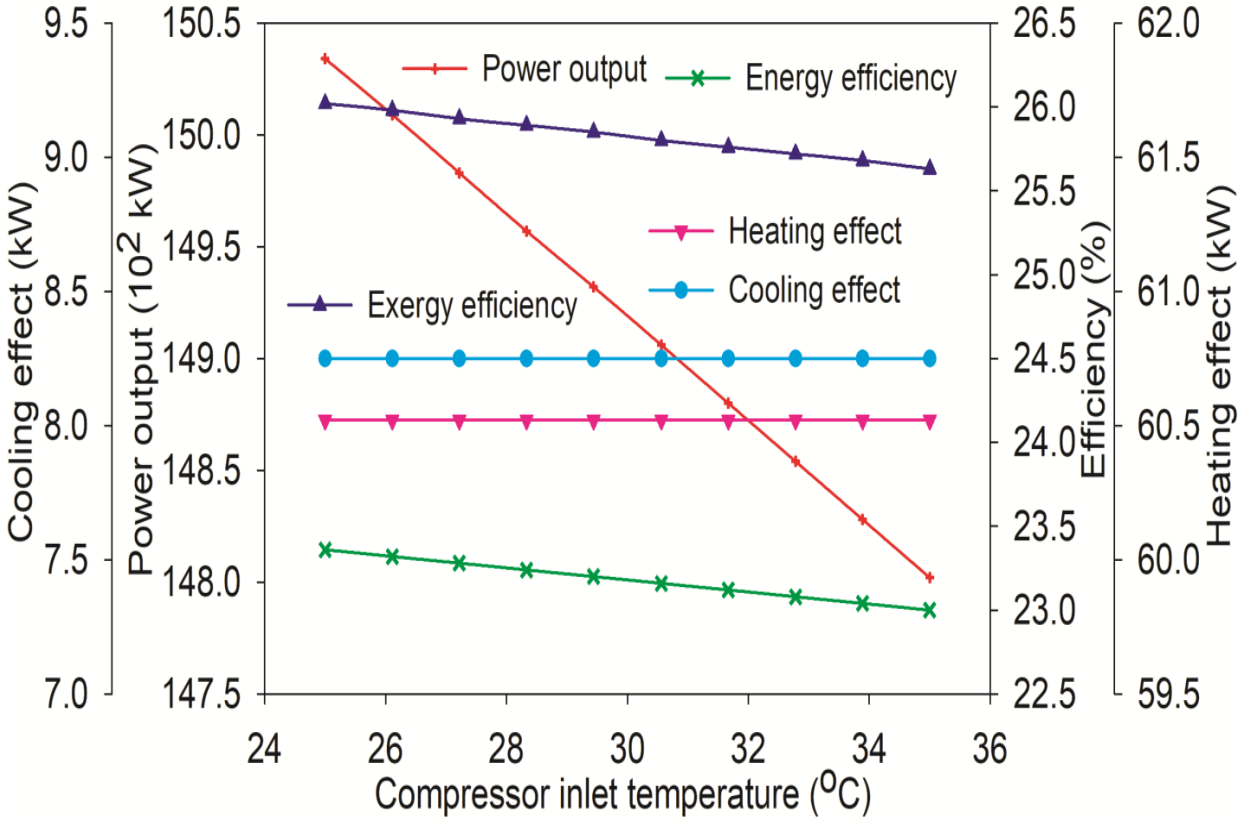

Figure 5.4 Performance variations with compressor inlet temperature (CIT)

5.1.6. Influence of ORC turbine input temperature on system performance

This section must address how the ORC turbine inlet temperature affects the system's performance. The temperature input to the ORC turbine caused a modest increase in the plant's overall efficiency. Net power output was more impacted, though. Energy and exergy efficiency increased by just 2.05% and 2%, respectively, at various constant values when the temperature rose from 150 °C to 200 °C, as illustrated in Figure 5.5. The rate of improvement of the output power is greater than the efficiency. The reason behind this is that as the temperature increased, the thermodynamic property at the inlet increased, which means that the overall enthalpy difference increased, which means net power output increased at a constant pressure ratio. In addition, by gradually raising the ORC turbine's inlet temperature, the cooling is further enhanced. The temperature rose from 150 °C to 200 °C, increasing the cooling capacity from 6.87 kW to 10.4 kW and the heating capacity from 55.87 kW to 59.4 kW. The rise in pressure after the turbine may be attributed to the pressure ratio's constant value in this parametric evaluation. Because the ORC turbine inlet temperature is rising, there is a rise in pressure.

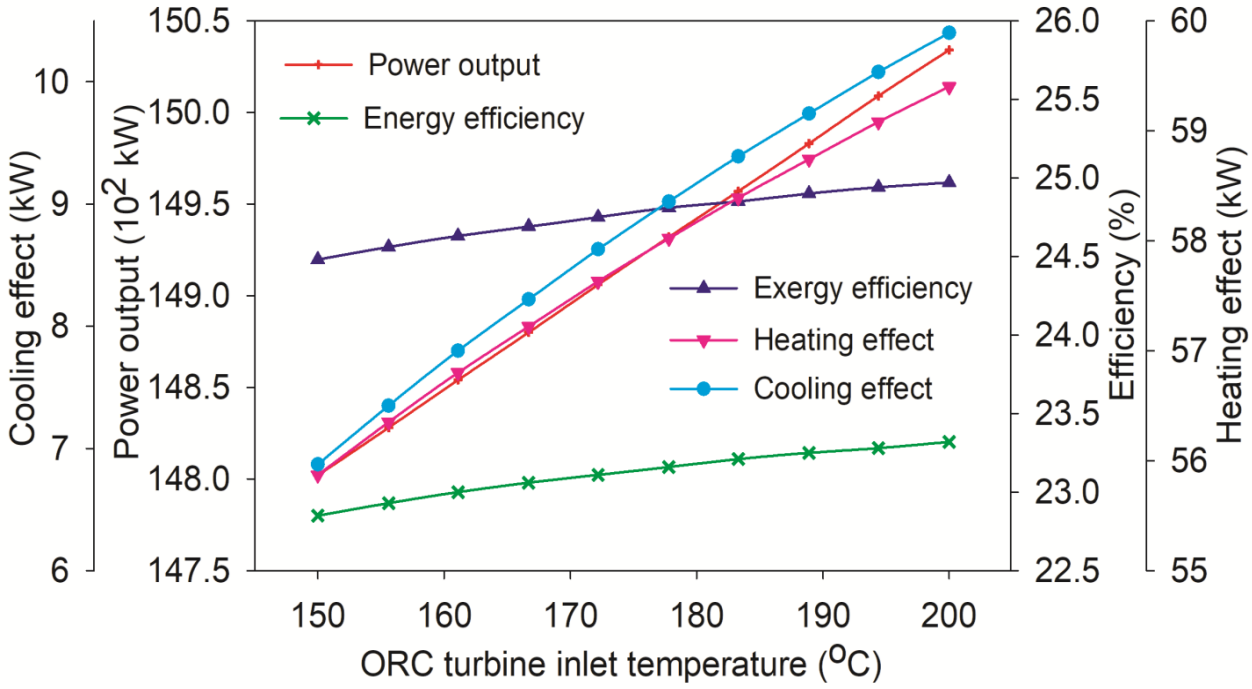

Figure 5.5 Performance variations with the ORC turbine input temperature

5.1.7. Performance variation with pump pressure ratio

The pump pressure ratio (PPR) influences the system's performance. A fixed value of 2.3 for CPR, 850 W/m^2 for DNI, and 800 °C was used to obtain the variations of the thermal performance. The overall plant efficiencies first increased and then decreased continuously. It has the optimum value at which it has maximum performance of the system. The optimal value of the PPR was 3.056, at which maximum energy efficiency and exergy efficiency of the overall plant were obtained as 25.12% and 23.30%, respectively, as seen in Figure 5.6. However, the cooling is not affected by the PPR, but the heating effects increased continuously with the PPR. Improvement in the PPR means increased pump work; however, improvement in the pump does not affect the evaporator temperature and pressure, which leads to no improvement in the refrigeration effects. While improvement in PPR means more extraction of heat through the condenser to balance the energy, it has to be rejected through the condenser, which means improvement in the heating load. With an increase in PPR of per 2.33%, the heating effect increased by 6.31%.

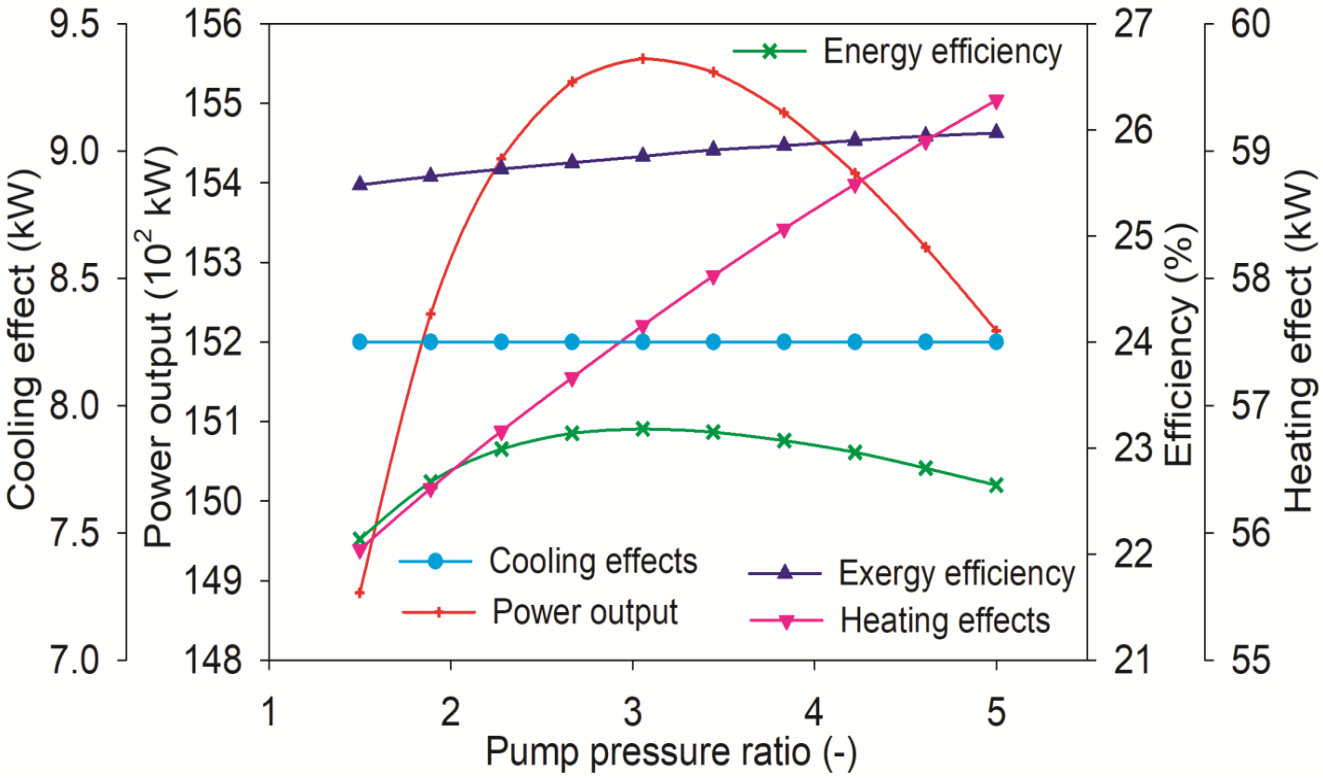

Figure 5.6 Useful output variation with the pump pressure ratio

5.1.8. Performance variation with evaporator temperature

Figure 5.7 illustrates the performance variation of the system with the evaporator temperature. In any cooling system, it is important to find out the effect of the evaporator on the performance of the trigeneration system. The energy and exergy efficiency and power output of the energy conversion system increased with the evaporator temperature continuously. As the temperature increased, the energy and exergy efficiency and output power increased from 22.85% to 23.32%, 24.48% to 24.92%, and 15802 kW to 16034 kW, respectively. It shows no effect on the heating loads while it much affects the cooling load. As it is known that the temperature of the evaporator did not affect the condenser thermodynamic parameters that mean no effect on the heating loads. However, the evaporator temperature increased the refrigeration effect, which means that it increased the evaporator pressure, which led to an improvement in cooling loads.

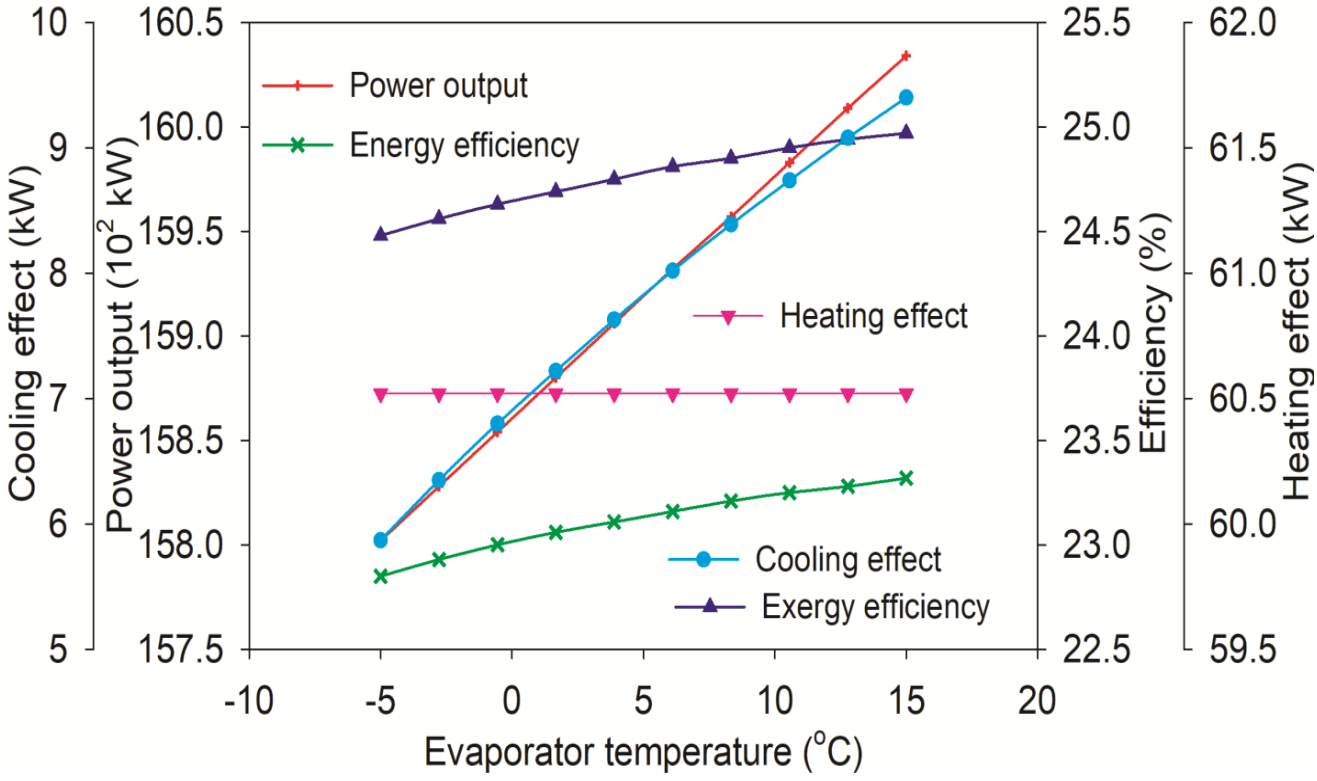

Figure 5.7 Useful output variation with evaporator temperature

5.1.9. Performance variation with solar direct normal irradiation

As per Indian climate conditions, the average value of DNI was found as 850 W/m^2. As DNI increased, the receiver efficiency would also be increased, which leads to enhanced energy performance of the plant. Energy, energy efficiency, and power output varied from 21.36% to 24.65%, 22.87% to 26.4%, and 13808 kW to 15928 kW as the DNI increased from 600 W/m^2 to 1000 W/m^2, as shown in Figure 5.8. Also, the cooling and heating loads are increasing with the DNI. When DNI increases, it gives a load of energy to the cycle, which converts a large amount of energy into a useful output, meaning more heating and cooling loads. Direct Normal Irradiance (DNI) improved from 600 W/m^2 to 1000 W/m^2, which resulted in an increase in the heating and cooling loads from 55.98 kW to 59.6 kW and 6.87 kW to 9.99 kW, respectively, as Figure 5.8 illustrates.

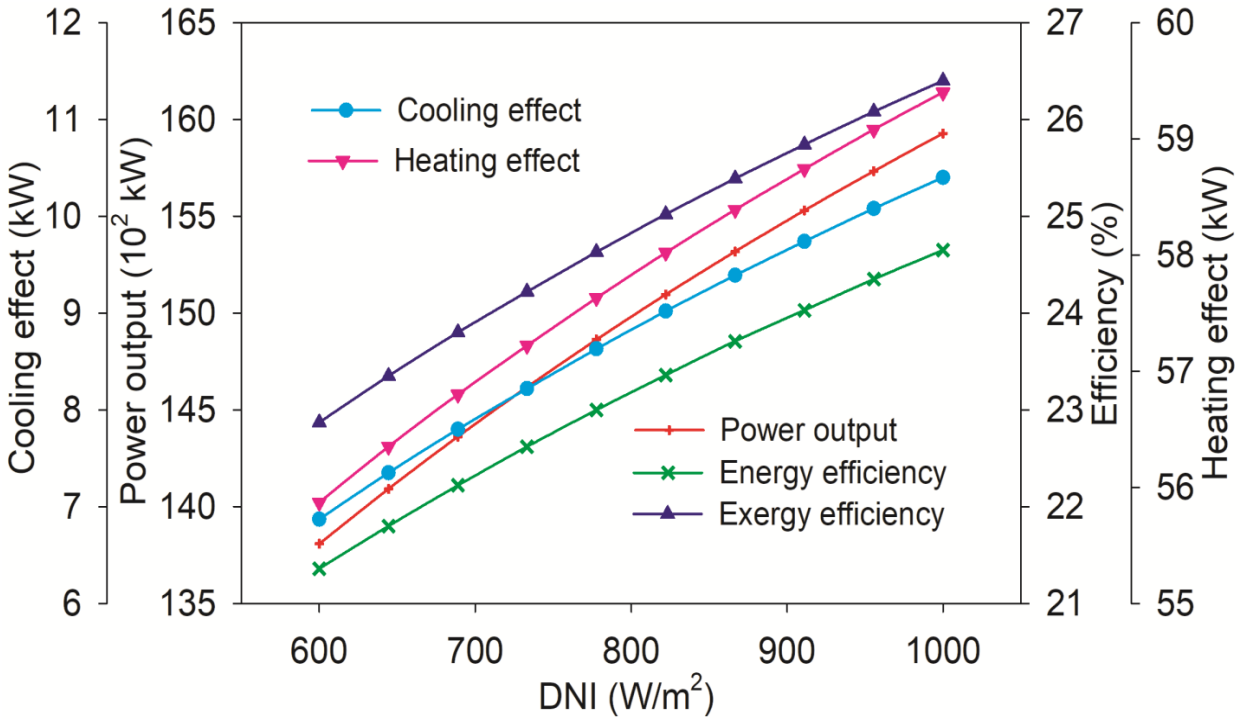

Figure 5.8 Useful output variation with DNI

5.1.10. Performance variation with solar heliostat efficiency

Apart from the combined cycle parameters, the effect of SPT design parameters needs to be discussed. Heliostat field efficiency is the main parameter that affects the performance of the plant. As the heliostat efficiency increased, the performance of the overall plant improved. Exergy, energy efficiency, and power output increased from 21.19 % to 30.83 %, 19.64 % to 28.65 %, and 13925 kW to 19728 kW, respectively, when heliostat efficiency increased from 0.6 to 0.85 as shown in Figure 5.9. This can be explained by the fact that when heliostat efficiency rose, there was a decrease in solar energy loss and a subsequent increase in power conversion. As a result, output of energy, energy, and power increased. Furthermore, an increase in heating and cooling loads is a result of the field efficiency. When the heliostat efficiency is increased from 0.6 to 0.85, the cooling loads and heating loads climb by 51.38% and 6.31%, respectively.

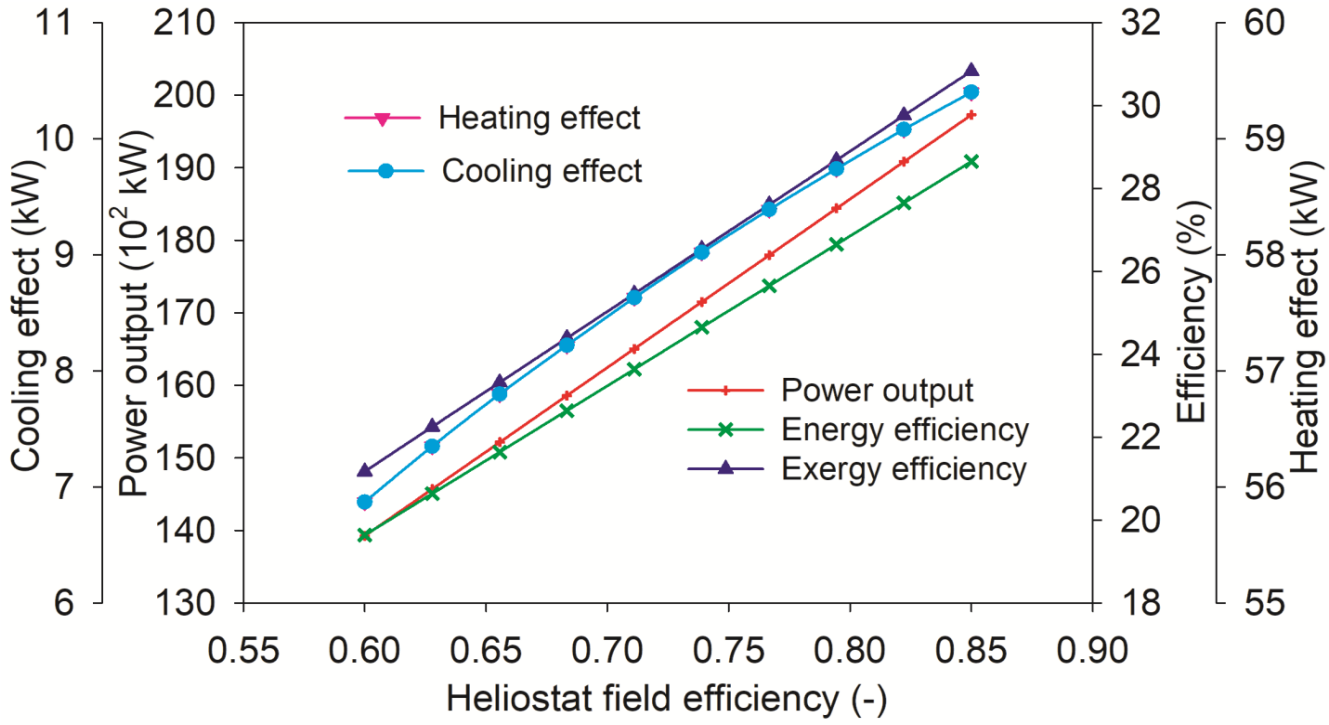

Figure 5.9 Useful output variation with the heliostat field efficiency

5.1.11. Comparison of results with earlier studies

A waste heat recovery ORC-ERS bottoming cycle, a helium Brayton cycle, and a solar (SPT) system make up the integrated system. Previous research has been compared with this system [71]. It's evident that the current system (exergy efficiency 25.12%) was exergetically performed better than the model developed by [71] (exergy efficiency 23.24%) with the minimum number of components. In reference [71], 17 components were included, while the present study included 14 components with higher energy efficiency for high-temperature SPT applications. Additionally, the proposed system is able to produce cooling and heating simultaneously for building applications such as hospitals, hostels, etc.

Table 5.3 performance comparison with previous studies

Systems	$\eta_{receiver}$	η_{field}	$\eta_{field} \times \eta_{receiver}$	DNI (kW/m^2)	η_{cycle} (%)	$\eta_{ex,plant}$ (%)	$\eta_{en,plant}$ (%)
Regenerative supercritical Rankine cycle [164]	0.9	0.75	--	0.8	42.1	27.4	25.7
Regenerative Rankine cycle [164]	0.9	0.75	--	0.8	37.9	24.5	22.9
Present plant	0.9	0.75	--	0.8	47.74	36.27	30.43
Combined tCO_2-ORC [121]	-	-	0.62	1	43.96	-	27.14
sCO_2 cycle [121]	-	-.	0.62	1	42.48	-	26.23
Present plant	--	--	0.62	1	48.45	39.98	34.67

5.2. SPT based combined HBC and ORC with cascade VAR-VCR integrated system

5.2.1. Verification of the suggested system

In order to verify the validity of the modelling technique, the data found in the literature is compared and confirmed with the obtained findings from the two derived models (HBC and VAR-VCR). Comparisons between the independent HBC efficiency values obtained in this study and those published by [74] are displayed in Figure 5.10. It's fine that only 0.55% of the data are different. Therefore, the present modelling approach seems authenticated. A validity check is

performed on the bottoming model (cascaded VAR-VCR) using research findings from the reference [116] at the same baseline conditions, such as operating fluid, evaporator and generator temperature. LiBr-H2O is the working fluid for the VAR in this study, while R410A is used for the VCR. The findings of the present system were validated with the results of the ref. [116] and listed in Table 5.4. It seems that the maximum deviation from the ref. results was found as 0.53% only. That is acceptable for further analysis.

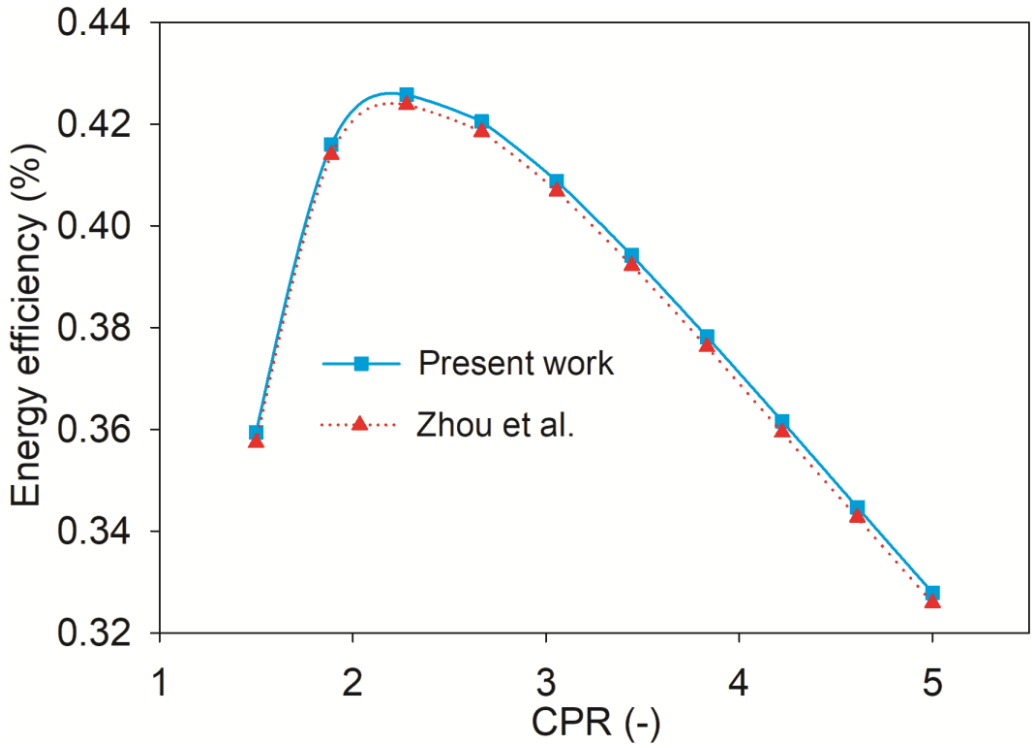

Figure 5.10 HBC system validations

Table 5.4 Cascaded VAR-VCR validation

Parameters	Ref. [116]	This work	Error estimated (%)
$COP_{Cascade}$	0.54	0.5393	0.12
COP_{VAR}	0.75	0.754	0.53
COP_{VCR}	4.41	4.405	0.11

5.2.2. Comparison of energetic and exergetic results among different components in a system

The basic assumptions and operating parameters for the suggested systems are listed in Table 3.2. In order to provide a summary of the energy and exergy evaluation of the cycle under consideration, Table 5.5 shows the values of the research findings for each subsystem at its ideal operating conditions. The total solar energy was obtained as 51569 kW. Only 14865 kW of solar energy was responsible for producing power and heating and cooling effects. Therefore, the energy efficiency of the whole SPT-trigeneration was obtained as 28.82% according to the data of energy analysis in Table 5.5. The heliostats were responsible for losing the majority of solar heat energy, about 12893 kW. That accounted for 25% of the total input heat. Therefore, the heliostat field is the critical component in the whole SPT system. It is suggested that the output of the SPT plant may be further enhanced by properly designing the heliostats. The HBC absorbs 34809 kW of heat energy via IHE. However, only 14774 kW of power was obtained from HBC. For this reason, the energy efficiency of the standalone HBC was 42.44%. However, the SPT-powered HBC system achieved an energy efficiency of 28.64%. It is evident that a significant quantity of energy was lost in the SPT system as a consequence of the increased temperature differential. On the other hand, as can be observed, the combined trigeneration system (HBC-VAR-VCR) has somewhat greater energy efficiency (42.82%). The trigeneration system received a total of 34809 kW of heat input. It produced 14774 kW of electricity as output, with the evaporator providing 30.7 kW of cooling and the condenser and absorber providing 87.63 kW of heating effect.

Table 5.4 shows a comparison of the COP of the combined VAR-VCR system with the VAR and VCR cycles. Under the parameters shown in Table 3.2, the COP of the VAR, VCR, and cascade VAR-VCR were determined to be 0.754, 4.405, and 0.5393, respectively. Nonetheless, the trigeneration system's COPs for heating and cooling were determined to be 1.539 and 0.5393, respectively.

Thermodynamic investigation revealed that the utmost exergy destruction component is the heliostat due to the heat energy received from the solar at high temperatures, such as 4500 K [196]. Additionally, the second maximum exergy destruction value occurred in the receiver due

to its higher surface temperature of approximately 1000 °C [70] compared to the other temperatures in the trigeneration system. The heliostat's energy efficiency was discovered to be 75%. The presence of combustion is the main source of irreversibility in traditional power systems. However, in the present work, combustion is absent in the IHE, and there is a also a negligible temperature difference between HTF and the helium within the IHE. Consequently, the trigeneration system (HBC-VAR-VCR) achieved a greater energy efficiency of 74.98%. Comparing the exergy efficiency of the overall plant along with the combined cycle is relatively low because of high exergy destruction in the solar components (heliostats and receiver), as Figure 5.11 illustrates. Solar components (receiver and heliostats) are responsible for exergy destruction of 40.99%. Heliostats and receiver exergy destructions are 21465 kW and 10725 kW, respectively. As a result, a 39.53% energy efficiency plant was observed. The energy associated with the absorber, condenser, and evaporator was 0.6991 kW, 3.582 kW, and 5.457 kW, respectively.

Table 5.5 Energetic and exergetic results under the specified operational parameters

Subsystem	Exergetic evaluation				Energetic evaluation			
	Input (kW)	Output (kW)	Destruction (kW)	Exergy efficiency	Input (kW)	Output (kW)	Loss (kW)	Energy efficiency
Heliostat field	48152	36114	12038	75%	51569	38676	12893	75%
Solar receiver	36114	25389	10725	70.30%	38676	34809	3868	90%
Trigeneration system	25389	19039	6350	74.98%	34809	14865	19944	42.7%
Overall plant	48152	19039	29113	39.53%	51569	14865	36704	28.82%

Parametric evaluation

For the purpose of analysing the effects of the independent variables such as the receiver and heliostat efficiency, temperature of generator, cascade condenser, evaporator, condenser temperature, HT inlet temperature, and compressor pressure ratio, parametric evaluation is required. As illustrated in Table 3.2, the values other variables' were maintained constant while the influence of changing one parameter was examined.

5.2.3. Effects of variation in compressor pressure ratio on efficiencies

The variation in CPR efficiency is also depicted in Figure 5.11. The CPR is one of the crucial variables for the Brayton cycle, and its impacts must be considered. The trigeneration system's performance was assessed using CPR, and as CPR grew, its efficiency first increased and then steadily decreased, reaching a maximum of 2.278 of CPR. At 2.278 CPR, respectively, the highest energy and exergy efficiency were obtained at 42.9% and 76.65%, respectively. Following the CPR's optimal values, it declines. This pattern can be explained by the fact that prior to the CPR optimal condition, As soon as the CPR rises, the expansion work would likewise grow. Nevertheless, in this part of the study, the rate at which expansion work improves outpaced the improvement in the rate of compression work. Consequently, network output is substantially boosted. This results in an improvement in the efficiency of both cycles. As demonstrated in Figure 5.11, the overall plant exergy and energy efficiency likewise first climbed quickly once the CPR reached its optimal value before slightly declining. The plant's highest energy and energy efficiency values, measured at 2.278 and 3.056 CPR, respectively, were determined to be 28.96% and 39.88%, respectively.

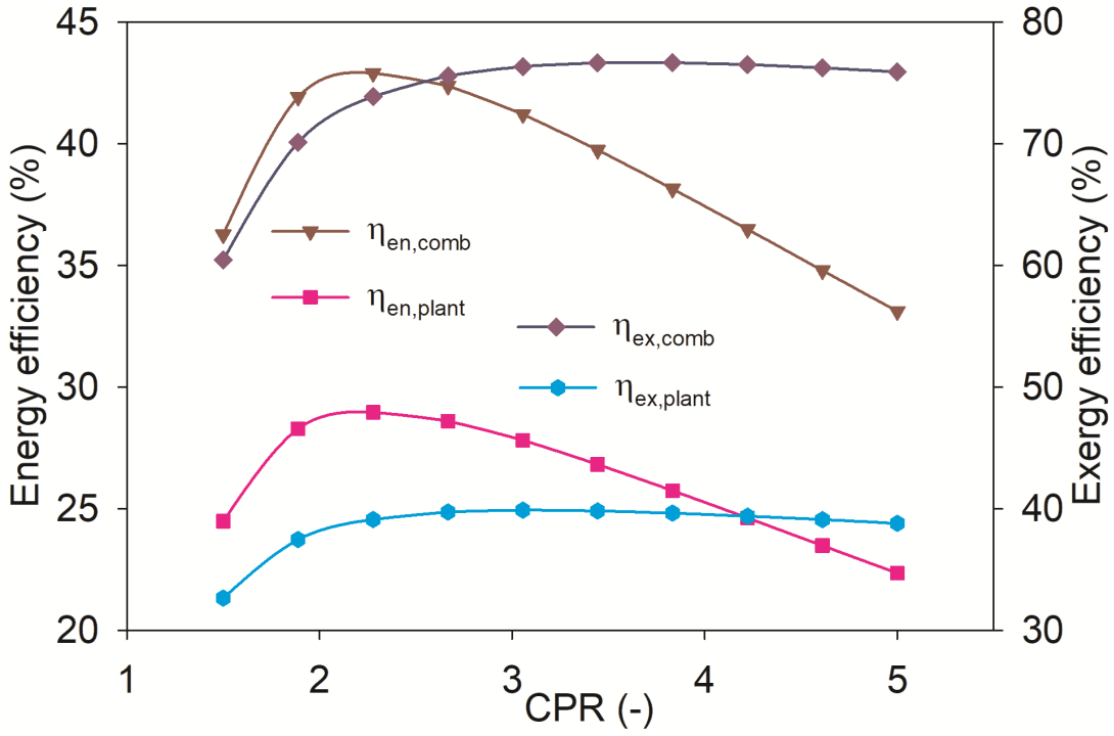

Figure 5.11 Variation in efficiencies with CPR

5.2.4. Effects of variation in compressor pressure ratio on COPs

Figure 5.12 shows how CPR affects power production,COP_c, and COP_h. The power output pattern and the efficiency pattern are comparable. The output of net power first increased before 2.278 of CPR, and then progressively declined. The maximum power was obtained at 2.278 of CPR with values of 14816 kW. As the CPR increased, heat transfer between hot and cold streams of helium in the recuperator decreased due to improvement in the cold side temperature. Therefore, heat available for the VAR-VCR is increased. As a result, as the CPR varied from 1.5 to 5,COP_c, and COP_h of the VAR-VCR cycle varied as well, from 0.5390 to 0.629 and 1.539 to 1.6291, respectively.

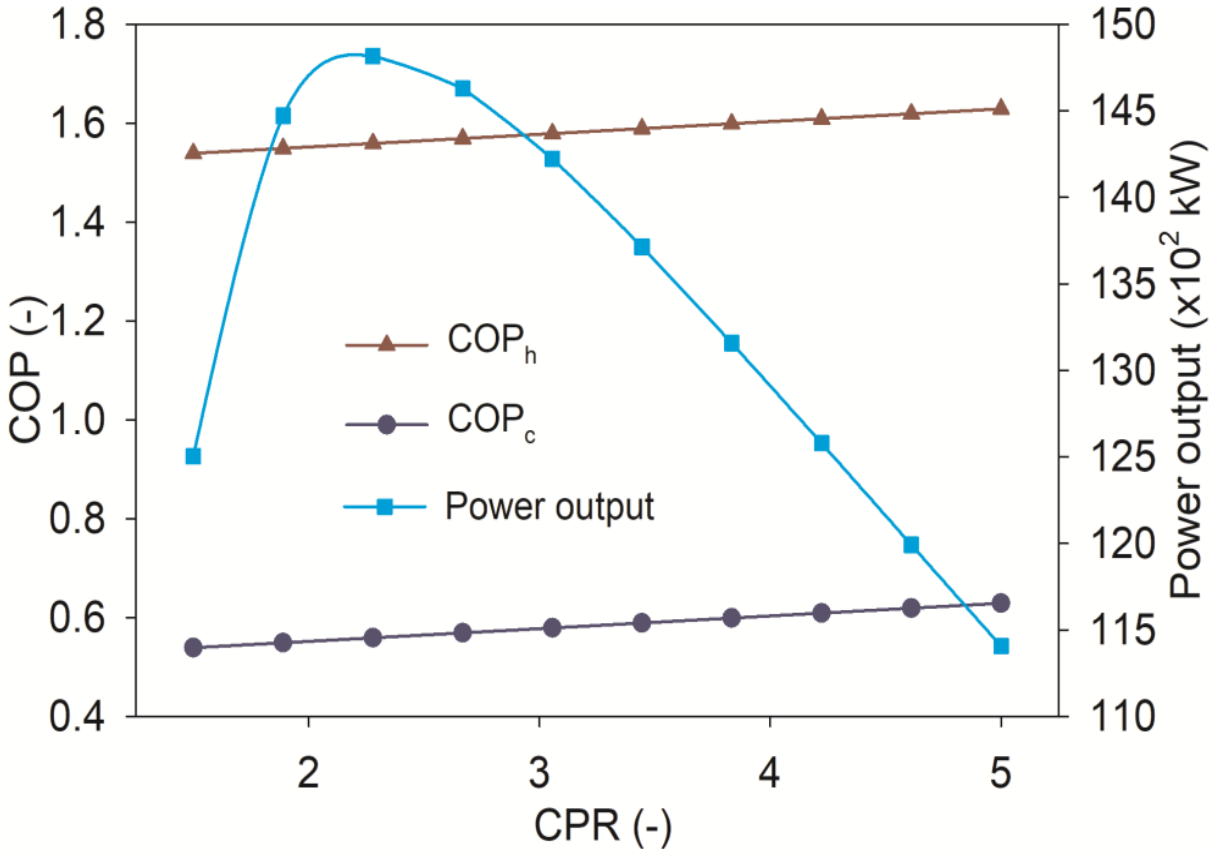

Figure 5.12 COPs and power output variation with CPR

5.2.5. Effects of variation in helium compressor inlet temperature on COP, power output and efficiency

Figure 5.13 illustrates how the helium compressor inlet temperature (HCIT) is known to affect the system performance. With the helium HCIT, The overall efficiency and net electricity production of the plant dropped. This is explained by the fact that when the compressor's inlet temperature rose, the enthalpy difference across the compressor likewise rose, increasing the compressor's output further. As a result, as compressor inlet temperature increased, plant performance as a whole dropped. Plant exergy and energy efficiency dropped from 39.13% to 38.16% and 29.27% to 28.3%, respectively. Additionally, as the temperature rose from 25 °C to 35 °C, output power dropped by 3.05%, as seen in Figure 5.13. On the other side, COP_h and COP_c rise from 1.539 to 1.63 and 0.539 to 0.6291, respectively. This could be brought on by the compressor's substantial heat removal from the generator's side, which lowers the generator's temperature.

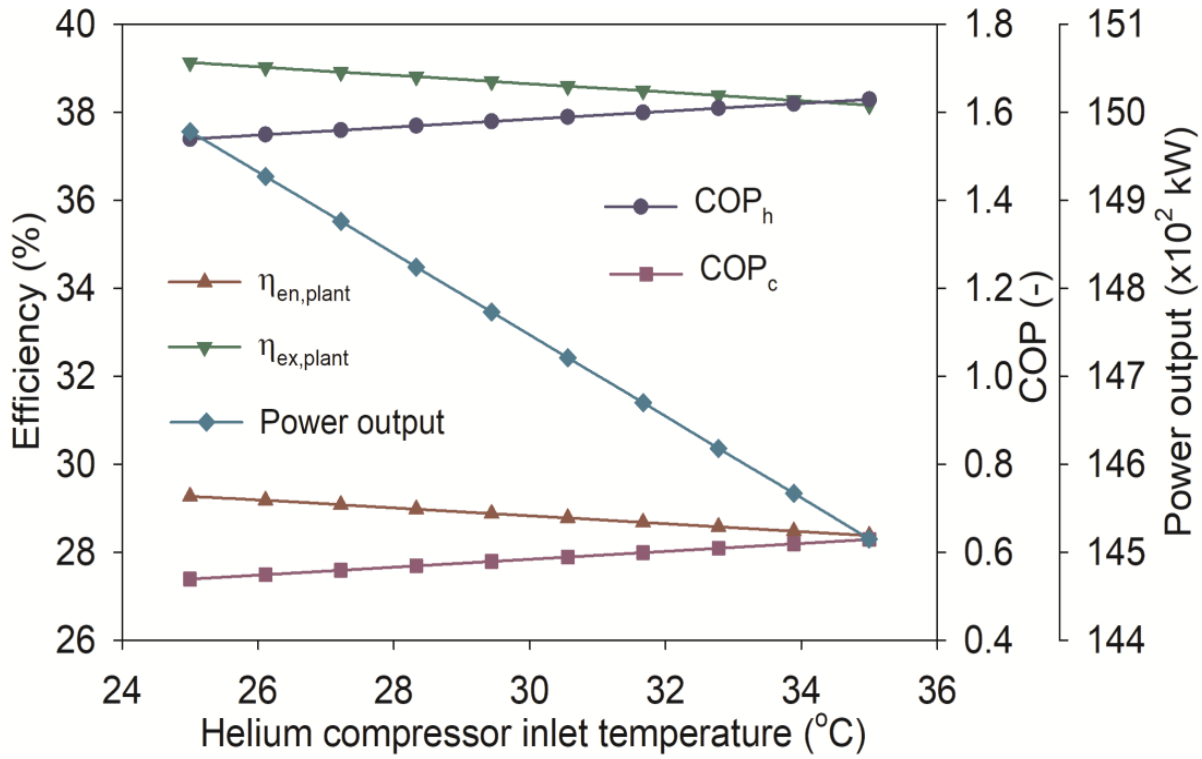

Figure 5.13 Performance variations with HCIT

5.2.6. Effects of variation in helium turbine's input temperature on efficiency, power output and COP

Figure 5.14 demonstrates how the HT inlet temperature (HTIT) affects the plant performance. The plant's output power, exergy and energy efficiency were increased by 22.38%, 14.1% and 23.36%, respectively, as the temperature changed from 700°C to 900°C. It seems acceptable since as the HTIT climbed, the turbine's differential increased as well. It indicates that there was an increase in net expansion effort, which improved net power production and consequently improved system performances. This variation was tested with a generating temperature of 80 °C, 850 W/m^2 of DNI, and an optimal CPR of 2.5. However, HTIT has the reverse effect on the COP_c and COP_h. As shown in Figure 6, the COP_c and COP_h fell from 14.32% and 5.24%, respectively, when the HTIT changed from 700 °C to 900 °C due to an improvement in the generator temperature, which led to lower COPs. It can be said that COP for cooling drops faster than the COP of heating due to slower heat rejection from the absorber and condenser HTIT temperature.

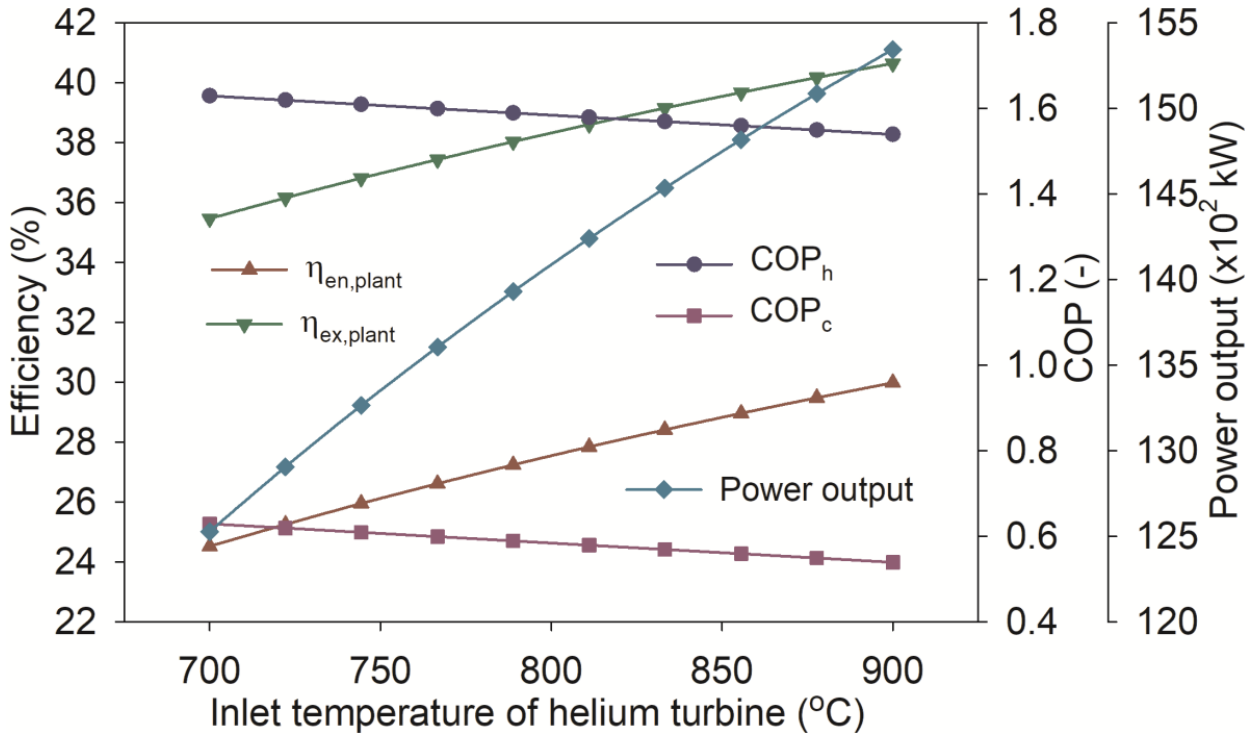

Figure 5.14 Performance variations with HTIT

5.2.7. Impact variation in generator temperature on COP, efficiency and power generation

Integration of the topping HBC parameters, more discussion is required regarding the impact of the bottoming cascaded VAR-VCR system parameters on plant performance. Figure 5.15 illustrates the generator temperature's influence on the output of the plant. The temperature of the generator caused a modest rise in the thermal efficiency of the plant. It increased from 28.82% to 28.88% with a rise in the temperature of the generator from 75 °C to 120 °C. Nonetheless, the plant's energy efficiency dropped as the temperature of the generator rose. It fell by 4.83% as the temperature of the generator improved by 60%. It is shown that the generator does not much affect the thermal efficiency. However, the generator's temperature had no effect on power output. Because generator temperature increases the VCR compressor work on their side, it also decreases the HC compression work. Therefore, net power output doesn't change with the generator temperature. As the temperature of the generator improved by 60%, COP_c and COP_hdeclined by 34.39% and 12.42%, respectively. It can be explained as refrigerant temperature rises with the generator temperature. That increases the average temperature of the absorber and VAR condenser, leading to an improvement in heat transfer losses. The COP for heating drops slower than the COP for cooling due to faster heat rejection from the absorber and condenser.

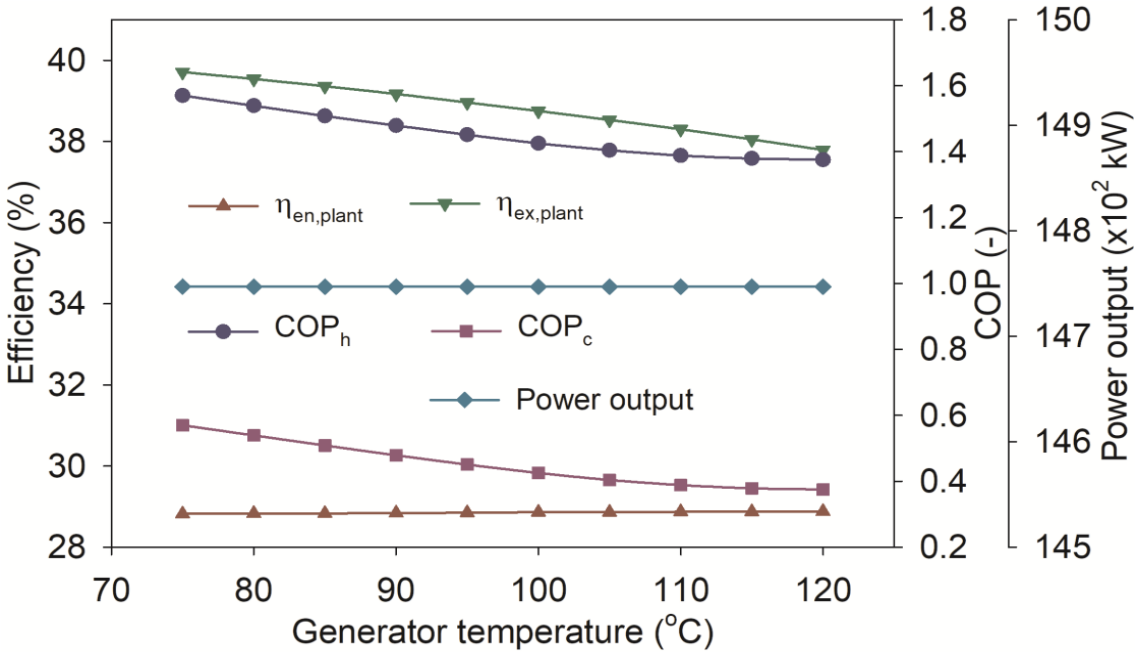

Figure 5.15 Performance variations with the effect of generator temperature

5.2.8. The effects of temperature change in the evaporator on COP, power output and efficiency

Figure 5.16 illustrates the effects of the evaporator temperature on plant performance. The plant's energy and exergy efficiency marginally declined as the temperature of the evaporator rose. The plant's exergy and energy efficiency fell by 0.06% and 0.068%, respectively, as the temperature of the evaporator rose by 25%. The IHE's heat duty is decreased since less compressor power is required when the evaporator temperature rises because the pressure ratio decreases. Consequently, the energy efficiency of the plant decreases. It is important to highlight that although the reduction in process heat represents the energy of low grade, the decrease in heat duty of the evaporator represents the energy of high grade. Therefore, a higher VCR evaporator temperature can be advised in this case if solar heat as the fuel supply. As the evaporator temperature rises, evaporator irreversibility decreases and energy efficiency is reduced. Consequently, there is very little net change in power output. The evaporator temperature enhanced the COP_c and COP_h. A rise in evaporator temperature leads to a rise in the cooling load of the evaporator as well as an improvement in the condenser and absorber heating load. Reduced operation of the compressor is concurrent on the other side. Hence, as seen in Figure 5.16, there is an increase in the COP_c and COP_h. The COP_h and COP_c improved by 1.68% and 4.8%, respectively, as the temperature of the evaporator increased by 25%. The rate of improvement in the COP for heating is slower than COP for cooling. This is due to slower heat rejection through the condenser and absorber that produces the heating effect.

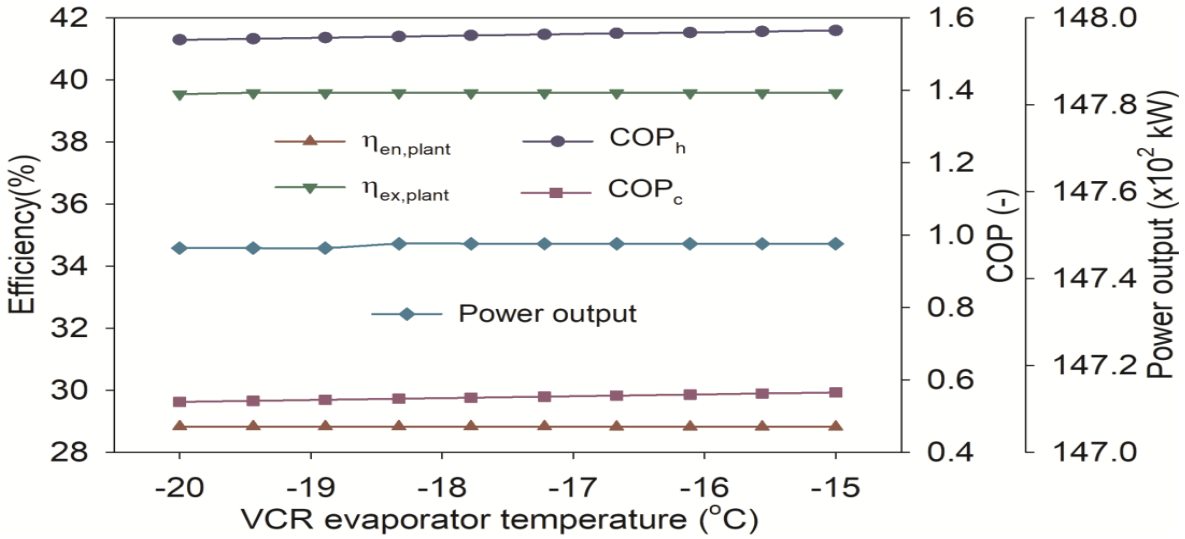

Figure 5.16 Impact of the evaporator temperature on plant performance

5.2.9. Effects of variation in cascade condenser temperature on power output, efficiency and COP

The effect of cascading condenser temperature on system performance is seen in Figure 5.17. At 13.89 °C, energy efficiency stays constant; however, it abruptly drops and then gradually rises due to the sudden change in thermodynamic properties of the working fluid within the cascade condenser at this temperature. The combined impact of the condenser and evaporator loads is also responsible for this type of pattern. The plant's thermal efficiency marginally climbed from 39.54% to 39.88% with the CC temperature. The compressor work increases with CC temperature, and the generator's requirement for heat decreases due to the higher pressure ratio brought on by an increase in the temperature of the cascade condenser. Consequently, there is an increase in the requirement for process heat generation as well as heat duty for the IHE. Both the exergy and energy efficiency slightly improve due to slight increments in the heat load in IHE and network output simultaneously. After decreasing slightly to 14847 kW, net output power abruptly jumped to 14876 kW at 14.33 °C. This is due to the sudden change in fluid properties at this temperature. However, both COP_c and COP_h, as shown in Figure 5.17, decrease with the CC temperature. This is due to a higher cascade condenser temperature resulting in more compression work being needed to compress the refrigerant, and the generator produces more heat as well, resulting in a slight decrement in the COPs.

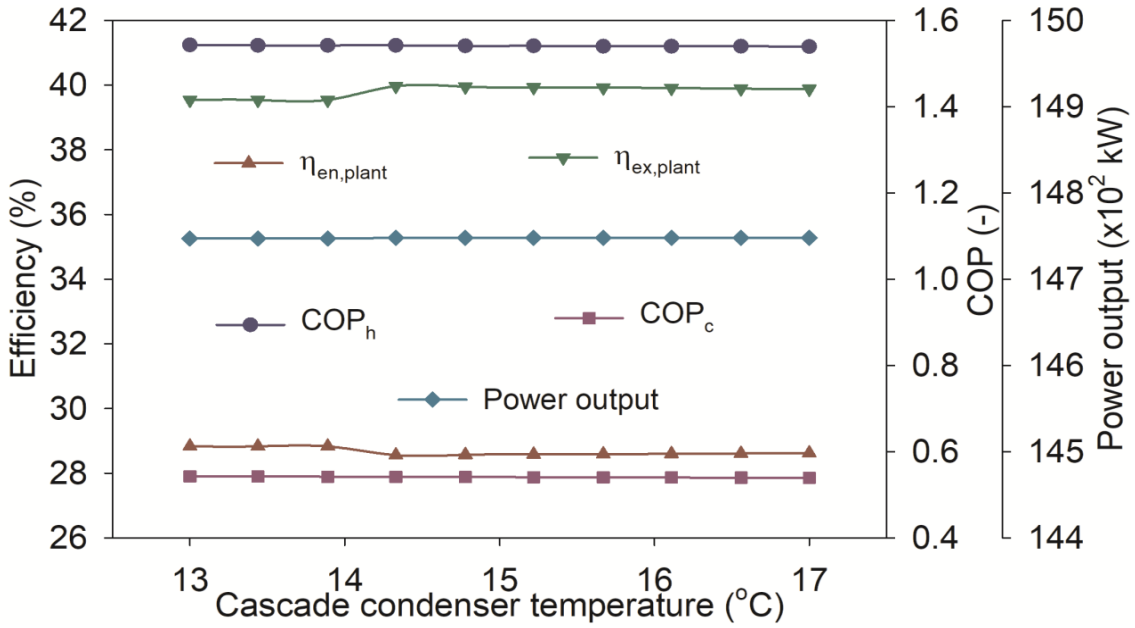

Figure 5.17 Performance variations with CC temperature

5.2.10. Effects of variation in absorber temperature on COP, power output and efficiency

Moreover, the effect of the absorber temperature on the function of the plant is shown in Figure 5.18. The plant's exergy and energy efficiency marginally decreased by 0.07% and 0.03%, respectively, as the absorber temperature increased by 28.57%. It can be seen that efficiencies were not affected much by the absorber temperature because improvement in the absorber temperature slightly increased the VAR compressor work. Therefore, net work output of the plant also decreases slightly. The generator must produce more heat as the absorber temperature increases, which lowers the quantity of process heat produced. IHE requires constant heat duty since absorber temperature does not affect the compression work performance. As a result, as the absorber temperature climbed, COP_h and COP_cincreased from 1.529 to 1.594 and from 0.5287 to 0.5938, respectively. As heat is produced, the absorber's temperature drops. Consequently, as Figure 5.18 depicts, the cooling and heating COPs went up. The absorber temperature, however, has minimal bearing on the output of net power. This is because an improvement in HBC power generation would offset a slight reduction in compressor work.

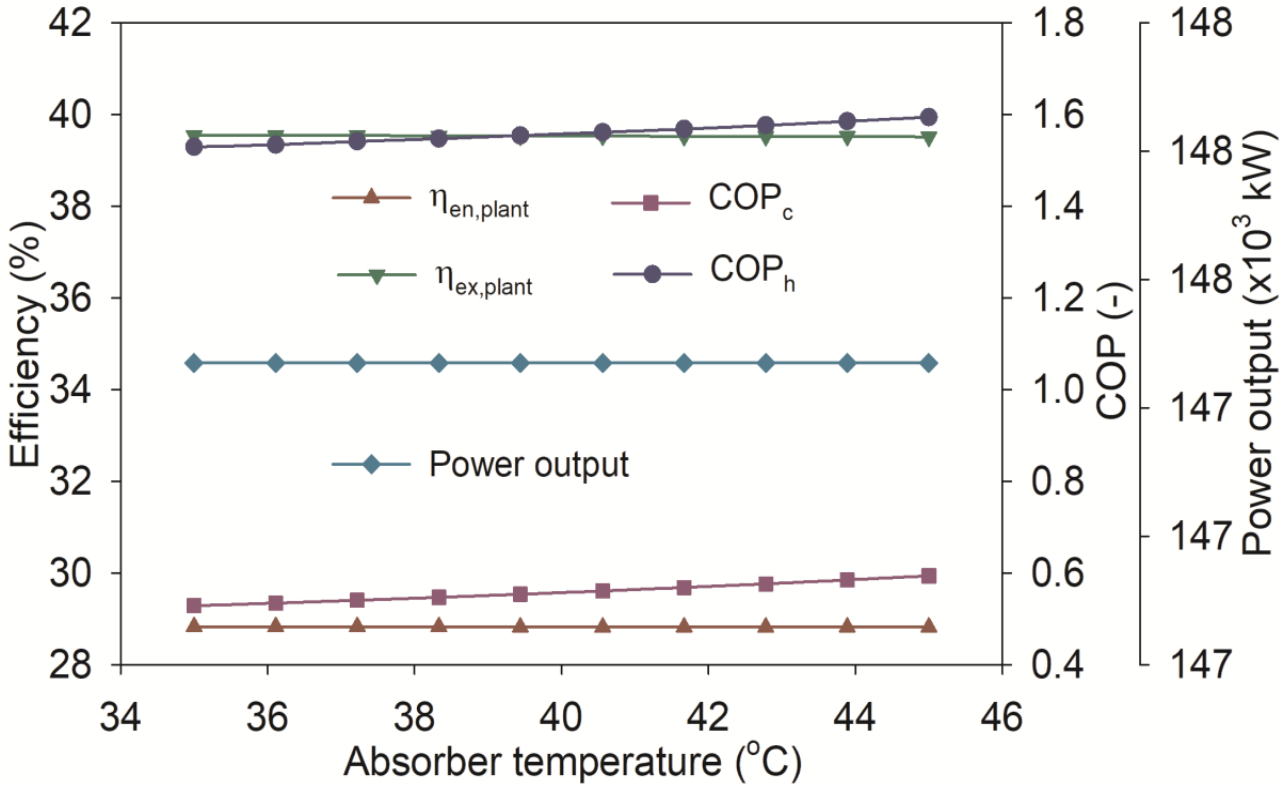

Figure 5.18 performance variations with absorber temperature

5.2.11. Effects of variation in VAR condenser temperature on COP, power output and efficiency

Figure 5.19 further examines the impact of VAR condenser temperature. The condenser temperature (because of an increase in pressure ratio) increases the compression work. As a result, the plant's net power output, energy and exergy efficiency, and condenser temperature all constantly dropped. As Figure 5.19 illustrates, the plant's energy, exergy, and power output dropped by 3.04%, 2.47% and 3.09%, respectively, with condenser temperature. Additionally, Figure 5.19 shows that when the condenser temperature changed from 30 ℃ to 35 ℃, $COP_c$and COP_hdecreased from 0.5427 to 0.5393 and 1.543 to 1.539, respectively. Since the generator internal pressure increases in direct proportion to temperature, a low amount of water vapor is released from the generator, which lowers efficiency and coefficient of performance.

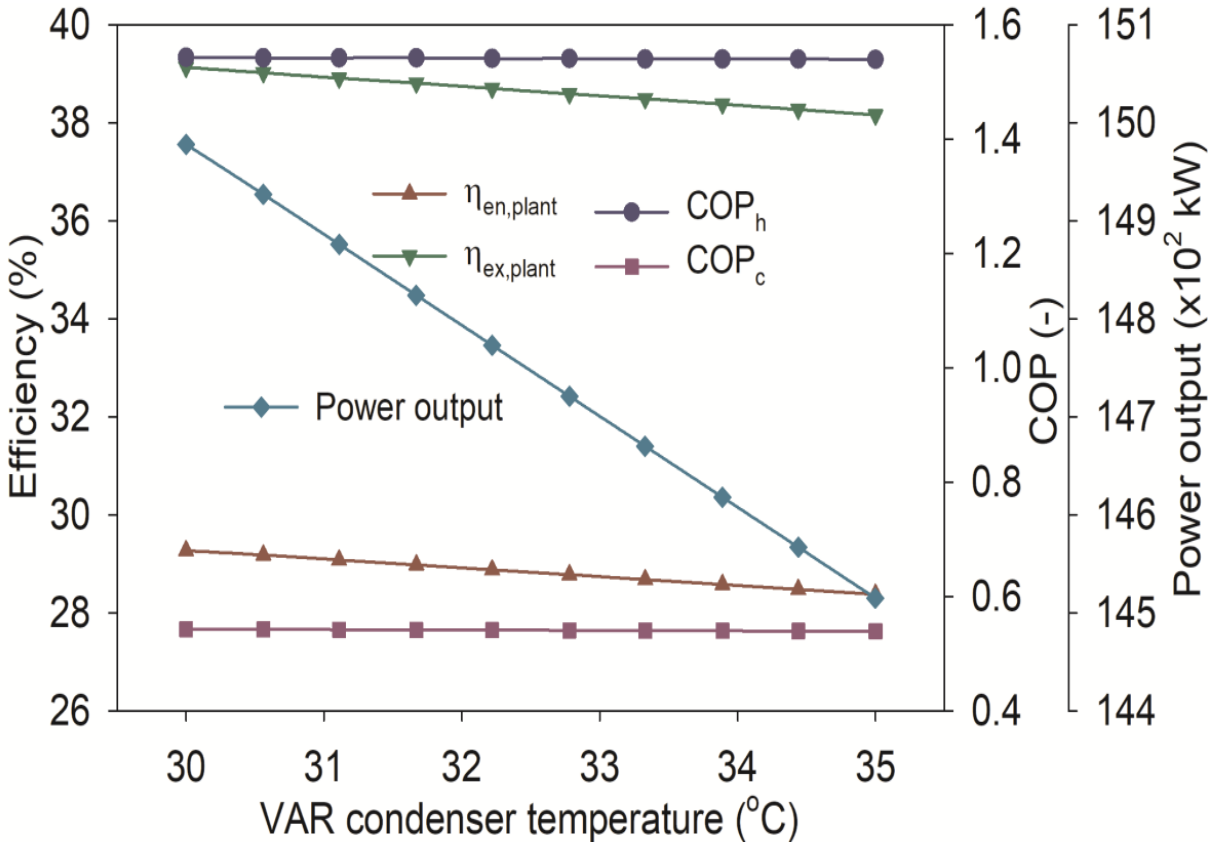

Figure 5.19 performance variations with the VAR condenser temperature

5.2.12. Effects of variation in heliostat field efficiency on COP, power output and efficiency

Verifying the effect of solar parameters on the system's overall performance is mandatory. The solar sub-section characteristics in the current investigation were receiver efficiency ($\eta_{recevier}$) and heliostat field efficiency (η_{field}). Figure 5.20 illustrates how η_{field} enhanced power production, energy efficiency, and exergy efficiency. More energy reaches to receiver as η_{field} rose because heat losses from the heliostat were reduced. Additionally, both the mass flow rate of helium and the mass flow rate of air in the receiver rose. As a result the net output power improves as a result. Since energy and exergy efficiency are directly correlated with power production, both were enhanced as well. Power production, energy efficiency, and exergy efficiency increased by 30.99%, 30.78%, and 30.5%, respectively, as field efficiency increased from 0.65 to 0.85.

COPs dropped with the field efficiency. As previously mentioned, the cycle's heat input rose due to the field efficiency. As a result, the generator temperature rises due to enhancement in input to the generator by the helium fluid that is flowing in the HBC. It is clear that both COPs fall due to improvement in the generator temperature. Therefore, it is said that lower field efficiency is beneficial for more cooling and heating effects, while higher field efficiency is advised for more power production. As illustrated in Figure 5.20, COP_h and COP_cdropped by 12.42% and 32.6%, respectively, as η_{field} increased from 0.65 to 0.85.

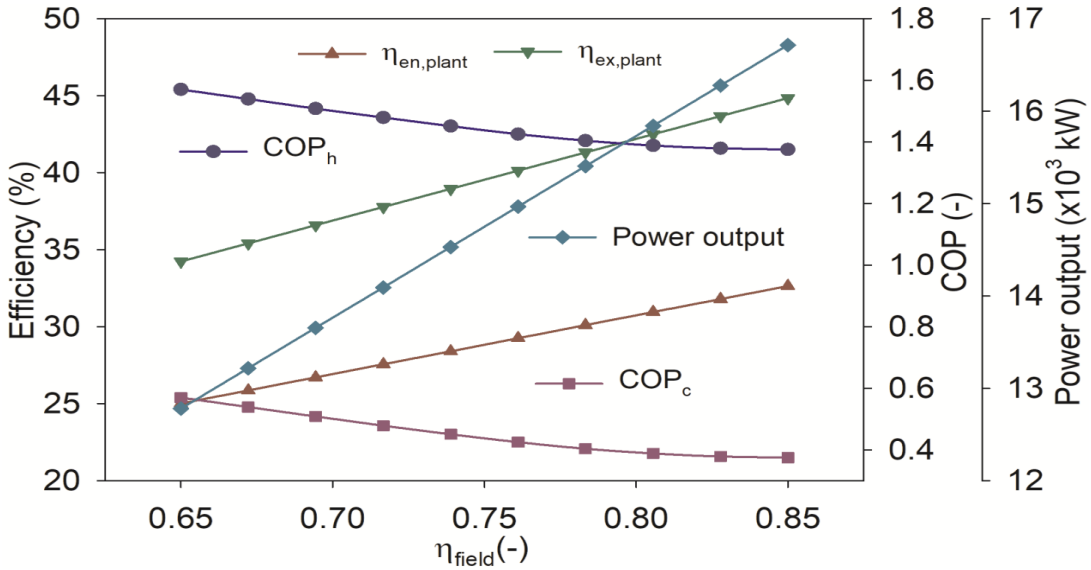

Figure 5.20 Performance variations with heliostat field efficiency

5.2.13. Effects of variation in heliostat field efficiency on COP, power output and efficiency

In addition to the field efficiency, another crucial solar subsystem parameter that influences the thermodynamic performance is$\eta_{recevier}$. Figure 5.21 illustrates how rising $\eta_{recevier}$ enhances thermal performance. Heat loss is reduced when the $\eta_{recevier}$ increased, as previously explained. The recipient will, therefore, get more energy, which leads to an increase in the air and helium mass flow rate. The power output will rise as a result. The same heliostat area, however, ensures a steady overall energy intake for the plant. As a result, energy efficiency is raised. When receiver efficiency was changed from 0.7 to 0.95, the plant's exergy efficiency, power output, and energy efficiency all improved by 35.38%, 35.99%, and 35.74%, respectively. However, $COP_c$and COP_hfell by 12.42% and 34.22%, respectively with receiver efficiency. The same explanation as for Figure 5.20 decline in COPs applies here.

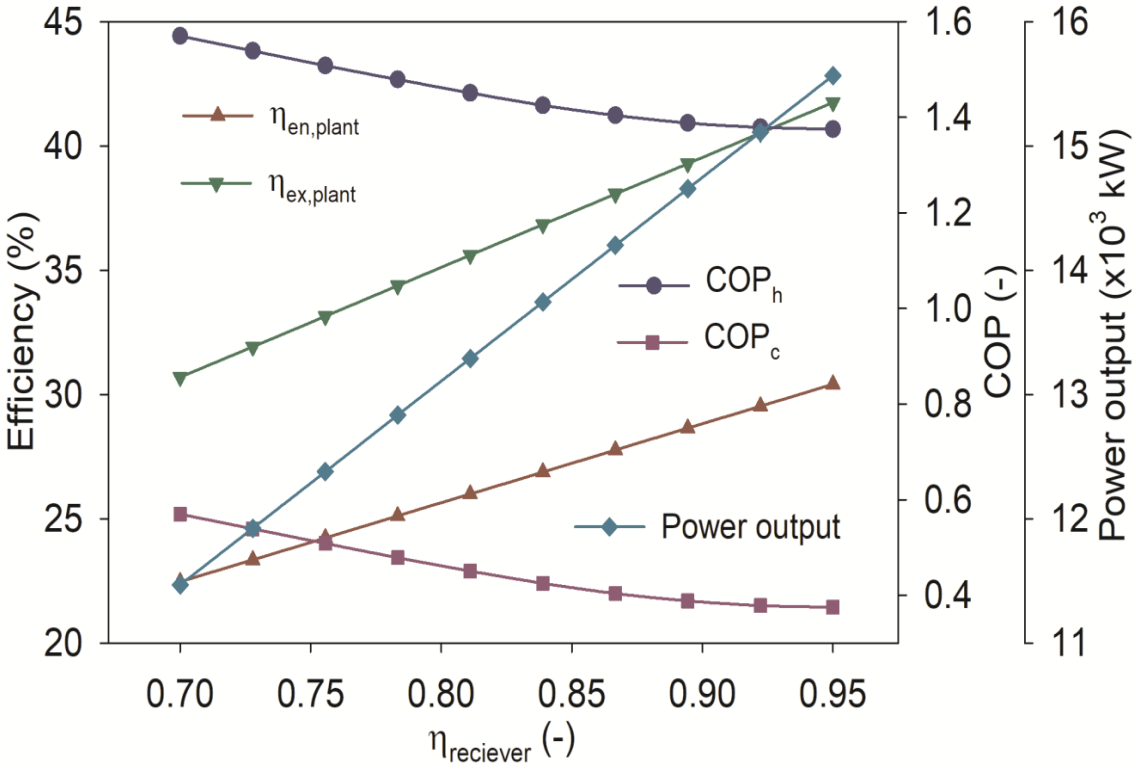

Figure 5.21 Performance variations with the receiver efficiency

5.2.14. Comparison of results with previous studies

As was previously indicated, there are various irreversibilities associated with the solar subsystem of SPT plants. Also, it is not possible to avoid. To improve the SPT plant performance, it is important to utilize energy generation units efficiently. In this regard, the SPT-based present energy generation unit or trigeneration system is compared with previous energy generation systems published by different authors. In order to conduct a true comparison, identical sunlight conditions are used, and Table 5.6 presents the results. The results demonstrate the superiority of the trigeneration system (HBC-VAR-VCR) unit proposed in this work over previous systems of a similar nature. It is evident that the plant utilized in this study generates energy with higher efficiency than the SPT-based supercritical CO_2 cycle and Rankine cycle.

Table 5.6 performance compression with previous studies

Systems	$\eta_{receiver}$	η_{field}	$\eta_{field} \times \eta_{receiver}$	DNI (kW/m^2)	η_{cycle} (%)	$\eta_{ex,plant}$ (%)	$\eta_{en,plant}$ (%)
Regenerative supercritical Rankine cycle [164]	0.9	0.75	--	0.8	42.1	27.4	25.7
Regenerative Rankine cycle [164]	0.9	0.75	--	0.8	37.9	24.5	22.9
Present plant	0.9	0.75	--	0.8	42.79	39.53	28.82
Combined tCO_2-ORC [121]	-	-	0.62	1	43.96	-	27.14
sCO_2 cycle [121]	-	N.A.	0.62	1	42.48	-	26.23
Present plant	--	--	0.62	1	46.32	42.02	31.89

5.3. SPT based combined HBC and ORC with cascade ERS-VRS integrated system

5.3.1. Validation of the proposed system

The proposed system was validated with the previous studies. HBC was validated with [74] efficiency, as shown in Figure 5.22. Results show the current model's accuracy. The bottoming ORC-ERS is assessed Using study data gathered from reference [129] at baseline conditions. Various variables are compared between the results of Ref. [129], including enthalpies and the relationship between heat and work. Based on the comparison data in Table 5.7, the largest disagreement discovered was 1.5%, a modest percentage suggesting high accuracy. However, the COP of the VCR output is validated with the reference [115]. The current study gives the COP of VCR as 4.405. However, the COP of the ref. was obtained as 4.41 at the given conditions of ref. It is seen the COPs have a good agreement with the ref. [115] with only 0.11% of error.

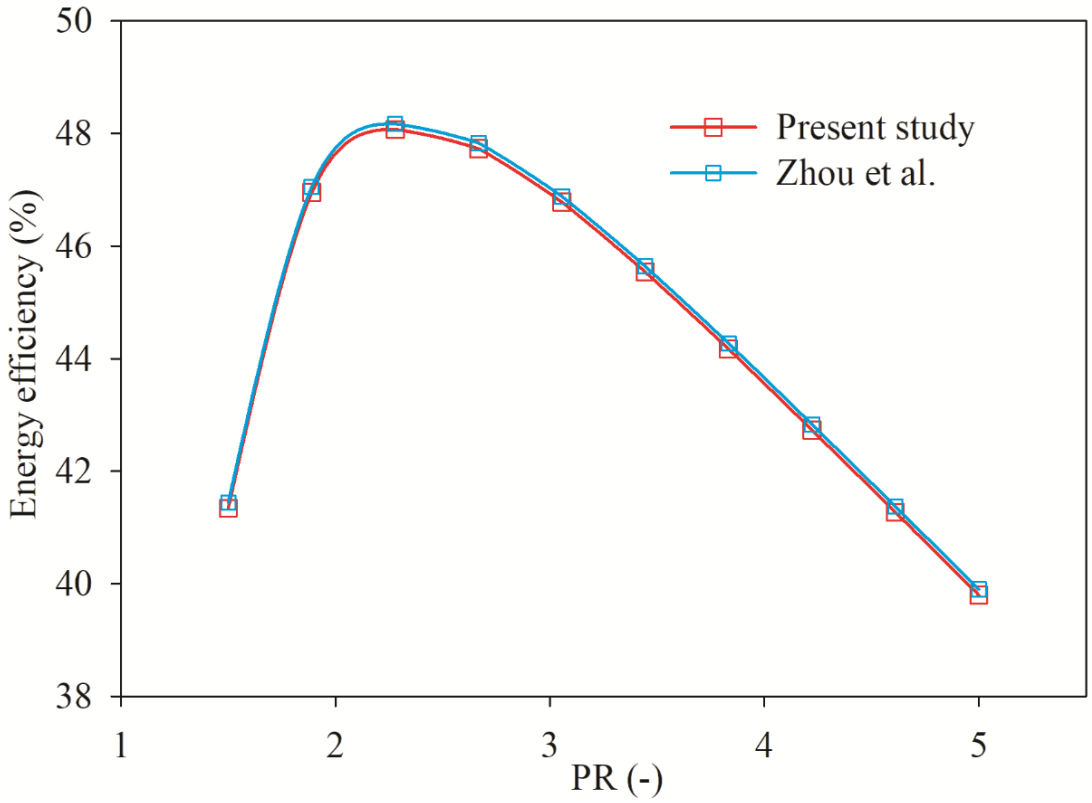

Figure 5.22Validation of HBC system

Table 5.7 ORC-ERS Verification

Variables	Current study	Ref. [129]	Deviation (%)
h_9	477.7	474.2	0.73
h_{10}	451.4	451	0.08
h_{11}	447.12	445.4	0.38
h_{12}	221.2	220.1	0.49
h_{13}	220.9	220.1	0.36
h_{14}	376.54	375.5	0.27
h_8	220.97	220.8	0.07
Q_E	60.7	60.4	0.49
$\dot{m}_c$	5.39	5.310	1.5
$\dot{m}_e$	0.391	0.389	0.51
$\dot{W}_{net}$	111.2	110.7	0.004

5.3.2. Comparison of energetic and exergetic results among different components in a system

The results obtained from the analysis at base conditions, as given in Table 3.3, have been specified in Table 5.8. It has been observed that the energy efficiency of the suggested trigeneration system (HBC-ORC-ERS-VCR) was 89.86%. It is much higher than any conventional trigeneration system. This is due to the effective utilization of the waste heat obtained from the conventional HBC system through the proposed trigeneration system. However, the overall proposed solar plant obtained an energy efficiency of 60.66%. Evidently, the overall proposed plant (SPT-HBC-ORC-ERS-VCR) efficiency is lower than the trigeneration system. This is due to the consideration of SPT system performance. It means higher heat loss is obtained in the heliostats field and the central receiver. However, the proposed plant's overall energy efficiency is 101.19% higher than the conventional system (SPT-HBC). This is due to much useful energy obtained from the proposed system in terms of heating, cooling effects and power generation. However, the network output from the proposed plant is 15585 kW. Heating

and cooling effects were obtained as 14967 kW and 730 kW for the industrial application and food storage application respectively.

The exergy efficiency of the conventional system (SPT-HBC) and the proposed plant were obtained as 32.29% and 35.55% respectively. The exergy efficiency of the suggested system is 10.09% greater than the proposed plant. However, the trigeneration system's exergy efficiency shows as 67.55%. This is due to the more useful output from the overall proposed system. However, the exergy destruction was obtained from the conventional system, trigeneration system and overall proposed plant as 32603 kW, 15625 kW and 31033 kW, respectively. It can be seen that the overall proposed solar plant's exergy efficiency is lower than the trigeneration system due to the higher irreversibilities present in the SPT components, i.e.in the central receiver and the heliostats field.

Table 5.8 Obtained results at base conditions

Parameters	SPT-HBC	HBC-ORC-ERS-VCR	SPT- HBC-ORC-ERS-VCR
Energy efficiency (%)	30.15	89.86	60.66
Exergy efficiency (%)	32.29	67.55	35.55
Net work output (kW)	15547	15585	15585
Heating effect (kW)	-	14967	14967
Cooling effect (kW)	-	730	730
Exergy destruction (kW)	32603	15625	31033
Total output energy (kW)	15547	31282	31282

Parametric analysis

The exergy, energy efficiency, network production, heating and cooling effects, and suggested solar-based plant (SPT-HBC-ORC-ERS-VCR) were taken into consideration as performance parameters. Investigations were conducted on how the various parameters affected the system's performance. It is presumed that other factors were maintained constant while assessing the effects of the individual parameters.

5.3.3. Effect of variation in heliostats field efficiency

Figure 5.23 reveals the effect of the heliostat field efficiency on the plant performance. It is seen that the performance of the plant increases continuously with the heliostat field efficiency. It can be explained as the efficiency improved, the effective application of solar energy also increased, and consequently, the performance of the system increased. The projected plant's energy and exergy efficiency grew from 52.57% to 68.75% and 30.81% to 40.29%, respectively, as the field efficiency climbed from 0.65 to 0.85. However, the network production was increased from 13507 kW to 17663kW with field efficiency. In addition, the heating and cooling effects of the cascading ERS-VCR system were enhanced by the heliostats' field efficiency. This is because solar energy is now converting at a faster pace to usable outputs. With the heliostats field efficiency increasing from 12971 kW to 16962 kW and 632.2 kW to 826.7 kW, respectively, the heating and cooling impacts were likewise amplified.

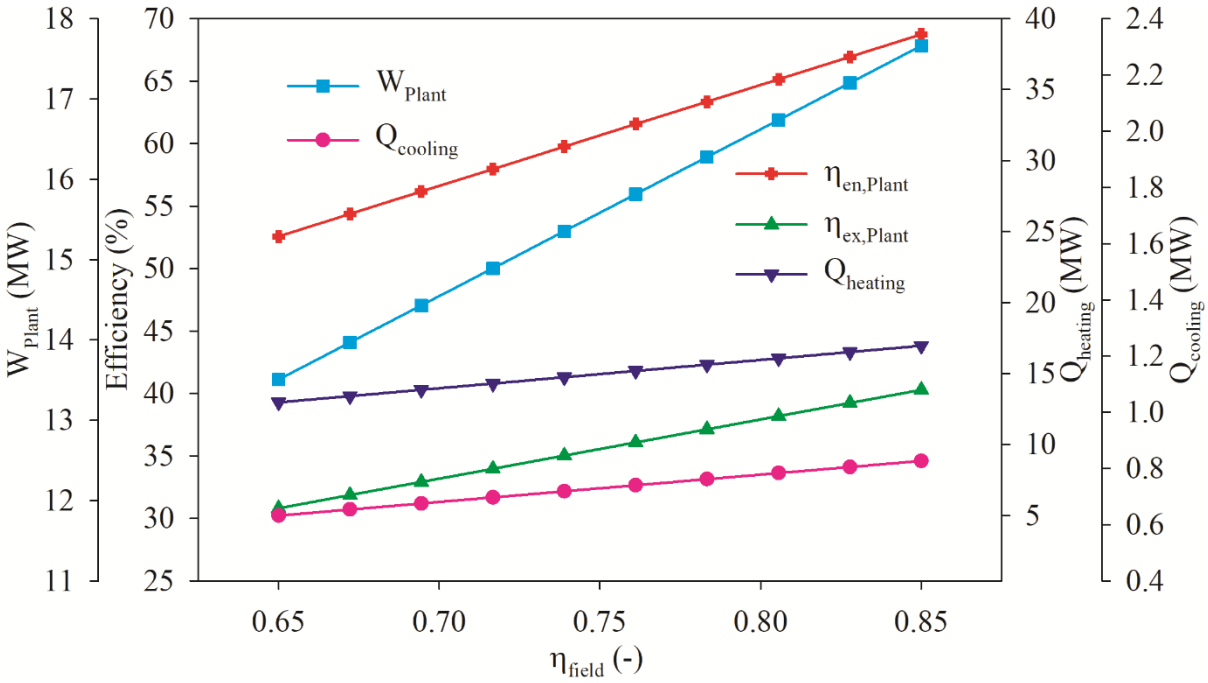

Figure 5.23 Effect of the heliostats field efficiency on the proposed plant performance

5.3.4. Effect of variation in receiver efficiency

Figure 5.24 shows that the performance of the plant increases with the efficiency of the receiver. As the receiver efficiency rises, the losses from the receiver decrease, which means a lot of the energy is valuable enough to be converted into a useful task. Therefore, receiver efficiency is an important parameter that needs to be designed carefully. The plant's network production, energy efficiency, and exergy output rise from 33.58% to 37.53%, 57.29% to 64.03%, and 14719 kW to 16450 kW, respectively, while the receiver efficiency climbs from 0.85 to 0.95. Apart from this the heating and cooling effects also increased with the receiver efficiency. As the efficiency of the receiver rose, also the heat rejection from the topping cycle increased, which meant a lot of the heat energy was available to be converted into useful work. The heating effect and the cooling effect increase from 14135 kW to 15798 kW and 688.9 kW to 770 kW, respectively.

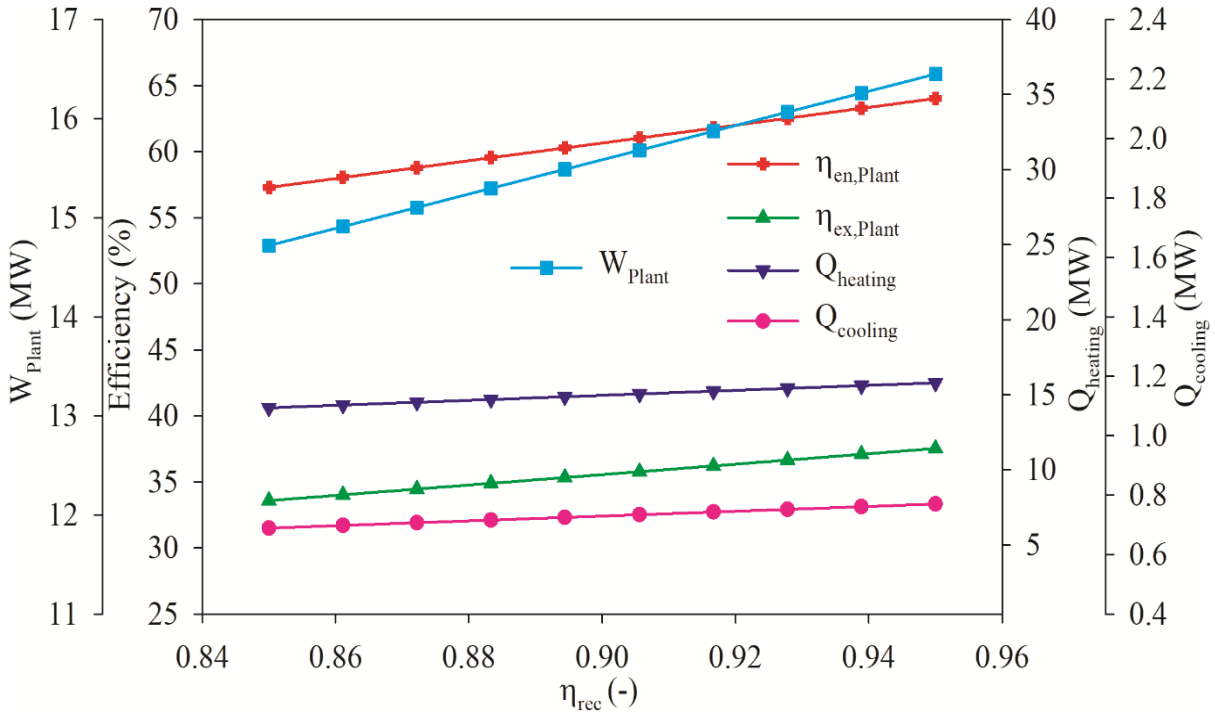

Figure 5.24 Effect of the receiver efficiency on the proposed plant performance

5.3.5. Effect of variation in compressor-1 pressure ratio

The influence of the compressor-1 pressure ratio (PR) has been discussed in Figure 5.25. The work output increased first then decreased. This trend can be rationalized by considering the enhanced expansion and compression works before reaching a CPR of 2.3. However, in this context, compared to expansion work, compression work has a slower rate of enhancement. Consequently, the network output increases, leading to improvements in the exergy efficiency of the plant. Subsequent to a CPR of 2.3, the results demonstrated a reverse trend. However, the energy efficiency first decreased sharply and then increased. These results from the heating and cooling effects working together obtained from the cascaded refrigeration system. Since the heating and cooling effect, decrement is much faster than the improvement rate of the network output. Therefore, overall energy output decreased first and then increased slowly after the optimum value of the PR. The highest value of the energy and exergy efficiency and network production of the integrated system was obtained as 98.43%, 35.49%, and 15552 kW, respectively, within the considered range of the PR.

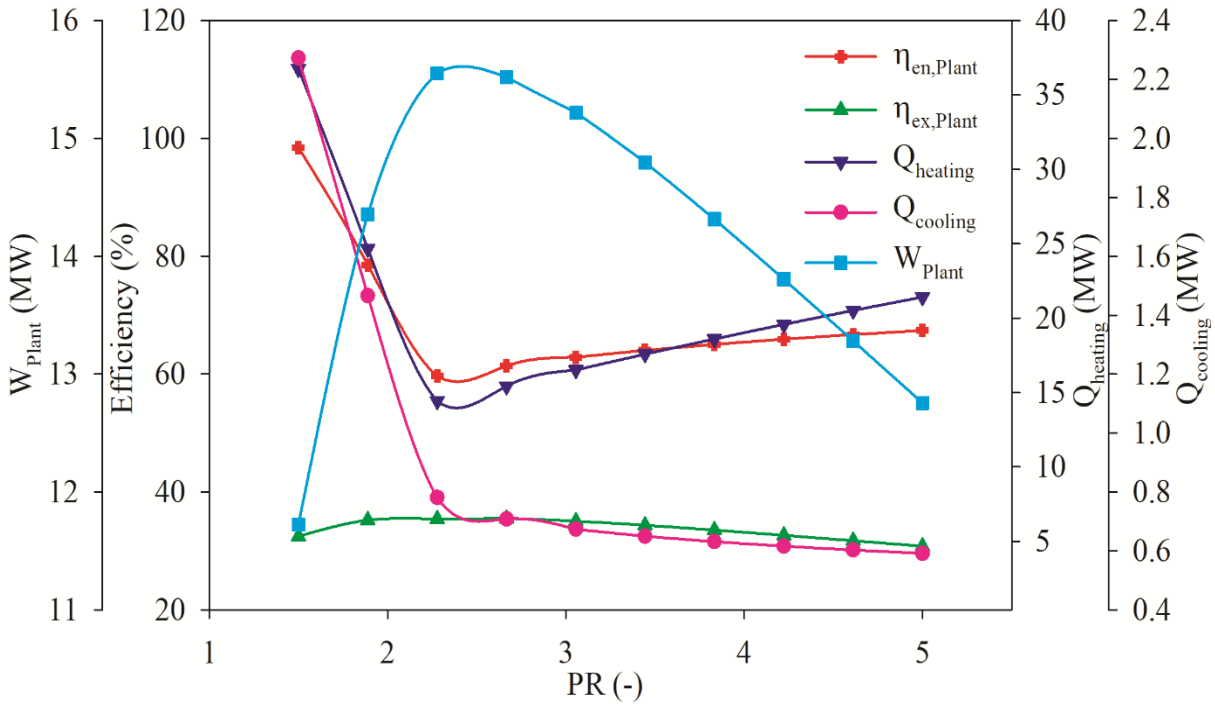

Figure 5.25 Effect of the compressure-1 pressure ratio on the performance of the plant

5.3.6. Effect of variation in turbine-1 inlet temperature

The performance of the system is significantly influenced by the turbine-1 inlet temperature (TIT). As depicted in Figure 5.26, when the TIT rose from 650 °C to 950 °C, the plant's energy, exergy efficiency, and power generation all increased: from 58.34% to 61.58%, 29.56% to 37.72%, and 12494 kW to 16695 kW, respectively. The reason for this is that as the input temperature rises, the enthalpy differential across the turbine increases. Consequently, there is a rise in net expansion effort, leading to enhancements in power generation and the overall performance of the integrated system. This modification was assessed under conditions of 197.4°C for the input temperature, 850 W/m² of DNI, and a PR of 2.5. Furthermore, the TIT affects the heating and cooling impacts as well as power generation and efficiency. The influence of cooling and heating was decreased with a rise in TIT. In particular, when the HTIT increased from 650°C to 950°C, the heating effect reduced from 16680 kW to 14394 kW and the heating load climbed from 913.6 kW to 669.7 kW. This relationship makes sense because rising TIT and ORC turbine input temperatures indicate greater heat energy getting into the ORC-ERS system and amplifying the cooling and heating impact.

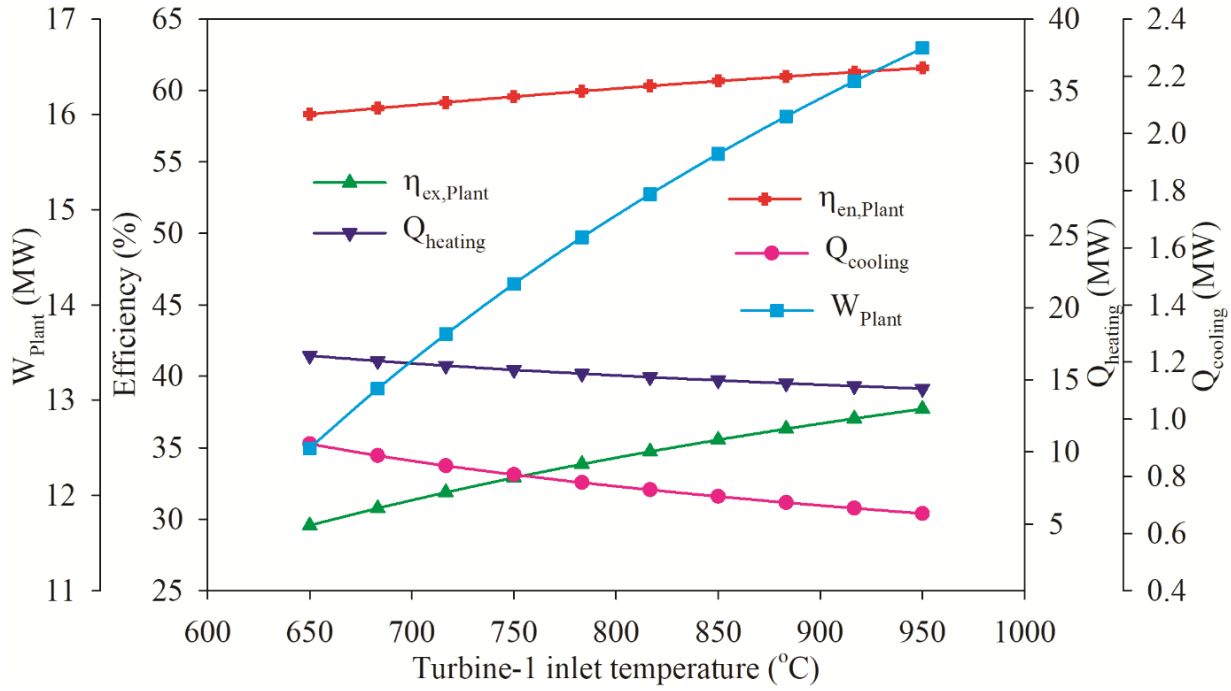

Figure 5.26 Effect of the turbine-1 inlet temperature on the performance of the plant

5.3.7. Effect of variation in compressor-1 inlet temperature

The system's performance declined with the compressor-1 inlet temperature (CIT). This is accounted by the fact that an increase in CIT also led to an increase in the enthalpy differential inside the compressor, which improved compressor work. As such, CIT decreased the system's overall efficiency between 35.79% and 35.31%, and the plant's overall exergy efficiency declined. As depicted in Figure 5.27, within the range of the CIT, the power output decreased from 15774 kW to 15391 kW. However, the heating and cooling loads increased with the CIT. The network generation from the T2 decreased as CIT rose, suggesting that the small rise in the condenser and evaporator loads was mostly unaffected by the output heat. The heating and cooling effects increased from 14143 kW to 15815 kW and 723 to 738 kW, respectively, within the range of the CIT.

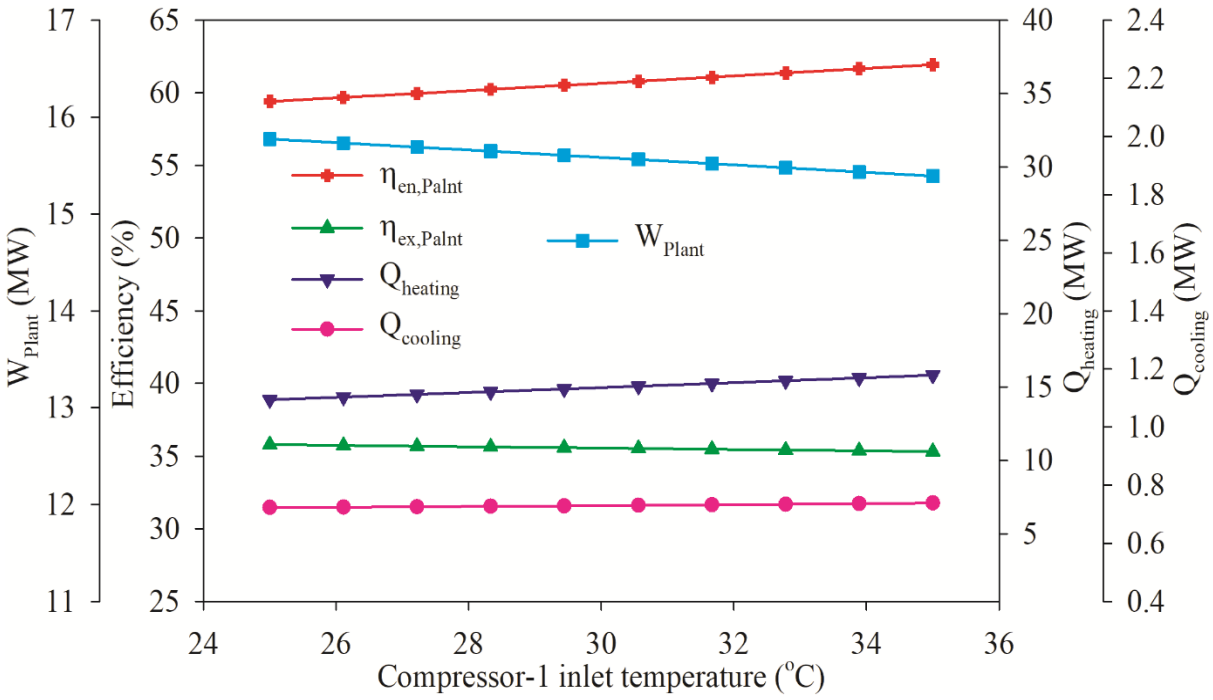

Figure 5.27 Effect of the compressor-1 input temperature on the plant performance

5.3.8. Effect of variation in pinch temperature difference in the HRVG

Figure 5.28 reveals the influence of the pinch temperature of HRVG on the output of the plant. It is evident that the plant's performance decreased as the temperature got closer to the pinch point. It was described as the pinch temperature increased, the temperature available to the bottoming cycles decreased, which means the pressure of the circulating fluid in the bottoming cycle increased, which leads to the reduction in the mass rate of the system. Consequently, the performance of the system decreased with pinch temperature. The reduction in the energy efficiency is faster than the exergy efficiency of the plant. Energy efficiency exergy efficiency, and network production decreased from 62 % to 59.32%, 35.7% to 35.41%, and 15586 kW to 15583 kW, respectively, as the pinch temperature increased from 5 ℃ to 15 ℃ respectively. However, the heating and cooling effect decreased from 15625 kW to 14318 kW and 761.5 kW to 697.3 kW, respectively, with a corresponding increase in pinch temperature of 5 ℃ to 15 ℃.

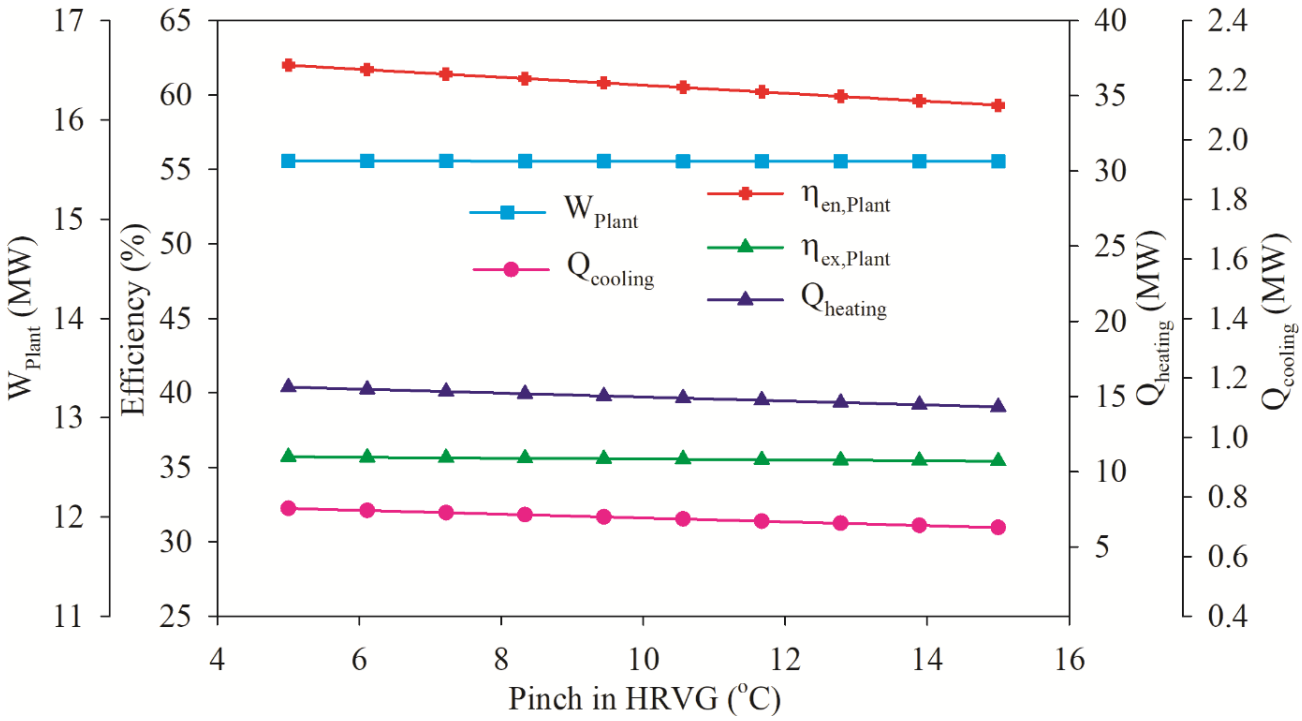

Figure 5.28 Effect of the HRVG pinch on the output of the plant

5.3.9. Effect of variation in entertainment ratio

The effect of the entertainment ratio on the performances has been discussed in Figure 5.29. The performance of the plant decreased with the entertainment ratio. As this ratio increased, the mass flow rate in the ERS circuit decreased, which led to a lower heating and cooling effect. As a result, the exergy and energy efficiency decreased. However, decrement in the energy efficiency is slower than the exergy efficiency. This is due to the faster rate of decrement in the heating and cooling effect, which contributed much to the efficiency of the plant. The energy, exergy efficiency, and network production all declined when the entertainment ratio rose from 1.5 to 4, going from 68.63% to 58.67%, 35.91% to 35.46%, and 15222 kW to 15675 kW, respectively. However, the heating and cooling loads decreased from 18709 kW to 14301 kW and 1459 kW to 547.1 kW, respectively, as the entertainment ratio rose from 1.5 to 4. It's observable this ratio much affected the cascaded ejector-VCR system rather than the topping cycle performance.

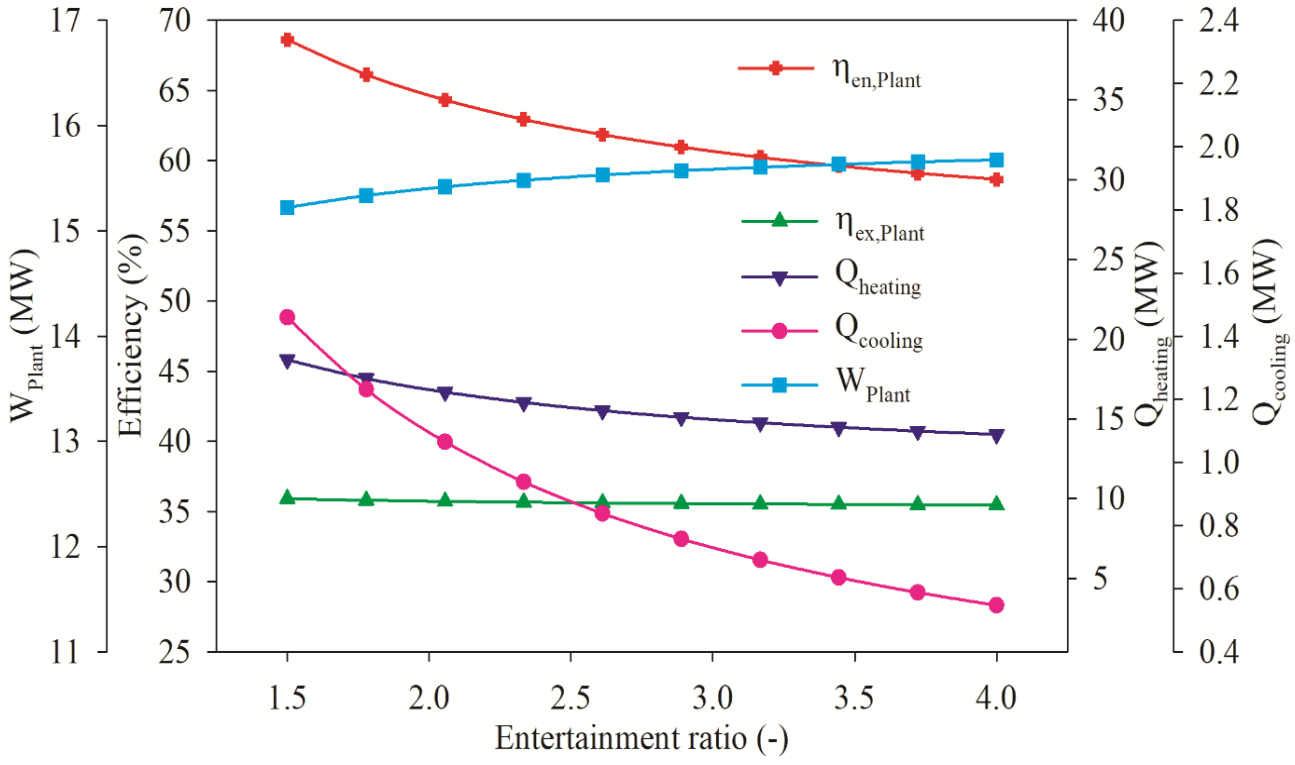

Figure 5.29 Effect of the Entertainment ratio on performance of the plant

5.3.10. Effect of variation in cascade condenser temperature

Figure 5.30 shows the influence of the cascade condenser temperature on the output of the plant. The energy and exergy efficiency of the system increases from 59.88 to 62.99% and 35.52% to 35.63%, respectively, as the CC temperature varies within ranges from -15 °C to 5 °C. However, the network output declines from 15612 kW to 15491 kW, respectively. As the CC temperature increases, the compressor work in the VCR system increases; consequently, the net work output from the system decreases. However, CC temperature works as the evaporator temperature in the ERS system. Therefore, the increase in this temperature mass rate of the operating fluid in the ERS circuit increases, which leads to the increment in the cooling and heating loads. Therefore, the combined effect improves the total energy output from the proposed plant. Therefore the energy efficiency increased with the CC temperature. However, the exergy efficiency improvement rate is slower than the energy efficiency. The heating and cooling effects increased from 14570 kW to 16175 kW and 697.5 kW to 818.1 kW, respectively, as the CC temperature improved from -15°Cto 5 °C.

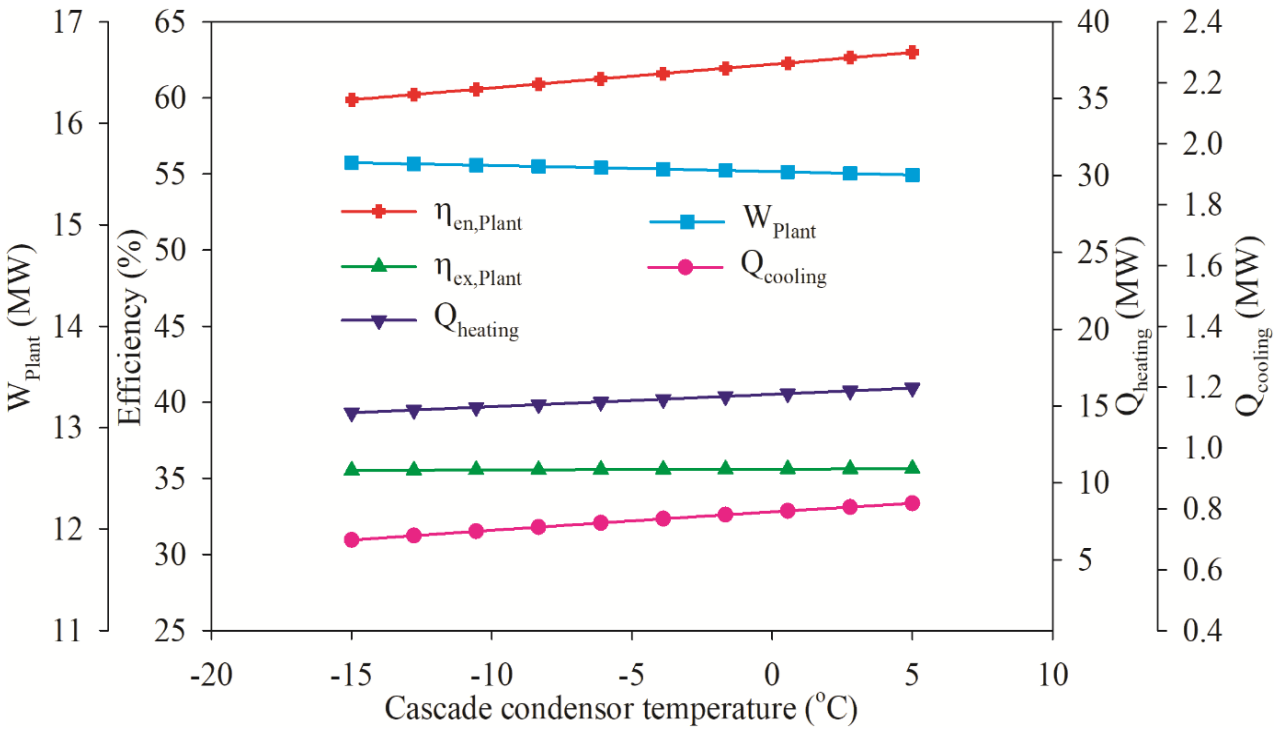

Figure 5.30 Effect of temperature of cascade condenser on plant performance

5.3.11 Effect of variation in evaporator temperature

The plant's performance varies with the evaporator temperature, as illustrated in Figure 5.31. The temperature of the evaporator boosted the plant's overall exergy, energy, and cooling effects. This is due to the reduction in the compressor-2 work input that leads to a slight improvement in the network output from the plant. Therefore the efficiencies increased with the evaporator temperature partially. However, evaporator temperature has no impact on the heating loads of the plant. Because the heating load is obtained from the condenser of the ORC-ERS system. The exergy, energy efficiency and power output raised from 59.91% to 61.37% and 35.10% to 35.85% and 15390kW to 15738kW, respectively, when evaporator temperature enhanced from -50 °C to -20°C respectively. However, cooling loads increased from 535.30kW to 912.4 kW respectively when the evaporator temperature rose from -50 °C to -20°C respectively.

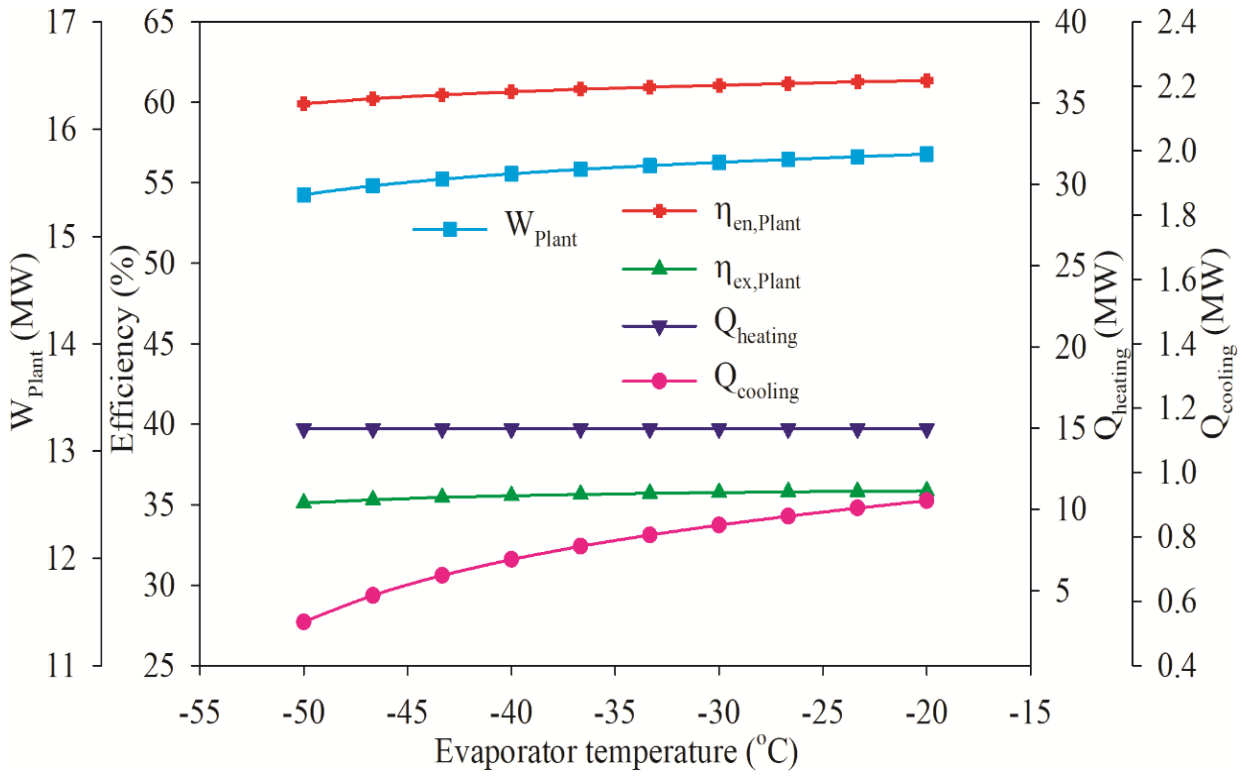

Figure 5.31 Plant performance variations with evaporator temperature

5.4. Combined Rankine-absorption power and refrigeration cycle with heating process integrated system

5.4.1. Validation of the proposed system

A simulation program for the combined power and absorption cooling system was created using the EES software based on the studies mentioned above. The obtained findings of the current model were compared to the outcomes of Mohtaram et al.'s integrated power and cooling cycle [208] that employed binary ammonia-water mixtures in the operating fluid. Comparing these results with those from the most recent model results reveals very strong agreement, as shown in Table 5.9.

Table 5.9 Validation of the computed results

Parameters	Comparison for binary ammonia-water mixture	
	Current work	Mohtaram et al. [208]
(a) Inputs		
Heat source inlet temperature (K)	573.15	573.15
Turbine inlet temperature (K)	558.15	558.15
Evaporator temperature (K)	248.15	248.15
(b) Results		
Turbine work (kW)	616.693	614.3
Pump work (kW)	5.971	2.774
Heat rejection in absorber (kW)	3244.35	3241
Heat rejection in condenser (kW)	458.59	458.59
Cooling effect (kW)	224.947	225.5
Heat inlet in boiler (kW)	2605.47	2612
Heat inlet in super heater (kW)	236.4	232.1
Heat exchanger heat input (kW)	1272.6	1282
power production (kW)	610.722	614.3
Net power and Refrigeration output (kW)	835.669	839.8
Heat input (kW)	4090.81	4091.82
Inlet exergy (kW)	1846.34	1846.34
Energy efficiency (%)	20.25	20.35
Exergy efficiency (%)	35.56	35.68

5.4.2. Simulation results of combined cycle

Heat sources such as gas turbine exhaust [209], solar energy [71], geothermal energy [210], or other readily available energy sources can be used to heat the proposed combined cycle. This work utilizes the waste heat from the outlet of fluid streams, consisting of 96.41% N2, 3.59% O2, 0.23% H2O, and 0.02% NO + NO2, as the heat source for the operation of the suggested system. The primary hypotheses are outlined in Table 3.4. Each state of the combined cycle's thermodynamic properties is listed in Tables 5.10 and 5.11, respectively [211]. Table 5.12 displays the outcomes of the thermal modelling as referenced in [212]. Table 5.13 illustrates the distribution of exergy and losses in each component of the combined cycle, with reference to [213]. The simulation is executed utilizing the EES program.

Parametric assessments are employed to analyze the impact of many factors on the cycle's outcomes, like ambient temperature, heat source temperature, inlet temperature, turbine pressure, cooling temperature, and ammonia mass fraction. When an input variable is being investigated, at the same time other variables are held constant. The basic settings are displayed in Table 3.4 [214].

Table 5.10 obtained outcomes from the thermodynamic investigation under the specified operating parameters

State	Temperature (K)	Pressure (bar)	Dryness	Enthalpy (kJ/kg)	Entropy (kJ/kgK)	Mass flow rate (kg/s)	Mass fraction (x)
1	298.15	25	0	118.127	0.4141	0.193084	0.9999
2	245.15	1.1941	0.17169	118.127	0.5373	0.193084	0.9999
3	268.15	1.1941	1	1283.15	5.2835	0.193084	0.9999
4	298.15	1.1941	0	-96.75	0.2818	1.46725	0.34
5	298.57	25	0	-92.68	0.2811	1.46725	0.34
6	432.24	25	0.17575	763.25	2.5541	1.46725	0.34
7	488.5	25	1	2538	6.202	1.27416	0.24
8	558.15	25	1	2745.5	6.537	1.27416	0.24
9	369.25	1.1941	0.93029	2240.41	6.8055	1.27416	0.24
10	334.69	25	1	1305.72	4.0322	0.386168	0.9999

11	298.15	25	0	118.127	0.4141	0.193084	0.9999
12	486.5	25	1	2539.24	6.2083	0.026106	0.24
13	432.4	25	0	541.8	1.96343	1.30027	0.24

Table 5.11 Heat source fluid simulation results

Molar composition				Mass flow rate (kg/s)	Entropy (kJ/kg K)	Enthalpy (kJ/kg)	Temperature (K)	State
N_2	O_2	H_2O	$NO + NO_2$					
0.9616	0.00359	0.0023	0.0002	20	7.41566	609.674	573.15	14
0.9616	0.00359	0.0023	0.0002	20	7.39417	597.473	562.398	15
0.9616	0.00359	0.0023	0.0002	20	7.13573	467.644	446.048	16
0.9616	0.00359	0.0023	0.0002	20	6.98558	405.083	388.678	17

Table 5.12 Performance of CCHP system (Each value is expressed in kW)

Turbine output work	616.693
Pump input work	5.971
Heat absorbed by the absorber	3244.35
Heat absorbed by the condenser	458.59
Cooling effect	224.947
Heat extracted in boiler	2605.47
Heat extracted in super heater	236.4
Heat extracted in heat exchanger	1272.6
Net power production	610.722
Net power and cooling effect	835.669
Input temperature	4090.81
Input exergy	1846.34
Energy efficiency (%)	20.25
Exergy efficiency (%)	35.56

Table 5.13 Exergy input, output, and losses

		Amount (kW)	Percentage (%)
Exergy Input	Super heater	1846.34	100
Exergy Output	Net Power	610.722	33.077
	Refrigeration	224.947	12.132
Exergy	Super heater	69.259	3.751
Destruction	Boiler	101.405	5.492
	Heat Exchanger	174.669	9.46
	Rectifier	36.277	1.96
	Condenser	47.7614	2.586
	Turbine	87.16	4.72
	Absorber	64.448	3.49
	Throttle Valve	16.116	0.872
	Evaporator	3.699	0.2
	Pump	11.6416	0.63
	Heat Exchanger Exhaust	398.235	21.63

A parametric evaluation is also done to check the effects of different variables on the power plant performance. The variation has been taken keeping constant other parameters listed in Table 1. The effects of the parameters were discussed one by one in the rest part of this section.

5.4.3. Effects of heat source temperature (T_{14})

From Figure 5.33, it can be observed that the power production increases as the heat source input temperature increases. This occurs as a result of the heat source's increased temperature raising the turbine's input temperature. Simultaneously, it will lead to an improvement in the rate of steam flow, leading in a higher overall power production. Furthermore, reducing the ammonia concentrations in the basic solution causes a rise in net power production. This is because a reduction in power output is caused by the ammonia in the mixture that passes through the turbine, as previously explained in prior research [215].

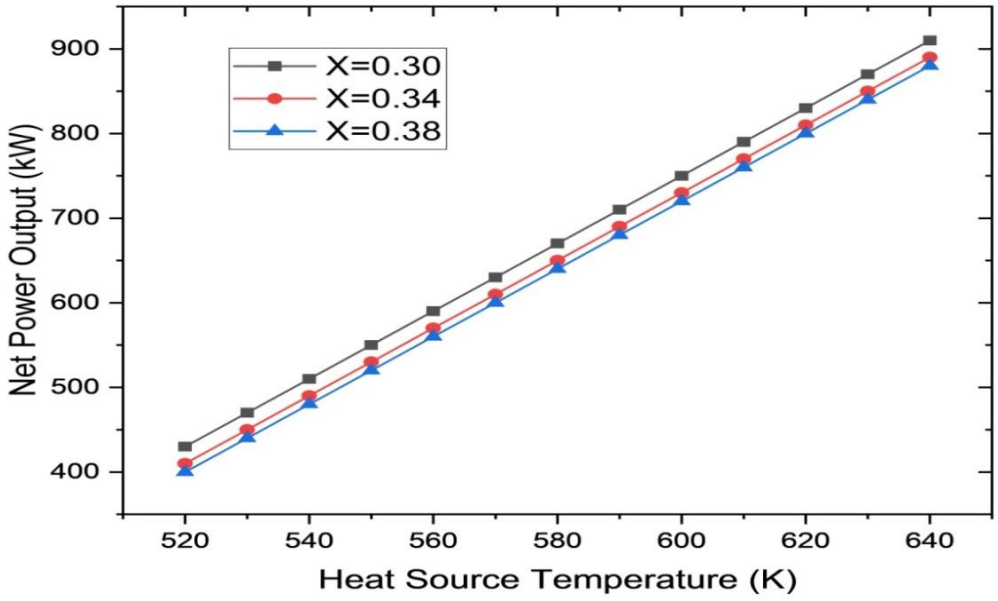

Figure 5.32Impact of heat source temperature on net power generation at various ammonia concentrations

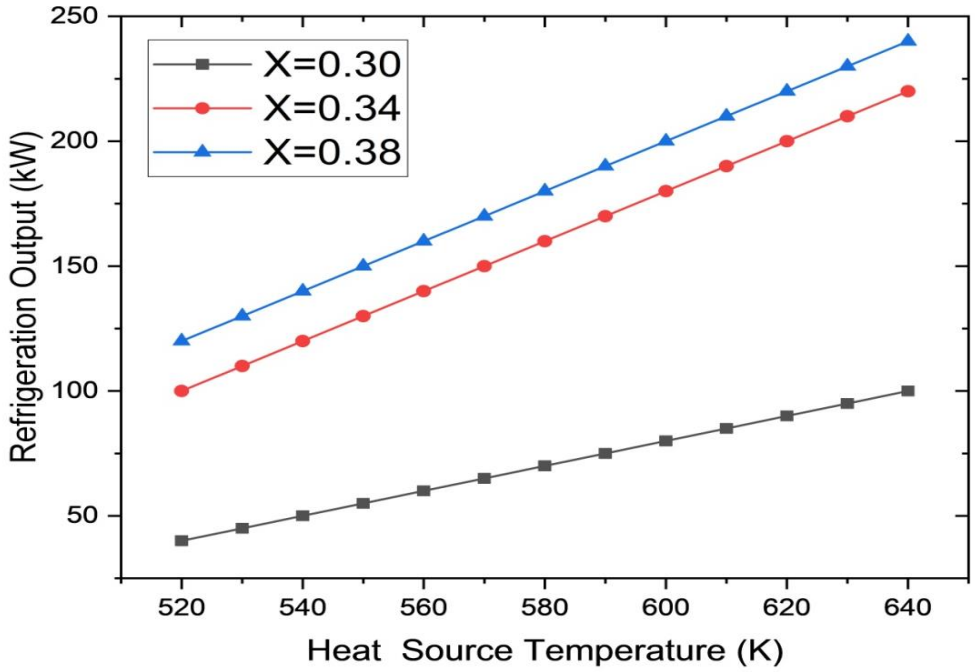

Figure 5.33Impact of heat source temperature on refrigeration output for various ammonia concentrations

Figure 5.34 illustrates how different heat source temperatures impact the refrigeration output when the ammonia concentrations in the basic solution are adjusted. The relationship between the refrigeration output and the heat source temperature is clearly evident since a temperature rise from the heat source causes a rise in the refrigeration output. The input temperature from the evaporator stays constant despite variations in the heat source's temperature. Nevertheless, elevating the heat source's temperature causes the evaporator's mass flow rate to increase. Therefore, it might be inferred that an increase in ammonia concentrations in a basic solution will lead to a higher refrigeration output, as a result of the greater amount of ammonia concentration passing through the evaporator. This indicates that an increased quantity of ammonia will lead to a greater cooling effect.

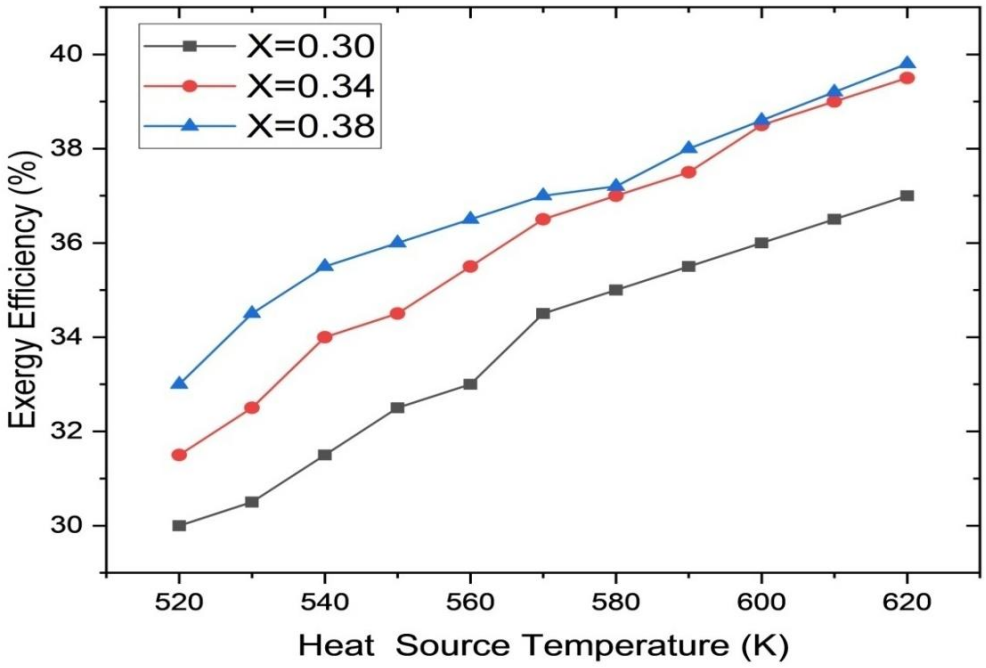

Figure 5.34Impact of heat source temperature on exergy efficiency for various ammonia concentrations

Figure 5.35 illustrates how the exergy efficiency is influenced by varying heat source temperatures and variable concentrations of ammonia in the basic solution. From the graphic, it is evident that as the heat source's temperature rises, the system's exergy efficiency rises as well. An elevated heat source temperature improves both the power production and the rate of cooling.

Thus, according to the given correlation for exergy efficiency, its resultant efficiency is enhanced. Furthermore, a greater concentration of ammonia in the dilution solution results in increased energy efficiency, as a larger quantity of ammonia flows through the evaporator. Ultimately, this will lead to an increased refrigeration output and a decreased net power output.

5.4.4. Effect of turbine inlet pressure (P_4)

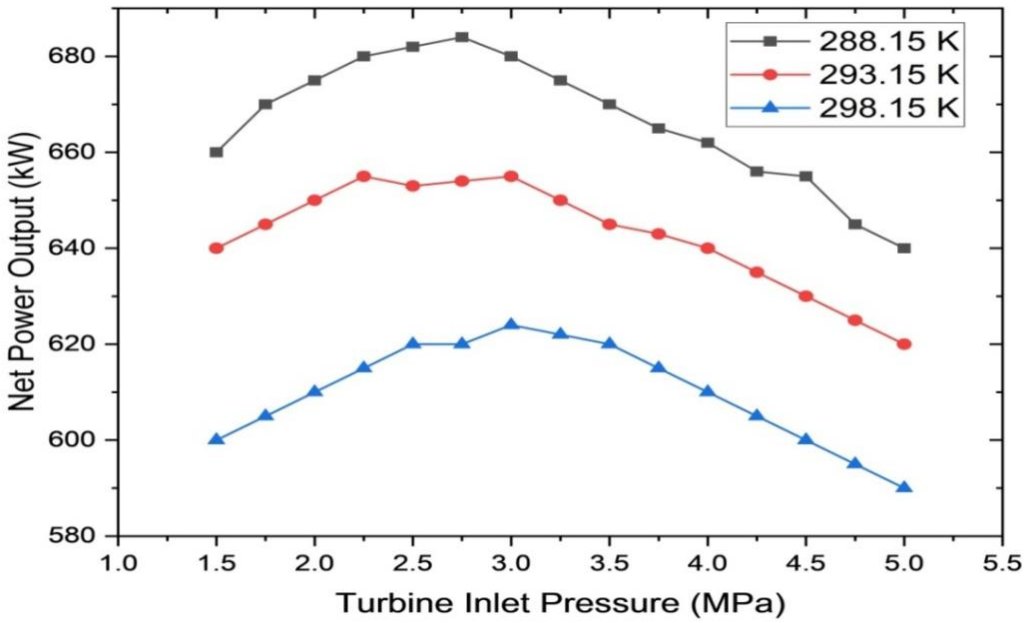

Figure 5.35Influence of turbine inlet pressure on net power production at varying ambient temperatures

As depicted in Figure 5.36, the net power production first rises as the turbine inlet pressure increases but subsequently decreases. The primary cause for the early rise in power production is the lowering of enthalpy in the turbine, resulting in rises in pressure ratio. As the process progresses and the pressure ratio increases further, the additional increase in the pressure ratio does not provide enough enthalpy to counteract the reduction in vapour flow rate. Consequently, the overall power production is decreased. Moreover, when ambient temperature rises, net power output falls. This phenomenon occurs because the condensation temperature rises as it absorbs the surrounding temperature, leading to an increase in the turbine's back pressure. Hence, the rise in pressure upstream of the turbine causes the turbine's total power output to decrease as explained in reference [84].

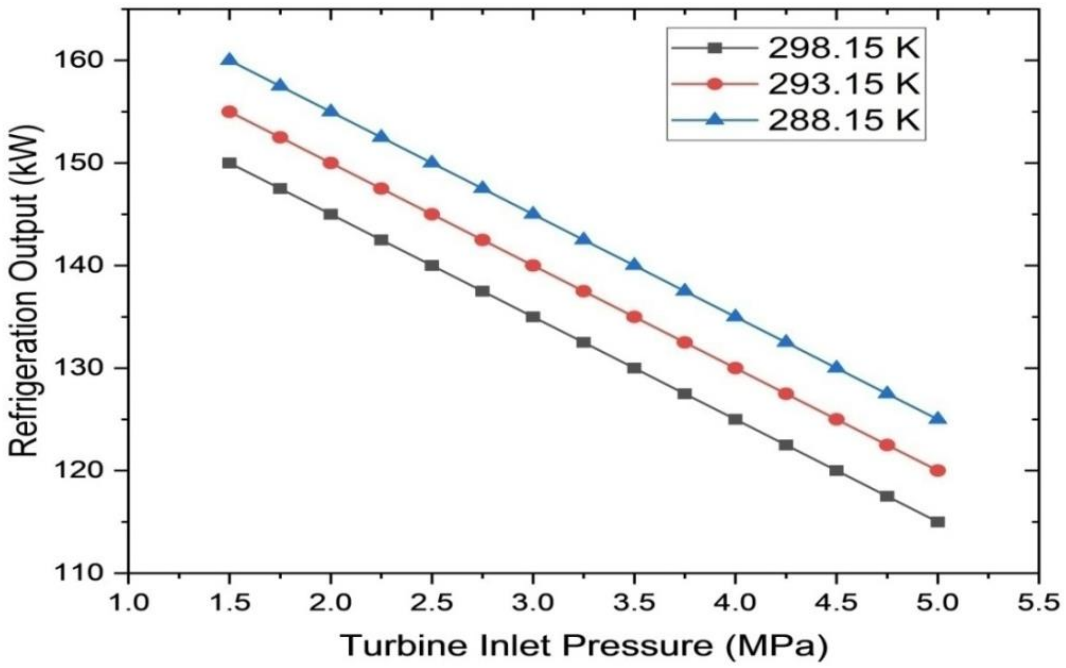

Figure 5.36Impact of turbine inlet pressure on refrigeration output at varying ambient temperatures

It's evident from Figure 5.37 that the refrigeration output decreases as the inlet pressure increases. The cause of this phenomenon is that increasing turbine inlet pressure decreases the pace at which mass flows through the evaporator. Put simply, a high inlet pressure in the turbine leads to a decrease in both the mass flow rate of the evaporator as well as the whole cycle mass flow rate. The refrigeration output is decreased when the ambient temperature increases. The intake pressure of the evaporator increases as the ambient temperature rises. The refrigeration output decreases as the evaporator's intake temperature rises.

A comparison of the exergy efficiency at various ambient temperatures with the turbine's input pressure is shown in Figure 5.38. It's clear from the diagram that when the turbine's input pressure rises, the exergy efficiency first rises but then drops. Moreover, when ambient temperature rises, exergy efficiency falls.

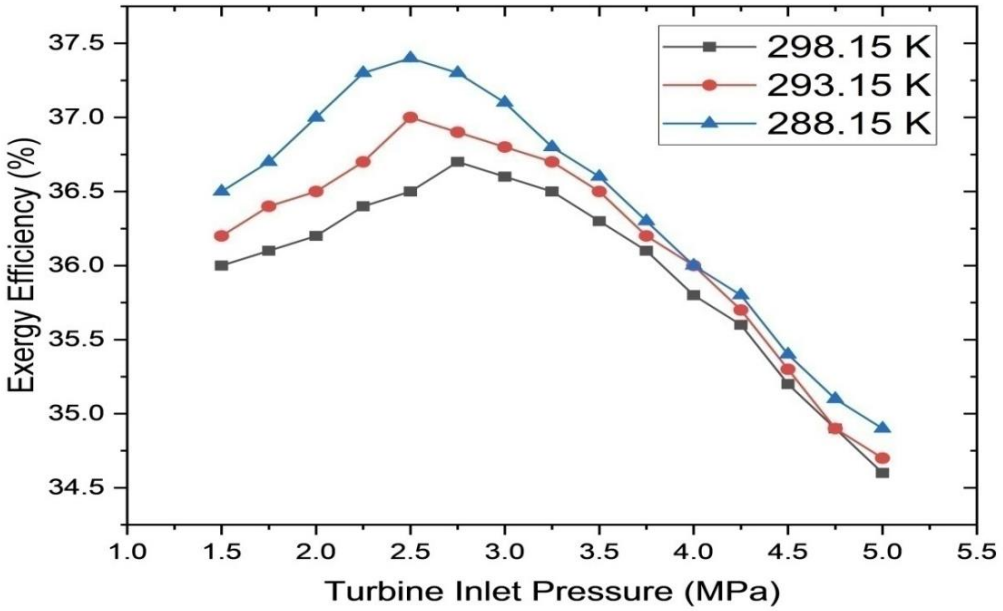

Figure 5.37 Effect of turbine inlet pressure on exergy efficiency for different environment temperatures.

5.4.5. Effect of refrigeration temperature (T_2)

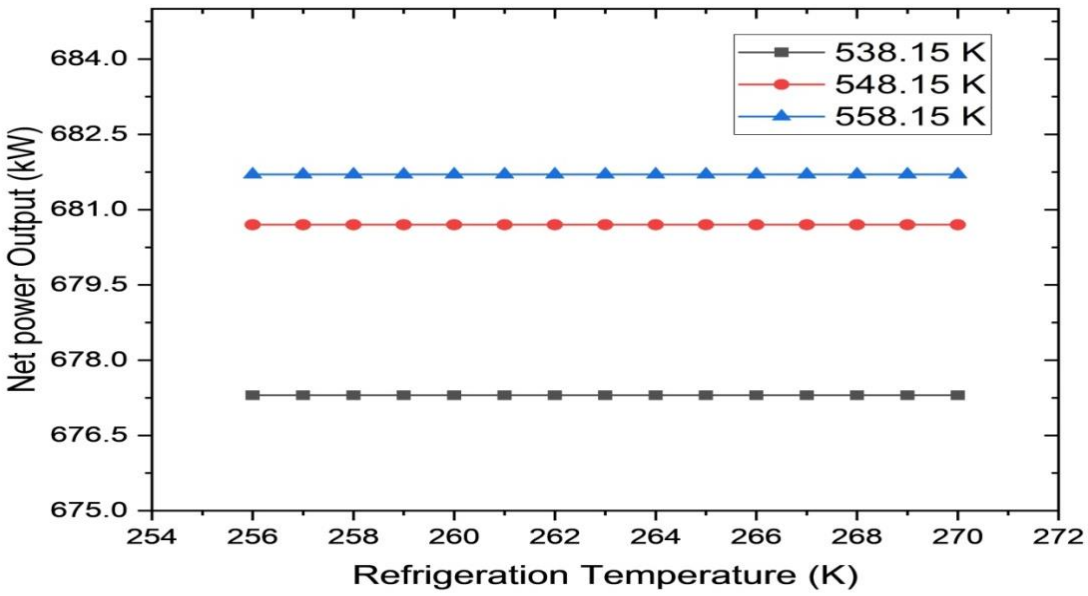

Figure 5.38Impact of refrigeration temperature on net power production at varying temperatures of turbine inlet

Figure 5.39 depicts the impact of the temperature of the refrigeration system on the net power generation at various turbine input temperatures. From the figure, it is evident that the net output power remains unchanged as the cooling temperature increases. A higher net output power is achieved when the turbine operates at higher intake temperatures. Modifying the temperature of the refrigeration does not impact the inlet and outlet state of the turbine, therefore keeping the power generation constant regardless of changes in refrigeration temperature. Previous research [211] has shown that increasing the input temperature of the turbine results in a larger power output, resulting in a higher net output power for the system.

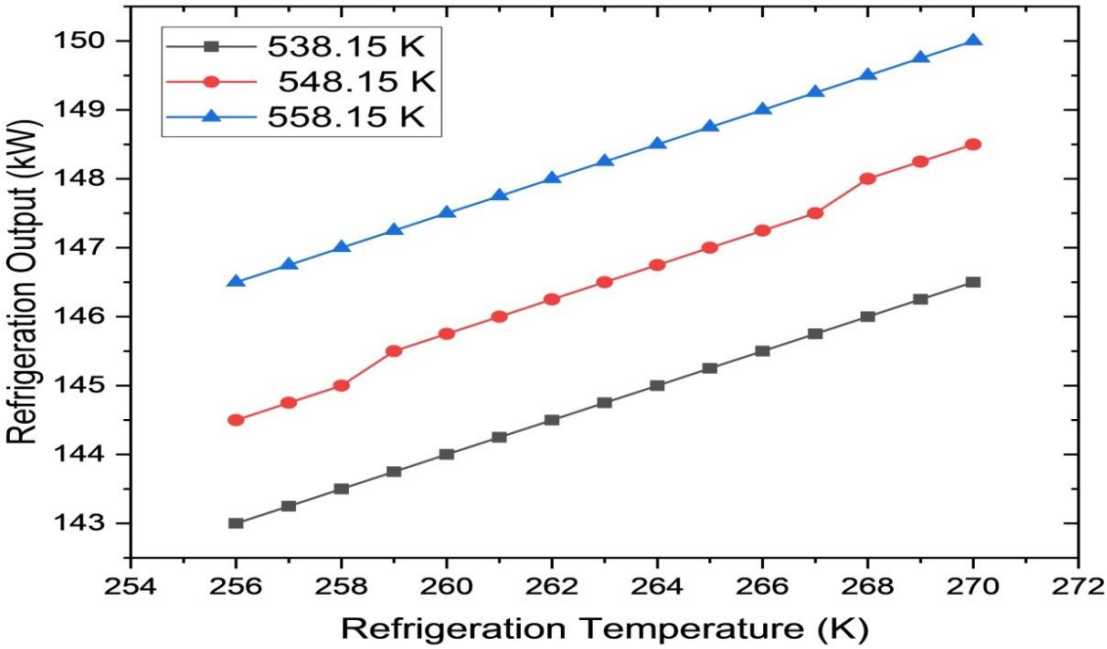

Figure 5.39Impact of refrigeration output temperature on various turbine inlet temperatures

Figure 5.40 illustrates how the refrigeration output is influenced by the refrigeration temperature when the turbine's inlet temperatures are adjusted. When the temperature in the refrigerator is raised, the output of the refrigeration system increases accordingly. A greater input temperature of the turbine leads to a decrease in cooling effect. This occurs as soon as the cooling temperature is exceptionally low and it is challenging to achieve a high refrigeration output. Essentially, In case we reduce the temperature for refrigeration, it’s going to be challenging to really achieve that temperature for cooling purposes. The reason for this is the rapid evaporation of ammonia in the evaporator, together with the surrounding temperature.

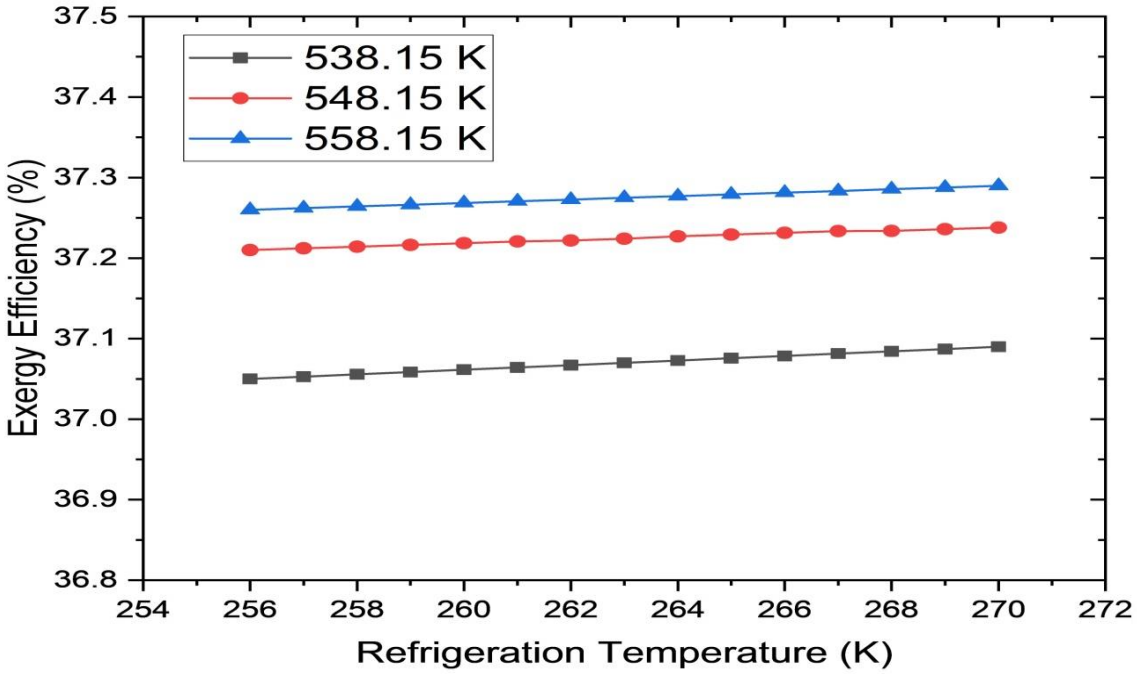

Figure 5.40Influence of refrigeration temperature on exergy efficiency at varying turbine input temperatures

Figure 5.41 illustrates how the efficiency of the exergy is influenced by the temperature at which the refrigeration process occurs while considering different turbine intake temperatures. This is apparent from the observation that the exergy efficiency decreases as the refrigeration temperature increases. Cooling occurs at a faster rate when the refrigeration temperature is raised. By taking into account the exergy evaluation, the exergy efficiency is enhanced, and a higher turbine inlet temperature leads to a greater thermal efficiency since it results in a larger power output from the turbine.

5.4.6. Distribution of input heat source energy among different components of the integrated system

Figure 5.42 displays how the system's components distributed the exergy associated with the heat source's energy input. It is noted that out of 100% input energy, approximately 33.077% and 12.132 % of the above-mentioned energy are converted into power and refrigeration production, respectively, while the leftover energy is lost to the environment as a result of entropy generation in the integrated system's components. The amount of energy that the condenser's cooling water dissipates is minimal. It has been noted that the heat exchanger exhaust produces the highest exergy loss, which is 21.63%. The percentage of exergy destroyed across the heat exchanger, boiler, turbine, superheater, absorber, condenser, and rectifier is 9.46%, 5.492 %, 4.72 %, 3.751 %, 3.48%, 2.586% and 1.96%, respectively. The percentage of exergy destruction in the remaining parts of the cycle was below one.

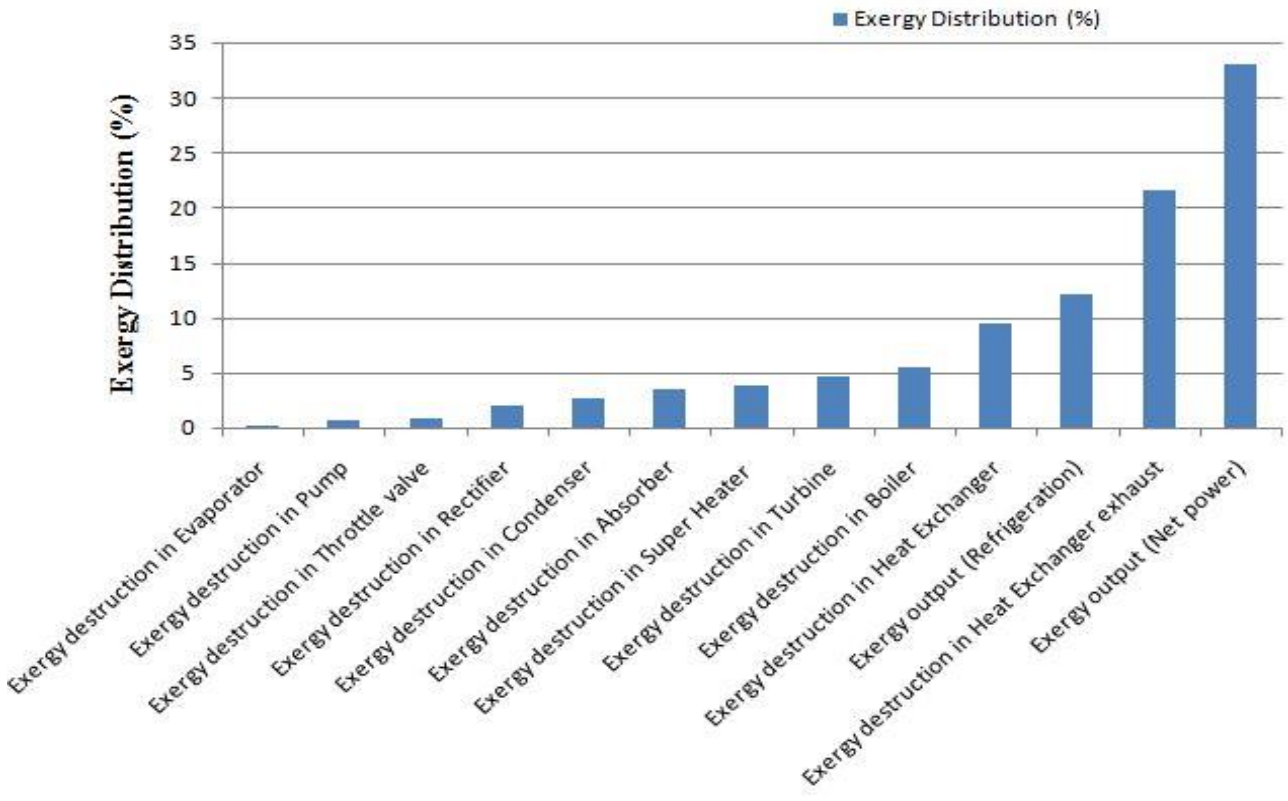

Figure 5.41Distribution of input heat source energy of the integrated combined cycle

The second law analysis's results, which were used to determine the component's local irreversibility, show that the heat exchanger and boiler require more attention because they were been identified as the primary sources of losses within the system [208]. The increased amount of exergetic loss through the heat exchanger and boiler can be attributed to the exchange of heat across a limited difference in temperature. The exergy destruction in the ejector is of greater amount because of the friction losses and irreversibility in the expansion process through a different section of the nozzle [216].

It may be asserted that various parameters have diverse influences on the efficiency, refrigeration effect and power production of the suggested cycle. Certain parameters in this cycle have a positive impact on efficiency, while others have a negative impact. Thus, based on the findings of this study, future investigations can enhance the efficiency of this cycle. The major variables chosen for investigation are the turbine's inlet pressure and temperature, as well as the ammonia concentration. It is believed that other parameters, including inlet variables, do not change.

These results are roughly in line with the findings derived from a comparable cycle by Mohtaram together with his associates (reference). The disparities between the current findings and [208] are negligible. The differences arise from the utilization of equations to compute the thermodynamic characteristics of an ammonia-water mixture.

5.5. Combined power, heating and cooling integrated system driven by Low-temperature heat source using various eco-friendly refrigerants

The current study illustrates the parametric study of ORC and the refrigeration cycle integrated with the fluid at low temperatures using eco-friendly refrigerants as the operating fluid. This cycle combines the ejector refrigeration system and the ORC. To analyze various operating fluids at various functional states, thermodynamic investigations were carried out. In addition, the influence of the most important operating conditions such as the evaporator temperature, heat source temperature and turbine input temperature was observed on the refrigeration output, exergy efficiency, entrainment ratio, thermal efficiency, total exergy destruction and distribution of exergy in different elements of the given system using different environmental friendly refrigerants (R-123, R-124, R-141b, R-290, R-134a, R-152a).

5.5.1. Validation of the proposed system

A simulation program for the combined power and ejector cooling cycle was created using the EES software based on the studies mentioned above [121]. The obtained findings of the current model were compared to the outcomes of reference [129], the suggested combined cycle, which used R-123 as the operating fluid. Comparing these results with those from the most recent model results reveals very strong agreement, as displayed in Table 5.14.

Table 5.14 Validation of computed results of current work

Parameters	Comparison for R-123	
	Present work	Ref. [129]
(a) Inputs		
Heat source inlet temperature (K)	413	413
Condenser temperature (K)	293	293
Evaporator temperature (K)	263	263
(b) Results		
Total heat in HRVG (kJ/kg)	1262	1246.96
Ejector's entrainment ratio	0.394	0.389
Pump input work (kJ/kg)	3.48	3.45
Turbine output work (kJ/kg)	116.18	114.14

Net Power output (kJ/kg)	113.53	110.69
Refrigeration output (kJ/kg)	62.34	60.44
$\dot{W}_{net}/\dot{Q}_{in}$	8.56	8.88
$\dot{Q}_E/\dot{Q}_{in}$	4.68	4.85
Refrigeration/Power ratio	0.36	0.35
Thermal efficiency (%)	13.67	13.72
Exergy efficiency (%)	22.75	22.2

5.5.2. Performance comparison of the proposed combined cycle using six different refrigerants.

For the six distinct refrigerants and input parameters specified in Table 3.5, the values of thermodynamic attributes like pressure, temperature, enthalpy and mass rate were determined for every stated point of Figure 3.5.The six different working fluids' performance is compared in Table 5.15 with the help of the above-mentioned thermodynamic properties.

Table 5.15 The proposed combined cycle performance using six different refrigerants

Variable	Unit	R-123	R-124	R-141b	R-290	R-134a	R-152a
μ	-	0.1261	0.1592	0.1023	0.1247	0.1436	0.1238
$\dot{m}$	kgs^{-1}	2.037	4.053	1.642	4.235	6.405	4.562
$\dot{E}D_{HRVG}$	kW	16.45	37.64	13.32	47.84	92.62	96.54
$\dot{E}D_{T}$	kW	9.546	9.435	9.74	9.68	10.86	13.64
$\dot{E}D_{EJE}$	kW	10.384	14.73	10.42	10.27	18.78	18.52
$\dot{E}D_{Reg}$	kW	1.423	9.123	1.344	11.416	40.72	27.46
$\dot{E}D_{C}$	kW	6.304	9.86	6.324	7.68	14.23	14.32
$\dot{E}D_{P}$	kW	0.1623	0.213	0.1604	0.1468	0.0351	0.1065
$\dot{E}D_{EV}$	kW	0.2536	0.34	0.2242	0.4247	0.6201	0.6271
$\dot{E}D_{E}$	kW	0.2351	0.3263	0.0713	0.2723	0.4715	0.4423
$\dot{W}_{T}$	kW	52.84	54.78	57.46	56.75	61.75	79.38
$\dot{W}_{P}$	kW	0.986	1.524	0.9547	1.81	0.2964	0.7846
$\dot{W}_{net}$	kW	51.854	53.256	56.5053	54.94	61.453	78.59
$\dot{Q}_{E}$	kW	20.52	21.43	22.42	37.47	24.85	31.72
$\dot{Q}_{in}$	kW	422.45	695.68	451.47	501.87	1305.87	1428.68
$\dot{E}_{E}$	kW	1.732	2.232	2.134	2.896	2.265	2.745
$\eta_{thermal}$	%	17.057	10.652	17.292	18.546	6.486	7.656
η_{exergy}	%	12.85	12.47	13.57	13.74	15.24	19.78

According to the aforementioned findings, the expansion valve and evaporator cause the least amount of exergy destruction for each working fluid, whereas HRVG and ejector cause the most. In terms of overall exergy destruction, R-134a and R-141b are the operating fluids that cause the greatest and least amounts of damage and R-134a is the most suitable working fluid [61]. The ejector's entrainment ratio ‘μ’ may be measured in all situations, and its maximum and minimum values are obtained for the refrigerants R-124 and R-141b, respectively. R-152a has the highest net power production, while R-123 produces the lowest. Additionally, R-290 has the largest combined cycle refrigeration output while R-123 has the lowest. Finally, the refrigerant R-290 has the best thermal efficiency, followed closely by R-141b and R-123, and has the lowest value for R-134a, while refrigerant R-152a has the maximum exergy efficiency, subsequently to R-134a, and possesses the lowest value for R-124 and R-123 respectively. R-152a (difluoroethane) has a higher exergy efficiency compared to R-123 (dichlorotrifluoroethane) primarily due to its lower molecular weight and better thermodynamic properties. R-152a has lower boiling and condensing temperatures, which can lead to higher energy efficiency in refrigeration systems. R-123 has a higher molecular weight and typically operates at higher temperatures, which can result in lower exergy efficiency compared to R-152a, the similar trends of results found by [128]. Additionally, R-123 is categorized as a chlorofluorocarbon (CFC), which has been discontinued due to its harmful effects on the ozone layer and replaced with more environmentally friendly alternatives. Additionally, R-152a has a lower GWP and ODP as compared to R-123, making it a more environmentally friendly option in many case studies in reference [217].

Parametric analysis

The following graphs illustrate how evaporator temperature, turbine input temperature and heat source fluid temperature at the constant evaporator, condenser and turbine inlet pressure affect refrigeration output, exergy efficiency, entrainment ratio, thermal efficiency, and total exergy destruction for different environmentally friendly refrigerants (R-290, R-152a, R-141b, R-134a, R-124, R-123).

5.5.3. Effect of variation in evaporator temperature (T_{12}=T_{13})

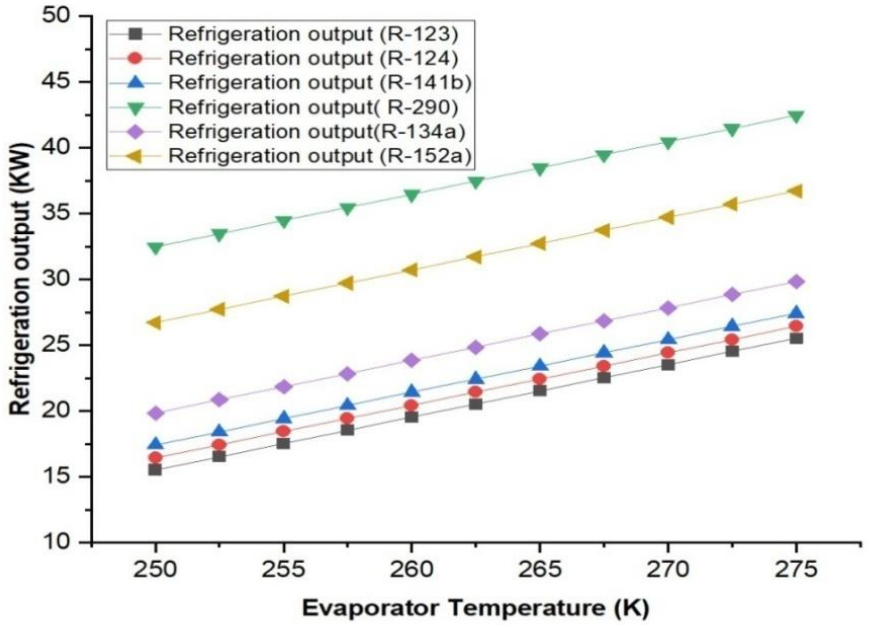

Figure 5.42Effect of the evaporator temperature on the refrigeration output

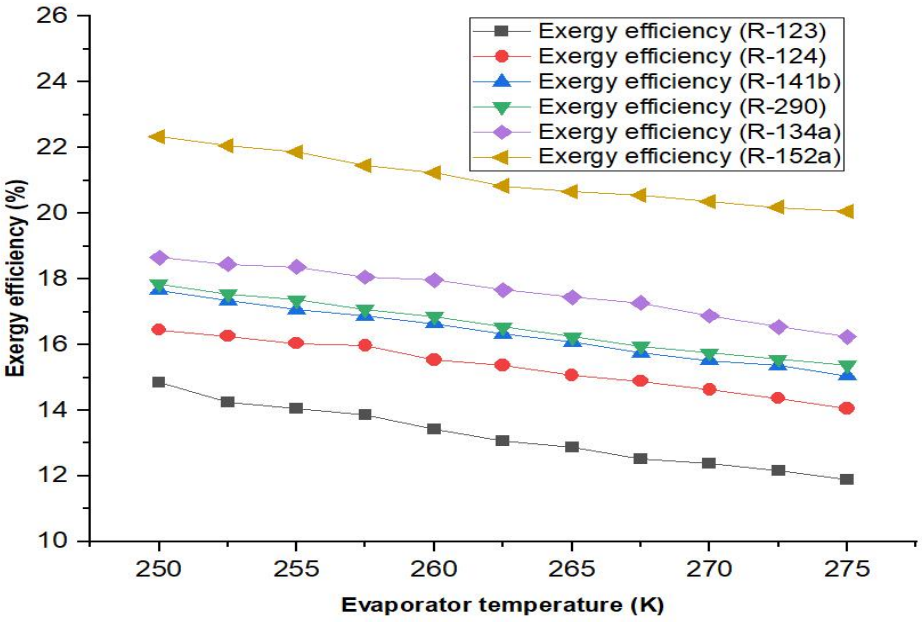

Figure 5.43Effect of the evaporator temperature on the exergy efficiency

Figure 5.43 illustrates how refrigeration output rises as evaporator temperature rises because primary flow pressure and mass flow rate remain constant while the mass rate of secondary flow rises as evaporator temperature rises. Correspondingly the refrigeration output rises. Additionally, it has been noted that R-290 produces more cooling effect than other eco-friendly refrigerants, whereas R-123 produces the least one [157].

Figure 5.44 demonstrates that as the evaporator temperature rises, exergy efficiency declines. The decrease in exergy output of refrigeration and the ejector's entrainment ratio are the primary causes of the decrease in exergy efficiency. Furthermore, it has been shown that out of all the refrigerants utilized, R-152a has the maximum exergy efficiency while R-123 has the lowest as discussed in reference [218].

According to the findings in Figure 5.45, as the evaporator temperature rises, the ejector's entrainment ratio falls for all operating fluids. Additionally, among all working fluids, R-124 exhibits the highest entrainment ratio and R-141b the lowest, as the same results were found by [128].

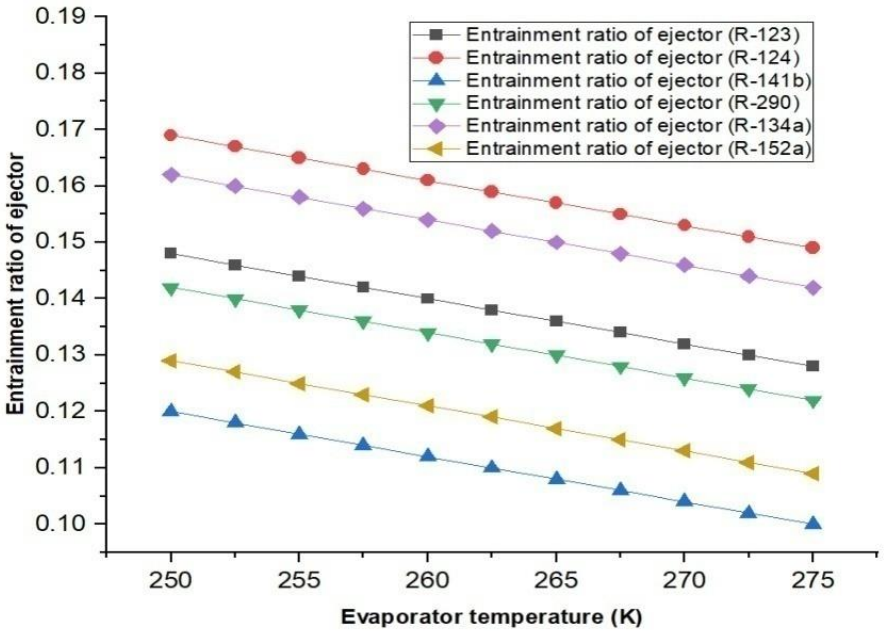

Figure 5.44Effect of the evaporator temperature on the ejector's entrainment ratio

5.5.4. Effect of variation in turbine inlet temperature (T4)

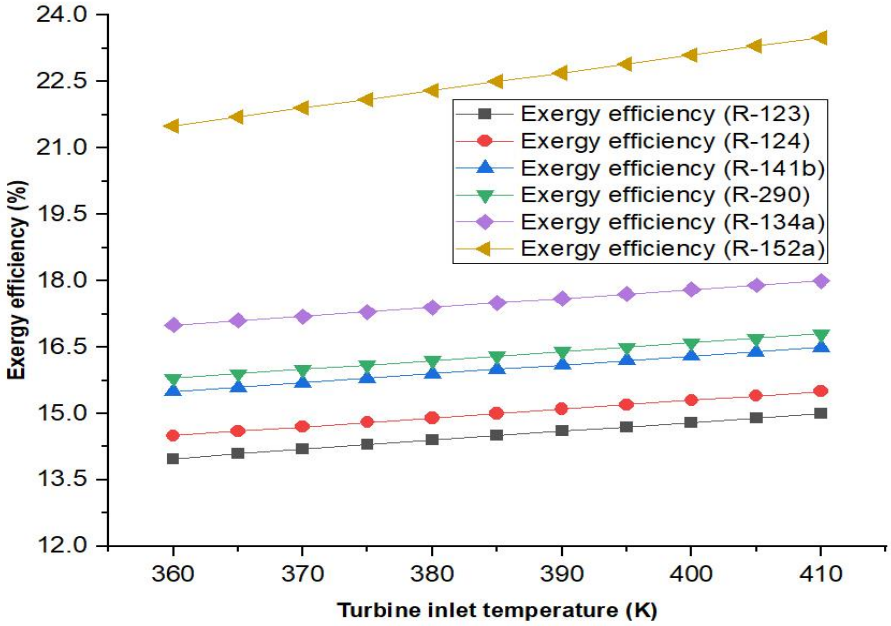

Figure 5.45Effect of the turbine inlet temperature on the exergy efficiency

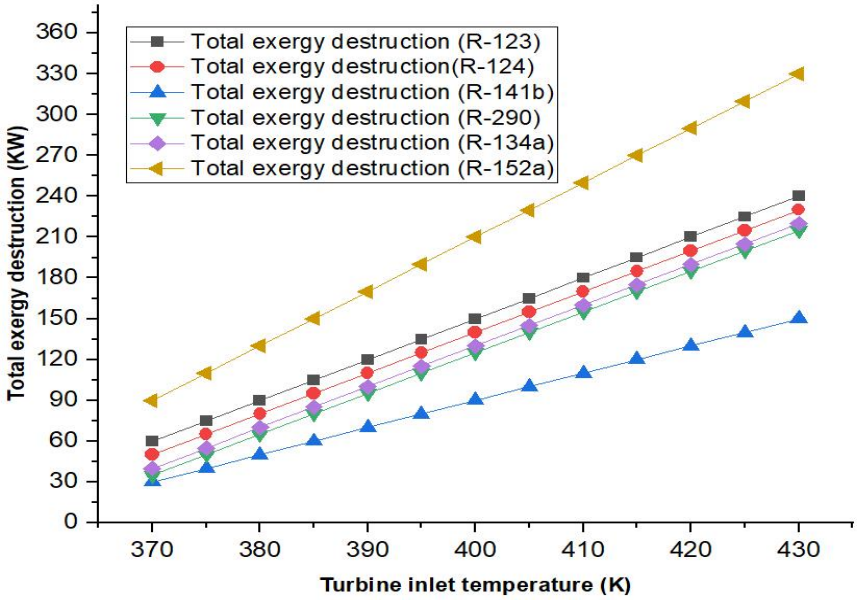

Figure 5.46 Influence of the turbine input temperature on the total exergy destruction

Figure 5.46 how the cycle's exergy efficiency improves in tandem with an increase in the turbine input temperature. The turbine input temperature will have an impact on the ejector entrainment ratio if the power-to-refrigeration ratio remains the same; this leads to an increase in the refrigeration output exergy [218].

Additionally, R-122 has the lowest exergy efficiency of all the refrigerants, whereas R-152a has the highest. In the same way, the cycle's total exergy destruction rises as the turbine input temperature does, as depicted in Figure 5.47. Furthermore, R-152a exhibits the most total exergy destruction in a cycle, while R-141b exhibits the lowest.

Figure 5.48 demonstrates that thermal efficiency also increases when the input temperature does. The entrainment ratio and power production both rise in accordance with the inlet temperature. Furthermore, among all refrigerants, R-290 has the best thermal efficiency and R-134a the lowest.

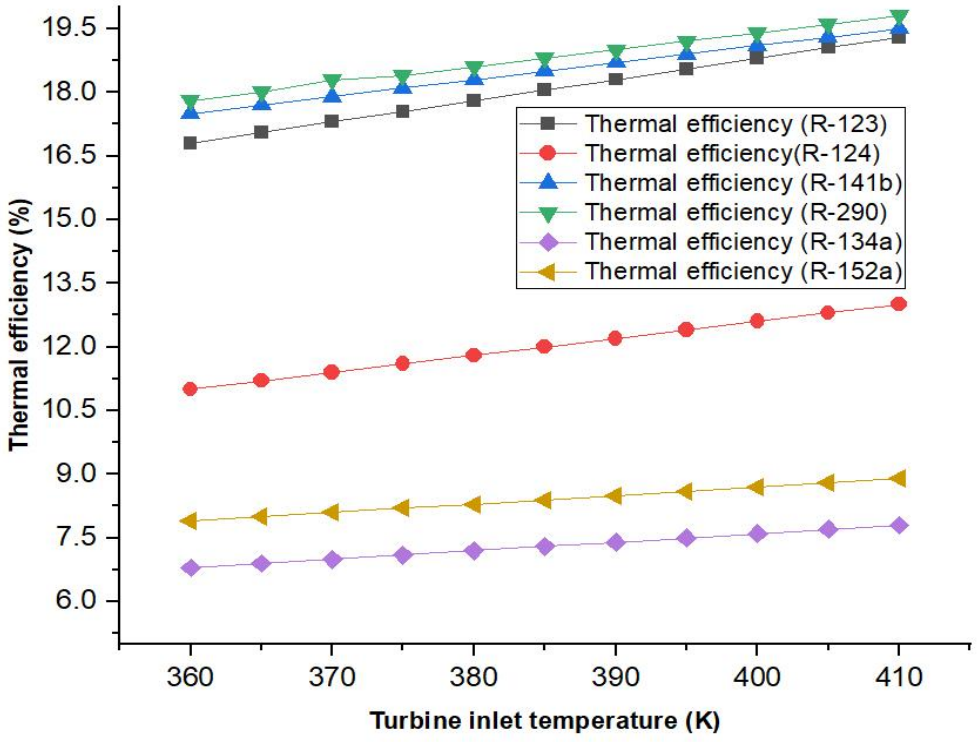

Figure 5.47 Influence of the turbine input temperature on the thermal efficiency

5.5.5. Effect of variation in heat source fluid temperature (T_{18})

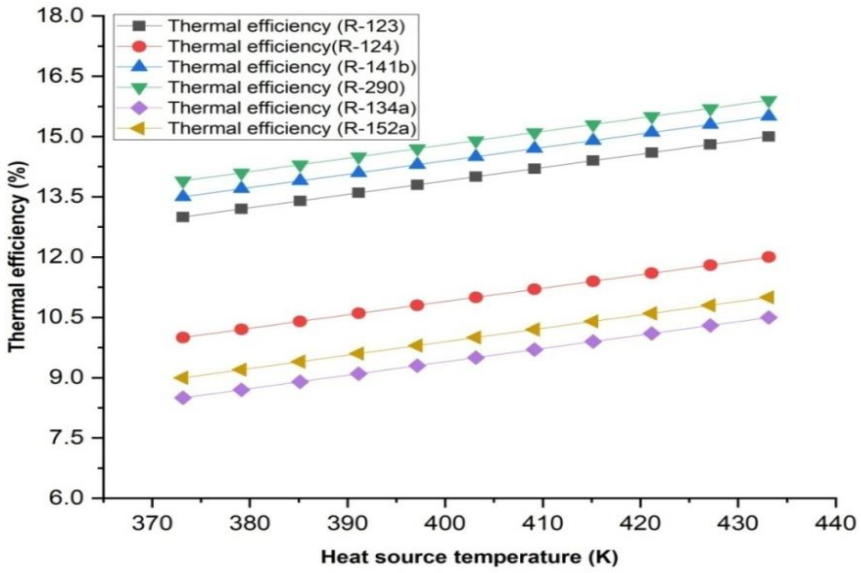

Figure 5.48 Influence of the heat source fluid temperature on the cycle's thermal efficiency

Figure 5.49 demonstrates how the rise in heat source fluid temperature leads to a rise in energy efficiency. As the temperature within the vapour generator rises, both the fluid rate across the turbine and the ejector's entrainment ratio increase as well. Additionally, it has been noted that among all refrigerants, R-290 produces the largest thermal efficiency, whereas R-134a produces the least already discussed in reference [128].

5.5.6. Distribution of input heat source energy among different components of a system

Figure 5.50 displays how the system's components distributed the exergy associated with the heat source's energy input. It is noted that out of 100% input energy, approximately 18.667% and 4.857% of the above-mentioned energy are converted into power and refrigeration production, respectively, while the leftover energy is lost to the environment as a result of entropy generation in the integrated system's components. The amount of energy that the condenser's cooling water dissipates is minimal. It has been noted that the HRVG exhaust experiences the highest exergy loss, which is 46.12%. The percentage of exergy destroyed across the HRVG, ejector, and condenser is 11.324%, 6.978% and 5.65% respectively. The percentage

of exergy destruction in the remaining parts of the cycle was below one. The second law analysis's results, which were used to determine the component's local irreversibility, show that the HRVG and ejector require more attention because they were been identified as the primary sources of losses within the system [71]. The increased amount of exergetic loss through the HRVG can be attributed to the exchange of heat across a limited difference in temperature. The exergy destruction in the ejector is greater because of the friction losses and irreversibility in the expansion process through a different section of the nozzle [185].

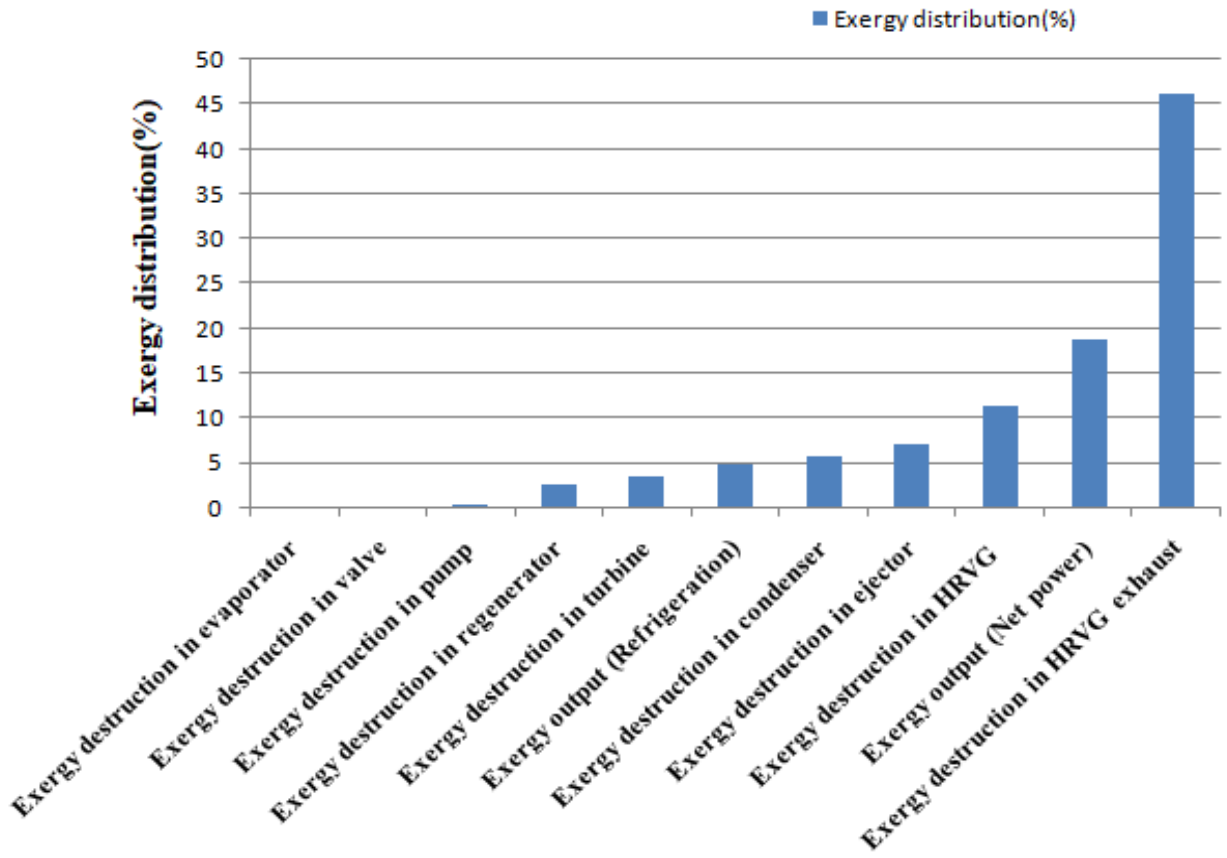

Figure 5.49 Distribution of input heat source energy of the integrated combined cycle

5.6 Comparisons of the proposed integrated systems

In conclusion, a comprehensive comparison of all the integrated systems considered was conducted, with the results summarized in Table 5.6. This analysis demonstrated that the SPT-based combined HBC and ORC system, integrated with the cascaded ERS-VCR cycle, exhibited superior performance compared to the other proposed systems. The findings also highlighted that integrating a cascaded cycle significantly enhances the overall system efficiency, underscoring the advantages of employing this configuration in optimizing performance.

Table 5.16 Comparisons of all the integrated systems considered

Parameter	Cycle	Reference	Proposed Model	Findings				
				η_{energy}	η_{exergy}	Power Output	Cooling Effect	Heating Effect
Sun's Apparent Temperature = 4500 K DNI = 850 W/m^2 HBC inlet Temperature = 800 ^{0}C η_{field} = 0.75 HC inlet Pressure = 2500 kPa η_{HT} = 0.9 OT inlet Temperature = 197.2 ^{0}C Evaporator Temperature = 10 ^{0}C Working Fluid – Isopentane	SPT-based combined HBC and ORC with an ejector refrigeration integrated system	[71, 74, 163, 195]	HBC-ORC-ERS integrated system	23.3 %	25.12 %	14998 kW	8.25 kW	60.52 kW
Sun's Apparent Temperature = 4500 K DNI = 850 W/m^2 HBC inlet Temperature = 850 ^{0}C η_{field} = 0.75 HC inlet Pressure = 2500 kPa	SPT-based combines HBC and ORC with a cascaded VAR- VCR integrated system	[71, 74, 115, 117]	HBC-ORC-VAR-VCR integrated system	28.82 %	39.53 %	14865 kW	110.83 kW	240.56 kW

η_{HT} = 0.9 CPR – 2.5 Absorber Temperature = 37 ^{0}C Condenser Temperature = 27 ^{0}C Working Fluid – R410a, LiBr-H_2O								
Sun's Apparent Temperature = 4500 K DNI = 850 W/m^2 T1 inlet Temperature = 850 ^{0}C η_{field} = 0.65 C1 inlet Pressure = 2500 kPa η_{T1} = 0.93 CPR – 2.5 ORC inlet Temperature = 197.4 ^{0}C Cascade Condenser Temperature = -10 ^{0}C Evaporator Temperature = -40 ^{0}C η_{nozzle} = 0.9, η_D = 0.95 Working Fluid – Isopentane, R410a	SPT-based combines HBC and ORC with a cascaded ERS - VCR integrated system	[71, 74, 123, 164]	HBC-ORC-ERS-VCR integrated system	60.66 %	35.55 %	15585 kW	730 kW	1967 kW
Inlet Temperature of turbine = 285 ^{0}C Inlet Pressure of turbine = 2.5 MPa $\eta_{iso,\,T}$ = 0.85 Evaporator Temperature = -25 ^{0}C Mass Fraction of Ammonia = 0.34 Operating Fluid	Waste heat-based combine Rankine-absorption power and cooling cycle	[201]	CCHP cycle integrated system	20.52 %	35.56 %	610.722 kW	224.947 kW	458.59 kW

Temperature = 300 ^{0}C Working Fluid – NH_3-H_2O								
Inlet Temperature of turbine = 100 ^{0}C Inlet Pressure of turbine = 0.6 MPa $\eta_{iso,\ T}$ = 0.85 Evaporator Temperature = -10 ^{0}C Extraction Ratio = 0.35 $\eta_{n\ =}$ 0.9, η_D = 0.85, $\eta_{m\ =}$ 0.85 Working Fluid – R123, R124, R141b, R290, R134a, R152a	Waste heat-based combine power, heating and cooling integrated system	[204]	ORC-ERS integrated system	13.67 %	22.75 %	113.53 kW	62.34 kW	112.52 kW

Chapter 6

Conclusions

This chapter summarises the results of thermodynamic investigations of the five systems considered in the study. The five systems that were examined for this investigation are listed as; SPT-based combined HBC and ORC with an ejector refrigeration integrated system, SPT-based combined HBC and ORC with a cascade VAR-VCR integrated system, SPT-based combined HBC and ORC with a cascade ERS-VRS integrated system, combined Rankine-absorption power and refrigeration cycle integrated system, and combined power, heating, and cooling integrated system driven by a low-temperature heat source using various eco-friendly refrigerants have been presented. The main conclusions of the current work were drawn from the thermodynamic investigations, and they are outlined below:

6.1. SPT based combined HBC and ORC with ejector refrigeration trigeneration system

Thermodynamic analysis of the SPT-powered combined HBC and ORC with ejector refrigeration cycle was investigated in this objective and the following conclusions were made;

1. The HBC-ORC-ERS cycle's Thermal and exergy efficiency improved by 5.26 % and 5.04%, respectively, by recovering waste heat using bottoming ORC.

2. The combined cycle's net power output and efficiency increased consistently with solar irradiation, helium turbine inlet temperature, ORC turbine inlet temperature, and evaporator temperature.

3. In addition, through the WHRU, the ORC-ERS unit could absorb 13,261 kW of waste heat out of 31,027 kW of solar heat absorbed by the HBC.

4. Combined cycle/trigeneration system (HBC-ORC-ERS) energy and exergy efficiency were found to be 48.33% and 64.4%, respectively, at the 2.3 of CPR and at the 850W/m^2 of DNI.

5. The overall plant obtained 25.12% exergy efficiency, 23.3% energy efficiency and 14,998kW power output; cooling and heating productions are 8.25 kW and 60.52 kW, respectively, at an optimum CPR of 2.3.

6. Only the receiver and heliostats in the SPT subsystem had the highest rate of exergy destruction. It represented roughly 83.20% (37,578 kW) of the plant's total exergy destruction (45,593 kW).

7. The advantage of the present analysis is to develop an efficient power system to generate carbon-free power, heating and cooling in future with fewer components compared to previous research.

8. The exergoeconomic and environmental analysis of the present work may be recommended for further study.

6.2. SPT based combined HBC and ORC with cascade VAR-VCR integrated system

In this section, performance evaluation of the SPT based combined HBC and ORC with cascade VAR-VCR integrated system as bottoming cycle using ultra-low GWP working fluid R410a were considered and the following conclusions have been made:

1. Integration of two different refrigeration cycles using a cascaded system and power cycle produces cooling at two different temperatures along power simultaneously.

2. The SPT-based plant (SPT-HBC-VAR-VCR) generates exergy and energy efficiencies of 39.53% and 28.82%, respectively, under typical operating conditions.

3. COPs were used to calculate the heating and cooling performance. Calculations revealed that COP_c and COP_h were, respectively, 0.5391 and 1.539.

4. The trigeneration system was obtained as 74.98% of exergy efficiency. However, the solar sub-system accounts for the largest portion of the plant's total exergy destruction, or about 78.18% (22763 kW).

5. Furthermore, the parametric evaluation revealed that the efficiency of the receiver and heliostat, CPR, HT turbine inlet temperature, and temperature of the evaporator and generator all had a significant impact on the performance of the plant.

6. In addition, the current system generated heating effects for applications like domestic water heating etc. and cooling at low temperatures for food preservation, etc.

7. Furthermore, a comparative analysis with relevant previous studies has shown that the proposed CCHP system outperforms systems based on supercritical CO_2 cycles and the Rankine cycles.

8. The proposed plant is limited to operating at peak load conditions due to the absence of a thermal energy storage system. The economic feasibility as well as optimization study of the present proposed work can be work for future research.

6.3. SPT based combined HBC and ORC with cascade ERS-VRS integrated system

In this third section, parametric analysis of the SPT based combined HBC and ORC with cascade ERS-VRS integrated system were investigated and the following conclusions were made:

1. The overall proposed solar plant (SPT-HBC-ORC-ERS-VCR) obtained energy efficiency and exergy efficiency of 60.66% and 35.55%, respectively. However, the net workout was obtained as 15585 kW.

2. Heating and cooling effects were obtained as 14967 kW and 730 kW for the industrial application and food storage application respectively.

3. The exergy efficiency of the conventional plant (SPT-HBC) was obtained as 32.29%. The exergy efficiency of the proposed system is 10.09% higher than conventional plants.

4. The high heat loss obtained in the heliostats field and the central receiver. This is due to much useful energy obtained from the proposed system in terms of heating, cooling effects and power generation.

5. It can be seen that the overall proposed solar plant's exergy efficiency is lower than the trigeneration system due to the higher irreversibility's present in the SPT components, i.e.in the central receiver and the heliostats field.

6. The energy, exergy efficiency and network production decreased from 68.63% to 58.67%, 35.91% to 35.46% and 15675 kW to 15222 kW, respectively, as the entertainment ratio increased from 1.5 to 4. However, the heating and cooling loads decreased from 18709 kW to 14301 kW and 1459 kW to 547.1 kW, respectively, as the entertainment ratio increased from 1.5 to 4.

7. Parametric analysis reveals that solar parameters affected the plant's performance.

8. The current study focuses solely on the thermodynamic analysis of the chosen working fluids. However, future studies will also incorporate an exergoeconomic analysis. In addition, a comprehensive thermo-economic analysis of the SPT system will be conducted in relation to other environmentally friendly refrigerants used as the working fluid in future research.

6.4. Combined Rankine-absorption power and refrigeration cycle integrated system

In this fourth section, parametric analysis of the combination of both absorption refrigeration and Rankine cycles has been carried out and the following conclusions were made:

1. The temperatures of the heat source, ambient environment, refrigeration turbine, as well as the inlet pressure and the concentration of the ammonia base solution (working fluid) significantly impact the refrigeration output, net output power, thermal efficiency, and exergy efficiency.

2. The results show that a gradual growth at turbine inlet pressure causes an eventual rise in energy efficiency and exergy efficiency of the combined cycle.

3. Heat exchanger exhaust is the biggest source of exergy destruction, followed by the heat exchanger, boiler, turbine, super-heater, absorber, condenser and rectifier, respectively.

4. Among binary working fluids as refrigerants, only an ammonia-water mixture can be employed in the combined power and refrigeration cycle. Like other fluids that are separated into refrigerant and absorbent, these fluids must function as absorbent and leave behind salty residues or sediments after passing through the turbine. Therefore, these fluids are not practically useful in turbines.

5. The cycle analyzed in this study, which includes components such as the evaporator and ejector, has the ability to generate greater refrigeration compared to other combined power and refrigeration cycles.
6. The economic feasibility as well as optimization study can be recommended for future research.

6.5. CCHP cycle using low-temperature heat source integrated system

This last section examined thermodynamic analysis of combined power, heating and cooling integrated systems driven by low-temperature heat sources using six ultra-low GWP eco-friendly refrigerants as a working fluid. The conclusions gathered from the results section have been listed below:

1. Among the several operating fluids examined in this article, R-152a and R-134a are the most appropriate from the perspectives of exergy efficiency and environmental impact for the suggested combined cycle.

2. The differences in molecular structure, operating conditions, and environmental impact contribute to the variations in exergy efficiency between R-152a and R-123, with R-152a generally having higher efficiency due to its favourable thermodynamic properties and lower environmental impact.

3. It is noted that out of 100% input energy, approximately 18.667% and 4.857% of the above-mentioned energy are converted into power and refrigeration production, respectively, while the leftover energy is lost to the environment as a result of entropy generation in the integrated system's components.

4. It has been noted that the HRVG exhaust experiences the highest exergy loss, which is 46.12%. The percentage of exergy destroyed across the HRVG, ejector, and condenser is 11.324%, 6.978% and 5.65% respectively. The percentage of exergy destruction in the remaining parts of the cycle was below one.

5. The second law analysis's results, which were used to determine the component's local irreversibility, show that the HRVG and ejector require more attention because they were been identified as the primary sources of losses within the system.

6. As the evaporator temperature rises, refrigeration output increases while exergy efficiency and entrainment ratio decline.

7. The thermal efficiency and exergy efficiency increase with the rise in temperature at the turbine input and at the heat source fluid temperature.

8. The suggested system may be recommended for future detailed studies, particularly experimental examination, to determine the specific utility of the suggested cycle to exploit various low-temperature heat sources and various eco-friendly refrigerants.

6.6. Recommendation from the conclusions

1. The ERS-ORS system is a preferred option for efficiently harnessing waste heat compared to the standard ORC system.
2. HFO working fluids are highly suggested to enhance the performance of combined power cycles and minimize both ozone depletion potential and global warming potential.
3. The ORC-ERS-VCR integrated system is the most efficient system that incorporates HBC for power production.
4. The SPT integrated system is strongly recommended above other CSP-driven systems because of its wide working temperature range.
5. The SPT based ORC-ERS system is a suitable choice for generating power, cooling, and heating simultaneously.
6. It is imperative to meticulously develop the SPT system to enhance the performance of the integrated system under investigation.

6.7. Scope for future work

1. In the future, one can utilize different genetic algorithms and optimization approaches to conduct cost analysis and multi-objective optimization of combined cycles.
2. Zoetropic mixtures can be recommended for the ORC system instead of organic fluids.
3. Thermal storage devices can be integrated into these systems to function at peak load conditions, ensuring uninterrupted solar energy and electricity output utilization. Furthermore, a comprehensive cost study of the SPT system must be conducted.
4. The exergoeconomic and environmental analysis of the present research is the future scope for further study.
5. The current work focuses exclusively on the parametric analysis and evaluation of the effects of a few selected SPT design factors on the combined cycle. Moreover, this system can be examined using additional SPT design parameters.
6. To achieve better performance, another working fluid can be examined.

References

1. Ahmad, T., & Zhang, D. (2020). A critical review of comparative global historical energy consumption and future demand: The story told so far. Energy Reports, 6, 1973-1991.
2. Ahmadi, P. (2013). Modeling, analysis and optimization of integrated energy systems for multigeneration purposes (Doctoral dissertation).
3. Ibrahim, O., Fardoun, F., Younes, R., &Louahlia-Gualous, H. (2014). Review of water-heating systems: General selection approach based on energy and environmental aspects. Building and Environment, 72, 259-286.
4. Ibrahim, O., Fardoun, F., Younes, R., &Louahlia-Gualous, H. (2014). Review of water-heating systems: General selection approach based on energy and environmental aspects. Building and Environment, 72, 259-286.
5. Liu, Z., Ciais, P., Deng, Z., Lei, R., Davis, S. J., Feng, S., ... &Schellnhuber, H. J. (2020). Near-real-time monitoring of global CO2 emissions reveals the effects of the COVID-19 pandemic. Nature communications, 11(1), 5172.
6. Spahni, R., Chappellaz, J., Stocker, T. F., Loulergue, L., Hausammann, G., Kawamura, K.,&Jouzel, J. (2005). Atmospheric methane and nitrous oxide of the late Pleistocene from Antarctic ice cores. Science, 310(5752), 1317-1321.
7. Ibrahim, O., Fardoun, F., Younes, R., &Louahlia-Gualous, H. (2014). Review of water-heating systems: General selection approach based on energy and environmental aspects. Building and Environment, 72, 259-286.
8. Day, C., & Day, G. (2017). Climate change, fossil fuel prices and depletion: The rationale for a falling export tax. Economic Modelling, 63, 153-160.
9. Dietrich, F., Chen, J., Shekhar, A., Lober, S., Krämer, K., Leggett, G.,&Röckmann, T. (2023). Climate Impact Comparison of Electric and Gas-Powered End-User Appliances. Earth's Future, 11(2), e2022EF002877.
10. Duffie, J. A., & Beckman, W. A. (1980). Solar engineering of thermal processes (p. 16591). New York: Wiley.
11. Zou, C., Zhao, Q., Zhang, G., & Xiong, B. (2016). Energy revolution: From a fossil energy era to a new energy era. Natural Gas Industry B, 3(1), 1-11.
12. Mishra, U. C. (2004). Environmental impact of coal industry and thermal power plants in India. Journal of environmental radioactivity, 72(1-2), 35-40.

13. Kar, S. K., & Gupta, A. (Eds.). (2017). Natural gas markets in India: Opportunities and challenges. Springer.
14. Briscoe, J. (2005). India's water economy, bracing for a turbulent future.TheWorld Bank, Oxford University Press, New Delhi, 1-79. 217.
15. Pandit, M. K., & Grumbine, R. E. (2012). Potential effects of ongoing and proposed hydropower development on terrestrial biological diversity in the Indian Himalaya. Conservation Biology, 26(6), 1061-1071.
16. Panwar, N. L., Kaushik, S. C., & Kothari, S. (2011). Role of renewable energy sources in environmental protection: A review. Renewable and sustainable energy reviews, 15(3), 1513-1524.
17. Demirbas, A. J. E. E. S. T. (2000). Recent advances in biomass conversion technologies. Energy Edu Sci Technol, 6, 19-41.
18. Thirugnanasambandam, M., Iniyan, S., &Goic, R. (2010). A review of solar thermal technologies. Renewable and sustainable energy reviews, 14(1), 312-322.
19. Winston, R., Miñano, J. C., & Benitez, P. G. (2005). Nonimaging optics. ElsevierAcademic Press, New York, 1-217, eBook ISBN 9780080479736.
20. Rai, G. D. (1996). Solar energy utilization, Khanna Publishers New Delhi, 1-644, ISBN-13978-81-7409-184-X.
21. Demirbas, M. F. (2007). Electricity production using solar energy. Energy Sources, Part A: Recovery, Utilization, and Environmental Effects, 29(6), 563-569.
22. Mills, D. (2004). Advances in solar thermal electricity technology. Solar energy, 76(1-3), 19-31.
23. Sharma, N. K., Tiwari, P. K., & Sood, Y. R. (2012). Solar energy in India: Strategies, policies, perspectives and future potential. Renewable and sustainable energy reviews, 16(1), 933-941.
24. Ansari, M. F., Kharb, R. K., Luthra, S., Shimmi, S. L., & Chatterji, S. (2013). Analysis of barriers to implement solar power installations in India using interpretive structural modeling technique. Renewable and sustainable energy reviews, 27, 163-174.
25. Kalogirou, S. A. (2004). Solar thermal collectors and applications. Progress in energy and combustion science, 30(3), 231-295.

26. Sharma, A. (2011). A comprehensive study of solar power in India and World. Renewable and Sustainable Energy Reviews, 15(4), 1767-1776.
27. Barlev, D., Vidu, R., & Stroeve, P. (2011). Innovation in concentrated solar power. Solar energy materials and solar cells, 95(10), 2703-2725.
28. Farges, O., Bézian, J. J., & El Hafi, M. (2018). Global optimization of solar power tower systems using a Monte Carlo algorithm: Application to a redesign of the PS10 solar thermal power plant. Renewable Energy, 119, 345-353.
29. Ahn, Y., Bae, S. J., Kim, M., Cho, S. K., Baik, S., Lee, J. I., & Cha, J. E. (2015). Review of supercritical CO2 power cycle technology and current status of research and development. Nuclear engineering and technology, 47(6), 647-661.
30. Tian, Z., Jiang, B., Malik, A., & Zheng, Q. (2019). Axial helium compressor for high-temperature gas-cooled reactor: A review. Annals of Nuclear Energy, 130, 54-68.
31. Ingersoll, D. T. (2004). Status of preconceptual design of the advanced high-temperature reactor (AHTR) (No. ORNL/TM-2004/104). Oak Ridge National Lab.(ORNL), Oak Ridge, TN (United States).
32. Macchi, E., & Astolfi, M. (Eds.). (2016). Organic rankine cycle (ORC) power systems: technologies and applications. Woodhead Publishing.
33. Tchanche, B. F., Lambrinos, G., Frangoudakis, A., & Papadakis, G. (2011). Low-grade heat conversion into power using organic Rankine cycles–A review of various applications. Renewable and Sustainable Energy Reviews, 15(8), 3963-3979.
34. Roy, J. P., Mishra, M. K., & Misra, A. (2011). Performance analysis of an Organic Rankine Cycle with superheating under different heat source temperature conditions. Applied Energy, 88(9), 2995-3004.
35. Quoilin, S., Van Den Broek, M., Declaye, S., Dewallef, P., &Lemort, V. (2013). Techno-economic survey of Organic Rankine Cycle (ORC) systems. Renewable and sustainable energy reviews, 22, 168-186.
36. Deb, K., Sindhya, K., & Hakanen, J. (2016). Multi-objective optimization. In Decision sciences (pp. 161-200). CRC Press.
37. Desai, N. B., & Bandyopadhyay, S. (2009). Process integration of organic Rankine cycle. Energy, 34(10), 1674-1686.

38. Liu, L., Yang, Q., & Cui, G. (2020). Supercritical carbon dioxide (s-CO2) power cycle for waste heat recovery: a review from thermodynamic perspective. Processes, 8(11), 1461.
39. Ahmadi, P., Rosen, M. A., & Dincer, I. (2011). Greenhouse gas emission and exergo-environmental analyses of a trigeneration energy system. International Journal of Greenhouse Gas Control, 5(6), 1540-1549.
40. Al Moussawi, H., Fardoun, F., &Louahlia-Gualous, H. (2016). Review of tri-generation technologies: Design evaluation, optimization, decision-making, and selection approach. Energy Conversion and Management, 120, 157-196.
41. Al-Sulaiman, F. A., Hamdullahpur, F., & Dincer, I. (2011). Trigeneration: a comprehensive review based on prime movers. International journal of energy research, 35(3), 233-258.
42. Anvari, S., Jafarmadar, S., &Khalilarya, S. (2016). Proposal of a combined heat and power plant hybridized with regeneration organic Rankine cycle: Energy-Exergy evaluation. Energy Conversion and Management, 122, 357-365.
43. Boyce, M. P. (2012). Combined cycle power plants. In Combined cycle systems for near-zero emission power generation (pp. 1-43). Woodhead Publishing.
44. Al-Sulaiman, F. (2010). Thermodynamic modeling and thermoeconomic optimization of integrated trigeneration plants using organic Rankine cycles.
45. Jouhara, H., Khordehgah, N., Almahmoud, S., Delpech, B., Chauhan, A., &Tassou, S. A. (2018). Waste heat recovery technologies and applications. Thermal Science and Engineering Progress, 6, 268-289.
46. Dincer, I. and Zamfirescu, C. (2011). Sustainable energy systems and applications. Springer Science & Business Media.
47. Feng, Y. Q., Wang, X., Niaz, H., Hung, T. C., He, Z. X., Zeb, A. J., & Xi, H. (2020). Experimental comparison of the performance of basic and regenerative organic Rankine cycles. Energy Conversion and Management, 223, 113459.
48. Ganapathy, V. (2014). Steam generators and waste heat boilers: For process and plant engineers. CRC press.

49. Garofalo, E., Bevione, M., Cecchini, L., Mattiussi, F., &Chiolerio, A. (2020). Waste heat to power: Technologies, current applications, and future potential. Energy Technology, 8(11), 2000413.
50. Kalogirou, S. A. (2004). Solar thermal collectors and applications. Progress in energy and combustion science, 30(3), 231-295.
51. Kim, Y. M., Sohn, J. L., & Yoon, E. S. (2017). Supercritical CO2 Rankine cycles for waste heat recovery from gas turbine. Energy, 118, 893-905.
52. Kim, M. S., Ahn, Y., Kim, B., & Lee, J. I. (2016). Study on the supercritical CO2 power cycles for landfill gas firing gas turbine bottoming cycle. Energy, 111, 893-909.
53. Cardemil, J. M., & da Silva, A. K. (2016). Parametrized overview of CO2 power cycles for different operation conditions and configurations–An absolute and relative performance analysis. Applied Thermal Engineering, 100, 146-154.
54. Mecheri, M., & Le Moullec, Y. (2016). Supercritical CO2 Brayton cycles for coal-fired power plants. Energy, 103, 758-771.
55. Park, S., Kim, J., Yoon, M., Rhim, D., & Yeom, C. (2018). Thermodynamic and economic investigation of coal-fired power plant combined with various supercritical CO2 Brayton power cycle. Applied Thermal Engineering, 130, 611-623.
56. Li, L., Ge, Y. T., Luo, X., &Tassou, S. A. (2018). Experimental analysis and comparison between CO2 transcritical power cycles and R245fa organic Rankine cycles for low-grade heat power generations. Applied Thermal Engineering, 136, 708-717.
57. Song, J., Li, X. S., Ren, X. D., & Gu, C. W. (2018). Performance improvement of a preheating supercritical CO2 (S-CO2) cycle based system for engine waste heat recovery. Energy Conversion and Management, 161, 225-233.
58. Neises, T., & Turchi, C. (2019). Supercritical carbon dioxide power cycle design and configuration optimization to minimize levelized cost of energy of molten salt power towers operating at 650 C. Solar Energy, 181, 27-36.
59. Fan, G., Li, H., Du, Y., Chen, K., Zheng, S., & Dai, Y. (2020). Preliminary design and part-load performance analysis of a recompression supercritical carbon dioxide cycle combined with a transcritical carbon dioxide cycle. Energy Conversion and Management, 212, 112758.

60. Khatoon, S., & Kim, M. H. (2020). Performance analysis of carbon dioxide based combined power cycle for concentrating solar power. Energy Conversion and Management, 205, 112416.
61. Yu, W., Gong, Q., Gao, D., Wang, G., Su, H., & Li, X. (2020). Thermodynamic analysis of supercritical carbon dioxide cycle for internal combustion engine waste heat recovery. Processes, 8(2), 216.
62. Ma, Y., Morozyuk, T., Liu, M., Yan, J., & Liu, J. (2019). Optimal integration of recompression supercritical CO2 Brayton cycle with main compression intercooling in solar power tower system based on exergoeconomic approach. Applied energy, 242, 1134-1154.
63. Garg, P., Kumar, P., & Srinivasan, K. (2013). Supercritical carbon dioxide Brayton cycle for concentrated solar power. The Journal of Supercritical Fluids, 76, 54-60.
64. Chacartegui, R., Sa´ nchez, D., Jime´ nez-Espadafor, F., Mun˜ oz, A., & Sa´ nchez, T. (2008, January). Analysis of intermediate temperature combined cycles with a carbon dioxide topping cycle. In Turbo Expo: Power for Land, Sea, and Air (Vol. 43123, pp. 673-680).
65. Wang, X., Liu, Q., Bai, Z., Lei, J., & Jin, H. (2017). Thermodynamic analysis of the cascaded supercritical CO2 cycle integrated with solar and biomass energy. Energy procedia, 105, 445-452.
66. Neises, T., & Turchi, C. (2014). A comparison of supercritical carbon dioxide power cycle configurations with an emphasis on CSP applications. Energy Procedia, 49, 1187-1196.
67. Chacartegui, R., De Escalona, J. M., Sánchez, D., Monje, B., & Sánchez, T. (2011). Alternative cycles based on carbon dioxide for central receiver solar power plants. Applied Thermal Engineering, 31(5), 872-879.
68. Sánchez, C., Juárez, R., Sanz, J., &Perlado, M. (2013). Design and analysis of helium Brayton power cycles for HiPER reactor. Fusion Engineering and Design, 88(9-10), 2679-2683.
69. Kusterer, K., Braun, R., Moritz, N., Lin, G., & Bohn, D. (2012, June). Helium Brayton cycles with solar central receivers: thermodynamic and design considerations. In Turbo

Expo: Power for Land, Sea, and Air (Vol. 44724, pp. 271-279). American Society of Mechanical Engineers.

70. Khan, Y., Singh, D., Caliskan, H., & Hong, H. (2023). Exergoeconomic and Thermodynamic Analyses of Solar Power Tower Based Novel Combined Helium Brayton Cycle-Transcritical CO2 Cycle for Carbon Free Power Generation. Global Challenges, 7(12), 2300191.
71. Zare, V., & Hasanzadeh, M. J. E. C. (2016). Energy and exergy analysis of a closed Brayton cycle-based combined cycle for solar power tower plants. Energy conversion and management, 128, 227-237.
72. Miao, X., Zhang, H., Sun, W., Wang, Q., & Zhang, C. (2022). Optimization of a recompression supercritical nitrous oxide and helium Brayton cycle for space nuclear system. Energy, 242, 123023.
73. Bi, Y., & Ju, Y. (2022). Design and analysis of an efficient hydrogen liquefaction process based on helium reverse Brayton cycle integrating with steam methane reforming and liquefied natural gas cold energy utilization. Energy, 252, 124047.
74. Zhou, J., Ali, M. A., Zeki, F. M., &Dhahad, H. A. (2023). Thermoeconomic investigation and multi-objective optimization of a novel efficient solar tower power plant based on supercritical Brayton cycle with inlet cooling. Thermal Science and Engineering Progress, 39, 101679.
75. Malik, A., Zheng, Q., & Lin, A. (2019). The design and performance analysis of highly loaded compressor of closed Brayton cycle HTGR power plant with helium xenon gas mixture as working fluid. Progress in Nuclear Energy, 117, 103084.
76. Tchanche, B., Quoilin, S., Declaye, S., Papadakis, G., &Lemort, V. (2010). Economic optimization of small scale organic Rankine cycles. In 23rd International Conference on Efficiency, Cost, Optimization, Simulation and Environmental Impact of Energy Systems.
77. Liu, B. T., Chien, K. H., & Wang, C. C. (2004). Effect of working fluids on organic Rankine cycle for waste heat recovery. Energy, 29(8), 1207-1217.
78. Saleh, B., Koglbauer, G., Wendland, M., & Fischer, J. (2007). Working fluids for low-temperature organic Rankine cycles. Energy, 32(7), 1210-1221.

79. Tchanche, B. F., Papadakis, G., Lambrinos, G., &Frangoudakis, A. (2009). Fluid selection for a low-temperature solar organic Rankine cycle. Applied Thermal Engineering, 29(11-12), 2468-2476.
80. Wang, X. D., & Zhao, L. (2009). Analysis of zeotropic mixtures used in low-temperature solar Rankine cycles for power generation. Solar Energy, 83(5), 605-613.
81. Lakew, A. A., & Bolland, O. (2010). Working fluids for low-temperature heat source. Applied Thermal Engineering, 30(10), 1262-1268.
82. Papadopoulos, A. I., Stijepovic, M., & Linke, P. (2010). On the systematic design and selection of optimal working fluids for Organic Rankine Cycles. Applied thermal engineering, 30(6-7), 760-769.
83. Mago, P. J. (2012). Exergetic evaluation of an organic Rankine cycle using medium-grade waste heat. Energy Sources, Part A: Recovery, Utilization, and Environmental Effects, 34(19), 1768-1780.
84. Ahmadi, P., Dincer, I., & Rosen, M. A. (2012). Exergo-environmental analysis of an integrated organic Rankine cycle for trigeneration. Energy conversion and Management, 64, 447-453.
85. Al-Sulaiman, F. A., Hamdullahpur, F., & Dincer, I. (2012). Performance assessment of a novel system using parabolic trough solar collectors for combined cooling, heating, and power production. Renewable Energy, 48, 161-172.
86. Lizarte, R., Palacios-Lorenzo, M. E., & Marcos, J. D. (2017). Parametric study of a novel organic Rankine cycle combined with a cascade refrigeration cycle (ORC-CRS) using natural refrigerants. Applied Thermal Engineering, 127, 378-389.
87. Xiao, S., Chen, X., Qi, L., & Liu, Y. (2020). Analysis of a supercritical organic Rankine cycle for low-grade waste heat recovery. Proceedings of the Institution of Civil Engineers-Energy, 173(1), 3-12.
88. Zhou, C. (2014). Hybridisation of solar and geothermal energy in both subcritical and supercritical Organic Rankine Cycles. Energy Conversion and Management, 81, 72-82.
89. Chen, H., Goswami, D. Y., &Stefanakos, E. K. (2010). A review of thermodynamic cycles and working fluids for the conversion of low-grade heat. Renewable and sustainable energy reviews, 14(9), 3059-3067.

90. Xu, G., Song, G., Zhu, X., Gao, W., Li, H., & Quan, Y. (2015). Performance evaluation of a direct vapor generation supercritical ORC system driven by linear Fresnel reflector solar concentrator. Applied Thermal Engineering, 80, 196-204.
91. Wang, T., Gao, N., & Zhu, T. (2018). Investigation on the optimal condensation temperature of supercritical organic Rankine cycle systems considering meteorological parameters. Energy Conversion and Management, 174, 54-64.
92. Braimakis, K., Preißinger, M., Brüggemann, D., Karellas, S., & Panopoulos, K. (2015). Low grade waste heat recovery with subcritical and supercritical Organic Rankine Cycle based on natural refrigerants and their binary mixtures. Energy, 88, 80-92.
93. Moloney, F., Almatrafi, E., & Goswami, D. Y. (2017). Working fluid parametric analysis for regenerative supercritical organic Rankine cycles for medium geothermal reservoir temperatures. Energy Procedia, 129, 599-606.
94. Shaaban, S. (2016). Analysis of an integrated solar combined cycle with steam and organic Rankine cycles as bottoming cycles. Energy conversion and management, 126, 1003-1012.
95. Guo, C., Du, X., Goswami, D. Y., & Yang, L. (2016). Investigation on working fluids selection for organic rankine cycles with low-temperature heat sources. International Journal of Green Energy, 13(6), 556-565.
96. Fu, B. R., Lee, Y. R., & Hsieh, J. C. (2016). Experimental investigation of a 250-kW turbine organic Rankine cycle system for low-grade waste heat recovery. International Journal of Green Energy, 13(14), 1442-1450.
97. Dai, Y., Hu, D., Wu, Y., Gao, Y., & Cao, Y. (2017). Comparison of a basic organic Rankine cycle and a parallel double-evaporator organic Rankine cycle. Heat Transfer Engineering, 38(11-12), 990-999.
98. Wang, E., Yu, Z., Zhang, H., & Yang, F. (2017). A regenerative supercritical-subcritical dual-loop organic Rankine cycle system for energy recovery from the waste heat of internal combustion engines. Applied Energy, 190, 574-590.
99. Singh, H., & Mishra, R. S. (2018). Performance evaluation of the supercritical organic rankine cycle (SORC) integrated with large scale solar parabolic trough collector (SPTC) system: An exergy energy analysis. Environmental Progress & Sustainable Energy, 37(2), 891-899.

100. Hoang, A. T. (2018). Waste heat recovery from diesel engines based on Organic Rankine Cycle. Applied energy, 231, 138-166.
101. Li, J., Ge, Z., Duan, Y., Yang, Z., & Liu, Q. (2018). Parametric optimization and thermodynamic performance comparison of single-pressure and dual-pressure evaporation organic Rankine cycles. Applied energy, 217, 409-421.
102. Bellos, E., Tzivanidis, C., & Torosian, K. (2018). Energetic, exergetic and financial evaluation of a solar driven trigeneration system. Thermal Science and Engineering Progress, 7, 99-106.
103. Bellos, E., &Tzivanidis, C. (2018). Investigation of a hybrid ORC driven by waste heat and solar energy. Energy Conversion and Management, 156, 427-439.
104. Zhang, X., Wu, L., Wang, X., & Ju, G. (2016). Comparative study of waste heat steam SRC, ORC and S-ORC power generation systems in medium-low temperature. Applied Thermal Engineering, 106, 1427-1439.
105. Moloney, F., Almatrafi, E., & Goswami, D. Y. (2017). Working fluid parametric analysis for regenerative supercritical organic Rankine cycles for medium geothermal reservoir temperatures. Energy Procedia, 129, 599-606.
106. Islam, S. M. S., & Saadon, S. (2020). Performance Analysis of Supercritical Organic Rankine Cycle System with Different Heat Exchangers Design Configuration. Journal of Advanced Research in Fluid Mechanics and Thermal Sciences, 65(2), 324-333.
107. Li, H., Bu, X., Wang, L., Long, Z., & Lian, Y. (2013). Hydrocarbon working fluids for a Rankine cycle powered vapor compression refrigeration system using low-grade thermal energy. Energy and buildings, 65, 167-172.
108. Hu, B., Bu, X., & Ma, W. (2014). Thermodynamic analysis of a Rankine cycle powered vapor compression ice maker using solar energy. The Scientific World Journal, 2014(1), 742606.
109. Molés, F., Navarro-Esbrí, J., Peris, B., Mota-Babiloni, A., &Kontomaris, K. K. (2015). Thermodynamic analysis of a combined organic Rankine cycle and vapor compression cycle system activated with low temperature heat sources using low GWP fluids. Applied Thermal Engineering, 87, 444-453.

110. Wu, C., Wang, S. S., Feng, X. J., & Li, J. (2017). Energy, exergy and exergoeconomic analyses of a combined supercritical CO2 recompression Brayton/absorption refrigeration cycle. Energy Conversion and Management, 148, 360-377.
111. Saleh, B. (2018). Energy and exergy analysis of an integrated organic Rankine cycle-vapor compression refrigeration system. Applied Thermal Engineering, 141, 697-710.
112. Li, H., Su, W., Cao, L., Chang, F., Xia, W., & Dai, Y. (2018). Preliminary conceptual design and thermodynamic comparative study on vapor absorption refrigeration cycles integrated with a supercritical CO2 power cycle. Energy Conversion and Management, 161, 162-171.
113. Pektezel, O., & Acar, H. I. (2019). Energy and exergy analysis of combined organic rankine cycle-single and dual evaporator vapor compression refrigeration cycle. Applied Sciences, 9(23), 5028.
114. Javanshir, N., Seyed Mahmoudi, S. M., & Rosen, M. A. (2019). Thermodynamic and exergoeconomic analyses of a novel combined cycle comprised of vapor-compression refrigeration and organic rankine cycles. Sustainability, 11(12), 3374.
115. Patel, B., Desai, N. B., Kachhwaha, S. S., Jain, V., & Hadia, N. (2017). Thermo-economic analysis of a novel organic Rankine cycle integrated cascaded vapor compression–absorption system. Journal of cleaner production, 154, 26-40.
116. Patel, B., Desai, N. B., &Kachhwaha, S. S. (2017). Optimization of waste heat based organic Rankine cycle powered cascaded vapor compression-absorption refrigeration system. Energy conversion and management, 154, 576-590.
117. Patel, B., Desai, N. B., &Kachhwaha, S. S. (2017). Thermo-economic analysis of solar-biomass organic Rankine cycle powered cascaded vapor compression-absorption system. Solar energy, 157, 920-933.
118. Faruque, M. W., Khan, Y., Nabil, M. H., & Ehsan, M. M. (2023). Parametric analysis and optimization of a novel cascade compression-absorption refrigeration system integrated with a flash tank and a reheater. Results in Engineering, 17, 101008.
119. Baniasad Askari, I., Ghazizade-Ahsaee, H., &Kasaeian, A. (2023). Investigation of an ejector-cascaded vapor compression–absorption refrigeration cycle powered by linear Fresnel and organic Rankine cycle. Environment, Development and Sustainability, 25(9), 9439-9484.

120. Li, H., Cao, F., Bu, X., Wang, L., & Wang, X. (2014). Performance characteristics of R1234yf ejector-expansion refrigeration cycle. Applied energy, 121, 96-103.
121. Wang, J., Dai, Y., & Sun, Z. (2009). A theoretical study on a novel combined power and ejector refrigeration cycle. International Journal of Refrigeration, 32(6), 1186-1194.
122. Liang, Y., Sun, Z., Dong, M., Lu, J., & Yu, Z. (2020). Investigation of a refrigeration system based on combined supercritical CO2 power and transcritical CO2 refrigeration cycles by waste heat recovery of engine. International Journal of Refrigeration, 118, 470-482.
123. Khan, Y., & Mishra, R. S. (2023). Performance analysis of a solar based novel trigeneration system using cascaded vapor absorption-compression refrigeration system. International Journal of Refrigeration, 155, 207-218.
124. Mosaffa, A. H. (2023). A new combined power and dual ejector refrigeration system using zeotropic mixtures with composition adjustable driven by geothermal resource: An exergoeconomic performance evaluation. Geothermics, 108, 102629.
125. Modi, B., Mudgal, A., & Patel, B. (2017). Energy and exergy investigation of small capacity single effect lithium bromide absorption refrigeration system. Energy Procedia, 109, 203-210.
126. Wang, J., Wang, J., Zhao, P., & Dai, Y. (2016). Thermodynamic analysis of a new combined cooling and power system using ammonia–water mixture. Energy Conversion and Management, 117, 335-342.
127. Rashidi, M. M., Bég, O. A., &Aghagoli, A. (2012). Utilization of waste heat in combined power and ejector refrigeration for a solar energy source. International Journal of Appl. Math and Mech, 8(17), 1-16.
128. Habibzadeh, A., Rashidi, M. M., & Galanis, N. (2013). Analysis of a combined power and ejector-refrigeration cycle using low temperature heat. Energy Conversion and Management, 65, 381-391.
129. Dai, Y., Wang, J., & Gao, L. (2009). Exergy analysis, parametric analysis and optimization for a novel combined power and ejector refrigeration cycle. applied thermal engineering, 29(10), 1983-1990.

130. Agrawal, B. K., & Karimi, M. N. (2013). Parametric, exergy and energy analysis of low grade energy based hybrid power and ejector refrigeration cycle. International Journal of Sustainable Building Technology and Urban Development, 4(2), 170-176.
131. Khaliq, A. (2017). Energetic and exergetic performance investigation of a solar based integrated system for cogeneration of power and cooling. Applied Thermal Engineering, 112, 1305-1316.
132. Khaliq, A., Agrawal, B. K., & Kumar, R. (2012). First and second law investigation of waste heat based combined power and ejector-absorption refrigeration cycle. International Journal of Refrigeration, 35(1), 88-97.
133. Keenan, J. H., Neumann, E. P., &Lustwerk, F. (1950). An investigation of ejector design by analysis and experiment.ASME Journal of Applied Mechanics, 72, pp.299–309.
134. Huang, B. J., Chang, J. M., Wang, C. P., & Petrenko, V. A. (1999). A 1-D analysis of ejector performance. International journal of refrigeration, 22(5), 354-364.
135. Ouzzane, M., &Aidoun, Z. (2003). Model development and numerical procedure for detailed ejector analysis and design. Applied Thermal Engineering, 23(18), 2337-2351.
136. Khaliq, A., & Kumar, R. (2007). Exergetic analysis of solar powered absorption refrigeration system using LiBr-H2O and NH3-H2O as working fluids. International Journal of Exergy, 4(1), 1-18.
137. Wang, X., & Dai, Y. (2016). Exergoeconomic analysis of utilizing the transcritical CO2 cycle and the ORC for a recompression supercritical CO2 cycle waste heat recovery: A comparative study. Applied energy, 170, 193-207.
138. Khaliq, A., Kumar, R., & Dincer, I. (2009). Exergy analysis of an industrial waste heat recovery based cogeneration cycle for combined production of power and refrigeration.
139. Njoku, I. H., Oko, C. O. C., &Ofodu, J. C. (2018). Performance evaluation of a combined cycle power plant integrated with organic Rankine cycle and absorption refrigeration system. Cogent Engineering, 5(1), 1451426.
140. Singh, H., & Mishra, R. S. (2018). Performance analysis of solar parabolic trough collectors driven combined supercritical CO2 and organic Rankine cycle. Engineering Science and Technology, an International Journal, 21(3), 451-464.

141. Akbari, A. D., & Mahmoudi, S. M. (2014). Thermoeconomic analysis & optimization of the combined supercritical CO2 (carbon dioxide) recompression Brayton/organic Rankine cycle. Energy, 78, 501-512.
142. Saleh, B. (2016). Parametric and working fluid analysis of a combined organic Rankine-vapor compression refrigeration system activated by low-grade thermal energy. Journal of advanced research, 7(5), 651-660.
143. Polyzakis, A. L., Koroneos, C., & Xydis, G. (2008). Optimum gas turbine cycle for combined cycle power plant. Energy conversion and management, 49(4), 551-563.
144. Ersayin, E., &Ozgener, L. (2015). Performance analysis of combined cycle power plants: A case study. Renewable and Sustainable Energy Reviews, 43, 832-842.
145. Hou, S., Cao, S., Yu, L., Zhou, Y., Wu, Y., & Zhang, F. (2018). Performance optimization of combined supercritical CO2 recompression cycle and regenerative organic Rankine cycle using zeotropic mixture fluid. Energy conversion and management, 166, 187-200.
146. Song, J., Li, X. S., Ren, X. D., & Gu, C. W. (2018). Performance analysis and parametric optimization of supercritical carbon dioxide (S-CO2) cycle with bottoming Organic Rankine Cycle (ORC). Energy, 143, 406-416.
147. Javanshir, A., Sarunac, N., &Razzaghpanah, Z. (2018). Thermodynamic analysis and optimization of single and combined power cycles for concentrated solar power applications. Energy, 157, 65-75.
148. Al-Sulaiman, F. A. (2014). Exergy analysis of parabolic trough solar collectors integrated with combined steam and organic Rankine cycles. Energy Conversion and Management, 77, 441-449.
149. Gao, W., Li, H., Nie, P., Zhang, Y., Yang, Y., Wang, Y., & Yao, M. (2017). Parameter and layout optimization of a high temperature solar combined cycle using low temperature thermal storage. Environmental Progress & Sustainable Energy, 36(4), 1234-1243.
150. AlZahrani, A. A., & Dincer, I. (2018). Comparative energy and exergy studies of combined CO2 Brayton-organic Rankine cycle integrated with solar tower plant. International Journal of Exergy, 26(1-2), 21-40.

151. García, J. M., Vasquez Padilla, R., & Sanjuan, M. E. (2017). Response surface optimization of an ammonia–water combined power/cooling cycle based on exergetic analysis. Journal of Energy Resources Technology, 139(2), 022001.
152. Saini, P., Singh, J., & Sarkar, J. (2020). Thermodynamic, economic and environmental analyses of a novel solar energy driven small-scale combined cooling, heating and power system. Energy Conversion and Management, 226, 113542.
153. Saini, P., Singh, J., & Sarkar, J. (2020). Proposal and performance comparison of various solar-driven novel combined cooling, heating and power system topologies. Energy Conversion and Management, 205, 112342.
154. Dabwan, Y. N., & Pei, G. (2020). A novel integrated solar gas turbine trigeneration system for production of power, heat and cooling: Thermodynamic-economic-environmental analysis. Renewable Energy, 152, 925-941.
155. Sheykhlou, H., Aghdash, M. M., Jafarmadar, S., &Aryanfar, Y. (2023). Multi-aspect prediction of the sensitivity of thermodynamic/thermoeconomic performance metrics of an innovative solar-driven trigeneration system utilizing thermal energy storage. Energy, 284, 128722.
156. Coca-Ortegón, A., Simón-Allué, R., Guedea, I., Brun, G., & Villén, R. (2023). Operational performance of trigeneration PVT-assisted HP system. Energy and Buildings, 296, 113383.
157. Chen, Y., Hu, X., Xu, W., Xu, Q., Wang, J., & Lund, P. D. (2022). Multi-objective optimization of a solar-driven trigeneration system considering power-to-heat storage and carbon tax. Energy, 250, 123756.
158. Tsimpoukis, D., Syngounas, E., Bellos, E., Koukou, M., Tzivanidis, C., Anagnostatos, S., &Vrachopoulos, M. G. (2021). Investigation of energy and financial performance of a novel CO2 supercritical solar-biomass trigeneration system for operation in the climate of Athens. Energy Conversion and Management, 245, 114583.
159. Alharthi, M. A., Khaliq, A., Alqaed, S., &Almehmadi, F. (2023). Investigation of new combined cooling, heating and power system based on solar thermal power and single-double-effect refrigeration cycle. Energy Reports, 9, 289-309.

160. Wang, M., Wang, J., Zhao, P., & Dai, Y. (2015). Multi-objective optimization of a combined cooling, heating and power system driven by solar energy. Energy Conversion and Management, 89, 289-297.
161. Boyaghchi, F. A., &Heidarnejad, P. (2015). Thermoeconomic assessment and multi objective optimization of a solar micro CCHP based on Organic Rankine Cycle for domestic application. Energy conversion and Management, 97, 224-234.
162. Mahdavi, N., Ghaebi, H., & Minaei, A. (2022). Proposal and multi-aspect assessment of a novel solar-based trigeneration system; investigation of zeotropic mixture's utilization. Applied Thermal Engineering, 206, 118110.
163. You, H., Xiao, Y., Han, J., Lysyakov, A., & Chen, D. (2023). Thermodynamic, exergoeconomic and exergoenvironmental analyses and optimization of a solid oxide fuel cell-based trigeneration system. International Journal of Hydrogen Energy, 48(66), 25918-25938.
164. Bellos, E., &Tzivanidis, C. (2018). Multi-objective optimization of a solar driven trigeneration system. Energy, 149, 47-62.
165. Li, Q., Erqi, E., & Qiu, Y. (2022). Triple-objective optimization of He Brayton cycles for ultra-high-temperature solar power tower. Energy Conversion and Management, 270, 116210.
166. Kelem, U. R., & Yilmaz, F. (2024). Development and assessment of a novel multigeneration plant combined with a supercritical CO2 cycle for multiple products. International Journal of Hydrogen Energy, 52, 1306-1318.
167. Sun, L., Wang, D., & Xie, Y. (2021). Energy, exergy and exergoeconomic analysis of two supercritical CO2 cycles for waste heat recovery of gas turbine. Applied thermal engineering, 196, 117337.
168. Khan, Y., Mishra, R. S., & Singh, A. P. (2024). Performance comparison of organic Rankine cycles integrated with solar based combined cycle: A thermodynamic and exergoenvironmental analysis. Proceedings of the Institution of Mechanical Engineers, Part C: Journal of Mechanical Engineering Science, 238(1), 233-248.
169. Qin, L., Xie, G., Ma, Y., & Li, S. (2023). Thermodynamic analysis and multi-objective optimization of a waste heat recovery system with a combined supercritical/transcritical CO2 cycle. Energy, 265, 126332.

170. Khatoon, S., & Kim, M. H. (2022). Preliminary design and assessment of concentrated solar power plant using supercritical carbon dioxide Brayton cycles. Energy Conversion and Management, 252, 115066.
171. Anjum, A., Mishra, R. S., & Samsher. (2024). Performance evaluation of a solar based Brayton cycle integrated vapor compression-absorption trigeneration system for power, heating and low temperature cooling. Proceedings of the Institution of Mechanical Engineers, Part C: Journal of Mechanical Engineering Science, 09544062241237418.
172. Anjum, A., Mishra, R. S., & Samsher. (2024). Thermodynamic assessment of a novel solar powered trigeneration system for combined power generation, heating, and cooling. Proceedings of the Institution of Mechanical Engineers, Part C: Journal of Mechanical Engineering Science, 09544062241230222.
173. Ahn, Y., Bae, S. J., Kim, M., Cho, S. K., Baik, S., Lee, J. I., & Cha, J. E. (2015). Review of supercritical CO2 power cycle technology and current status of research and development. Nuclear engineering and technology, 47(6), 647-661.
174. Dunham, M. T., & Iverson, B. D. (2014). High-efficiency thermodynamic power cycles for concentrated solar power systems. Renewable and Sustainable Energy Reviews, 30, 758-770.
175. Olumayegun, O., Wang, M., & Kelsall, G. (2016). Closed-cycle gas turbine for power generation: A state-of-the-art review. Fuel, 180, 694-717.
176. Mohammadi, A., Kasaeian, A., Pourfayaz, F., & Ahmadi, M. H. (2017). Thermodynamic analysis of a combined gas turbine, ORC cycle and absorption refrigeration for a CCHP system. Applied Thermal Engineering, 111, 397-406.
177. Rostamzadeh, H., Ebadollahi, M., Ghaebi, H., Amidpour, M., &Kheiri, R. (2017). Energy and exergy analysis of novel combined cooling and power (CCP) cycles. Applied Thermal Engineering, 124, 152-169.
178. Ibrahim, T. K., Mohammed, M. K., Awad, O. I., Abdalla, A. N., Basrawi, F., Mohammed, M. N., ... & Mamat, R. (2018). A comprehensive review on the exergy analysis of combined cycle power plants. Renewable and Sustainable Energy Reviews, 90, 835-850.

179. Sadreddini, A., Fani, M., Aghdam, M. A., & Mohammadi, A. (2018). Exergy analysis and optimization of a CCHP system composed of compressed air energy storage system and ORC cycle. Energy conversion and management, 157, 111-122.
180. Farges, O., Bézian, J. J., & El Hafi, M. (2018). Global optimization of solar power tower systems using a Monte Carlo algorithm: Application to a redesign of the PS10 solar thermal power plant. Renewable Energy, 119, 345-353.
181. Doiphode, G. V., & Najafi, H. (2019, July). An Energetic and Exergoeconomic Analysis of a CCHP System With Micro Gas Turbine, Organic Rankine Cycle and Ammonia-Water Absorption Refrigeration Cycle. In Energy Sustainability (Vol. 59094, p. V001T16A003). American Society of Mechanical Engineers.
182. Kumar, P., & Singh, O. (2019). Thermoeconomic analysis of SOFC-GT-VARS-ORC combined power and cooling system. International journal of hydrogen energy, 44(50), 27575-27586.
183. Gkountas, A. A., Benos, L. T., Nikas, K. S., & Sarris, I. E. (2020). Heat transfer improvement by an Al2O3-water nanofluid coolant in printed-circuit heat exchangers of supercritical CO2 Brayton cycle. Thermal Science and Engineering Progress, 20, 100694.
184. Chai, L., &Tassou, S. A. (2020). A review of printed circuit heat exchangers for helium and supercritical CO2 Brayton cycles. Thermal Science and Engineering Progress, 18, 100543.
185. Wang, S., Liu, C., Li, J., Sun, Z., Chen, X., & Wang, X. (2020). Exergoeconomic analysis of a novel trigeneration system containing supercritical CO2 Brayton cycle, organic Rankine cycle and absorption refrigeration cycle for gas turbine waste heat recovery. Energy Conversion and Management, 221, 113064.
186. Yağlı, H., Koç, Y., & Kalay, H. (2021). Optimisation and exergy analysis of an organic Rankine cycle (ORC) used as a bottoming cycle in a cogeneration system producing steam and power. Sustainable Energy Technologies and Assessments, 44, 100985.
187. Manzolini, G., Lucca, G., Binotti, M., &Lozza, G. (2021). A two-step procedure for the selection of innovative high temperature heat transfer fluids in solar tower power plants. Renewable Energy, 177, 807-822.
188. Tsimpoukis, D., Syngounas, E., Bellos, E., Koukou, M., Tzivanidis, C., Anagnostatos, S., &Vrachopoulos, M. G. (2021). Investigation of energy and financial performance of a

novel CO2 supercritical solar-biomass trigeneration system for operation in the climate of Athens. Energy Conversion and Management, 245, 114583.

189. Altarawneh, O. R., Alsarayreh, A. A., Ala'a, M., Al-Kheetan, M. J., &Alrwashdeh, S. S. (2022). Energy and exergy analyses for a combined cycle power plant in Jordan. Case Studies in Thermal Engineering, 31, 101852.

190. Khan, Y., Caliskan, H., & Hong, H. (2023). A comparative study of combined cycles for concentrated solar power for efficient power generation using low Global Warming Potential (GWP) fluids to reduce environmental effects. IET Renewable Power Generation, 17(16), 3741-3754.

191. Paty, F. (2016). Conception of an ORC module for High Temperature recovery, Master ofScience Thesis, KTH industrial engineering and management.

192. Oyewunmi, O. A., Ferré-Serres, S., Lecompte, S., van den Broek, M., De Paepe, M., & Markides, C. N. (2017). An assessment of subcritical and trans-critical organic Rankine cycles for waste-heat recovery. Energy Procedia, 105, 1870-1876.

193. Karakoc, T. H., Ozerdem, M. B., Sogut, M. Z., Colpan, C. O., Altuntas, O., Açıkkalp, E. Sustainable aviation: energy and environmental issues, First Edition, Springer international publishing Switzerland, 2016, 1-423, ISBN-13: 978-3319341798.

194. Fayaz, H., Rasachak, S., Ahmad, M. S., Kumar, L., Zhang, B., Mujtaba, M. A., ... & Omidvar, M. R. (2022). Improved surface temperature of absorber plate using metallic titanium particles for solar still application. Sustainable Energy Technologies and Assessments, 52, 102092.

195. Belkhode, P. N., Shelare, S. D., Sakhale, C. N., Kumar, R., Shanmugan, S., Soudagar, M. E. M., & Mujtaba, M. A. (2021). Performance analysis of roof collector used in the solar updraft tower. Sustainable Energy Technologies and Assessments, 48, 101619.

196. Xu, C., Wang, Z., Li, X., & Sun, F. (2011). Energy and exergy analysis of solar power tower plants. Applied Thermal Engineering, 31(17-18), 3904-3913.

197. Khan, Y., & Mishra, R. S. (2020). Parametric (exergy-energy) analysis of parabolic trough solar collector-driven combined partial heating supercritical CO2 cycle and organic Rankine cycle. Energy sources, part a: recovery, utilization, and environmental effects, 1-27.

198. Hao, X., Shan, S., Gao, N., Chen, G., Wang, Q., & Gu, T. (2023). Performance analysis of a novel combined cooling, heating and power system with solar energy spectral beam splitting. Energy Conversion and Management, 276, 116500.
199. Ho, C. K., Sims, C. A., & Christian, J. M. (2015). Evaluation of glare at the Ivanpah solar electric generating system. Energy Procedia, 69, 1296-1305.
200. Li, M., Wang, J., He, W., Gao, L., Wang, B., Ma, S., & Dai, Y. (2013). Construction and preliminary test of a low-temperature regenerative Organic Rankine Cycle (ORC) using R123. Renewable energy, 57, 216-222.
201. Mohtaram, S., Chen, W., Zargar, T., & Lin, J. (2017). Energy-exergy analysis of compressor pressure ratio effects on thermodynamic performance of ammonia water combined cycle. Energy Conversion and Management, 134, 77-87.
202. Mohtaram, S., Lin, J., Chen, W., & Nikbakht, M. A. (2017). Evaluating the effect of ammonia-water dilution pressure and its density on thermodynamic performance of combined cycles by the energy-exergy analysis approach. Mechanics, 23(2), 209-219.
203. Wang, J., Dai, Y., & Gao, L. (2008). Parametric analysis and optimization for a combined power and refrigeration cycle. Applied energy, 85(11), 1071-1085.
204. Abam, F. I., Briggs, T. A., Ekwe, E. B., Kanu, C. G., Effiom, S. O., Ndukwu, M. C., ... & Ofem, M. I. (2019). Exergy analysis of a novel low-heat recovery organic Rankine cycle (ORC) for combined cooling and power generation. Energy Sources, Part A: Recovery, Utilization, and Environmental Effects, 41(13), 1649-1662.
205. Calm, J. M. (1994). Refrigerant safety. ASHRAE journal, 36(7), 17-26.
206. Shukla, A. K., Sharma, A., Sharma, M., & Nandan, G. (2019). Thermodynamic investigation of solar energy-based triple combined power cycle. Energy Sources, Part A: Recovery, Utilization, and Environmental Effects, 41(10), 1161-1179.
207. Cengel, Y. A. and M.A. Boles. (2004). Thermodynamics An Engineering Approach (5^{th} edition), McGraw-Hill publication. New York. USA.
208. Mohtaram, S., Chen, W., & Lin, J. (2017). Investigation on the combined Rankine-absorption power and refrigeration cycles using the parametric analysis and genetic algorithm. Energy Conversion and Management, 150, 754-762.

209. Cao, Y., & Dai, Y. (2017). Comparative analysis on off-design performance of a gas turbine and ORC combined cycle under different operation approaches. Energy Conversion and Management, 135, 84-100.
210. Franco, A., & Vaccaro, M. (2014). A combined energetic and economic approach for the sustainable design of geothermal plants. Energy Conversion and Management, 87, 735-745.
211. Liu, M., & Zhang, N. (2007). Proposal and analysis of a novel ammonia–water cycle for power and refrigeration cogeneration. Energy, 32(6), 961-970.
212. Chen, Y., Han, W., & Jin, H. (2016). Thermodynamic performance optimization of the absorption-generation process in an absorption refrigeration cycle. Energy conversion and management, 126, 290-301.
213. Fallah, M., Mahmoudi, S. M. S., Yari, M., &Ghiasi, R. A. (2016). Advanced exergy analysis of the Kalina cycle applied for low temperature enhanced geothermal system. Energy conversion and management, 108, 190-201.
214. Zheng, D., Chen, B., Qi, Y., & Jin, H. (2006). Thermodynamic analysis of a novel absorption power/cooling combined-cycle. Applied Energy, 83(4), 311-323.
215. Zhang, N., Cai, R., & Lior, N. (2004, January). A novel ammonia-water cycle for power and refrigeration cogeneration. In ASME International Mechanical Engineering Congress and Exposition (Vol. 47012, pp. 183-196).
216. Yang, X., Zheng, N., Zhao, L., Deng, S., Li, H., & Yu, Z. (2016). Analysis of a novel combined power and ejector-refrigeration cycle. Energy conversion and management, 108, 266-274.
217. Al-Sayyab, A. K. S., Navarro-Esbrí, J., & Mota-Babiloni, A. (2022). Energy, exergy, and environmental (3E) analysis of a compound ejector-heat pump with low GWP refrigerants for simultaneous data center cooling and district heating. International Journal of Refrigeration, 133, 61-72.
218. Jafarmadar, S., & Habibzadeh, A. (2017, August). Study of a Combined Power and Ejector Refrigeration Cycle with Low-temperature Heat Sources by Applying Various Working Fluids. In IOP Conference Series: Earth and Environmental Science (Vol. 83, No. 1, p. 012008). IOP Publishing.

219. Kumar, S., & Gautam, R. (2022). Prospects of Factor Affecting Biodiesel Selection Strategies Based on Various Aspects: An Indian Perspective. Journal of Engineering Research (2307-1877).
220. Kumar, S., & Gautam, R. (2023). Energy and exergy assessment of diesel-tallow biodiesel blend in compression ignition engine for engine design variables. Sustainable Energy Technologies and Assessments, 57, 103305.

List of Publications

International Journals

1. A. Anjum, R. S. Mishra, and Samsher "Thermodynamic assessment of a novel solar powered trigeneration system for combined power generation, heating, and cooling." Part C: Journal of Mechanical Engineering Science (2024): 1230222.
2. A. Anjum, R. S. Mishra, and Samsher "Performance evaluation of a solar based Brayton cycle integrated vapor compression-absorption trigeneration system for power, heating and low temperature cooling." Part C: Journal of Mechanical Engineering Science (2024): 1237418.
3. A. Anjum, R. S. Mishra, and Samsher "Energy and Exergy Analysis of Combined Ejector Refrigeration Cycle Using Eco-Friendly Refrigerants." Recent Trends in Mechanical Engineering, Lecture Notes in Mechanical Engineering (2021): 131-142,
4. R.S. Mishra, A. Anjum and Samsher "Thermodynamic analysis of combined power, heating and cooling in a trigeneration system-A Review." International Journal of Research in Engineering and Innovation, Vol-2, Issue-2 (2018), 209-221

International Conferences

1. A. Anjum, R. S. Mishra, and Samsher " Thermodynamic analysis of a combined power, cooling and heating system driven by low temperature heat source using various alternative refrigerants" International conference on Advances in Renewable and Green Energy Technology, ICARGET-2023.
2. A. Anjum, R. S. Mishra, and Samsher "Thermodynamic analysis of a combined power, heating and cooling cycle in a trigeneration system using low temperature heat source with various eco-friendly refrigerants" 2nd International conference on optimization techniques in engineering and technology, ICOTET-2024.